Stability improvement of a sagnac cold atom interferometer : towards continuous operation

Indranil Dutta

UPMC SORBONNE UNIVERSITÉS

l'Observatoire de Paris — SYRTE

Systèmes de Référence Temps-Espace

THÈSE DE DOCTORAT
DE L'UNIVERSITÉ PIERRE ET MARIE CURIE

Spécialité : Physique

École doctorale : « Physique en Île-de-France »

réalisée

à SYRTE, Observatoire de Paris

présentée par

Indranil DUTTA

pour obtenir le grade de :

DOCTEUR DE L'UNIVERSITÉ PIERRE ET MARIE CURIE

Sujet de la thèse :

Stability Improvement of a Sagnac Cold Atom Interferometer: towards Continuous Operation

soutenue le 20/11/2015

devant le jury composé de :

M.	Ekkehard Peik	Rapporteur
M.	Daniel Comparat	Rapporteur
M.	John Close	Examinateur
M.	Thomas Lévèque	Examinateur
Mme.	Saïda Guellati-Khelifa	Examinatrice
M.	Arnaud Landragin	Directeur de thèse
M.	Remi Geiger	Membre invité

When I was a child, I thought as a child.
But now I have put away childish things. ...
I must be scientific.

Philip K. Dick
The Man in the High Castle

To my parents and my mentor

Acknowledgements

The transition from being a Master to a Docteur is challenging. Especially if it has to happen in three years. To put your knowledge and wit from pen and paper to practical experimentation is the challenge that I learned in a rigorous and also favourable way. As I say I "learned", I imply that someone was there to teach me. And this someone isn't just a single person. Of course scientifically some people have contributed more to guide me in this three year path, but others also have been vital to help me cross the finish line.

I started working at SYRTE with my Master thesis in March 2012 in the "Atom Interferometry and Inertial Sensors" team and fore-mostly I met ARNAUD LANDRAGIN. He introduced me to the team and I started working under his supervision. Since, then he has moved on from being the team in-charge to be the director of SRYTE but never have I felt he has stopped being my mentor. And by mentor I just don't mean professionally; directly and indirectly, I learned from him how to mature from being a student to a researcher both professionally and mentally. He was there to answer (most of) my calls and no matter weekday or weekend, day or night, professional or personal, he was always there providing the help I needed. So I profoundly acknowledge him and I was more than glad to be under his supervision for the past three and half years. What I missed out on above is to mention that when Arnaud became the director of SYRTE, he had (and still has) the responsibility of the entire research at SYRTE and in that time we had a new permanent researcher joining our team. This researcher arrived when I was handling the experiment by myself and he came and taught me that discipline and information management is the key of being a good researcher. It was hard to follow his guidelines as I was very inefficient in these terms but he always motivated and helped me to be more articulate especially in updating the experimental logbook, every single day. It did eventually help me to write and justify all the details that I have provided in this thesis report and even spend his time gruesomely correcting this manuscript. This person is REMI GEIGER and I will always be in-

debted to him for his help and support. I was also appointed a godfather in the form of SEBASTIAN BIZE and he provided me the supplementary guidance that I needed every other time and I will always be obliged to him. When I joined at SYRTE, the director of the laboratory was NOEL DIMARCQ. He has always been supportive of the work that I have been doing at SYRTE and I thank him for always being kind and helpful. I invariably thank EKKEHARD PEIK and DANIEL COMPARAT for their valuable intake on this thesis manuscript and being the rapporteurs from my thesis defense jury. I also thank SAÏDA GUELLATI-KHELIFA, THOMAS LÉVÈQUE and JOHN CLOSE for their priceless participation in my thesis defense as examinateurs in the jury for my defense.

Professionally speaking, these were not the only people who aided me to hone my skills as a research aspiring student. FRANCK PEREIRA DOS SANTOS is now our team in-charge and is always there to answer questions of the tiniest detail. I will always be thankful to him. Among other permanent staff in the team, SEBASTIAN MERLET and CARLOS L. GARRIDO ALZAR requires a special mention as they have been there professionally and personally to discuss and resolve several topics throughout my thesis period. Another special thanks goes to CHRISTINE GUERLIN who is now a permanent researcher. I worked with her during the starting period of my PhD when she was a post-doc and she always pushed me from the start and trusted me with the experiment. She was also there for a difficult time I had to go through and I will always be thankful for her heart-warming support.

Now that the professional acknowledgement is out of the way, time comes to appreciate how important the support of my fellow colleagues were. Presently, BESS FANG (post-doc) and DENIS SAVOIE (the following PhD student) is working on the cold-atom gyroscope and both have supported me and also I have supported them during the past year since they joined. My thanks also goes out to the previous PhD student, MATTHIEU MEUNIER, whose mantle I took up and he made sure the handing over of the experimental work was as smooth as possible and we shared some good times in the way. It was also a nice experience to work with the interns ISABELLE RIOU and GUILLAUME PAYET who worked on the cold-atom gyroscope and also help CAMILLA DE ROSSI and CAMILLE JANVIER who worked on the other interferometry experiments.

The times spend in the experimental room was also complemented with the time I spend at my work-desk, and my office mates played a big role to provide me company in the time that I spend working at my office and I shared a great camaraderie with them.

My office mates even included Arnaud and they kept on changing like the change of the seasons. I spend two years with JEAN LAUTIER as my office colleague and it was a grand pleasure to share my workspace with him. After he left finishing his thesis, there is now MEHDI LANGLOIS, MEROPI MORFOULI and CHRISTOPHE SCHMIT in the same office and they have always withstood me for my tantrums and blabbering and I extend my gratitude to them.

When I joined the team, my initiation was smoothened by previous fellow PhD students of the team ADELE HILICO, BRUNO PELLE, TRISTAN FARAH, JEAN-MARIE DANET, WENHUA YAN, VINCENT DUGRAIN, RINAT TYUMENEV, RAMON SZMUK, with Matthieu and Jean included. These few lines are dedicated to the friendship that we have shared for those past years and the memories we shared will always reside in my mind. Now, all the above mentioned PhD students have went along with their careers and I have had new memories to cherish with the new students who have arrived to pursue their doctoral thesis. They include CYRILLE SOLARO, PIERRE GILLOT, SATYANARAYANA BADE, MARC-ANTOINE BUCHET, KONSTANTIN OTT, XAVIER ALAUZE, NICOLAS MIELEC, ROMAIN BOUCHAND, Mehdi and Denis. I wish them a grand success in their journey and a well-deserved finale to their thesis. The post-doctoral researchers MATTHIAS LOPEZ, KATHARINA PREDEHL, SINDA MEJRI, ULRICH EISMANN, VERA GUARRERA and Bess also was there to set an example for me and I will always cherish our friendly discussions on not just physics but also on varied topics.

Among the other permanent researchers, I gladly thank RODOLPHE LE TARGAT, EMERIC DE CLERCQ and MICHEL ABGRALL for providing me with information that was crucial to shape and prepare my thesis report. There were other permanent researchers including OUALI ACEF, JOCELYNE GUENA, JEROME LODEWYCK, PETER WOLF, PHILIP TUCKEY, LUIGI DE SARLO that are among the mentionable who have assisted me throughout my thesis period. A special thanks also goes out to CHRISTIAN BORDE for his pedagogical support time to time.

The administrative team of MARINE PAILLER, FRANCIA DECOSTIER and CHRISTEL COMTE and former employees like ANNE QUEZEL deserve a good round of applause as they have always given their best when it came to handle administrative workload arriving from my part. The electronics team of MICHEL LOURS, JOSE PINTO and LAURENT VOLODIMER also deserve thanks for helping me build electrical and electronic system that I never believed I was capable of building. The me-

chanics team of DAVID HOLEVILLE, BERTRAND VENON, FLORENCE CORNU, LOUIS AMAND and STEVENS RAVILY helped me providing all the details and fabricating the mechanical systems that I worked on during my thesis work.

All my acknowledgements above was concerned with the life that I spend concentrated with my thesis at SYRTE, but during this time nothing would have been possible without the support of my beloved parents, my father SANAT KUMAR DUTTA and mother SIPRA DUTTA. They have not only been my backbone from 8000 kms away in my home city, Kolkata; but also an inspiration as the hard-working and lovely parents they are who has devoted everything for my success and there is no word to express my gratitude to them. Mentioning about family, I was also very lucky to have a part of my roots living near me: my aunt and uncle, the KINTZs' in Paris and abit further in London and Istanbul, the DUTTAs' including my cousins and they have always supported me for my study choices spanning from India to France. I also extend my thanks to my family in India living in Delhi, Mumbai and Kolkata and my loving cousins whom I gladly treat as my very own sisters. Without any question, I also extend my thanks to all my friends here in Paris who have been with me, supported me through thick and thin. They include friends from India who came to Paris to study and also the great friends I have had the honour to meet in my séjour parisien.

At last I come to an end of appreciating each and every person who have been a part of my thesis journey, mentioned or not. They were was crucial to accomplishing my work here at SYRTE. Before I go on to the scientific discussions in this report, I would like to thank CNES and FIRST-TF for the financial support of my work and CNRS and OBSERVATOIRE DE PARIS for providing me the work contract during this entire thesis period.

Contents

Chapter 1

Introduction

Rotation Sensing by Atom Interferometry

Rotation sensors are useful tools in both industry and fundamental scientific research. Highly accurate and precise rotation measurements find applications in real-time inertial navigation [1], studies of geodesy and geophysics [2], and tests of general relativity [3]. Since the early 1900s, there have been many realizations of Georges Sagnac's classic experiments [4] that utilize the Sagnac interference effect (explained in the next chapter) to measure rotation, both with light and with massive particles such as atoms [5, 6]. Recent developments in rotation sensing using matter-wave interferometers have been reviewed in [7].

Among atom interferometers (AIs), the first experiments that exploited the rotational sensitivity were carried out by Riehle *et al* [8] using optical Ramsey spectroscopy with a calcium atomic beam in 1991. They were the first to demonstrate the validity of Sagnac effect for atomic waves. In the later half of that decade, light pulses were used in [5] to manipulate a beam of cesium (Cs) atoms. The main advantage of using light pulses to interact with the atoms is their versatility and precision. One can easily modify the strength, bandwidth and phase of the light-matter interaction through precise control of the laser parameters. With the conclusion of these proof-of-principle experiments, the study of atomic gyroscopes entered a new phase, which focused primarily on developing them as rotation sensors. This meant understanding and reducing sources of noise and systematic error, as well as improving the short-term sensitivity, linearity, long-term stability and accuracy of the devices.

Improvements in Light-pulse Atom Gyroscope

By the early 2000s, Sagnac interferometers based on atomic beams had been significantly improved, compared to the first experiments in the 1990s [5, 6, 8, 9], but cold atom gyroscopes using atomic ensembles allowed higher scaling to rotation with compact set-ups. The cold-atom gyroscope experiment that started at SYRTE (France) in the early 2000s was the demonstration of this fact and its first results were published in [10]. Here, two counter-propagating clouds of Cs atoms were launched in strongly curved parabolic trajectories. Three Raman beam pairs, pulsed in time, were successively applied in three orthogonal directions leading to the measurement of the three axes of rotation and acceleration, thereby providing a full inertial base with 4 mm^2 of area. In parallel, the gyroscope of University of Hannover was constructed with an area of 19 mm^2 and recently obtained promising results [11] using composite light-pulse interferometry where the AI area was increased to 41 mm^2. This led to improvement in their short-term rotation sensitivity.

For both the above experiments the strategy to enhance the sensitivity of the gyroscope essentially consists of increasing the interferometer area. This is where the new generation of atom gyroscopes are headed. They simultaneously used two atomic clouds travelling in opposite directions in order to distinguish rotation from acceleration. In our case, we are now able to perform atom interferometry with an area as large as 11 cm^2 using only one cold atomic source which we launch in a vertical trajectory. We also use a four-pulse interferometer instead of the three pulse system, acquiring an even higher scaling to rotation and also able to cancel sensitivity to DC acceleration. This sets a benchmark for large-area AIs and make them potentially applicable in the field of geophysics, as demonstrated in the optical domain by laser-based gyroscopes [12].

Main Limitation in Inertial Atom Interferometry

The first SYRTE cold-atom gyroscope, that is mentioned above, was limited in sensitivity by the quantum projection noise. For a larger area of the gyroscope, the noise limit then comes from the rotation and acceleration fluctuations (vibrations) at frequencies higher than the sampling rate of the instrument. In our case, where we are using Raman lasers retro-reflected by a mirror/mirrors, the vibration noise is linked to the displacement of the mirror/mirrors. The impact of the Raman mirror vibrations is a commonly encountered problem in cold atom inertial sensors, and has been ad-

dressed in various works, e.g. in atomic gravimeters [13]. The corresponding limit to the sensitivity arises from the dead-time between consecutive measurements (due to the cold atom cloud preparation and detection) which results in an aliasing effect when the high frequency noise is projected onto the low frequency range. In other words, the dead-time corresponds to a loss of information on the vibration noise spectrum, making it difficult to be removed from the measurements. Fortunately, the elimination of the dead time and the increase of the sampling frequency of the experiment have been also realized now for atom interferometry through our atom gyroscope after the proof of principle was established in [14].

For long-term stability, it has been demonstrated in [15] that fluctuations of the atomic trajectories to the imperfection in the wavefront of the Raman laser is the limiting factor. The use of our vertical configuration with the four pulses, the wavefornt imperfections are no longer limiting and the reasoning has been explained in detail in [16].

Table 1.1: Long term stability comparions of present light interferometers versus our cold atom gyroscope.

Type of Gyroscope	Type of System	Interferometric Area	Long-term stability (rad/s)	Integration Time (s)
Light	Fiber-Optic (IXBLUE)(2014) [17]	3 km long fiber loop	7×10^{-11} (long-term drift)	38 days
	Gross-Ring (Germany)(2014) [18]	16 m^2 (vertical axis)	6×10^{-13}	2 hours
Cold Atom	Three-pulse (SYRTE)(2009) [15]	4 mm^2 (3 axis)	1×10^{-8}	30 mins
	Four-pulse (this work)	11 cm^2 (horizontal axis)	1.8×10^{-9}	~3 hours

Table 1.1 shows the long-term stability achieved recently by light gyroscopes and in comparison shows the present performance of our cold-atom gyroscope. The light gyroscopes have better stability in the long term with an area as big as 16 m^2 [18]. This helps them to study variation of earth's rate of rotation below 10^{-12} rad/s level. For our large area cold atom gyroscope, we are presently in the 10^{-9} rad/s sensitivity level with an area of 11 cm^2, which is $\sim1.5\times10^4$ times smaller than the Gross-Ring gyroscope. Our aim is to reach down to $\sim10^{-10}$ rad/s stability to be useful for geophysical applications with similar integration time as for our present case [Table 1.1].

Purpose of the Thesis Work

The design and construction of the present experimental set-up was achieved at the end of the thesis period of Thomas Lévèque [19]. The first four-pulse gyroscope measurement was obtained during the thesis work of Matthieu Meunier [16]. The first demonstration of the joint mode of operation giving interferometric stability enhancement in the clock configuration was also achieved during this thesis period. I started my thesis work when Matthieu was preparing the experiment for joint operation. My thesis work specifically focussed on maximizing the interferometric area to increase the rotation sensitivity and finding the best way to reject the parasitic vibration noise. In the experiment, atoms are trapped and launched in a fountain geometry. Using laser manipulation, a Mach-Zehnder interferometric structure is formed. According to the well-known Sagnac effect, the sensitivity of the interferometer to rotation is proportional to the area enclosed. We use counter-propagating Raman transitions to produce two paths of the AI to perform four-pulse interferometry. The four-pulse gyroscope has a maximum Sagnac area of 11 cm^2 and performing atom interferometry with such a big area will establish a benchmark for ground based AIs. The proof of principle for continuous measurement will also be achieved, where there is no longer any loss of information due to the dead time. This is the first ever implementation of no-dead-time operation for a cold-atom AI sensitive to inertial forces.

Plan of the Thesis Report

Chapter 2: Gyroscope using Cold Atoms

Here, I will present the theoretical basis of atom interferometry and its application as a gyroscope with four-light-pulse interferometry. I will establish the sensitivity functions for a change of phase due to external effects on the interferometer. It will then be extended to establish how acceleration and rotation of the experimental set-up will affect our four-pulse gyroscope.

Chapter 3: Experimental Set-Up and Characterizations

This chapter explains the experimental system: the main structure including the cold atomic source and the supplementary systems required to perform interferometry. The principal supplementary part is the laser system, whose characterisation is presented in this chapter. The other parts include the atomic state selection component which prepares the cold atoms in a magnetically insensitive

state before they are used for interferometry. Near the end of the chapter, a protocol for the large-area four-pulse interferometry is presented specific to our experimental set-up.

Chapter 4: Optimization of Inertial and Non-inertial Systems

In this chapter, I will describe the different optimization methods that we have followed to have an optimum signal to noise ratio for our four-pulse gyroscope. We will look into the optimizations with respect to (w.r.t.) two aspects: non-inertial and inertial noise sources. The non-inertial noise include the noise from the laser system and the detection system. The inertial noise includes mainly the vibration noise. I will show how we have isolated and compensated for vibration noise at frequency lower than 1 Hz and how it better stabilizes the experiment.

Chapter 5: Rotation Signal Extraction and Characterizations

This chapter handles the removal of the residual vibration noise after the optimization methods were established. This vibration noise is substantial, its rejection from the interferometric signal will give us finally the rotation sensitivity of our four-pulse gyroscope. To reject the vibration noise, we used external vibration sensors and used different methods and algorithms to find the best correlation between the interferometric signal and the signal treated from these external sensors. The methods we characterized using a four-pulse interferometer of an area 2.4 cm^2 and later applied to the 11 cm^2 area interferometer to obtain the best results for a cold atom gyroscope .

Chapter 6: Continuous System for Inertial Interferometry

Here, I will address the proof of principle method we performed for continuous cold-atom interferometry with no dead time operation. We used a two-pulse Ramsey interferometer for the proof of principle and I will show how the continuous operation enables for a faster averaging of the local oscillator (LO) noise down to the atom shot noise level. I will also show how we extended the continuous operation to an interleaved system where we carry out more than two atom interferometric measurements simultaneously. In the end, the application of the continuous operation will be presented for the first time for an inertial interferometer: our four-pulse 11 cm^2 area gyroscope.

An overall conclusion of the above work is presented in the end.

Chapter 2

Gyroscope using Cold Atoms

Atom interferometry is the method of coherently manipulating atomic de Broglie waves [20] to form the interferometer. Since the concept of AI was patented in 1973 (Altschuler and Franz, United States Patent 3,761,721 1973), various types of atom interferometers are used to probe fundamental physics [21, 22], studying quantum mechanical phenomena and making new types of measurements [23]. In the present day, one of the most useful applications of AIs is as inertial sensors [6], which can perform measurements with very high sensitivity. In this chapter, I will briefly describe the basic evolution of atomic interferometers to gyroscopes and the theoretical foundation our four pulse gyroscope.

2.1 Light-Pulse Atom Interferometry

Atom interferometry, in general, is performed by applying a sequence of coherent beam-splitting processes, to an ensemble of particles, separated either in time or space.

2.1.1 Basics of Interferometry

An atom interferometer is analogous to a light interferometer. In case of light interferometry, the interference takes place between two light paths manipulated by mirrors

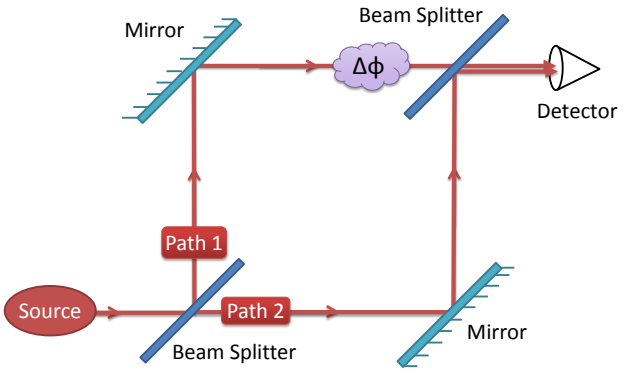

Figure 2.1: A scheme of an atom interferometer (AI) in Mach-Zehnder configuration.

and beam splitters (Fig. 2.1). This scheme illustrates Mach-Zehnder Interferometer (MZI), where the two paths encloses an area after recombination.

2.1.2 Atom Interferometry

Like in the case of an optical interferometer, the reflecting and beam-splitting conditions can be established by applying the concept of light-matter interaction between coherent light pulses and the atoms at specific intervals and of controlled durations [24]. We use cold Cs atoms as the particle used for interferometry and manipulate them using resonant light pulses from a laser source.

2.1.2.1 Stimulated Raman Transition

To perform AI, the light pulses are used to drive Raman transitions between two hyperfine ground states of the Cs atom. A Raman transition couples two atomic levels by the absorption of a photon in one laser beam and the stimulated emission of another in the other laser beam.

In our case, the states $|1\rangle$ and $|2\rangle$ in Fig. 2.2 are the states $|6S^{1/2}, F = 3\rangle$ and $|6S^{1/2}, F = 4\rangle$ of Cs , respectively. $|e\rangle$ is a far detuned level from $|6P^{3/2}, F' = 2\rangle$. To study the coherent evolution of this three-level Λ-system, we perform a quantum mechanical treatment by the time dependant Schrödinger equation (SWE),

$$i\hbar\frac{d}{dt}\Psi(t) = \widehat{H}(t)\cdot\Psi(t), \tag{2.1}$$

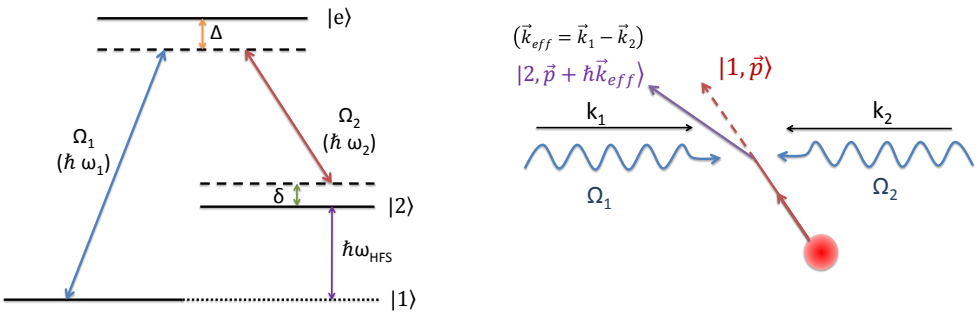

(a) three-level Raman-Λ transition (b) Counter-propagating Raman transition

Figure 2.2: Schematic of velocity selective Raman transition

where, $\widehat{H}(t) = \widehat{H}^0 + \widehat{V}(t)$ is the full Hamiltonian, the unperturbed Hamiltonian $\widehat{H}^0$ defines the energy levels of the atom, the operator $\widehat{V}(t)$ is for the time-dependant interaction of the atom and the electromagnetic field and $\Psi(t)$ denotes the wave atomic function. Here, $\widehat{V}(t) = -\hat{\vec{d}}\cdot(\vec{E_1}(t)+\vec{E_2}(t))$, where $\vec{d}$ is the dipole moment in the electric field and $\vec{E}_{1,2}$ are the electric field vectors. The coupling strength of the interaction is characterized by the Rabi frequency, $\Omega = \vec{d}\cdot\vec{E}/\hbar$. For the Raman-Λ transition, the Rabi frequencies are defined by Ω_1 and Ω_2, the total $\vec{E}$ field is:

$$\vec{E} = \vec{E}_1 e^{i(\vec{k}_1\cdot\vec{x}-\omega_1 t+\phi_1)} + \vec{E}_2 e^{i(\vec{k}_2\cdot\vec{x}-\omega_2 t+\phi_2)}. \tag{2.2}$$

The fields induce a stimulated, two-photon Raman transition in the three-level atomic system, carried out by a counter-propagating field of two laser beams with the frequencies ω_1 and ω_2 [25]. The total Hamiltonian of this system can be written as:

$$\widehat{H} = \frac{\widehat{p}^2}{2m} + \hbar\omega_1|1\rangle\langle 1| + \hbar\omega_2|2\rangle\langle 2| + \hbar\omega_e|e\rangle\langle e| - \hat{\vec{d}}\cdot\vec{E}. \tag{2.3}$$

Here, $\widehat{p}$ operates on the momentum part of the atomic state. In the momentum basis, the spatial dependance arises via the translation operator $e^{i\vec{k}\cdot\vec{x}}$ as:

$$e^{i\vec{k}\cdot\vec{x}}|\vec{p}\rangle = |\vec{p}+\hbar\vec{k}\rangle. \tag{2.4}$$

Upon interacting with the light field, the atom gains a momentum $\vec{k}_{eff}$ imparted by the two counter-propagating laser fields. If the lasers are in perfect superposition, then $\vec{k}_1 \simeq -\vec{k}_2$. Then, $\vec{k}_{eff} = \vec{k}_1 - \vec{k}_2 \simeq 2\vec{k}$. The atom then starts following a separate path

in space from its original path due to this momentum transfer, as shown in Fig. 2.2(b).

The state vector $\Psi(t)$ for the three-level system can be expressed as a superposition of the eigenstates corresponding to the levels $|e\rangle$, $|1\rangle$ and $|2\rangle$:

$$|\Psi(t)\rangle = C_e(t) \cdot |e\rangle + C_1(t) \cdot |1\rangle + C_2(t) \cdot |2\rangle. \tag{2.5}$$

The solution of the SWE is obtained by putting Eqn. (2.5) in Eqn. (2.1). Considering the intermediate excited level $|e\rangle$ evolves with fast oscillations for the far-detuned case from state $|e\rangle$ (detuning of the Raman lasers ω_1 and ω_2 from $|e\rangle$, $\Delta \gg$ linewidth of $|e\rangle$, Γ), we can consider adiabatic elimination of $|e\rangle$ [26]. Therefore, in the SWE, $\dot{C}_e = 0$. This leads to an effective Hamiltonian:

$$\widehat{H}_{eff} = \frac{\widehat{p}^2}{2m} + \hbar\omega_1|1\rangle\langle 1| + \hbar\omega_2|2\rangle\langle 2| + \left[\hbar\Omega_{eff}e^{i(\vec{k}_{eff}\cdot\vec{x}-\omega t)}|1\rangle\langle 2| + \hbar\Omega^*_{eff}e^{-i(\vec{k}_{eff}\cdot\vec{x}-\omega t)}|2\rangle\langle 1|\right]. \tag{2.6}$$

where, $\omega = \omega_1 - \omega_2$, and $\Omega_{eff} = \frac{\Omega_1\Omega_2}{2\Delta}$. We perform the rotating wave approximation, $|1\rangle = e^{i\omega_1 t}|1\rangle$ and $|2\rangle = e^{i\omega_2 t}|2\rangle$. Then, Eqn. 2.6 becomes,

$$\widehat{H}_{eff} = \frac{\widehat{p}^2}{2m} + \left[\hbar\Omega_{eff}e^{i(\vec{k}_{eff}\cdot\vec{x}-\phi(t))}|1\rangle\langle 2| + \hbar\Omega^*_{eff}e^{-i(\vec{k}_{eff}\cdot\vec{x}-\phi(t))}|2\rangle\langle 1|\right]. \tag{2.7}$$

This Hamiltonian describes the transition from $|1\rangle$ to $|2\rangle$ with a transfer of momentum $\hbar\vec{k}_{eff}$ and the phase $\phi(t)$ is imprinted from the light pulse to the atom during their interaction. The time evolution of the quantum state in Eqn. (2.5) can then be expressed as

$$|\Psi(t)\rangle = \widetilde{C}_1(t) \cdot |1,\vec{p}\rangle e^{-i\frac{|p|^2}{2m\hbar}t} + \widetilde{C}_2(t) \cdot |2,\vec{p}+2\hbar\vec{k}\rangle e^{-i\frac{|\vec{p}+2\hbar\vec{k}_{eff}|^2}{2m\hbar}t} e^{i\phi(t)}. \tag{2.8}$$

Using Eqn. (2.8) and Eqn. (2.7) in Eqn. (2.1), we get

$$\begin{aligned} |\widetilde{C}_1|^2 &= 1 - \Lambda \cdot \sin^2\left(\frac{\Omega_{eff}}{2}\tau\right), \\ |\widetilde{C}_2|^2 &= \Lambda \cdot \sin^2\left(\frac{\Omega_{eff}}{2}\tau\right), \end{aligned} \tag{2.9}$$

where, $|\widetilde{C}_{1,2}|^2$ is the population of the states $|1\rangle$ and $|2\rangle$. Egn.2.9 defines a Rabi oscillation of the two hyperfine (HF) states, where $\Lambda = \Omega^2_{eff}/\Omega^2_R$, is the amplitude of the population oscillation; $\Omega_R = \sqrt{\Omega^2_{eff} + \delta^2}$ is the generalized Rabi frequency and Ω_{eff} is the effective Rabi frequency. δ is the shift from two photon resonance. δ includes Doppler shift, recoil shift, and light shift. In Eqn. (2.9). For small detuning,

i.e., $\delta \ll \Omega_{eff}$, Eqn. (2.9) simplifies into

$$|\widetilde{C}_2|^2 = \frac{1}{2}(1 - \cos\Omega_{eff}\tau). \tag{2.10}$$

2.1.2.2 Atom Optics: Beam-splitter and Mirror

If an atom is in the state $|1\rangle$ ($|\widetilde{C}_1|^2 = 1$), and it interacts with the light pulse, there are two cases of interest for the atom interferometer:

π Pulse This case corresponds to a pulse duration of $\tau = \tau_\pi = \pi/\Omega_{eff}$. Then Eqn. (2.10) gives:

$$|\widetilde{C}_2|^2(\tau_\pi) = 1. \tag{2.11}$$

This process transfers the atom from state $|1\rangle$ to $|2\rangle$ and produces a path for $|2\rangle$ spatially separated from the original path of the atom in $|1\rangle$.

$\pi/2$ Pulse This case corresponds to a pulse duration of $\tau = \tau_{\pi/2} = \pi/(2\Omega_{eff})$. Then Eqn. (2.10) gives:

$$|\widetilde{C}_2|^2(\tau_{\pi/2}) = \frac{1}{2}. \tag{2.12}$$

This process creates a superposition of states $|1\rangle$ and $|2\rangle$ and produces two spatially separated paths corresponding to each state.

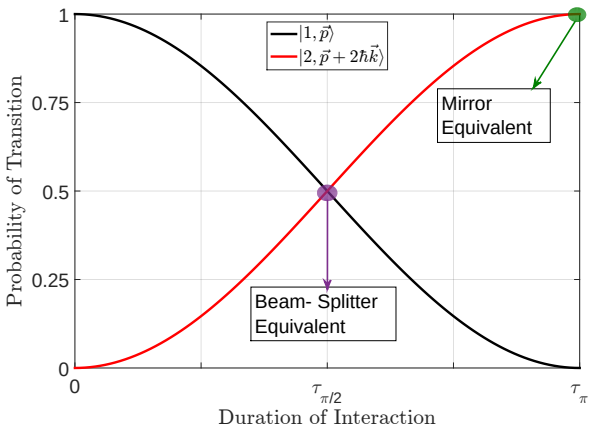

Figure 2.3: The evolution of the probability of transition of an atom interacting with a laser field

The above Eqn.s (2.12) and (2.11) are also true for $\widetilde{C}_1$ if the atom is in the state $|2\rangle$ at the beginning. Fig. 2.3 shows the evolution of the probability of transition

for $|1\rangle$ and $|2\rangle$ states for varying pulse duration τ. At $\tau = \tau_{\pi/2}$ and τ_π we have the beam-splitter and mirror equivalent for interferometry, respectively.

2.1.2.3 Mach-Zehnder Atom Interferometer

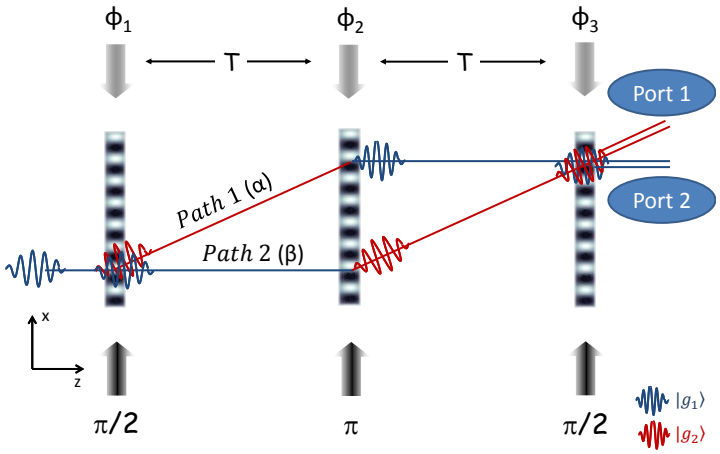

Figure 2.4: 3 pulse Mach-Zehnder AI

The structure of the 3 pulse Mach-Zehnder AI is shown in Fig. 2.4. The two superposed interferometric paths 1 and 2 are created at the first $\pi/2$ Raman pulse. Then, these paths are reflected with a π pulse and recombined with the final $\pi/2$ pulse. We can choose either Port 1 or 2 to detect the interference, e.g. by fluorescence of the interfered wavepacket with a resonant laser. For a 3 pulse MZ AI, the total laser phase accumulated during interference of the atomic wavepacket is [24]

$$\begin{aligned} \Delta\Phi_{3p} &= (\phi_1 - \phi_2) - (\phi_2 - \phi_3) \\ &= \phi_1 - 2\phi_2 + \phi_3. \end{aligned} \tag{2.13}$$

In the above equation, the sign convention of arrives from comes from the fact that if the initial state of the atom is $|1\rangle$, then after the laser interaction, the phase imprinted is $+\phi$. If the initial state is $|2\rangle$, the phase imprinted is $-\phi$.

2.2 Inertial Effects in Atom Interferometry

In the previous section, we saw how a MZI creates a superposition of two hyperfine atomic states. The separation between the paths depends on the two-photon recoil of

the atoms and also the time interval between each of the light pulses. The larger the path separation, the larger is the sensitivity of the interferometer to inertial forces, e.g. acceleration and rotation.

For a three-pulse MZ AI, when the atoms are subjected to a constant acceleration $\vec{a}$, the total differential phase $\Delta\Phi_a$ due to this acceleration is [24]:

$$\begin{aligned}\Delta\Phi_a &= \vec{k}_{eff} \cdot (\vec{r}(0) - 2\vec{r}(T) + \vec{r}(2T)) \\ &= \vec{k}_{eff} \cdot \vec{a}T^2.\end{aligned} \tag{2.14}$$

The product $\vec{a}T^2$ comes from the double integration of $\vec{a}$ which provides the displacement $\vec{r}(0)-\vec{r}(T)$ and $\vec{r}(2T)-\vec{r}(T)$ in Eqn. (2.14). $\Delta\Phi_a$ is the inertial phase accumulated due to acceleration, and is equivalent to a phase shift added in the interferometric path.

2.2.1 Sagnac Effect

In 1913, Georges Sagnac showed experimentally that when light from a coherent source was split and recombined enclosing a certain area, the interference pattern shifted in phase when the entire set-up was rotated [4]. This phase shift he found was in-fact proportional to the rotation rate, $\vec{\Omega}$. This is what came to be known as the famous Sagnac effect. For a MZI , this phase shift is accumulated between the two interferometric paths. For a non-zero area $\vec{A}$ enclosed by the MZI, the phase difference is also proportional to this area. Hence, bigger the area of the interferometer, the larger is the phase sensitivity to rotation. This shift in phase between the two paths is called the Sagnac phase shift, which depends on the rotation rate via the following expression:

$$\begin{aligned}\Delta\Phi_\Omega &= \frac{1}{\hbar c^2} \oint (\vec{\Omega} \times \vec{r}) E \cdot d\vec{r} \\ &= \frac{2E}{\hbar c^2} \vec{A} \cdot \vec{\Omega},\end{aligned} \tag{2.15}$$

where E is the rest mass energy of the quanta used for interferometry and $\vec{A}$ is the physical area enclosed by the interferometer. The instrument that is sensitive to this phase is principally a gyroscope. This definition of the Sagnac phase shift has been established for matter-waves (for electron interferometry) in [27] and [28]. The same dependence of Sagnac phase on $\vec{A}$ and $\vec{\Omega}$ is also true for light interferometers [29]. In this context, Eqn. (2.15) reveals the advantage of using AI over light interferometer. Namely, for equal interferometric area, comparing the total energy of a photon in an optical interferometer ($E_{photon} = h\nu$); and the total energy of an atom in an atom

interferometer ($E_{atom} \approx mc^2$), the ratio gives

$$\frac{E_{atom}}{E_{photon}} \approx 10^{11}. \tag{2.16}$$

The above equation warrants a huge increase in sensitivity using AI. For the three-pulse MZ AI, we consider the atom travels with an initial velocity $\vec{v}_0$ in Fig. 2.4 and the interferometer is subjected to a constant rotation $\vec{\Omega}$ in the xz-plane (rotation axis perpendicular to $\vec{k}_{eff}$ and $\vec{v}_0$). The angular displacement of the AI due to $\vec{\Omega}$ is Ωt at time t. Then, we have,

$$\Phi_t = -\vec{k}_{eff} \cdot r = -k_{eff}(v_0 t \sin(\Omega t) + v_r t \cos(\Omega t), \tag{2.17}$$

where $v_r = \hbar k_{eff}/m$ is the recoil velocity. For the three Raman pulses at $t = 0$, T and $2T$, we will have,

$$\begin{aligned} \Phi_1 &= 0, \\ \Phi_2 &= -k_{eff} v_0 T \sin(\Omega T) - k_{eff} v_r T \cos(\Omega T), \\ \Phi_3 &= -k_{eff} v_0 2T \sin(\Omega 2T) - k_{eff} v_r 2T \cos(\Omega 2T). \end{aligned} \tag{2.18}$$

Putting Eqn. (2.18) in Eqn. (2.13), we have:

$$\Delta\Phi_{rot} = -2k_{eff}\Omega v_0 T^2. \tag{2.19}$$

We obtain the above equation considering only the first order terms in ΩT. This establishes the Sagnac phase accumulated for a three-pulse interferometer. In the vectorial form Eqn. (2.19) is

$$\Delta\Phi_{rot} = -\vec{k}_{eff}(2\vec{\Omega} \times \vec{v}_0)T^2. \tag{2.20}$$

The above derivation is carried out in detail in [30]. Using, equation 2.19 and 2.15, we have the total Sagnac area for a three-pulse interferometer as,

$$A = \frac{\hbar}{m} k_{eff} v_0 T^2. \tag{2.21}$$

2.2.2 Four-pulse Atom Gyroscope

The four-pulse AI basically is a double MZI using a set of four counter-propagating Raman pulses $\pi/2 - \pi - \pi - \pi/2$ separated symmetrically in time by $T/2 - T - T/2$.

This makes the total interferometric time $2T$.

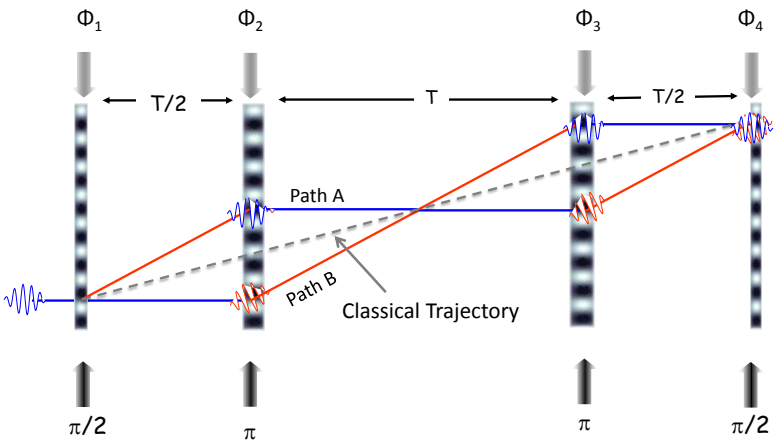

(a) Four-pulse Mach-Zehnder AI ; "Butterfly" configuration

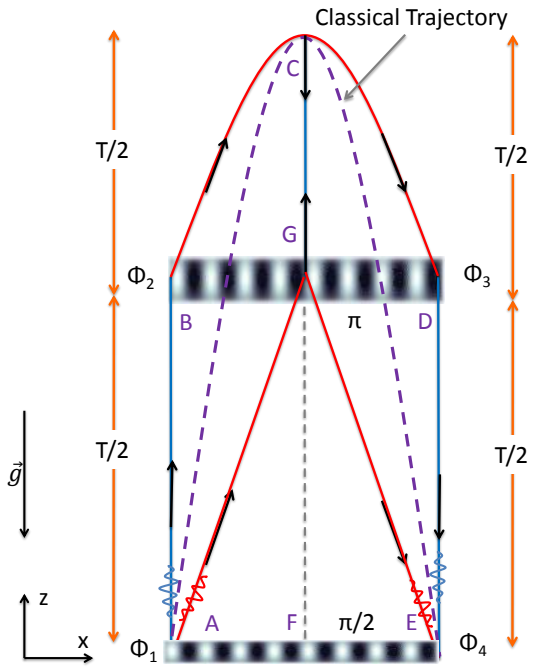

(b) Fountain geometry

Figure 2.5: 2.5(a) shows the scheme of the Mach-Zehnder four-pulse configuration. 2.5(b) shows the same configuration but in a fountain geometry

This four-pulse configuration in Fig. 2.5(a) is known as the "Butterfly" configuration [10]. Between the two π pulses the superposed paths cross each other to form two Sagnac areas, which looks like two wings of a butterfly. This configuration is utilized in our experiment in the fountain geometry: where the classical trajectory of the atomic paths represents an atomic fountain. The principal sensitivity comes from the rotation of this configuration in the xz-plane (Fig. 2.5). The laser phase accumulated in this four-pulse configuration is

$$\begin{aligned}\Delta\Phi_{4p} &= (\Phi_1 - \Phi_2 + \Phi_3 - \Phi_4)_A - (\Phi_2 - \Phi_3)_B \\ &= (\Phi_1 - 2\Phi_2 + 2\Phi_3 - \Phi_4),\end{aligned} \tag{2.22}$$

where the two paths of the interferometer are A and B (Fig. 2.5(a)). To find the rotation phase sensitivity, we first estimate the total area under the AI in the fountain geometry in Fig. 2.5(b). Since the AI is symmetric about the apogee, the total is twice the area enclosed by ABCGA in Fig. 2.5(b). The total area, A_{ABCGA} can be segmented in two parts:

$$A_{ABCGA} = A_{ABG} + A_{BCG}. \tag{2.23}$$

To find these two values of area, we first write down the velocity of the atoms in the x and z axis.

$$\begin{aligned}v_z(t)\hat{z} &= (v_0 - gt)\hat{z}, \\ v_x(t)\hat{x} &= \frac{\hbar k_{eff}}{m} t\hat{x},\end{aligned} \tag{2.24}$$

where v_0 is the initial velocity of the atoms. In this geometry, when the atom is at the apogee, $v_z(T) = 0$, Hence, $v_0 = gT$. Hence, area A_{ABG} can be approximated as the area of a triangle, since $v_0 \gg \hbar k_{eff}/m$,

$$\begin{aligned}A_{ABG} &= \frac{1}{2} \cdot z_{AB} \cdot x_{BG} \\ &= \frac{1}{2} \cdot \left(gT\frac{T}{2} - \frac{1}{2}g\left(\frac{T}{2}\right)^2 \right) \cdot \frac{\hbar k_{eff}}{m}\frac{T}{2} \\ &= \frac{3}{32} g \frac{\hbar k_{eff}}{m} T^3.\end{aligned} \tag{2.25}$$

For A_{BCG}, we neglect for now the parabolic path comprising $v_z\hat{z}$ and $v_x\hat{x}$, and also

compute the area of the triangle,

$$\begin{aligned} A_{BCG} &= \frac{1}{2} \cdot z_{GC} \cdot x_{BG} \\ &= \frac{1}{2} \cdot \left(g\frac{T}{2}\frac{T}{2} - \frac{1}{2}g\left(\frac{T}{2}\right)^2 \right) \cdot \frac{\hbar k_{eff}}{m}\frac{T}{2} \\ &= \frac{1}{32} g \frac{\hbar k_{eff}}{m} T^3. \end{aligned} \tag{2.26}$$

Hence, the total area of the four-pulse AI in Fig. 2.5(b) is

$$A = 2 \times (A_{ABG} + A_{BCG}) = \frac{1}{4}\frac{\hbar}{m}(\vec{g} \times \vec{k}_{eff})T^3. \tag{2.27}$$

Note that the above equation gives the actual area of the four-pulse interferometer despite our simplification. Putting Eqn. (2.27) in Eqn. (2.15), we get the Sagnac phase for the four-pulse interferometer:

$$\Delta\Phi_\Omega = \frac{1}{2}\vec{k}_{eff} \cdot \left(\vec{g} \times \vec{\Omega}\right)T^3. \tag{2.28}$$

The phase sensitivity above scales as T^3 for a four-pulse fountain "Butterfly" geometry because the velocity of the atom has to be proportional to the $\vec{g}$ and T, which is the time of flight to the apogee from the first pulse. Now, for a DC acceleration $a\hat{x}$, we use Eqn. (2.22) and we show for a four-pulse AI, the phase accumulated due to this DC acceleration is:

$$\begin{aligned} \Delta\Phi_a &= k_{eff}\hat{x} \cdot \left(\vec{x}(0) - 2\vec{x}\left(\frac{T}{2}\right) + 2\vec{x}\left(\frac{3T}{2}\right) - \vec{x}(2T) \right) \\ &= k_{eff}a \cdot \left(0 - 2\left(\frac{T}{2}\right)^2 + 2\left(\frac{3T}{2}\right)^2 - (2T)^2 \right) \\ &= 0. \end{aligned} \tag{2.29}$$

Hence, the DC sensitivity to acceleration for the four-pulse AI is zero. This is a big advantage as the interferometric signal will give a pure DC sensitivity to rotation and not a mix of acceleration and rotation.

2.3 Sensitivity Function for Four-pulse Interferometer

The sensitivity function describes how a system will respond to a given perturbation. Normally, the response is characterised w.r.t. an impulse or a Dirac function. We can also use a specific function and study the response of the system. In our case, this system is the interferometer, and the perturbations appears as phase perturbations from different sources, e.g., Raman lasers, inertial effects, etc.

2.3.1 Sensitivity to Change of Phase

For an interferometer, we calculate the impulse response for an infinitesimal change $\delta\phi$ of the phase of the lasers. This impulse response defines the sensitivity function of the interferometer. This formalism will allow us to calculate the sensitivity of the interferometer to change in acceleration and rotation during interferometry. If the phase difference between the Raman lasers gives a variation of $\delta\phi$ at an instant t during interferometry, this produces a change δP in the transition probability P. We define the sensitivity function as twice ratio of this change in probability of transition w.r.t. $\delta\phi$, when $\delta\phi$ tends to zero, i.e.,

$$g_\phi = 2 \lim_{\delta\phi \to 0} \frac{\delta P(\delta\phi,t)}{\delta\phi}. \tag{2.30}$$

P is related to the interferometric phase Φ as $P = \frac{1}{2}(1 + C\cos(\Phi))$. We measure P to determine the interferometric phase Φ. For maximum sensitivity, we place ourselves at mid-fringe, where $\Phi = \frac{\pi}{2}$. In Eqn. (2.30) we assumed the contrast, $C = 1$. In this case,

$$g_\phi = \lim_{\delta\phi \to 0} \frac{\delta\Phi(\delta\phi,t)}{\delta\phi}. \tag{2.31}$$

The phase shift in the interferometer can be hence calculated for an evolution of the Raman phase $\phi(t)$ with the help of the sensitivity function.

$$\Delta\Phi = \int_{-\infty}^{+\infty} g_\phi(t) d\phi(t) = \int_{-\infty}^{+\infty} g_\phi(t) \frac{d\phi(t)}{dt} dt. \tag{2.32}$$

In the temporal domain, for the four-pulse interferometer, the temporal sensitivity function to phase for a constant Rabi frequency, Ω_R is

$$g_\phi(t) = \begin{cases} 0 & t \leq -(T+3\tau) \\ -\sin\Omega_R(t+T+3\tau) & -(T+3\tau) \leq t \leq -(T+2\tau) \\ -1 & -(T+2\tau) \leq t \leq -(T/2+2\tau) \\ \sin\Omega_R(t+T/2+\tau) & -(T/2+2\tau) \leq t \leq -T/2 \\ +1 & -T/2 \leq t \leq T/2 \\ -\sin\Omega_R(t-T/2-\tau) & T/2 \leq t \leq (T/2+2\tau) \\ -1 & (T/2+2\tau) \leq t \leq (T+2\tau) \\ \sin\Omega_R(t-T-3\tau) & (T+2\tau) \leq t \leq (T+3\tau) \\ 0 & (T+3\tau) \leq t \end{cases} . \tag{2.33}$$

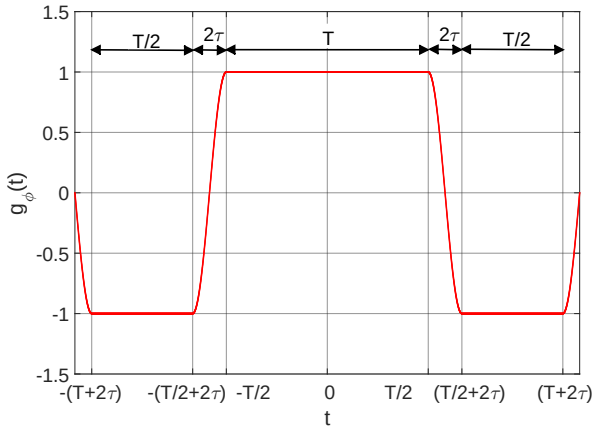

Figure 2.6: Temporal sensitivity function for the four-pulse interferometer with a total interaction time of 2T, and a $\tau_{\pi/2} = \tau$.

Considering the fact that $T >> \tau$, we can simplify $g_\phi(t)$ to:

$$g_\phi(t) = \begin{cases} -1 & 0 \leq t \leq T/2 \\ +1 & T/2 \leq t \leq 3T/2 \\ -1 & 3T/2 \leq t \leq 2T \end{cases} .$$

We use this temporal sensitivity function to phase to find the transfer function of the interferometer in frequency. We will convolve the transfer function with the input inertial noise to measure the output inertial phase noise. In the Fourier space the convolution transforms into a product. We hence make an analysis of an impulse noise at frequency ω at a given phase ψ. Then we derive the transfer function in terms of

power spectral density as a function of ω. At the same time, if we also possess the power spectral density (PSD), $S_\phi(\omega)$ of the inertial noise (in acceleration or rotation terms), we can calculate the corresponding expected variance of the phase noise, σ_ϕ^2 [31]:

$$\sigma_\phi^2 = \int_0^{+\infty} |H_\phi(\omega)|^2 S_\phi(\omega) \frac{d\omega}{2\pi}, \tag{2.34}$$

where $H_\phi(\omega)$ is the transfer function in frequency . This is the Fourier transform of g_ϕ in Fig. 2.6. For the four-pulse AI, it takes the form:

$$|H_\phi(\omega)|^2 = 64 \sin^2\left[\frac{\omega T}{2}\right] \sin^4\left[\frac{\omega T}{4}\right]. \tag{2.35}$$

2.3.2 Phase Sensitivity to Acceleration

The study of sensitivity to acceleration for the four-pulse interferometer is important to characterize the phase noise introduced by the acceleration noise from external sources. If the interferometric instrument is subjected to an acceleration $\vec{a}$, the evolution of the phase due to $\vec{a}$ is:

$$\frac{d^2\phi(t)}{dt^2} = \vec{k}_{eff} \cdot \vec{a}(t). \tag{2.36}$$

The Fourier transform of Eqn. (2.36) gives

$$\omega^2 \widetilde{\phi}(\omega) = k_{eff} \widetilde{a}(\omega), \tag{2.37}$$

where $\widetilde{\phi}$ and $\widetilde{a}$ are the Fourier transforms of ϕ and a. Using Eqn. (2.37) and Eqn. (2.35), we deduce the sensitivity function for acceleration is:

$$\begin{aligned} |H_a(\omega)|^2 &= \frac{k_{eff}^2}{\omega^4} |H_\phi(\omega)|^2 \\ &= 64 \frac{k_{eff}^2}{\omega^4} \sin^2\left[\frac{\omega T}{2}\right] \sin^4\left[\frac{\omega T}{4}\right]. \end{aligned} \tag{2.38}$$

To find the contribution of the acceleration noise, we put a commercial accelerometer on the experiment and measure the acceleration PSD, $S_a(\omega)$. Then using Eqn. (2.34), we have the variance of the phase noise for acceleration as

$$\sigma_\phi^2 = \int_0^{\infty} |H_a(\omega)|^2 S_a(\omega) \frac{d\omega}{2\pi}. \tag{2.39}$$

To express the phase sensitivity as a function of integration time τ in discrete time intervals of the cycle time T_c, we can express:

$$\sigma_\phi^2(\tau_m) = \frac{1}{\tau_m} \sum_{n=1}^{\infty} |H(2\pi n f_c)^2| S_a(2\pi n f_c). \tag{2.40}$$

Where, $f_c = 1/T_c$, and $\tau_m = mT_c$ [32].

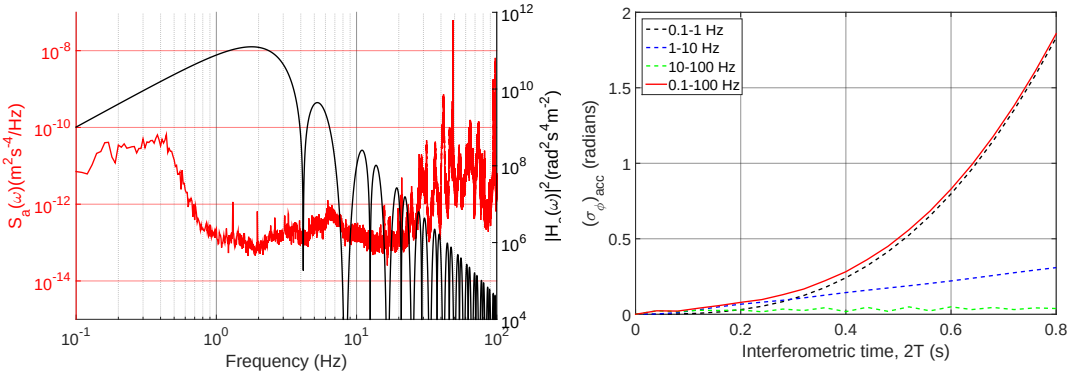

(a) (b)

Figure 2.7: 2.7(a) shows $S_a(\omega)$ and $|H_a(\omega)|^2$ for a four-pulse AI with 2T = 480 ms. $S_a(\omega)$ was recorded from an external sensor. The measurement was done when the experiment was resting on a vibration isolation platform. 2.7(b) shows the estimated phase noise due to acceleration vs the interferometric time $2T$.

Using the $S_a(\omega)$ shown in Fig. 2.7(a), we estimate the phase noise due to acceleration for different interferometric times, i.e., by varying T in Eqn. (2.38). Here, the largest contribution in the phase noise comes from the 0.1-1 Hz frequency range, peaking at ∼0.4 Hz. This is the natural frequency of the isolation platform [33] on which the experimental apparatus is resting. Since our interferometer has large interaction times, we see in Fig. 2.7(a) that $|H_a(\omega)|^2$ is maximum at $1/2T$, which is in the low frequency range. Hence, we are focused to study the effect of acceleration noise around this range. A deeper analysis of this acceleration phase noise shown in Fig. 2.7(b) and its rejection from the interferometric signal is performed in the forthcoming chapters.

2.3.3 Phase Sensitivity to Rotation

The rotation sensitivity comes from the relative angular displacement of the Raman beams (attached with the main experimental structure) with respect to the atoms. The experiment is itself rotating with the Earth and hence has a bias phase of rotation. Since the experimental structure is rests on a vibration isolation platform, one source

of the rotation noise is the rotation of the structure in the horizontal axis perpendicular to the Sagnac area.

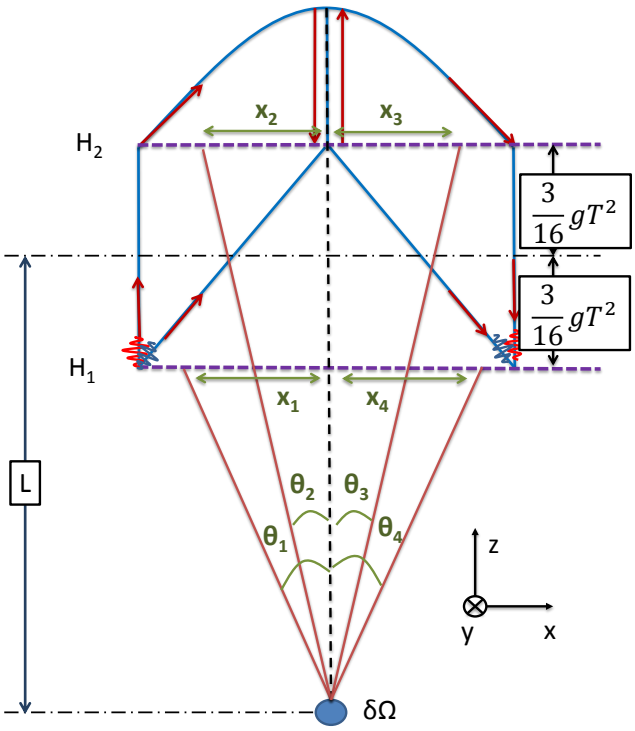

Figure 2.8: four-pulse "Butterfly" geometry considering parasitic rotation noise. The axis of the parasitic rotation is distance L from the geometrical centre of the two Raman beams placed at H_1 and H_2.

In Fig. 2.8, if we consider that the rotation axis is parallel to the y-axis, then the displacement along x-axis of the Raman beams at the two different heights of H_1 and H_2 can be considered as the tangential displacement due to the rotation acting upon the entire experimental structure. Then,

$$\begin{aligned} x_1 &= -\theta_1\Big(L - \frac{3}{16}gT^2\Big), \\ x_2 &= \theta_2\Big(L + \frac{3}{16}gT^2\Big), \\ x_3 &= \theta_3\Big(L + \frac{3}{16}gT^2\Big), \\ x_4 &= -\theta_4\Big(L - \frac{3}{16}gT^2\Big). \end{aligned} \tag{2.41}$$

To find the total phase imprinted by the Raman laser beams considering the displacements in Eqn. (2.41), we use Eqn. (2.22), where we denote $\Phi = k_{eff}x$ for each of the pulses. We define here the rotation noise as $\Omega(t) = \Omega_\omega \cos(\omega t + \psi)$. Then $\theta(t) = -\frac{\Omega_\omega}{\omega}\sin(\omega t + \psi)$. Following this formulation of θ,

$$\begin{aligned}
\theta_1 &= \theta(0) = -\frac{\Omega_\omega}{\omega}\sin(\psi),\\
\theta_2 &= \theta\left(\frac{T}{2}\right) = -\frac{\Omega_\omega}{\omega}\sin(\frac{\omega T}{2} + \psi),\\
\theta_3 &= \theta\left(\frac{3T}{2}\right) = -\frac{\Omega_\omega}{\omega}\sin(\frac{3\omega T}{2} + \psi),\\
\theta_4 &= \theta\left(2T\right) = -\frac{\Omega_\omega}{\omega}\sin(2\omega T + \psi).
\end{aligned} \tag{2.42}$$

Combining eqns.2.41 and eqns.2.42, we use them to find the total phase noise due to rotation. At a certain frequency ω and phase ψ of the rotation $\Omega(t)$, we obtain,

$$\begin{aligned}
\Delta\Phi_\omega &= k_{eff}(x_1 - 2x_2 + 2x_3 - x_4)\\
&= -8k_{eff}\frac{\Omega_\omega}{\omega}\cos(\omega T + \psi)\sin(\frac{\omega T}{2})\Big[L\cos^2\frac{\omega T}{2} + \frac{3}{16}gT^2\sin^2\frac{\omega T}{4}\Big]\\
&= -(\Omega_\omega\cos(\omega T + \psi))|H_\Omega(\omega)|.
\end{aligned} \tag{2.43}$$

From the above equation, we define the sensitivity function for rotation $|H_\Omega(\omega)|^2$ as

$$|H_\Omega(\omega)|^2 = 64\frac{k_{eff}^2}{\omega^2}\cdot\sin^2\frac{\omega T}{2}\Big[L\cos^2\frac{\omega T}{4} + \frac{3}{16}gT^2\sin^2\frac{\omega T}{4}\Big]^2. \tag{2.44}$$

This sensitivity is defined for a specific L in the above equation. When $L = 0$, the cosine term in Eqn. (2.44) disappears. This means there is no DC component in the transfer function $|H_\Omega(\omega)|$ if the rotation axis is midway between the Raman beams. When, $L \gg \frac{3}{16}gT^2$, the cosine term dominates the RHS of in Eqn. (2.44). In this case, for low frequency $\omega \to 0$, there is a DC component in $|H_\Omega(\omega)|$ which appears as a steady bias in the rotation phase. One such bias is added by the Earth's rotation as the rotation axis of Earth is far away from the experiment apparatus and has a projection along the y-axis of the experiment (Fig. 2.8).

Fig. 2.9 shows how the transfer function changes if the rotation axis originates at different positions from the geometric centre of the two Raman beams, determined by the distance L. The larger the L, the bigger is the DC component in $|H_\Omega(\omega)|^2$. In practice, the situation is more complicated as L becomes a function of ω. Then there is not a single axis of the rotation noise, but several. Using Eqn. (2.44), we can find

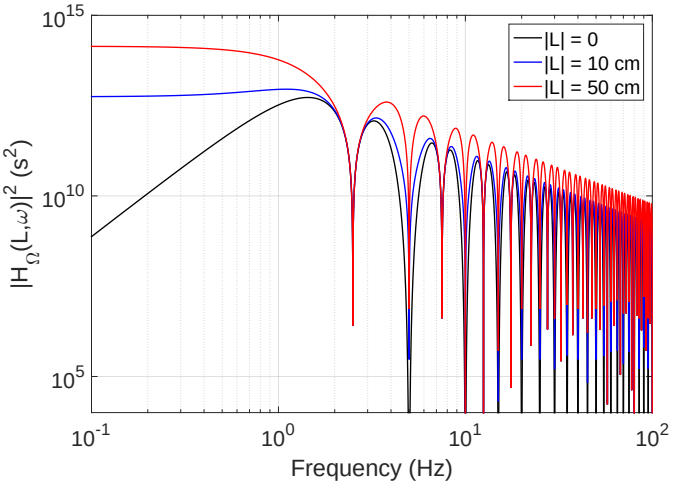

Figure 2.9: Sensitivity function for rotation for four-pulse fountain "Butterfly" geometry, with 2T = 800 ms

the variance of the rotation phase noise following Eqn. (2.39),

$$\sigma_\phi^2 = \int_{\omega_1}^{\omega_2} |H_\Omega(\omega)|^2 S_\Omega(\omega) \frac{d\omega}{2\pi}, \tag{2.45}$$

where $S_\Omega(\omega)$ stands for the rotation noise spectrum of the experimental support.

2.4 Conclusion

In this chapter we established the theoretical definition of an atom interferometer where we use light-matter interactions to produce a superposition of two paths for the interference. When the AI has a certain area and is rotated w.r.t. the lab-frame, this gives rise to rotation sensitivity in the form of the Sagnac phase shift. This phase depends on the interferometric area and the rotation rate. This gives the basis of an atom gyroscope. We present our four-pulse "Butterfly" gyroscope in a fountain geometry which has zero DC sensitivity to acceleration. We show how the rotation sensitivity for this gyroscope scales as T^3, much larger than a normal T^2 phase scaling of a three-pulse Mach-Zehnder AI. Next, we derived the phase noise transfer function in this chapter which will help us later to characterize the inertial noise in the form of acceleration and rotation and find an appropriate protocol for rejecting the inertial noise from the interferometric signal.

Chapter 3

Experimental Set-Up and Characterizations

In this chapter the details of the experimental apparatus will be presented including the systems that we use to prepare the cold Cs atoms used in interferometry, the layout of interferometric chamber, the detection system; and the protocols used to perform interferometry with large interaction times.

3.1 Experimental Components

The experimental apparatus is a long vacuum chamber assembled from shorter sections. The total height is approximately 1.7 m. The vacuum system looks like a tower where we use the fountain geometry for the gyroscope and the atoms are launched from the base to upto 1.4 m from the point of launch.

Fig. 3.1 shows the vacuum tower which is maintained at $< 10^{-9}$ mbar of pressure, with two ion pumps and two getter pumps at the top of the interferometric zone; one ion pump at the bottom (used at the 3D-MOT stage). The vacuum chamber is made of a titanium alloy $Ti^{6}Al^{4}V$, which is non-magnetic and has very weak electrical conductivity [34, 35]. It considerably reduces the parasitic magnetic fields as a result

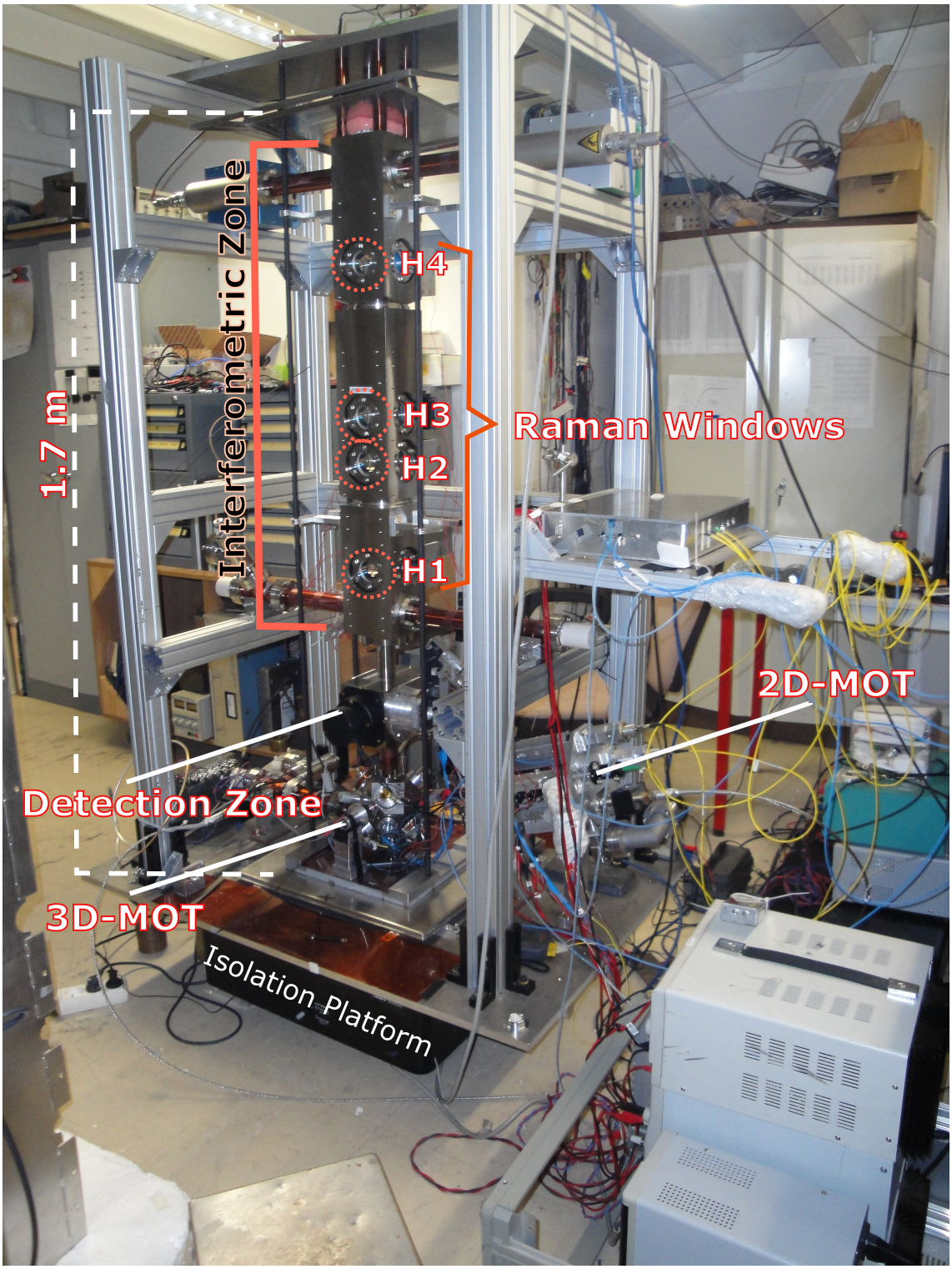

Figure 3.1: The experimental apparatus comprising the different sections of atom trapping, interferometry and detection to acquire interferometric signal.

of Eddy currents which can perturb the quantization axis of the experiment. This alloy also has almost three orders of magnitude lower out-gassing rate w.r.t. stainless steel vacuum chambers. This assures an ideal environment for precision measurements.

Among the other components attached to the experimental set-up directly, the magnetic shields form an integral part. They are made of μ-metal which has high magnetic permeability and used for shielding the apparatus against static and low frequency external magnetic field variations. There are two layers: the first layer shields the interferometric and the detection region, and the 3D-MOT separately; the second layer is an envelope for the interior layers combined. The two layers are separated by 130 mm of air with a magnetic field attenuation of a factor of 500 [19]. To set the magnetic quantization axis for the experiment, four vertical copper bars of diameter 10 mm runs from the top to the bottom to the experiment. by sending current through these bars, we can have around 40 mG of homogeneous $\vec{B}$ field near the trajectory of the atoms, defining the quantization axis of the stimulated Raman transition. These bars also work as a support system for the whole experiment in the vertical direction. We will now describe the different section of the experiment.

3.1.1 The Cold Atomic Source

3.1.1.1 2D-MOT

This is the section from where thermal Cs atoms are initially prepared in a longitudinal 2D Magneto Optical Trap (MOT). The basic structure is similar to the 2D-MOT prepared for slow atom beams in [36, 37] and was characterised for this experiment in [19, 32]. A sketch of the 2D-MOT and the 3D-MOT systems is shown in Fig. 3.2. The Cs atoms are initially trapped in this 2D trap from a Cs vapour cell and then pushed by a near-resonant laser beam towards the 3D-MOT. These optical fibers carry three input laser beams into the system: two beams for trapping in the two orthogonal directions, Π_H and Π_V, and a third beam supplying the pushing beam in the longitudinal axis Π_{push} of the trap. The fiber outputs of Π_H and Π_V are fed to home-made collimators that produce an output beam with $1/e^2$ diameter of 24 mm. The pushing fiber has a collimator which produces a waist of 1 mm. The input power for the fibers are: Π_H = 13 mW; Π_V = 13 mW; Π_{push} = 1.2 mW. A low power of the pusher is necessary for Π_{push} so that the 3D-MOT is able to capture the Cs atoms loaded from this 2D-MOT. It pushes the trapped Cs atoms producing a flux of $4{\times}10^9$ atoms/s with an average longitudinal speed of 20 m/s which is loaded into a 3D-MOT 34 cm away.

In the trap, each of the orthogonal trapping beams are divided in three parts by

polarizing beam splitting cubes and deflected towards the atoms. The laser beams are retro-reflected passing through a $\lambda/4$ plate, which produces a σ^+/σ^- configuration for the trapping. The resulting trap is elliptical of length 90 mm and width 25 mm. Around the trap lies the corresponding rectangular magnetic coils to create a longitudinal trap in 2D. Each rectangular magnetic coil pair (150 mm × 50 mm) uses approximately a current of 2.3 A, producing a field gradient of 20 G/cm. The 2D-MOT is switched on for about 50 ms before the start of the 3D-MOT for loading of the atoms.

3.1.1.2 3D-MOT

Basic Structure The vacuum in 3D-MOT chamber is maintained at around 10^{-10} mbar. The 3D MOT cools the loaded atoms along three directions in space. The laser cooling is carried out by 3 pairs of beams and in each pair the beams are counter-propagated on each other in σ^+/σ^- polarizations. The six laser beams form the six vertices at two oppositely pointing tetrahedra. This trapping structure was first demonstrated in [38]. Each beam has a $1/e^2$ diameter of 9 mm [30]. The center of the trap is fixed by the zero of the magnetic field, around which a gradient of about 10 G/cm is generated by a pair of anti-Helmholtz coils. The cooling beams are provided by six fibers: 3 for the Top beams (Π_{T1},Π_{T2},Π_{T3}) and 3 for the Bottom beams (Π_{B1},Π_{B2},Π_{B3}).

Table 3.1: Input and output power of the 6 3D-MOT fibers

Fiber:	Input (mW)	Coupling efficiency (%)	Output (μW)	I_{centre} (mW/cm^2)	I/I_{sat}
Π_{T1}	2.3	5.4	123	0.20	0.18
Π_{T2}	3.3	4.4	144	0.23	0.21
Π_{T3}	3.6	4.7	168	0.26	0.24
Π_{B1}	3.0	4.4	133	0.21	0.19
Π_{B2}	2.9	3.6	106	0.17	0.15
Π_{B3}	3.4	3.0	103	0.16	0.15
Total	18.5		777	1.23	1.12

I_{sat} for the cycling transition of $|6S_{1/2},F=4\rangle \longleftrightarrow |6P_{3/2},F'=5\rangle$ is 1.1 mW/cm^2. From Table 3.1, we see that the total laser intensity incident on the atoms from the 3D-MOT is $I = 1.12 I_{sat}$. The Doppler temperature of the atoms achieved in 3D-MOT is given by the expression [39, 40]:

$$k_B T = -\frac{\hbar\Gamma}{4}\frac{1 + I/I_{sat} + (2\Delta/\Gamma)^2}{2\Delta/\Gamma}. \tag{3.1}$$

By setting $\Delta = -1.4\Gamma$, we get the Doppler cooling temperature of the atomic cloud is 222 μK, from Eqn. (3.1).

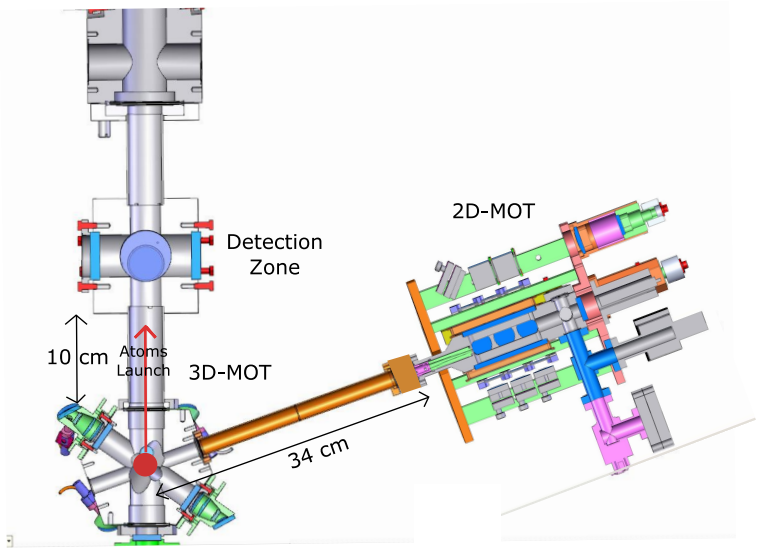

Figure 3.2: The assembly of 2D and 3D-MOT. A pushing beam is used to load the atoms from the 2D to the 3D-MOT and the trapped atoms are launched vertically.

Molasses and Launching After the trapping, we prepare the optical molasse in a method similar to [41] and launch the atomic cloud in the vertical direction. The 3D-MOT magnetic field is shut down in less than 1 ms and the atoms are conserved in an **optical molasse** stage for 6 ms with the laser detuning fixed at -5Γ. The following **launching** procedure was demonstrated in [42]. We symmetrically ramp the detuning of the top versus (vs.) the bottom set of lasers in opposite directions by $\pm\delta\nu$. Due to this frequency ramp, the atoms will stay trapped in the same temperature in its moving frame while adiabatically following the change of frequency. The relative laser power equilibrium is also changed at the initial stage of the launch, by putting less power in the top three laser beams so as to provide an initial kick. This change in power equilibrium is made from 1:1 to around 2:3 and the kick lasts for 0.6 ms. The expression of the launch velocity of the atoms v_0 is given by:

$$v_0 = \frac{\sqrt{3}}{2}\delta\nu \cdot \lambda. \tag{3.2}$$

To launch the atoms up to the top of the interferometric chamber in Fig. 3.1, we need $v_0 = 5$ m/s, and $\pm\delta\nu = 3.38$ MHz (using Eqn. (3.2)). This will provide a total interferometric time of $2T = 800$ ms for the four-pulse fountain gyroscope. The ramp

in the detuning is carried out by a Direct Digital Synthesizer AD9959 [43] which has a resolution of 32 bits for the frequency step and uses a frequency reference of 500 MHz.

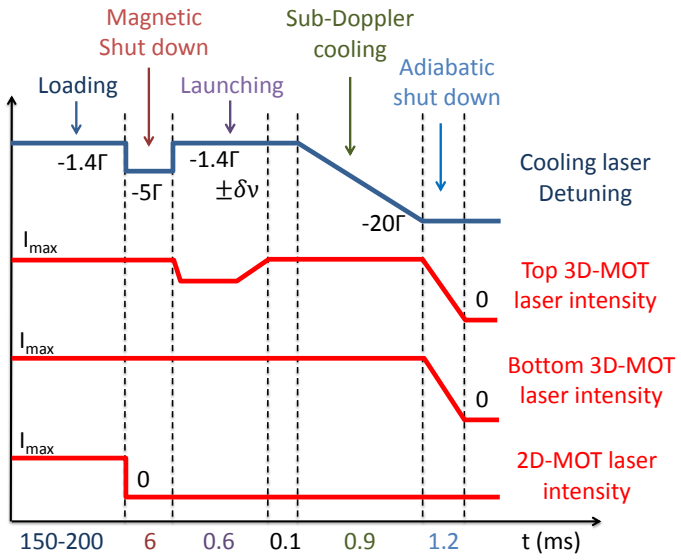

Figure 3.3: The total scheme of trapping and launching the atomic cloud w.r.t the power of the MOT lasers and the frequency detuning at the different stages. The time axis is not drawn to scale.

The atomic cloud is then cooled progressively via **sub-Doppler cooling** by linearly varying the detuning of the cooling laser down to -20Γ. The sub-Doppler cooling temperature for the atoms is given by the expression [44, 45]:

$$k_B T = \frac{\hbar\Gamma^2}{2|\Delta|}\frac{I}{I_{sat}}\left[\frac{29}{300} + \frac{254}{75}\frac{1}{4(\Delta/\Gamma)^2+1}\right], \tag{3.3}$$

which is derived for $\sigma^{\pm}$ light. This gives a sub-Doppler temperature of 0.7 μK with $\Delta = -20\Gamma$. This stage lasts for 0.9 ms. The final stage is the **adiabatic shut-down** of the laser beams whose power is progressively decreased to zero in 1.2 ms. This completes the sequence of cooling and launching the Cs atoms, and is illustrated in Fig. 3.3.

3.1.1.3 Cooling Lasers

The cooling bench comprises of the lasers used for trapping and launching of the Cs atoms via the 2D and the 3D-MOTs. The bench consists of 4 diode lasers:

Repumping Laser, L1 This laser is fixed at the transition frequency corresponding to $|6S_{1/2},F=3\rangle \longleftrightarrow |6P_{3/2},F'=2/3\rangle$. It is locked at the above mentioned crossover transition by means of spectroscopy [46]. This laser serves as the reference of frequency for the other lasers. A part of this laser is combined with the cooling lasers before it they are injected into the fibers for the 2D and 3D-MOTs. A final part is used in the detection system for repumping the atoms from $|F=3\rangle$ to $|F=4\rangle$.

Cooling Laser, L2 This laser is locked on transition of $|6S_{1/2},F=4\rangle \longleftrightarrow |6P_{3/2},F'=5\rangle$. L2 frequency locked on L1 with a beat note of a microwave frequency ∼8.8 GHz, which is compared with an external reference of 8.9 GHz provided by the frequency chain. A part of this laser is bifurcated to injection lock the two slave diode lasers (see below). The rest of the power is used for the detection of the atoms by fluorescence.

2D-MOT Slave Laser This is a diode laser injection locked at the frequency of L2. This laser is used for the 2D-MOT cooling. After fiber injection, the output is divided by a beam-splitting system for the two orthogonal directions of trapping for the 2D-MOT. A residual part is taken for the pushing beam. The final power values for these three beams is given in Section 3.1.1.1.

3D-MOT Slave laser This is the second laser injected by L2. This laser is used for the 3D-MOT cooling system. Its power is divided into two parts for the Top and Bottom beams of the 3D-MOT. The divided powers are then fiber injected into a beam splitting system to provide the 6 beams for the 3D-MOT. The final power values used in the MOT are mentioned in Table 3.1.

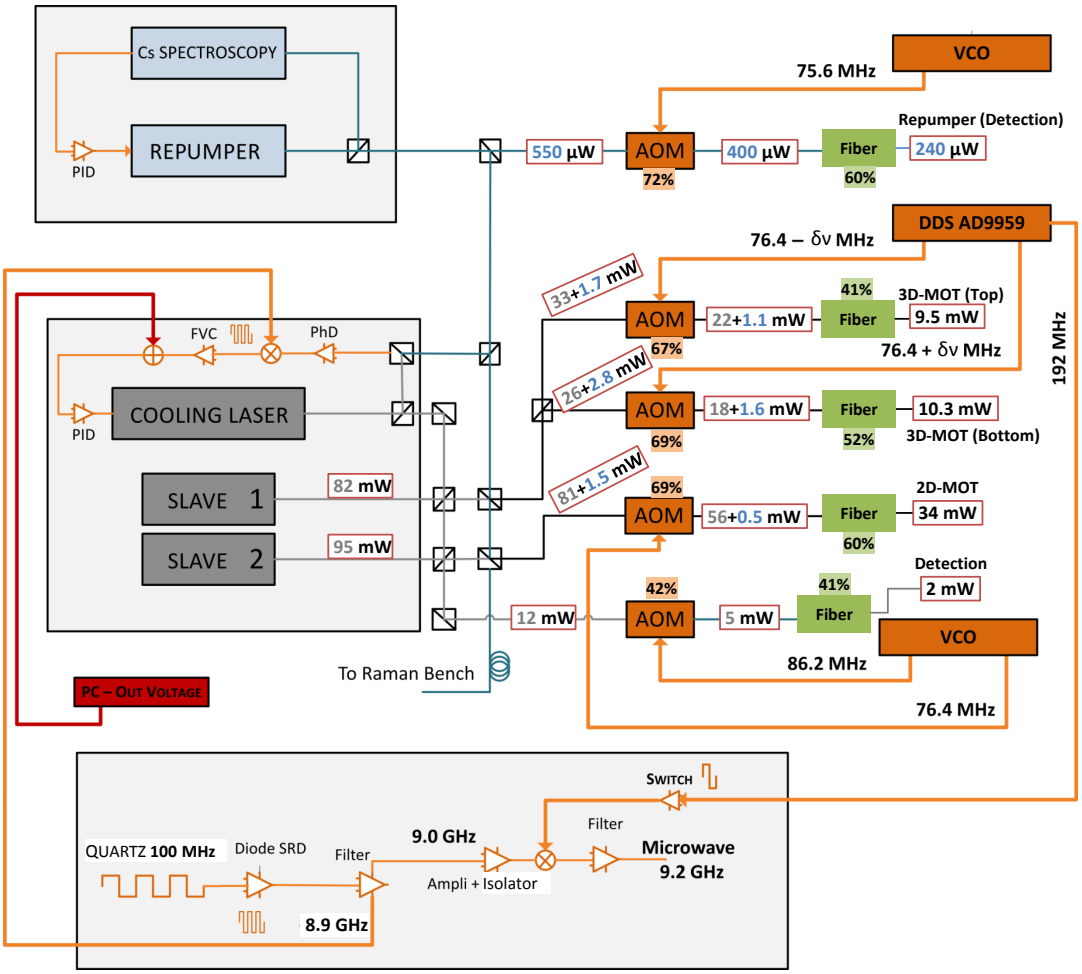

Figure 3.4: Schematic of the cooling bench. The bench has two extended cavity diode laser and two slave diode lasers. All the input and output powers for the AOMs and Fibers have been mentioned in the schematic.

Fig. 3.4 shows a detailed sketch of the cooling laser bench. All the above laser beams , before fiber injection, are frequency shifted by acousto-optic modulators (AOM). For all of them, we select the +1 diffraction order.

Table 3.2: Laser power values from the AOM inputs to the fiber outputs for the laser in the cooling bench.

Laser:	AOM				Optical Fiber	
	Frequency Shift (MHz)	Input (mW)	Coupling to +1 Order (%)	AOM Output/ Fiber Input (mW)	Coupling (%)	Output (mW)
Repumper	75.6	0.55	72	0.4	60	0.2
Detection	86.2	12.0	42	5.0	41	2.0
2D-MOT	76.4	82.5	69	56.5	60	34.0
3D-MOT:						
(Top)	76.4-$\delta\nu$	34.7	67	23.1	41	9.5
(Bottom)	76.4+$\delta\nu$	28.8	69	19.6	52	10.3

Table 3.2 is a comprehensive chart of the distribution of the laser powers from the cooling bench to the experimental apparatus, via the optical fibers. The output of the optical fiber of the 3D-MOT (Top) and 3D-MOT (Bottom) are each divided into three parts. Hence, in Table 3.1, $\Pi_{T1} + \Pi_{T2} + \Pi_{T3}$ corresponds to 3D-MOT (Top) output power and $\Pi_{B1} + \Pi_{B2} + \Pi_{B3}$ corresponds to 3D-MOT (Bottom) output power. The corresponding values from Table 3.1 and Table 3.2 are not equal as they were taken on separate occasions but they agree within 0.5 mW.

3.1.1.4 Characterization of the Atomic Cloud

Temperature of the atoms To verify the temperature of the atoms, we launch the atoms and shine a counter-propagating Raman π-pulse on the atomic cloud. We then observe the spectrum of Raman pulse varying the frequency difference between the two Raman lasers, δ from the hyper-fine frequency f_{HFS}.

The spectrum in Fig. 3.5 shows the Doppler peak, shifted from f_{HFS} according to the velocity of the atomic cloud v_{atom} at the corresponding height of the Raman π pulse. The width, W of this peak defines the temperature of the launched cloud. We choose a long duration of the pulse, $\tau_\pi = 97$ μs, so that the width of the peak is not limited by the frequency spread due to the duration of pulse. A least-square fit to a Lorentz profile gives a full width at half maximum (FHWM) W = 48±0.9 kHz, corresponding to a RMS velocity spread, σ_v of

$$\sigma_v = \frac{W}{2\sqrt{2\ln 2}\cdot\omega_{2ph}}\cdot v_{rec} = (2.48 \pm 0.05)\, v_{rec}. \tag{3.4}$$

where we have used the two-photon recoil, $\omega_{2ph} = 8.265$ kHz. For a recoil velocity, v_{rec}

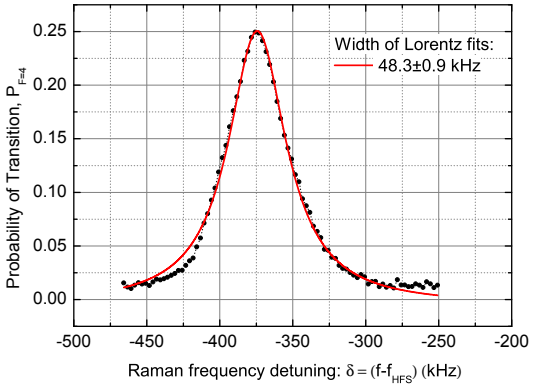

Figure 3.5: Raman Spectroscopy with pulse duration of 97 μs around the Doppler peak where v_{atom} = 2.3 m/s at the time of the pulse. The red curve is the Lorentz least-square fit of the Doppler peak.

= 3.52 mm/s, the temperature of the atoms is related to σ_v as:

$$T_{cloud} = \frac{m}{k_B}\sigma_v^2 \simeq 1.2\,\mu K. \tag{3.5}$$

T_{cloud} is reference temperature of the atomic cloud during this flight.

Number of Atoms Launched The number of atoms launched was measured by observing the absorption of the laser light in the detection chamber at the end of the flight. We load the 3D-MOT for 250 ms, launched the cloud with v_0 = 2.5 m/s and observed the absorption signal via a photo diode and compared the two conditions : detected light without atoms, V_{tot}; and detected light after absorption by the atoms, $V_{tot-abs}$. Hence, the absorption signal is , $V_{abs} = V_{tot} - V_{tot-abs}$. The V_{tot} corresponds to a total incident power of P_{tot} = 1 mW, with a total incident intensity, $I_{tot} = P_{tot}/A_{det}$ = 0.33 mW/cm^2, where A_{det} is an area of 3 cm×1 cm. The absorbed power is $P_{abs} = V_{abs} \cdot P_{tot}/V_{tot}$. This makes I_{tot} = 0.33 mW/cm^2. Now, the total number of atoms N_{at} corresponding to P_{abs} with the probe beam on resonance is given by the equation [16]:

$$N_{at} = P_{abs}/\left[\frac{\Gamma}{2}\cdot\left(\frac{I_{tot}/I_{sat}}{1+I_{tot}/I_{sat}}\right)\cdot h\nu\right], \tag{3.6}$$

where P_{abs} is the total power scattered; $\frac{\Gamma}{2}\cdot\left(\frac{I_{tot}/I_{sat}}{1+I_{tot}/I_{sat}}\right)$ is the scattering rate; and $h\nu$ is the of a single photon. We then varied the detuning of the MOT laser, Δ and studied the dependence of N_{at} vs. Δ. Fig. 3.6 shows that the detuning for optimum

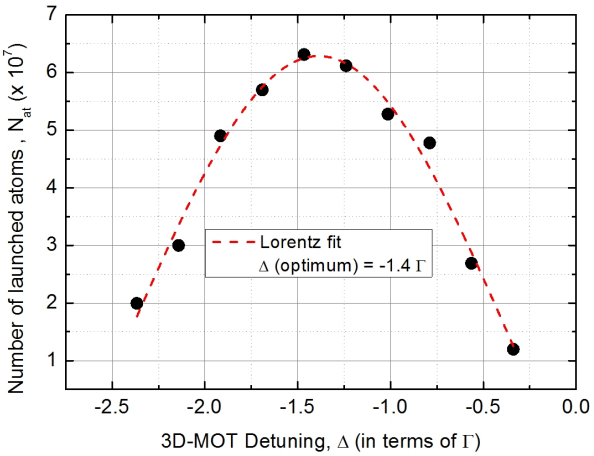

Figure 3.6: The dependence of the number of atoms of the launched atomic cloud vs. the detuning of the 3D-MOT lasers. The optimum detuning is at -1.4Γ.

launching is -1.4Γ. We obtained this value from the least square fit of a Lorentzian profile. This is the value we set for the detuning in the 3D-MOT which we used earlier in Eqn. (3.1).

3.1.2 The Interferometric Zone

After the atoms are launched from the 3D-MOT region, they go first through the detection zone and then enter the interferometric zone. This is a 1 m long chamber with a inner diameter of 46 mm. This long chamber has 17 windows (60 mm diameter) placed at different heights. These windows are for the access of the laser pulses to perform Raman transitions on the atomic cloud. The different combinations possible for a four-pulse system is given in Table 3.3.

Table 3.3: Four-pulse Interferometric configurations for different interrogation times.

Interrogation time 2T(ms)	Cloud launch velocity, v_0 (m/s)	Time of flight to Detection t_{TOF}, (ms)	Raman windows used	$\pi/2$ - π pulse separation (cm)	Interferometric Area (cm^2)
104	3.15	575	H1	4	0.025
313	4.03	771	H2-H3	10	0.675
480	3.91	745	H1-H2	21	2.437
572	4.20	808	H1-H3	39	4.124
800	5.04	988	H1-H4	58	11.28

3.1.3 Detection Zone

The detection zone lies between the 3D-MOT chamber and the interferometric zone. After the atoms are launched and when they are in free fall after interferometry, the atomic cloud is detected by fluorescence in this region. For optical access, there are two windows of 60 mm diameter which lets through three sheets of laser light used for the detection process. Two other windows on the orthogonal direction allows the collection of the fluorescence from the atoms using an lens system directed on to a two-quadrant photodiode.

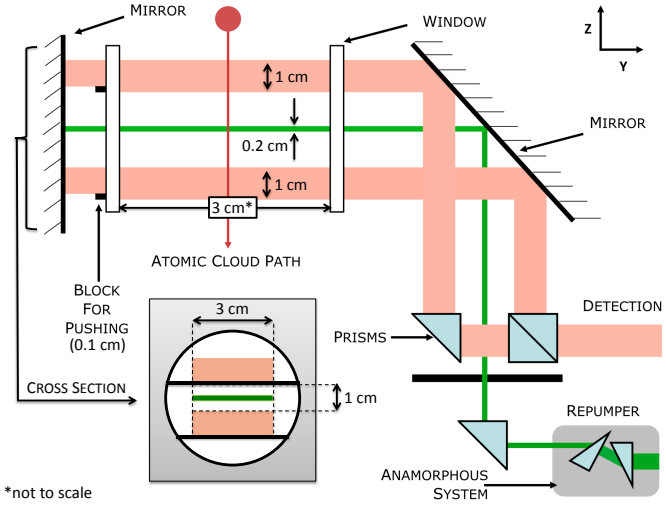

Figure 3.7: The detection zone schematic. The atoms fall vertically from the top on to the two detection light sheets each of width 1 cm. Between the two sheets lies a repumper light sheet of 0.2 cm width. The sheets are send from two collimators, each entering a prism system and are retro-reflected by a mirror on the other side.

The detection scheme shown in Fig. 3.7 is an inspiration from [15]. The two detection light sheets of 1 cm $\times$ 3 cm cross-section (in light orange) is at the frequency of transition of $|6S_{1/2},F=4\rangle \longleftrightarrow |6P_{3/2},F'=5\rangle$. The repumper light sheet is of 0.2 cm $\times$ 3 cm cross-section and is midway between the two detection light sheets. It repumps the $|6S_{1/2},F=3\rangle$ to $|6S_{1/2},F=4\rangle$ atoms, so that these corresponding $|F=3\rangle$ atoms can be detected after their state change to $|F=4\rangle$. The atoms in the $|F=4\rangle$ state fluoresce at the top light sheet. This fluorescence corresponds to the number of atoms in $|F=4\rangle$ state, N_4. They are then pushed by the top light sheet and then the $|F=3\rangle$ atoms are repumped by the middle light sheet and fluoresce in the $|F=4\rangle$ state at the bottom light sheet. Hence, the fluorescence signal for the bottom light sheet corresponds to the number of the atoms in $|F=3\rangle$, N_3. We acquire

the probability of transition from $|F = 4\rangle$ to $|F = 3\rangle$ as

$$P = \frac{N_4}{N_4 + N_3}. \tag{3.7}$$

In the above equation N_4+N_3 is the total number of atoms falling through the detection and P gives the transition probability which provides the interference signal. The distance between the centers of the top and bottom detection light sheets is 2 cm. The light-sheets are retro-reflected as the detection is not saturated. The bottom part of the first light sheet is blocked by only 0.1 cm in retro-reflection to get maximum fluorescence signal as to push the atoms in $|F = 4\rangle$ after they have been detected already and will not fluoresce twice. The light sheets are of 3 cm $\times$ 3 cm in area along the horizontal plane to collect all the atoms launched from the 3D-MOT to the maximum height. The atomic cloud expands during the time-of-flight and its RMS width, $\sigma_R(t)$ assuming a Gaussian distribution is given by

$$\sigma_R(t) = \sqrt{\sigma_R^2(0) + \sigma_v^2 t^2}, \tag{3.8}$$

where σ_v is the RMS velocity of the atomic cloud we obtained from Eqn. (3.5). Using $t = t_{TOF}$ for the maximum interferometric time $2T$ = 800 ms (from Table 3.3) and σ_v = 2.5 v_{rec}, we get $\sigma_R^{max} \simeq 1$ cm, for $\sigma_R(0) = 0.5$ cm. Since $\sigma_R^{max} < 3$ cm, we are sure to collect all the atoms in the detection even after we launch them for the maximum interferometric time of 800 ms.

The detection and the repumping light sheets are produced by two collimators with a fiber input. Their output power values are mentioned in Table 3.2. The detuning of the detection light is maintained at $+0.5\Gamma$, optimized for optimum pushing of the atoms in the $|F = 4\rangle$ states so that they are not detected in the bottom light sheet.

The photodiode we use for detection is the Hamamatsu bi-quadrant photodiode S5870 [47]. Each quadrant is intended to collect light from one detection light sheet. The photodiode is placed perpendicular to the light sheet directions and has a total collection efficiently of 4% (2 % for each quadrant) [19]. The output of the photodiodes is taken separately and fed through a transimpedance circuit before it is put in for digital acquisition. The digital acquisition system is a 16-bit National Instruments acquisition card PCIe 6341 which has a voltage noise of 0.3 mV/$\sqrt{\text{Hz}}$. The detailed noise analysis for this acquisition system is presented in Chapter 4.

One of the main drawback of the detection system is the crosstalk. This is the part of the signal that appears mistakenly in photodiode for the corresponding light sheet.

There are three types of this crosstalk:

Fluorescence Crosstalk The photons fluoresced from the atoms for each light sheet travels isotropically in all directions. Hence, some photons corresponding to the fluorescence of the first light sheet is detected by the photodiode corresponding to the second light sheet, and vice-versa. This is the fluorescence crosstalk. This is the same for the two light sheets as they have the same intensity. It is calibrated to be 1.5% and numerically compensated.

Repumping Crosstalk The repumping light sheet diffracts in the chamber, and may repump the atoms in the $|F = 3\rangle$ state when they fall through the top light sheet. The results in some $|F = 3\rangle$ atoms to be wrongly detected as $|F = 4\rangle$ atoms. We monitor the number of atoms detected in both light sheets as a function of the

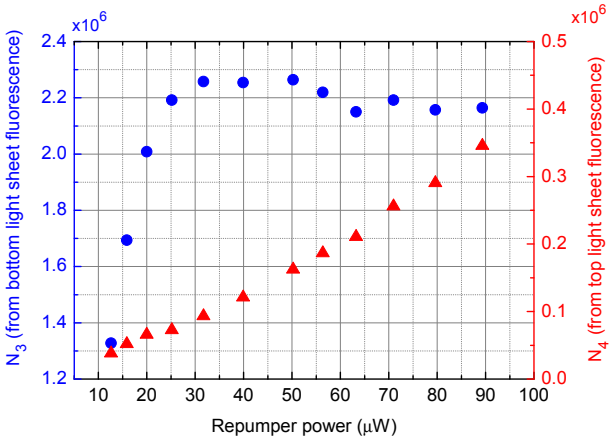

Figure 3.8: The plot of atoms in $|F = 3\rangle$ and wrongly detected $|F = 4\rangle$ vs. the power in the Repumper at the detection. We see a saturation of detected atoms in $|F = 3\rangle$ at ~ 35 μW.

repumper power (see Fig. 3.8), and find an optimal repumping power of 38 μW which ensures a maximal signal of N_3 and the least repumping corsstalk.

Unpushed Crosstalk We have set the detuning of the detection laser for detecting the $|F = 4\rangle$ atoms at $+0.5\Gamma$. This is the optimum value of the best pushing efficiency but, there is still some atoms originally in $|F = 4\rangle$ which ends up getting fluoresced again by the bottom light sheet especially at large launch velocities. This is the crosstalk due to the unpushed atoms in the first light sheet. The blocking sheet

(Fig. 3.7) was not made more than 0.1 cm thick so that the detection signal is not compromised.

Table 3.4: Unpushed crosstalk dependence on Interferometric Time and atomic launch velocity.

Interferometric Time 2T (ms)	Launch Velocity (m/s)	Height Launched (m)	Unpushed Crosstalk (%)
480	3.91	0.78	14
800	5.04	1.3	50

Table 3.4 shows the unpushed crosstalk values observed for the two atomic velocities corresponding to the four-pulse interferometric times, $2T = 480$ ms and 800 ms. The ratio of the two crosstalks is 3.5, although the ratio of the velocities is 1.3. This difference in the ratios can be explained by the ratio of Doppler force exerted by the pushing light sheet on the atoms at the two different velocities.

3.1.4 Raman Transition System

The Raman transitions are carried out by the retro-reflected laser pulses.

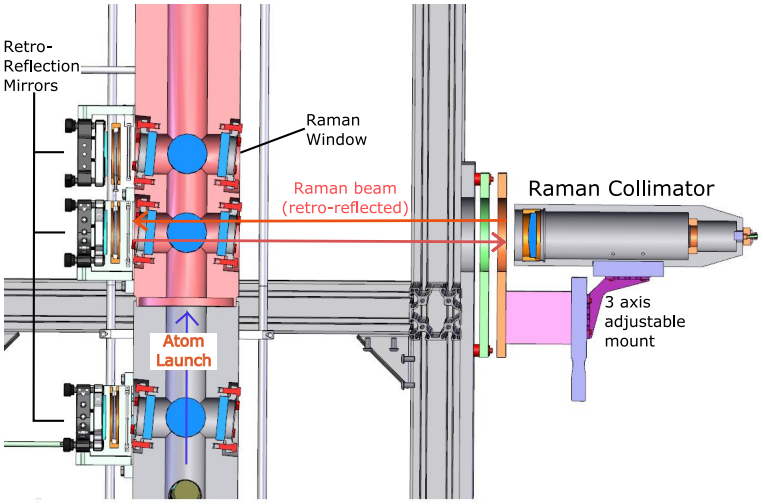

Figure 3.9: The Raman collimator with a fiber input and a Gaussian beam output. The beam is retro-reflected by a 50 mm diameter mirror on the other side of the Raman window. The windows are tilted to compensate for the tilt in the Raman beam.

The two Raman lasers locked at the frequencies of ω_1 and ω_2 is injected through the Raman collimator which delivers beam with $1/e^2$ diameter of 24 mm (Fig. 3.9). The two lasers come in the same linear polarization which is rotated by 90° by a $\lambda/4$

plate upon reflection. The incoming and the reflected beams thus do not interfere. This gives two the counter-propagating Raman pairs with a crossed polarization ($L_{in} \perp L_{in}$). In either case, the total momentum transfer to the atoms is $\hbar k_{eff} = \hbar(k_1 + k_2)$ but with opposite directions. To lift the degeneracy, the Raman collimator is inclined by a small angle θ w.r.t. the direction of the launching of the atoms. For a non-zero vertical velocity of the atoms, the Doppler shift is given by:

$$\omega_D = \vec{v}(t) \cdot \vec{k}_{eff} = \pm(v_0 - gt) \cdot \sin\theta \cdot k_{eff}. \tag{3.9}$$

This depends on the relative alignment of atom launch velocity v_0 and $\vec{k}_{eff}$. By changing the frequency difference of the two Raman lasers, we can scan through the Doppler peaks where the maximum momentum transfer takes place from the lasers to the atoms.

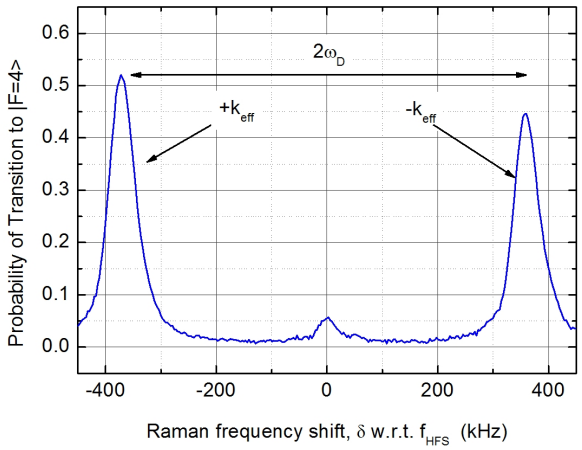

Figure 3.10: The Doppler resonant peaks observed while scanning the frequency difference of the Raman laser pair. The two peaks are for $+k_{eff}$ and $-k_{eff}$. The middle small peak is for the co-propagating transition at clock frequency.

In Fig. 3.10, the Raman pulse duration used is 24 μs, where the pulse is subjected at the first window H1, which is 55 cm above the point of launch of the atoms. The two different peaks we observe correspond to $+\vec{k}_{eff}$ and $-\vec{k}_{eff}$. The atoms were launched at $v_0 = 3.91$ m/s vertically. At that velocity it reaches the first Raman window H1 in $t_{H1} = 161$ ms. This makes $v = v_0 - gt_{H1} = 2.33$ m/s in Eqn. (3.9) . The frequency difference between the two peaks in Fig. 3.10 is 732 kHz. This is the Doppler shift between $\pm k_{eff}$. Using Eqn. (3.9), we find $\theta = 3.85^{o}$.

3.1.4.1 Raman Lasers

The Raman laser, utilized for the manipulation of the atomic wavepackets, comprises two optical frequencies detuned by the clock frequency of cesium, f_{HFS} (=9.192631770 GHz) which lies in the microwave domain. For this dual frequency system we use two extended cavity diode lasers (L3 and L4) which are phase locked around f_{HFS}. L3 provides a power of 29 mW and L4 of 32 mW.

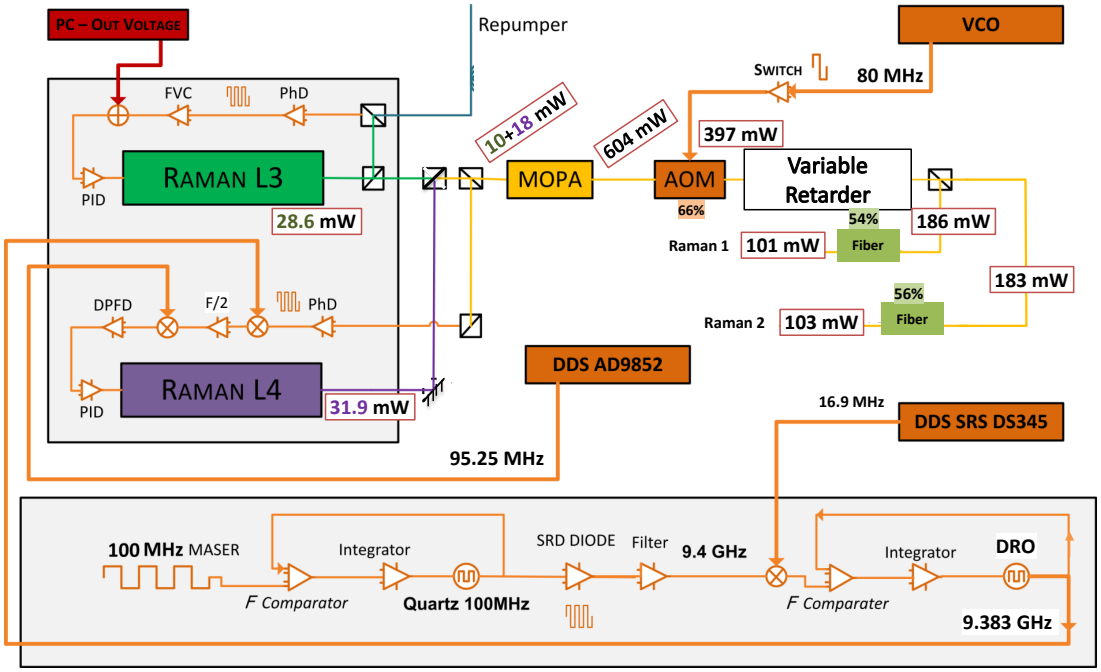

Figure 3.11: Schematic of the Raman bench. There are two extended cavity laser in this bench: Raman L3 and L4. The variable retarder shifts the laser power from Raman 1 to Raman 2 collimators by turning the polarization.

Fig. 3.11 shows the complete laser bench diagram for the Raman transition system. The laser L3 is is locked w.r.t. to L1 (repumper) by means of a frequency lock of their beat note at 350 MHz. L3 is thus sufficiently far red detuned from the crossover transition of $|6S_{1/2}, F = 3\rangle \longleftrightarrow |6P_{3/2}, F' = 2/3\rangle$. This limits the spontaneous emission at the time of the stimulated Raman transition while maintaining a high value of Ω_{eff} to address all velocity classes of the atomic cloud. The laser L4 is phase-locked with L3 by the method mentioned in [48]. Here, a part of L3 and L4 are superposed and the

beating signal is observed on a photoconductor. This beating frequency which is f_{HFS} is mixed with a reference signal at 9.383 GHz, generated from the Raman frequency chain, giving a radio-frequency (RF) beating at ∼190 MHz. This RF frequency is divided by two and compared with a reference RF signal from a digital synthesizer (DDS AD9852) ∼95 MHz. The comparison of these two in phase provides the error signal which is used in the phase locked loop and the correction signal is fed back to the L4. This above locking scheme is portrayed in the bottom section of Fig. 3.11.

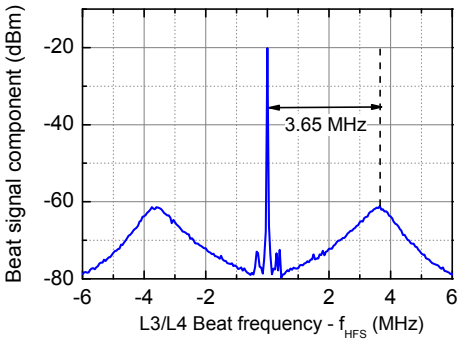

(a) L3/L4 lock spectrum

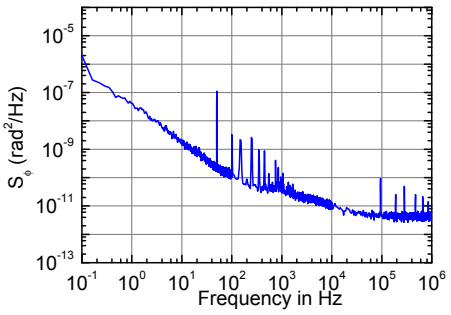

(b) L3/L4 lock noise

Figure 3.12: Plots showing the frequency spectrum and Phase noise spectrum of the Raman laser pair (L3 and L4). The phase noise corresponds to $\sigma_\phi = 7{\times}10^{-3}$ rad/$\sqrt{\text{Hz}}$ for an ideal four-pulse interferometer of 100% contrast.

Fig. 3.12(a) shows the frequency spectrum of the beating of L3 and L4 after L4 is phase-locked. the bandwidth of this lock is 3.65 MHz in optimum conditions. The spurious peak around the primary frequency , f_{HFS} was due to noise in the signal from the DDS (providing the 95 MHz signal). The DDS signal was later improved and the spurious peaks were rejected. In Fig. 3.12(b), we observe the error signal of this lock. We found the equivalent phase noise for this noise spectrum from the product of transfer function $H_\phi(\omega)$ (established in Chapter 2) and S_ϕ in Fig. 3.12. For the frequency range plotted in Fig. 3.12, it gives a total phase noise, $\sigma_\phi = 7{\times}10^{-3}$ rad/$\sqrt{\text{Hz}}$ for an ideal interferometer with a contrast of 100%. In terms of the signal of the four-pulse interferometer, it corresponds to a noise in the probability of transition $\sigma_{\mathbf{P}} = 2.5{\times}10^{-3}$.

After this lock of L3 and L4, the major part of the two lasers are directed towards a tapered amplifier (TA). This TA chip is manufactured by Eagleyard (EYP-TPA-0850-01000-4006-CMT04-0000). It gives a maximum of 1 W power output at 2.2 A of operational current and its minimum input power in 10 mW. The details of this optical

amplification process and the above locking system is described in [49]. We provide a total power of 28 mW (10 mW from L3) and 18 mW from L4) at the input of the TA and get a total output of 604 mW from the output of the isolator, placed after the TA. This power is then send to an AOM modulated at 80 MHz. We choose here the -1 diffraction order of the AOM and its gives a coupling power efficiency of 66%. The output of $\simeq$ 400 mW is fed through a Variable Retarder. It consists of a liquid crystal whose polarization axis changes according to the amplitude of modulation of the crystal. Hence, we can choose to inject L3+L4 in either of two optical fibers for the Raman beams. Each fiber has an input power of $\simeq$ 185 mW and an output power $\simeq$ 100 mW , providing a coupling efficiency of 55%.

3.2 State Selection for Interferometry

After the launching process of the atomic cloud, the atoms are selected in a magnetically-insensitive state. This is necessary so that during interferometry the atoms are not perturbed by the residual external magnetic field fluctuations. We use a bias magnetic field which lifts the degeneracy of the magnetic hyperfine states of Cs in $|F = 4\rangle$, m_F=-4,..,0..,+4 via Zeeman effect. Then we drive a microwave π-transition to select the atoms in the m_F=0 state. The microwave pulse for selection is at the hyperfine state frequency f_{HFS}=9.192631770 GHz. It is carried out by a microwave antenna placed at the bottom of the 3D-MOT chamber. The microwave pulse is used right at the end of the launching stage, driving a transition $|6S_{1/2},F = 4\rangle \longrightarrow |6S_{1/2},F = 3\rangle$. This transition starts at $|F = 4\rangle$ state as the atoms are trapped in that state.

The frequency of the microwave pulse is generated by mixing a 192 MHz component (RF) originating from one of the four ports of the DDS AD9959 and a 9 GHz microwave signal. The mixed microwave signal at f_{HFS} is of strength 4 dBm and is amplified later by a microwave amplifier with an output of 24 dBm. This signal is fed to a microwave antenna which is a copper ring connected to the microwave input wire. The Zeeman selection field is set by a pair of coils which sets up a bias B_z field in the direction perpendicular to the atom launching direction.

The coils have been calibrated to deliver 0.28 mG/mA. By setting I_{coil} = 57 mA, we have B_z = 16 mG. The total Landé g factor g_μ = 350 Hz/mG. This sets the Zeeman shift in frequency $\delta\nu = g_\mu B_z$ = 5.6 kHz. Fig. 3.13 shows the microwave spectrum acquired for B_z = 16 mG. For this microwave spectrum we had set the pulse duration, $\tau_{\mu w}$ = 2 ms. There are 7 m_F states for $|F = 3\rangle$ and 9 m_F states for $|F = 4\rangle$. If

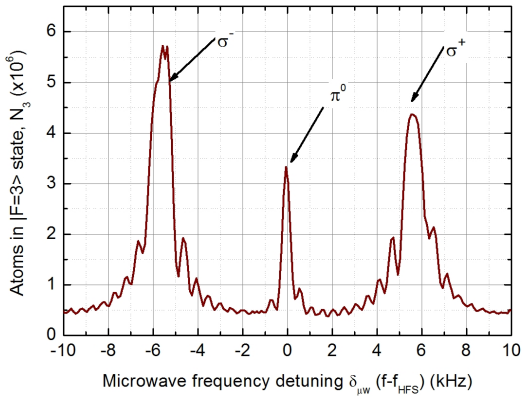

Figure 3.13: Microwave spectroscopy of the antenna used for selection. Here we see a zoom on the π^0, σ^+ and σ^- transitions. The π^0 transition corresponds to 11% transfer of atoms from $|F = 4\rangle$ to $|F = 3\rangle$ hyperfine state.

we consider the initially trapped atoms in $|F = 4\rangle$ are equally distributed in the corresponding m_F states after Zeeman splitting, we should expect 11% of transfer of the atoms from $|F = 4; m_F = 0\rangle$ to $|F = 3; m_F = 0\rangle$ via the π^0 transition.

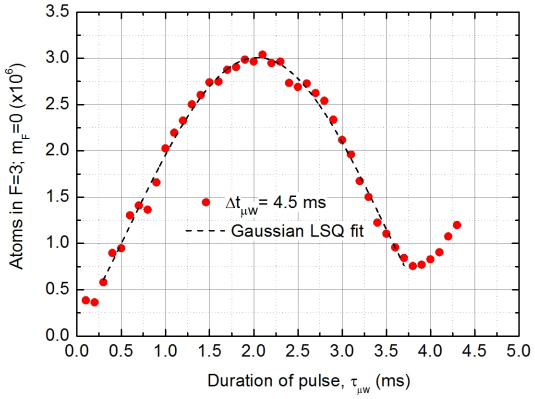

Figure 3.14: Rabi Oscillation for different durations of the microwave selection pulse.

Fig. 3.14 shows the Rabi oscillation at the f_{HFS} frequency of the selection pulse. Observing the Rabi oscillation in the Fig. 3.14, we set the π^0 pulse duration, $\tau^{\pi}_{\mu w} = 2.05$ ms. We apply the pulse $\Delta t_{\mu w}$ time after the end of the launching process of the atoms. This timing is set according to the following conditions:

- The selection pulse has to start after the proper adiabatic shut-down of the 3D-

MOT lasers to avoid any distortion in the launching of the cloud.

- The selection pulse has to be applied before the atomic cloud leaves the 3D-MOT chamber. The higher the launch velocity, the shorter has to be $\Delta t_{\mu w}$.

In this characterization process, we loaded the MOT for 150 ms and launched $\sim 3\times10^7$ atoms in $|F = 4\rangle$. With the π^0 transition, we are able to transfer 10% of the atoms from $|F = 4\rangle$ to $|F = 3\rangle$. Hence, we verify that the π^0 transition is optimized.

3.3 Frequency Reference Systems

The frequency chain provides the reference frequency signals for the laser and the microwave components in the experiment. The main reference is a state of the art Hydrogen Maser provided by SYRTE which has a short term frequency stability of 3.4×10^{-14} at 1 s [50]. We filter the 100 MHz signal from the H-Maser and first lock a quartz oscillator to this signal.

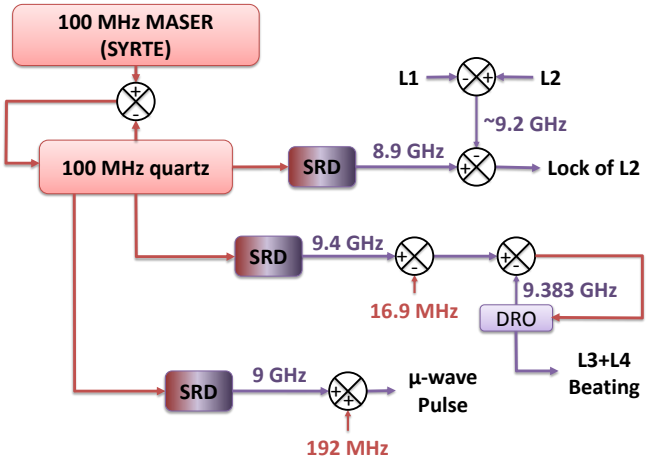

Figure 3.15: A simple schematic of the microwave frequency chain providing reference signals for the phase lock of lasers and also for the microwave selection pulse.

The signal of this quartz oscillator is used for three purposes where a SRD (Step Recovery Diode) is used to produce a frequency comb upto microwave range and filter out the required frequency. This scheme is shown in fig. 3.15 and the three sections shown in the schematic are:

Locking of L2 A part of the 100 MHz quartz oscillator signal is fed to a SRD and we filter out the 8.9 GHz frequency component. This frequency is compared with the

beating of the repumper L1 and and cooling L2 lasers. The error signal is used to lock the frequency of L2 as shown in Fig. 3.4.

Reference of L3+L4 Frequency Beating Another part of the quartz signal is again fed to another SRD for microwave comb generation and we filter out the 9.4 GHz component this time. The 9.4 GHz is first mixed with a RF signal ∼17 MHz from a SRS RF generator [51]. The resulting frequency is around $f_{DRO} = 9.383$ GHz and is used to lock the DRO (Dielectric Resonator Oscillator).

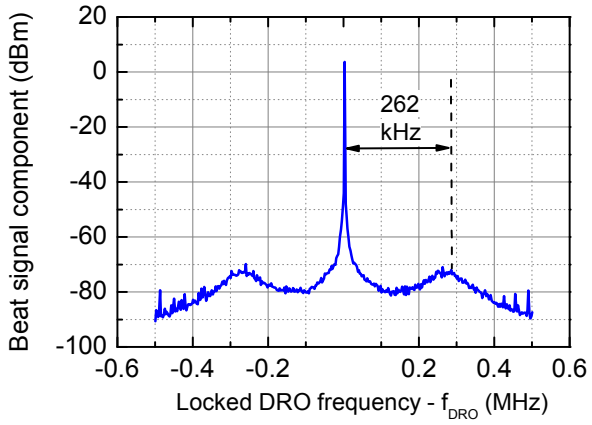

Figure 3.16: Frequency spectrum of the DRO locked with proportional gain and integrator. The band of the lock is 262 kHz.

Fig. 3.16 shows the frequency spectrum of the DRO after the locking. There is a proportional gain and an integrator in the lock loop and it has a bandwidth of 262 kHz. This f_{DRO} is used as the reference frequency for comparison of the frequency beating of the Raman lasers, L3 and L4. The rest of the scheme for the lock of L3 and L4 is explained in Section 3.1.4.1.

Microwave Selection Reference A third part of the quartz is fed to another SRD and this time we filter out the 9 GHz microwave component and mix it with the RF 192 MHz from the DDS, as mentioned before. This mixing produces the 9.192 GHz microwave signal for the π_0 selection pulse.

3.4 Experimental Protocol for Large-area Interferometry

According to de Broglie's hypothesis, there is interference in matter-wave interferometry when the distance between the two interfering paths at the exit port is smaller that the coherence length of the source used. For the case of the cold atomic ensemble, it is the velocity distribution of the atoms which defines the coherence length [52]. To fulfill the above condition, multiple Raman beams have to be aligned parallel to each other in the 3D space within a certain tolerance angle which is related to L_{coh}. For our four-pulse Butterfly interferometer, there are two positions in space where the Raman beams interacts with the atoms. It is crucial to carefully set the parallelism of the Raman beams in the vertical and the horizontal directions. To find the coherence length of the atoms used, we consider Heisenberg's uncertainity principle. The limiting case for the uncertainty in position and momentum is $\Delta x \Delta p = \hbar/2$. Considering the position - momentum distribution of the atomic cloud is isotropic in the phase space, we have $\Delta x = \hbar/(2\Delta p)$. Considering a Gaussian distribution of position and velocity of the atoms, the coherence length is related to the RMS velocity by,

$$L_{coh} = \sigma_x = \frac{\hbar}{2m\sigma_v}. \tag{3.10}$$

From Fig. 3.5, we found for the Cs atoms that we launch, we have $\sigma_v = 2.5\ v_{rec} = 8.8$ mm/s. This provides us with a $L_{coh} = 27.5$ nm. To close the two interferometric paths within this coherence length, we have to align the two Raman beams parallel to each other within a certain minimum angle in the horizontal and the vertical directions.

3.4.1 Parallelism of Raman Beams

In the vertical direction the parallelism is set by the equality of the Doppler angle of the Raman beams. To find the minimum angle necessary for interference of the two paths, we consider that each Raman beam communicates with the clouds with a recoil momentum. If there is a shift of the parallelism of the two beams, by conservation of momentum, the two interferometric paths finish at two separate places at the moment of the last $\pi/2$ pulse. According to the shift in the parallelism, $\delta\theta_z$ in the vertical direction and $\delta\theta_y$ in the horizontal direction, we can find the minimum of these two relative angles by using Heisenberg's uncertainty principle and the law of conservation of momentum.

In the vertical case, the relative angle between the Raman beams is $\delta\theta_z$. This displaces the two interferometric pulses by $2 \cdot v_{rec} \cdot \sin(\delta\theta_z) \cdot T$ but in opposite direc-

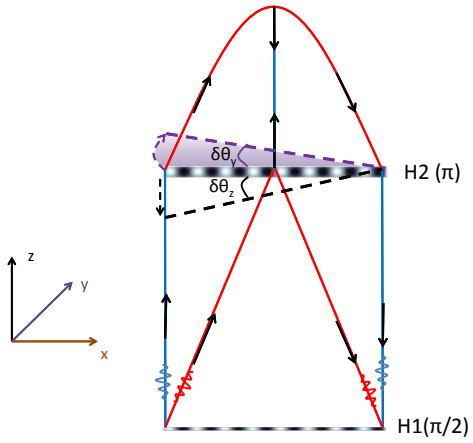

Figure 3.17: The four-pulse butterfly interferometer showing the case of non-parallelism of H1 and H2 Raman beams. The difference in the angles of H1 and H2, can be in the horizontal ($\delta\theta_y$) and in the vertical ($\delta\theta_z$)

tions, where 2T is the total interaction time and $v_{rec} = \hbar k_{eff}/m$. Hence the final displacement is:

$$\delta Z \approx 4 \cdot v_{rec} \cdot T \cdot \delta\theta_z. \tag{3.11}$$

In the y-direction, a relative angle $\delta\theta_y$ results in a change in the length of $\vec{k}_{eff}$ by a factor $\cos\delta\theta_y$, giving rise to a spatial separation of

$$\delta Y \approx 4 \cdot v_{rec} \cdot T \cdot \delta\theta_y^2. \tag{3.12}$$

To meet the minimum condition of Heisenberg's uncertainty principle, $\delta\theta_z \leqslant L_{coh}/(4 \cdot v_{rec} \cdot T)$ and $\delta\theta_y \leqslant \sqrt{L_{coh}/(4 \cdot v_{rec} \cdot T)}$. This defines the tolerance in the parallelism of the two Raman beams.

Table 3.5: Maximum angle tolerance for the parallelism of the Raman beams, θ_y^{max} in the horizontal axis and θ_z^{max} in the vertical axis.

Windows	Inter-window distance (cm)	$2T$ (ms)	$\delta\theta_z^{max}$ (μrad)	$\delta\theta_y^{max}$ (mrad)
H1 - H2	20.5	480	8.2	4.0
H1 - H4	57.7	800	4.9	3.1

Table 3.5 shows the maximum limit of $\delta\theta_z^{max}$ and $\delta\theta_y^{max}$ for the four-pulse interference for the two interferometric case of $2T = 480$ ms and 800 ms.

3.4.1.1 Alignment of Vertical Parallelism

For the vertical alignment for the parallelism of the two Raman beams, we first used a three-pulse interferometer. The Raman beams are placed at at angle to the acceleration due to gravity, $\vec{g}$ to lift the degeneracy of $\pm k_{eff}$. Then $\vec{g}$ will give a bias phase shift in the interferometer:

$$\Delta\Phi_g = k_{eff} \cdot g \cdot \sin\theta_z \cdot T^2. \tag{3.13}$$

We can compensate for phase shift by applying a linear ramp in the frequency difference of the Raman lasers while the atoms are in flight, such that $\Delta\Phi(t) = 2\pi \cdot f(t) \cdot t = 2\pi \cdot r_g \cdot t^2$, where r_g is the ramp rate in Hz/s. Then, we can have

$$\Delta\Phi_{ramp} = 4\pi \cdot r_g \cdot T^2 = \Delta\Phi_g. \tag{3.14}$$

This gives

$$r_g = \frac{k_{eff} \cdot g \cdot \sin\theta_z}{4\pi} \tag{3.15}$$

This is a common method used in gravimetry with atoms [32] where the determination of this ramp results in a more sensitive measurement of acceleration. In our case, we use a three-pulse interferometer ($\pi/2 - \pi - \pi/2$) of small interaction time at the positions of H1 and H2 separately to precisely make θ_z for H1 and H2 as similar as possible. The frequency ramp is carried out by the 48-bit DDS (AD9852) [53] providing the 95 MHz reference for the Raman L3+L4 beat lock, changing the frequency by steps of few hundreds of mHz in an interval of 333 ns. The extra factor 2 in Eqn. (3.14) comes from the fact that this frequency is doubled before participating in the L3+L4 beat lock. We first carry out the three-pulse interferometer at the two different interrogation times $2T_1$ and $2T_2$ for H1. This gives

$$\begin{aligned} \Delta\Phi_{T1} &= \left(k_{eff} \cdot g \cdot \sin\theta_z^{H1} - 4\pi \cdot r_g\right) \cdot T_1^2, \\ \Delta\Phi_{T2} &= \left(k_{eff} \cdot g \cdot \sin\theta_z^{H1} - 4\pi \cdot r_g\right) \cdot T_2^2. \end{aligned} \tag{3.16}$$

The difference of the above two equations give,

$$a_{H1} = \left(g \cdot \sin\theta_z^{H1} - \frac{4\pi \cdot r_g}{k_{eff}}\right) = \frac{\Delta\Phi_{T1} - \Delta\Phi_{T2}}{k_{eff}(T_1^2 - T_2^2)}. \tag{3.17}$$

We correct the ramp of frequency, such that when the ramp $= r_g$, we reach the minimum value for a_{H1} in Eqn. (3.17). The larger the difference between T_1 and T_2, the better is the resolution on a_{H1}. For H1, we reached the maximum of $2T_2 = 60$ ms, and

a minimum of $2T_1 = 32$ ms. We found the optimized ramp to be $\delta f = 256.358$ mHz in $\delta t = 333$ ns. This sets $r_g = 769.84$ kHz/s.

After finding the correct frequency ramp, we followed the same three-pulse interferometry protocol for H2. We start with a small difference between T_1 and T_2 and gradually increase their difference. During that process, we kept the frequency ramp fixed at r_g we found for H1, and changed the angle θ_z^{H2} so we get the minimum in a in Eqn. (3.17), but this time for H2. We reached upto $2T_2 = 60$ ms, with $T_1 = 30$ ms. We found a worse sensitivity for a_{H2} w.r.t. a_{H1} because θ_z^{H2} was adjusted by changing the vertical alignment of the retro-reflective mirror for the Raman beam at H2. This was carried out manually by a turning the mirror mount screw and was susceptible to hysteresis in the pitch of the screw grooves and the sensitivity of the displacement of our fingers.

The above method gives $\delta\theta_z$ as

$$\delta\theta_z = \theta_z^{H1} - \theta_z^{H2} \approx \frac{a_{H1} - a_{H2}}{g}. \tag{3.18}$$

Putting the values of a_{H1} and a_{H2} in Eqn. (3.18), we get $\delta\theta_z \approx 0.3$ μrad. Hence, by this method we have reached within the maximum value of $\delta\theta_z$ for a four-pulse interferometer between H1-H2.

3.4.1.2 Alignment of Horizontal Parallelism

The previous method of alignment of the Raman beams led to alignment of the Raman beams in the vertical plane. To align them in the horizontal plane, we use the four-pulse Ramsey-Bordé interferometry [54]. This method has already been used in [55].

The Ramsey-Bordé interferometer in Fig. 3.18 comprises of four $\pi/2$ pulses. the two first pulse we perform at H1 and the other two at H2. The time interval between the first two and between the last two pulses is dT. This creates a separation of $2 \cdot v_{rec} \cdot dT \cos\theta_y$ between the two parallel paths of interferometry. The larger the dT, the higher is the precision required for the alignment of the Raman beams to be set parallel to each other, in the y and z directions. We increased the time dT gradually starting from 500 μs upto 12 ms. We cannot go further up in dT, as the atomic cloud spends just above 12 ms at H1 so it can reach upto to H2. Here, the frequency ramp r_g is also necessary to avoid the shift in the bias phase of the interferometer.

Since $\delta\theta_z$ has already been minimized to a certain extend as shown in the previous

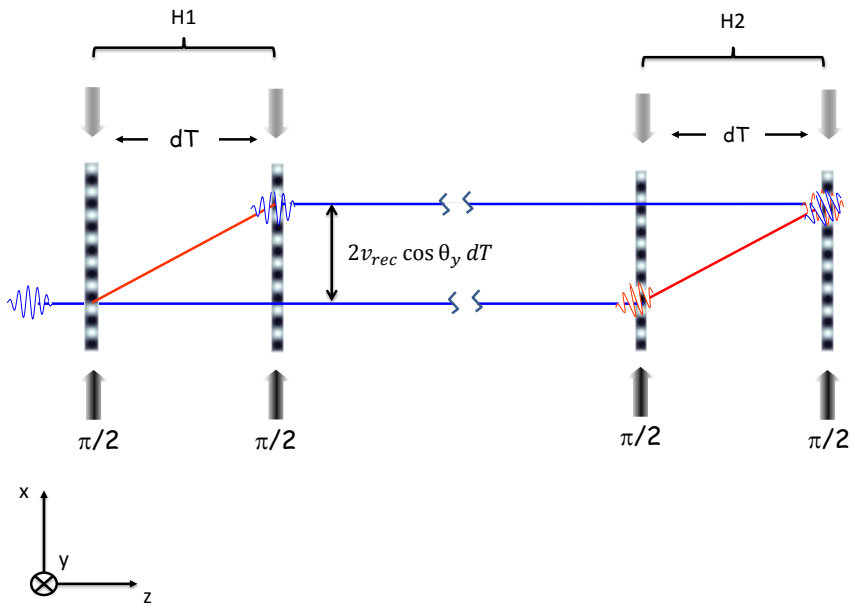

Figure 3.18: The four-pulse Ramsey Bordé Interferometer. For best contrast, the Raman beams from H1 and H2 have to be aligned parallely in the y and z directions.

section, the Ramsey-Bordé interferometer is used to minimize $\delta\theta_y$. If there is a small change of angle at H1 and H2 in the y- axis, then the two interferometric arms will be shifted by

$$\begin{aligned} dL &= 2v_{rec}dT(\cos\theta_y^{H1} - \cos\theta_y^{H2}) \\ &\approx v_{rec}dT\delta\theta_y^2. \end{aligned} \tag{3.19}$$

Hence, the condition for interference gives,

$$\delta\theta_y^{RB} = \sqrt{\frac{L_{coh}}{v_{rec}dT}} \tag{3.20}$$

As told before, we change dT from 500 μs to 12 ms. At each step, we rotate the retro-reflection mirror of the Raman beam at H2 horizontally by adjusting the mirror mount alignment screws. For one value of dT, when we have reached the optimum contrast, we move on to higher dT, until we reach the maximum value of $dT = 12$ ms. Using this method, we can get to $\delta\theta_y^{RB} = 18$ mrad.

3.4.2 Final Optimization using Four-pulse Butterfly Interferometer

After we achieved a intermediate minimization of $\delta\theta_z = 0.3$ μrad and $\delta\theta_y = 18$ mrad, we finally set up the four-pulse Butterfly interferometer as the gyroscope. The ultimate optimization of the parallelism of the two Raman beams at H1 and H2 is achieved by optimizing the contrast for this four-pulse interferometer. We follow the similar method as we did for Ramsey-Bordé interferometer: to first align the θ_z of the retro-reflection mirror at H2 w.r.t. H1 and then move on to θ_z. We repeat the process a few times until we reach the maximum of contrast. The maximum contrast that we obtained for 2T= 480 ms (using H1 and H2 windows) was 25%. All the above processes for the alignment of the Raman beams has been also discussed in [16].

3.5 Conclusion

This chapter explains the different components that comprise the experimental set-up. The supporting systems necessary, e.g., the laser system and the frequency chain were also included in the explanation. The atomic source for the launch of the cold atomic cloud was also characterized and it was shown how the selection of the the atoms into a magnetically insensitive state was made. After the explanation of the experimental system the mechanism for interferometry was described in detail. This mechanism is a protocol for the condition of interferometry in the four-pulse "Butterfly" interferometer in the fountain geometry. We established the tolerance of the parallelism of the Raman beams necessary in the vertical and the horizontal directions and followed them to perform interferometry with interrogation time, $2T = 480$ ms. The protocol we used proved to be very efficient to obtain large area interferometry using two Raman beams separated in space and we will use the protocol later to perform interferometry with even larger area of 11 cm^2. The details of the interferometric signal characterizations will be explained in the following chapter.

Chapter 4

Optimization of Inertial and Non-inertial Systems

In this chapter, I will present to you the active and passive optimization methods we implemented to increase the signal to noise ratio for the four-pulse gyroscope in the fountain geometry. The first half of the chapter handles the optimization and rejection of non-inertial effects and the second half for inertial effects. All these effects appears as the noise in the interferometric signal as parasitic noise.

We break down the phase of the four-pulse interferometer into different contributions:

$$\Phi = \Phi_{\Omega}^{DC} + \delta\Phi_{\Omega} + \delta\Phi_{vib} + \Phi_{LS} + \delta\Phi_{L} + \delta\Phi_{det}. \tag{4.1}$$

Φ_{Ω}^{DC} is the DC phase shift due to a constant rotation experienced by our apparatus, principally the Earth's rotation. By measuring this value, we can find the sensitivity of our gyroscope to Earth's rotation. $\delta\Phi_{\Omega}$ is the residual rotation phase noise, which will define the sensitivity of our gyroscope. Since the four-pulse fountain geometry is

insensitive to DC acceleration, the only remaining inertial contribution is due to the vibration noise $\delta\Phi_{vib}$ imprinted by the retro-reflected Raman beams onto the atoms. Φ_{LS} is the phase shift due to light shift [56] when the Raman laser pair interact with the atoms. $\delta\Phi_L$ is the noise due to the Raman lasers imprinting on the atoms during interferometry due to imperfect phase lock of the Raman laser. Finally, $\Delta\Phi_{det}$ comprises of the noise added by the detection and the signal acquisition system.

Table 4.1: Different physical aspects of the four-pulse AI for different interferometric times

Interrogation time 2T(ms)	Raman windows used	$\pi/2$ - π pulse separation (h_V) (cm)	Area (cm^2)	S_Ω (s)
104	H1	4	0.025	1.0×10^4
313	H2-H3	10	0.675	2.8×10^5
480	H1-H2	21	2.437	1.0×10^6
572	H1-H3	39	4.124	1.7×10^6
800	H1-H4	58	11.28	4.6×10^6

4.1 Optimization of Raman Pulses

In order to obtain a good signal to noise ratio for the interferometric signal, the optimization of the Raman pulses are necessary. To have a good contrast in the four-pulse AI, the Raman beam has to be optimized for momentum transfer to the maximum number of launched atoms. This will lead to the optimization of beam-splitter and mirror conditions. The details of the different configurations of the four-pulse interferometers is given in Table 4.1.

Fig. 4.1 shows optimized Rabi oscillations we obtained for $2T = 480$ ms (Fig. 4.1(a)) and for $2T = 800$ ms (Fig. 4.1(b)). In both cases, we observe that the Rabi oscillation becomes less efficient as the atomic cloud travels further in time. This is a consequence of our thermal cloud at 1.22 μK expanding progressively through its time of flight.

4.1.1 Optimization of Verticality

Next, we made sure the experiment is completely vertical. If the atoms are not launched vertically, there would be a difference between the angle seen by the atoms w.r.t. the Raman beam at the earlier and the later part of the atomic trajectory. The verticality is set w.r.t. the central axis of the experiment througt the interferometric zone. Hence,

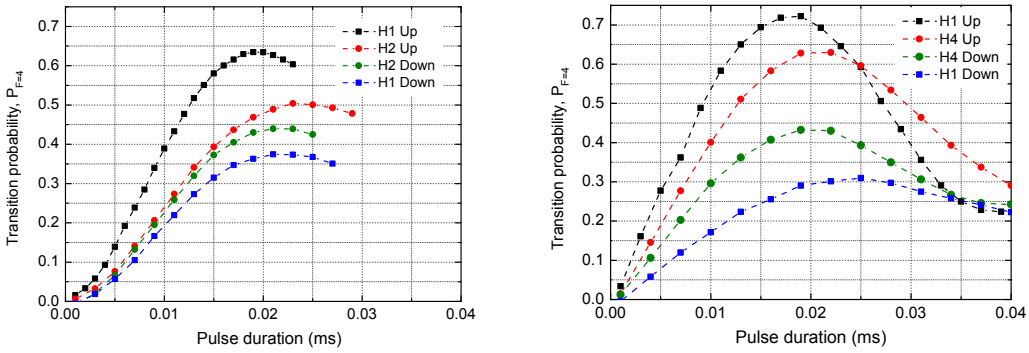

(a) $2T = 480$ ms (b) $2T = 800$ ms

Figure 4.1: Fig. 4.1(a) shows the optimized Rabi oscillation v/s pulse duration, for the four-pulses used between the positions H1 and H2 ($2T = 480$ ms). Fig. 4.1(b) shows the same for the four-pulse between positions H1 and H4 ($2T = 800$ ms).

the atomic cloud will be subjected to different projections of $\vec{g}$ when they experience Raman pulses.

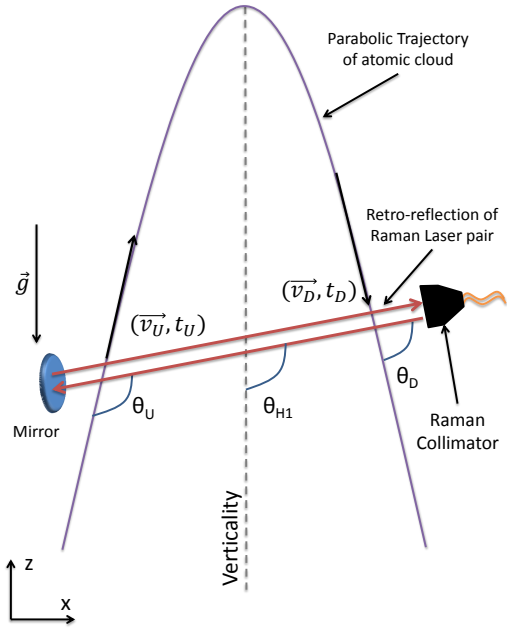

Figure 4.2: Schematic showing parabolic launch of atoms. In this case, the angle of the Raman beams w.r.t. the atomic cloud is not the same while the atoms cross the beam while going up and coming down.

In Fig. 4.2, the angle of the beam is θ_{H1} w.r.t. $\vec{g}$ at $t = t_U$. Due to the parabolic (non-vertical) launch of the atomic cloud, when the cloud crosses H1 with a velocity v_U at time t_U, its angle with the Raman beam is θ_U. When it is falling down, at the crossing of H1 with velocity v_D at time t_D, the angle is θ_D. Due to the parabolic flight of the cloud, $\theta_U \neq \theta_D$.

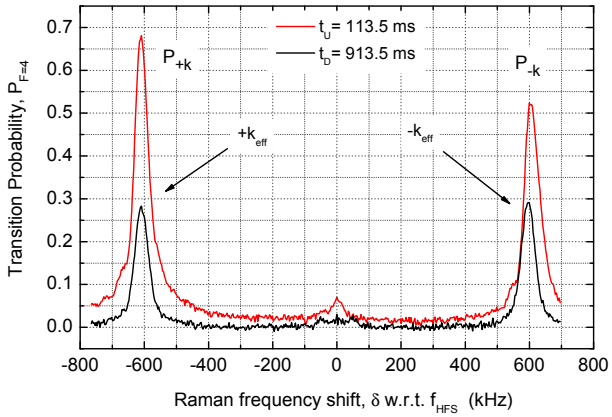

Figure 4.3: Raman spectroscopy at H1 at two time instants: when the cloud is crossing H1 going up (black) and down (red). The velocity of the cloud is 5.04 m/s.

The inequality of θ_U and θ_D, leads to difference in the projection of $\vec{g}$. Hence, the compensation for $\vec{g}$ by ramping the frequency difference of the Raman lasers (see previous chapter in Section 3.4.1.1) is no longer perfect giving rise to DC sensitivity to $\vec{g}$ in the four-pulse gyroscope. To set the verticality, we study the Raman spectroscopy of the atomic cloud at H1 where the atoms are going up and coming down. In Fig. 4.3, we see the Raman spectroscopy at the two time instants $t_U = 113.5$ ms and $t_D = 913.5$ ms, with launching velocity, $v_0 = 5.04$ m/s. The Doppler shifts due to the different angles are,

$$\begin{aligned} f_U &= \pm\frac{k_{eff}}{2\pi}(v_0 - gt_U)\sin\theta_U = \frac{(f_U^{+k} - f_U^{-k})}{2}, \\ f_D &= \pm\frac{k_{eff}}{2\pi}(v_0 - gt_D)\sin\theta_D = \frac{(f_D^{+k} - f_D^{-k})}{2}. \end{aligned} \tag{4.2}$$

We perform Lorentz fits of the peaks for $+k_{eff}$ and $-k_{eff}$ for the spectroscopies of up and down to find (f_U^{+k}, f_U^{-k}) and (f_D^{+k}, f_D^{-k}) in Fig. 4.3. This gives, f_U = 1216526±434 Hz; f_D = 1204888±324 Hz. Using these values in Eqn. 4.2, we get, θ_U = 3.82±0.0014°; θ_D = 3.72±0.001°. This sets the difference $(\theta_U - \theta_D)$ at 0.1±0.0017°.

We corrected this non-vertical launch by tilting the experiment along the axis of the Raman beam by adding or removing small masses on the experimental platform. We clamped a tiltmeter from Applied Geomechanics (now Jewell Instruments) [57] on the experimental structure at a height of 70 cm from the bottom of the platform. This sensor has a sensitivity of 1 mrad/V (at low gain setting) and 100 μrad/V (at high gain setting). We can only reach $(\theta_U - \theta_D)$ down to ± 15 μrad limited by the resolution of the Lorentz fit on the Doppler peak. The above method is a passive optimization of the verticality. In a later section an active optimization method is presented.

4.1.2 Characterization of Doppler Resonance Peaks

We note that in Fig. 4.3, when the Raman spectroscopy was made while the atoms were going up, there is a substantial difference in the Doppler peak heights for $+k_{eff}$ (P_{+k}) and for $-k_{eff}$ (P_{-k}). This can be explained by the intensity profile of the detection light sheet.

Fig. 4.4 shows the atomic path for $+k_{eff}$ and $-k_{eff}$ momentum transfer from the Raman pulse at H1. We launched the atoms at different values of velocity v_0, and integrated the intensity (given by the profile in Fig. 4.4) seen by the atomic cloud when it falls through the detection light sheet. This intensity is not uniform about the centre of the light sheet as we see from Fig. 4.4. We derived the size of the cloud, $d = \sigma_R$ when it crosses the detection light sheet. We know, $\sigma_R = \sqrt{\sigma_R(0)^2 + \sigma_v^2 t^2}$, we set $\sigma_R(0) = 0.5$ cm; we found σ_v is 2.5 v_{rec}; and t is the time of flight of the cloud. For different v_0, we have different t and different size of the cloud falling through the detection sheet. The displacement of the cloud due to the momentum transfer, d_k is symmetric for $\pm k_{eff}$, and increases with increasing v_0. We can simulate the ratio of the transition probability for $+k_{eff}$ and $-k_{eff}$ momentum transfers by integrating for the number of photons , N fluoresced by the same number of atoms falling through the detection intensity profile. This intensity is a function of the horizontal axis, x of the detection in Fig. 4.4. We note that the intensity of the detection light sheet $I_{det} < I_{sat}$, hence the fluorescence signal is proportional to the light sheet intensity. This is due to the limited intensity available from the detection laser. So the simulated probability will have a proportionality to the intensity profile as:

$$\begin{aligned} P_{+k}^{sim} &\propto \int_{-d_k-\sigma_R/2}^{-d_k+\sigma_R/2} I_{det}(x)dx, \\ P_{-k}^{sim} &\propto \int_{d_k-\sigma_R/2}^{d_k+\sigma_R/2} I_{det}(x)dx. \end{aligned} \tag{4.3}$$

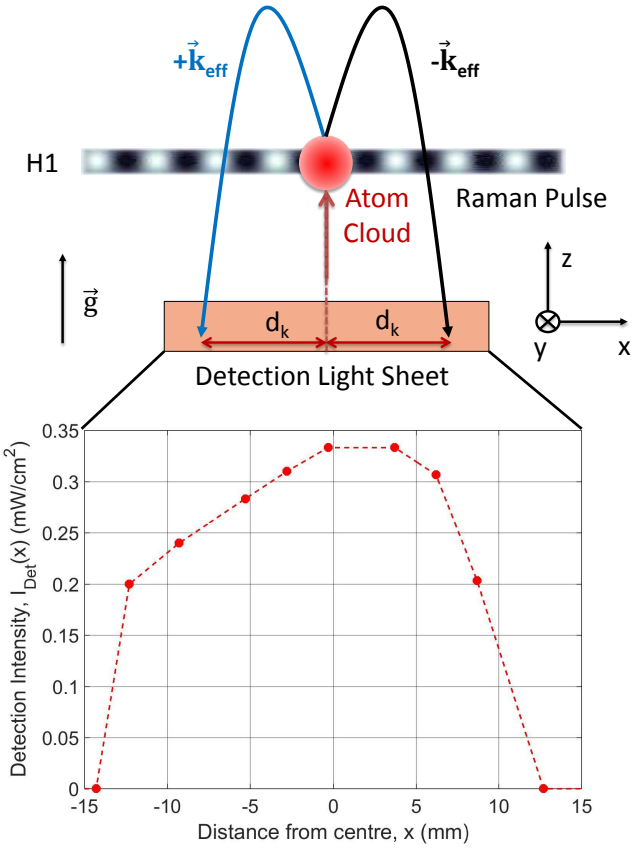

Figure 4.4: The scheme shows using a single Raman pulse at Raman window H1 and the corresponding projectile path of the atoms undergoing $+k_{eff}$ or $-k_{eff}$ momentum transfer. The detection light sheet has an intensity profile shown in the lower half of the figure. The strength of the different values of fluorescence signal is determined by this profile, since the light sheet intensity is $< I_{sat}$.

In the above equation, we consider the $+k_{eff}$ momentum transfer displaces the atoms in the negative direction in x and the reverse for $-k_{eff}$ transfer. The proportionality is maintained considering that the distribution of the atoms in the cloud is homogeneous, hence the number of atoms is not considered in Eqn. (4.3) as it will be cancelled out when we do the ratio. We then compare the ratio for the experimental probability P_{+k}/P_{-k} v/s the simulated probability $P^{sim}_{+k}/P^{sim}_{-k}$.

Table 4.2 gives the different values for the observed and simulated ratios of the transition probabilities for different launch velocities. In the above we assumed that the atom launch axis is vertical and coincides with the centre of the detection. We see the experimental and the simulated ratios are in good agreement and hence the difference in the probability for the $+k_{eff}$ and $-k_{eff}$ momentum transfer is well explained.

Table 4.2: Comparison of the measured vs. simulated values of the probability ratios for $+k_{eff}/-k_{eff}$ considering zero shift of launch w.r.t. detection

Atom velocity v_0 (m/s)	Time of flight t (ms)	Cloud radius σ_R (mm)	Recoil displacement d_k (mm)	P_{+k} vs. P_{-k}	P_{+k}^{sim} vs. P_{-k}^{sim}
3.15	575	11.2	2.0	**1.07**	**1.01**
3.79	718	13.5	3.9	**1.19**	**1.15**
3.91	745	13.9	4.1	**1.20**	**1.18**
5.04	988	17.0	6.2	**1.30**	**1.35**

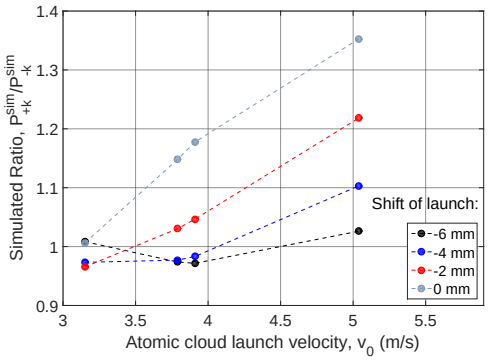

Figure 4.5: The plot of the simulated ratio, $P_{+k}^{sim}/P_{-k}^{sim}$ vs. atomic cloud launch velocity, v_0. The different plots represents the launch of the atomic cloud along a vertical axis which is shifted from the centre of the detection for varied distances. When this shift is -6 mm, the simulated ratios are $\simeq 1$ for all v_0.

Fig. 4.5 shows the plot of the simulated ratio, $P_{+k}^{sim}/P_{-k}^{sim}$ vs. v_0. The different plots represents the atom cloud being launch along a vertical axis which is shifted from the center of the detection. We see for a shift of -6 mm, the simulated ratios are $\simeq 1$ irrespective of v_0. Unless a higher intensity of the detection light is available to saturate the transition, this shift may provide a way of compensating for the inhomogeneity in the detection light sheet intensity and acquire equal transition probability for $\pm k_{eff}$ momentum transfer and a comparable interferometric contrast for $\pm k_{eff}$ momentum transfer.

4.2 Estimation of Non-inertial Noise

In the process of noise characterisation, we are quantifying the contributions of the AI phase noise that come from non-inertial sources. The principal contributors are

the detection system and the Raman lasers. The detection system comprises of the detection laser beams and the acquisition system. The acquisition is made by a 16 bit NI 6341 PCIe Analog to Digital acquisition card [58]. This card has an acquisition noise of 270 μV rms on the full scale of +/-10 V. To quantify the laser and acquisition noise, we observe the detection signal when there are no atoms launched. This condition can be easily achieved by switching off the atom source. The signal that we see can be treated as pseudo-interferometric signal and calculate the technical noise in probability added by the detection and acquisition system, σ_P^{tech}. We can convert it to corresponding phase noise according to the interferometer we use at a later stage.
To find the noise contribution of the Raman lasers, we performed a non-inertial interferometer. We use the fountain geometry in the clock mode by using two $\pi/2$ pulses in the co-propagating mode. In this case, the pulses will only cause hyperfine state transfer in the atoms, without momentum transfer. The two pulses are produced by the same Raman beam at position H1 and the total time of this two-pulse Ramsey interferometer is set to $T = 480$ ms. This interferometer has a total contrast, $C = 50\%$.

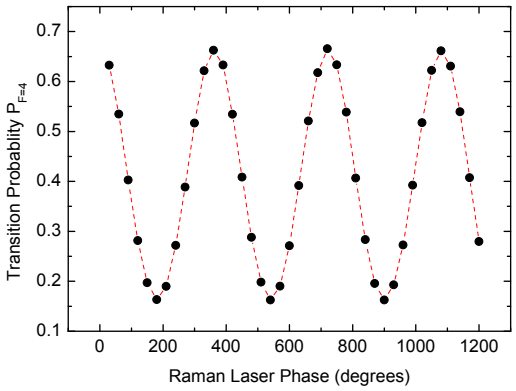

Figure 4.6: the interferometric fringe pattern for Ramsey two-pulse interferometer with $T = 480$ms and a contrast , C = 50%.

We find the Allan deviation of the probability by performing the so called $\pm\pi/2$ measurements at central fringe. This means we fix the laser phase Φ_L at the centre fringe, which is maximally sensitive to phase change, and flip Φ_L by 180^o every cycle. This eliminates the probability offset noise for the Ramsey interferometer (Fig. 4.6). This provides us with the total phase noise contributed by the technical system and the Raman lasers, σ_Φ^{det+L}.

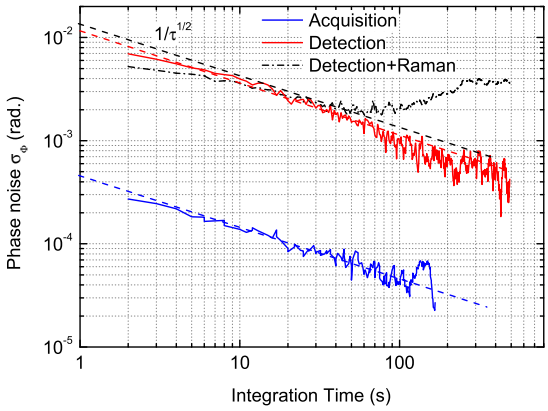

Figure 4.7: Allan deviation of the phase noise for the Ramsey two-pulse interferometer observed for :(a) the detection system (red curve) and only the acquisition system (blue curve) and; (b) Detection + Raman laser contribution (dotted-dash line). The detection system shows a noise level very similar to the total noise including Raman laser noise. This means the total noise is detection limited. The drift in the black curve is due to light shift. The dashed lines are guide to the eyes for $1/\sqrt{\tau}$ dependence of the sensitivity to integration time.

To quantify the phase noise for the detection and the laser contributions, we express the deviation of the probability noise in terms of phase noise of the Ramsey interferometer as σ_Φ. Referring to Fig. 4.7 we get,

$$\begin{aligned} \sigma_\Phi^{det+L} &= 13.5 \times 10^{-3}\, rad/\sqrt{Hz}, \\ \sigma_\Phi^{det} &= 11.5 \times 10^{-3}\, rad/\sqrt{Hz}, \\ \sigma_\Phi^{acq} &= 4.5 \times 10^{-4}\, rad/\sqrt{Hz}. \end{aligned} \tag{4.4}$$

σ_Φ^{acq} is the noise contribution from the acquisition system of the detection. This noise is included inside σ_Φ^{det}. From the above numerics, we separately find $\sigma_\Phi^L = \sqrt{(\sigma_\Phi^{det+L})^2 - (\sigma_\Phi^{det})^2} = 7{\times}10^{-3}$ rad/$\sqrt{\text{Hz}}$. In the above Eqn. (4.4), the total noise contribution can be expressed in probability terms as σ_P^{det+L}= $3.3{\times}10^{-3}/\sqrt{\text{Hz}}$. The above phase noise values is an estimate of the noise contribution from the Raman lasers and the technical components of the detection system. In case of the four-pulse gyroscope, we can consider the σ_Φ^{det+L} as the phase noise coming for the non-inertial experimental components, where the noise is mainly limited by the detection. The non-inertial noise not only comprises the detection noise, but also the quantum projection noise (QPN). We do a study of the QPN limit in our experiment according to

the number of atoms launched from the MOT, post magnetic selection. We study the equivalent probability noise, σ_P using the Ramsey Interferometer while varying the 3D-MOT loading time.

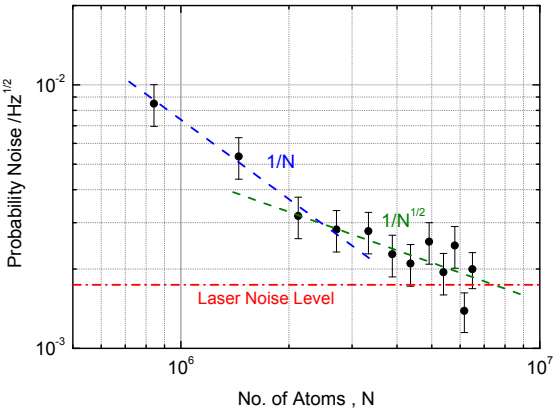

Figure 4.8: Study of probability noise in state $|F = 4\rangle$ for the two-pulse Ramsey interferometer by changing the MOT loading time. The curves changes slope from $1/N$ where it is detection limited, to $1/\sqrt{N}$ where it is QPN limited. The dashed lines are guide to the eyes and the dotted-dashed line in the laser noise limit obtained previously.

When the QPN is the limiting factor, $\sigma_P \propto 1/\sqrt{N}$ [59], where N is the number of atoms reaching the interferometric zone after magnetic selection. On the other hand, when the detection is dominant, $\sigma_P \propto 1/N$. In Fig. 4.8, we observe that for $N < 2 \times 10^6$, the limiting factor in σ_P is technical noise. The probability noise, σ_P is QPN limited, for $N > 2 \times 10^6$. This requires a MOT loading time of more than 150 ms. Hence, we favourably set the MOT loading time > 150 ms while performing interferometry.

4.3 Elimination of One Photon Light Shift

The phase shift at the output of the interferometer $\Delta\Phi_{LS}$ is produced due to the non-zero one photon light shift taking into account the supplementary phase $\Phi_\delta^{1,4}$ imprinted on the atomic wavepacket only during the first and the fourth Raman $\pi/2$ pulses:

$$\Delta\Phi_{LS} = \Phi_\delta^4 - \Phi_\delta^1 = \frac{d\delta_4}{\Omega_{eff}} - \frac{d\delta_1}{\Omega_{eff}}. \tag{4.5}$$

Here, Ω_{eff} is the effective Rabi frequency $= \Omega_1\Omega_2/\Delta$; Δ is the detuning of the Raman lasers from the level $|e\rangle$; and Ω_1 and Ω_2 are the Rabi frequencies for level $|1\rangle$ and $|2\rangle$, respectively. In Eqn. (4.5), $d\delta$ represents the one-photon light shift $= \delta - \delta_{LS}$. The study of the de-phasing due to the light shift has been incorporated for interferometry with Raman beams in [60]. In Eqn. (4.5), for $d\delta_4 - d\delta_1 = 400$ Hz, we will have 1 mrad of interferometric phase added due to a non-zero light shift between states $|1\rangle$ and $|2\rangle$. This shift occurs when the two Rabi frequencies set by the two Raman lasers fluctuate relative to each other. This fluctuation can be interpreted as a fluctuation of the power ratio of the Raman laser pair. Eqn. (4.5) hence can also be transformed into a comparison of the intensity ratio I_2/I_1 of the Raman laser pairs:

$$\Delta\Phi_{LS} = \frac{1}{2\alpha_0^{3/2}}(d\alpha_4 - d\alpha_1). \tag{4.6}$$

In the above equation, we define $\alpha_{1,4} = I_2/I_1|_{1,4}$ which are the intensity ratios for the 1st and the 4th pulse of the four-pulse interferometer. α_0 is the original ratio of I_2/I_1 when intensity fluctuation does not occur. The above derivation has been done in detail in [30]. We already measured the ratio of power of the Raman laser pairs $I_2/I_1 = 1.8$, and the total power entering each Raman beam is $\simeq 100$ mW. Hence, if we consider $\Delta\Phi_{LS} = 1$ mrad, we will have to control the power of the each of the Raman lasers within 0.2%. This is a difficult task without an active feedback control, and we find other ways to be insensitive to the fluctuation of $\Delta\Phi_{LS}$.

We first try to set the light shift to zero. The ratio of the two Raman laser powers is adjusted such that the light shift for the two levels are equal. This can be set by studying the Raman spectroscopy. We focus on the co-propagating component in the Raman spectroscopy (the middle peak in Fig. 4.3). This peak will be shifted from f_{HFS} in the presence of δ_{LS}. We reset this shift to zero by changing the power ratio of our Raman lasers, I_2/I_1 : L4/L3.

In Fig. 4.9(a), we adjust the L4/L3 ratio and observe the Raman spectroscopy around f_{HFS}. We obtained a final $\delta_{LS} = 0.82\pm0.2$ kHz (uncertainty given by the Gaussian fit). This gives $\Delta\Phi_{LS} = 2.1\pm0.5$ mrad. In Fig. 4.9(b) we display how we had set the light shift to the minimum for the Raman beam positions H1 and H2. We note that δ_{LS} at H1 and H2 differs by $=1.5\pm0.3$ kHz even though we use the same set of Raman lasers at H1 and H2. This happens as we do not use the same optical fiber for the two Raman beams: one is polarizing and the other is polarization maintaining. This can produce a relative polarization fluctuation between the two beams, resulting

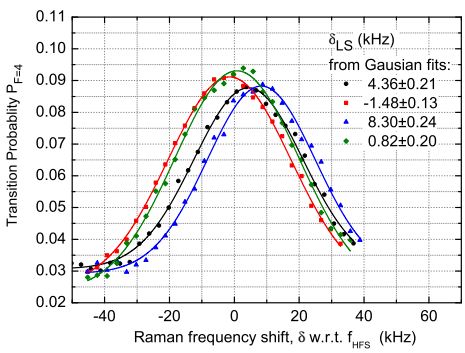

(a) Optimization of light shift for H1

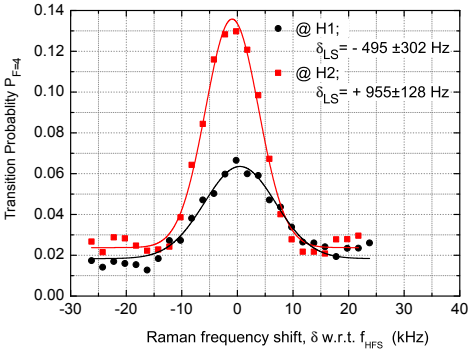

(b) Co-propagating component for H1 and H2

Figure 4.9: Fig 4.9(a) shows the adjustment towards minimum light shift δ_{LS} by Raman spectroscopy at H1. We optimize for the minimum δ_{LS} by varying the ratio of the two Raman lasers and hence changing their relative Rabi frequency. Fig. 4.9(b) shows the co-propagating peaks adjusted optimally near zero light shift in frequency for the Raman beams at H1 and H2. There is a frequency shift of 1.5±0.3 kHz between H1 and H2 beams which means the ratio of laser powers are not the same in the two Raman beams.

in a difference in the L4/L3 power ratio. The resulting difference in δ_{LS} for H1 and H2 can be resolved later by using two separate pairs of Raman laser beams for the two different Raman windows and set δ_{LS} =0 separately for each beam.

4.3.1 Removal of Long Term Drift due to Light Shift

Although $\Delta\Phi_{LS}$ has been minimized, due to a slow drift of the power ratio of the two Raman lasers, the light shift always appears in the interferometric phase in the long term. To remove this effect we will utilize the interferometry with $+k_{eff}$ and $-k_{eff}$ alternatively. The selection of $+k_{eff}$ or $-k_{eff}$ as the momentum transfer from the lasers to the atoms depends on which Doppler resonant frequency we choose as the frequency difference between the Raman lasers L3 and L4. Now, when we change the interferometric state from $+k_{eff}$ to $-k_{eff}$, all inertial phase reverses in sign, except $\delta\Phi_{LS}$. This is because inertial noise is proportional to $\vec{k}_{eff}$. The other noise contributions from the lasers and the technical systems stays random.

$$\begin{aligned}\Phi_{+k_{eff}} &= \Phi_{\mathrm{LS}} + \Phi_{\Omega}^{DC} + \delta\Phi_{\Omega} + \delta\Phi_{vib} + (\delta\Phi_{L} + \delta\Phi_{det}),\\ \Phi_{-k_{eff}} &= \Phi_{\mathrm{LS}} - \Phi_{\Omega}^{DC} - \delta\Phi_{\Omega} - \delta\Phi_{vib} + (\delta\Phi_{L} + \delta\Phi_{det}).\end{aligned} \tag{4.7}$$

In the above equation, if we induce the interferometer to be at the middle of the fringe (the maximally sensitive region) and switch from $\Phi_{+k_{eff}}$ to $\Phi_{-k_{eff}}$. Then, we can perform a half-sum and a half-difference analysis of the alternating k_{eff} states. The half-difference (half-Δ) will give us the inertial phase sensitivity and the half sum (half-Σ) will provide us with a sensitivity to $\delta\Phi_{LS}$ and other non-inertial noise terms. Hence, using the half-Δ for $\pm k_{eff}$ interferometers, we can eliminate the light shift noise.

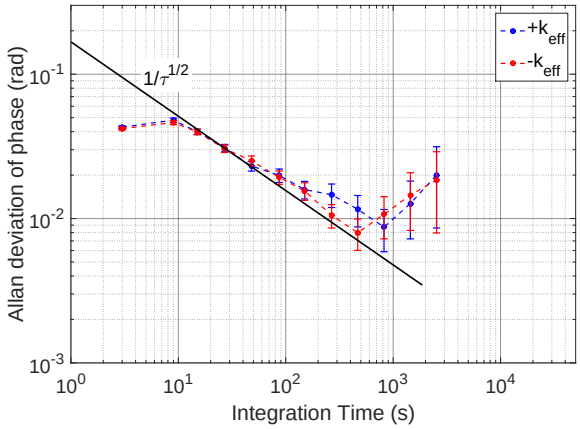

Figure 4.10: Allan deviation of phase noise for $+k_{eff}$ and $-k_{eff}$ data points for $2T$ = 104 ms. It was obtained by the $\pm\pi/2$ method, which removes the probability offset noise. We clearly see the drift due to light shift at around 70 s at a level of 8 mrad of phase noise. The solid black line is the guide to the eyes for $1/\sqrt{\tau}$ dependence of the sensitivity to integration time.

We performed this operation as a test for a four-pulse gyroscope of interrogation time, $2T$ = 104 ms using only H1. We perform the half difference in phase method to remove probability offset noise. In Fig. 4.10. We can observe the drift of the deviation in the long-term starting from a level of 8 mrad of phase noise at around 70 s.

We perform half-Σ and half-Δ of the $\pm k_{eff}$ data points used for Fig. 4.10. We then observe in Fig. 4.11, the half-Σ extracts the drift due to $\delta\Phi_{LS}$. The half-Δ extracts the inertial noise, including $\delta\Phi_{\Omega}$ and $\delta\Phi_{vib}$. Hence, the Allan deviation corresponding to half-Δ is higher at short term, mainly because $\delta\Phi_{vib}$ has not been removed but the drift due to $\delta\Phi_{LS}$ has been eliminated. This happens as the $\Delta\Phi_{LS}$ drifts at a time scale higher than two cycles of the experiment and hence is eliminated easily for long-term integration. We will use the same method for $\delta\Phi_{LS}$ elimination for $2T$ = 480 ms and $2T$ = 800 ms; four-pulse gyroscopes, after we correlate and remove $\delta\Phi_{vib}$. We note that at short-term the phase noise is lower in half-Σ case as the vibration

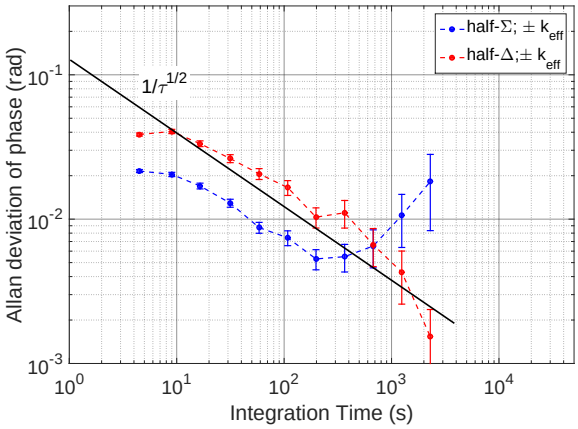

Figure 4.11: Allan deviation of phase noise for half-Σ and half-Δ of $\pm k_{eff}$ interleaved data points for $2T = 104$ ms. The solid black line is the guide to the eyes for $1/\sqrt{\tau}$ dependence of the sensitivity to integration time.

noise is correlated cycle-to-cycle at low frequency. This is possible as we will establish later that the vibration noise affecting the interferometer is at time scale < 1 s, where the cycle time is $\simeq 1$ s for the different interferometric conditions we have performed so far.

4.4 Use of Vibration Noise Sensor

We already established previously that the use of the four-pulse fountain geometry leads to a null sensitivity to DC acceleration. However, we are still sensitive to accelerations, i.e., AC vibrations. Our in the next chapter will be to correctly estimate this vibration noise using an external sensor. In this chapter, we need the vibration sensor to estimate the vibration noise for the analytical purposes later. Let us recapitulate the transfer function we require between vibration and phase to characterize the sensor signal into interferometric phase.

4.4.1 Temporal Transfer Function in Velocity and Acceleration

In Chapter 2, we established that a change in the interferometric phase can be expressed as a phase evolution in the Raman pulses:

$$\Delta\Phi = \int_{-\infty}^{+\infty} g_\phi(t) \frac{d\phi(t)}{dt} dt. \tag{4.8}$$

The above equation represents the phase shift imprinted on the atoms from the Raman pulses. Due to the vibration of the retro-reflection mirror of the Raman beam, the fluctuation produced in the laser wavefront also gets imprinted as the phase noise. If we use a velocity vibration sensor to record this vibration during interferometry, then we can interpret $d\phi/dt$ in Eqn. (4.8) in terms of the velocity signal of the vibration sensor. In our case, we use a Guralp CMG 40T seismometer [61] to record the velocity signal. This seismometer gives a signal in volts with a scaling to velocity, $A_{vel} = 400$ V/(ms^{-1}), so that.

$$\frac{d\phi}{dt} = k_{eff} \cdot \frac{dx}{dt} = k_{eff} \frac{V_{vel}}{A_{vel}}. \tag{4.9}$$

This gives us the vibration phase noise as:

$$\delta\Phi_{vib} = \frac{k_{eff}}{A_{vel}} \int_0^{2T} g_\phi^v(t) \cdot V_{vel}(t) dt. \tag{4.10}$$

Here, g_ϕ^v is the transfer function for velocity and is similar to g_ϕ. In comparison to the velocity sensor, we can also use an acceleration sensor: the Nanometrics Titan Accelerometer [62]. It has a scaling from volts to acceleration, $A_{acc} = 8.16$ V/(ms^{-2}). In that case,

$$\frac{d^2\phi}{dt^2} = k_{eff} \cdot \frac{d^2x}{dt^2} = k_{eff} \frac{V_{acc}}{A_{acc}}. \tag{4.11}$$

In terms of acceleration, $\delta\Phi_{vib}$ will be calculated as

$$\delta\Phi_{vib} = \frac{k_{eff}}{A_{acc}} \int_0^{2T} g_\phi^a(t) \cdot V_{acc}(t) dt, \tag{4.12}$$

where,g_ϕ^a is the acceleration transfer function in time.

$$g_\phi^a(t) = \int g_\phi^v(t') dt'. \tag{4.13}$$

The two temporal transfer functions, g_ϕ^v and g_ϕ^a are given in Fig. 4.12. Better the estimation of the vibration noise via the external sensor, higher will be our ultimate signal to noise ratio.

Table 4.3 shows the comparison of the different physical aspects of the Guralp seismometer and the Titan accelerometer. It is mostly clear that the accelerometer is a better choice due to its smaller dimension, light-weight and larger bandwidth. however, it has a higher intrinsic noise and has a DC offset drift proportional to the temperature change. We are going to use both systems to estimate the vibration noise and establish which is the better sensor for estimating the correct vibration noise

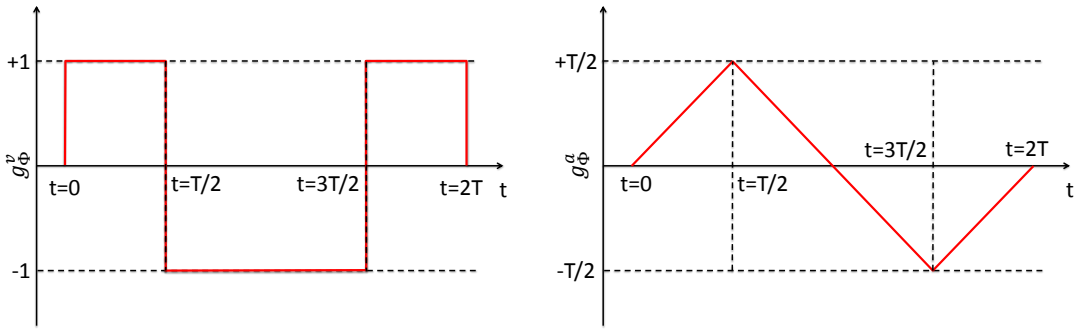

(a) Velocity transfer function,g_ϕ^v (b) Acceleration transfer function, g_ϕ^a

Figure 4.12: Temporal transfer function from acceleration and velocity to interferometric vibration phase, $\delta\Phi_{vib}$

Table 4.3: Comparison of the Guralp seismometer and the Titan accelerometer in its different aspects

Particulars:	Guralp Seismometer	Titan Accelerometer
Dimensions l×b×h (cm^3)	16.8×16.8×21	14×8.5×5.8
Weight (kgs)	2.49	0.96
Bandwidth (Hz)	Upto 40	DC - 430 Hz
Type of Coupling	AC	DC
Intrinsic Noise ($dB/m^{-2}s^{-4}Hz^{-1}$)	-172	-150
Temperature Sensitivity	$<1.5\times10^{-4}$ m/s for 1°C	5.9×10^{-4} ms^{-2}/°C offset drift

affecting the AI .

4.5 Passive Vibration Isolation

Before trying to rejecting the vibration noise, we first tried to passively minimize it. For this study, we installed passive vibration isolation systems for the experimental set-up and used the external vibration sensor to estimate the rejection of the vibration noise for the corresponding four-pulse interferometer.

Fig. 4.13 shows the the power spectral density, S_a in m^2s^{-4}/Hz for a frequency range of 0.1-500 Hz. The figure shows the corresponding curves as an outcome of the following vibration isolation methods:

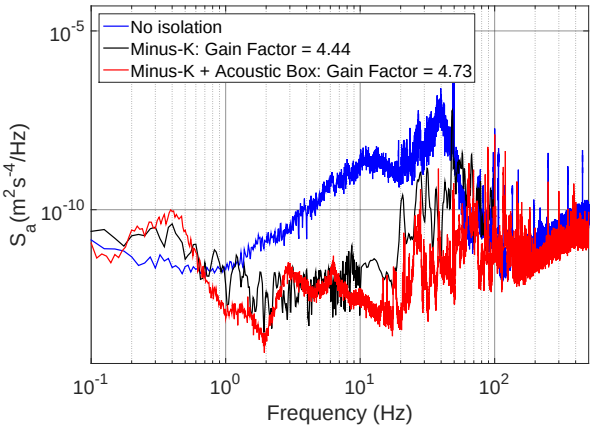

Figure 4.13: The acceleration noise spectrum S_a :(i) without vibration isolation (blue curve); (ii) isolation only by the Minus-K (black curve); and (iii) isolation using the acoustic box and the Minus-K (red curve). The corresponding gain factor is computed for the phase noise of a four-pulse interferometer of $2T = 480$ ms.

Isolation platform The initial step in the vibration isolation was to balance the entire experimental set-up on a bench top vibration isolation platform. This is the standard Minus-K 650BM-1 Platform [33]. When the platform is in the floating mode, it has a natural frequency of 0.5 Hz and it goes from 0 dB to -60 dB of vibration isolation from 1 Hz to 100 Hz in the horizontal axis. The Minus-K platform has a nominal payload range of 227 -309 kg, where as our net experimental structure presently weighs $\approx$ 300 kg.

Acoustic box To avoid further vibration noise due to acoustic sources, we placed a box lined with 57 mm thick foam which encompasses the entire experiment. The walls of the box is made rigid by sheets of polyethylene (3 mm thick) panels sandwiched between thin layers of aluminium, and the foam covering was fixed on the panels by a special adhesive . The experiment is covered on the five sides: 4 panels for the side-walls and one for the top cover. The total volume of this box is 8 m^3. The foam has a density of 20 kg/m^3 and it has an attenuation of -21 dB at 125 Hz. The set-up and characterization of the box is described in detail in [16].

In Fig. 4.13, we see that first when the Minus-K platform is working, it transmits the noise in the range of 0.8 - 70 Hz and converts the energy of the high frequency vibration to low frequency around its natural frequency. Here, the payload is near the maximum weight, which shifts the natural frequency to 0.4 Hz. Using the acoustic box,

Table 4.4: Vibration phase noise for four-pulse interferometer for different combination of isolation system

a : $2T = 480$ms

Isolation	σ_Φ^{vib} (rad)			
	0.1-1 Hz	1-10 Hz	10-100 Hz	Total
None	0.25	2.43	1.42	2.82
Minus-K	0.42	0.45	0.17	0.64
Box + Minus-K	0.51	0.30	0.03	0.59

b : $2T = 800$ms

Isolation	σ_Φ^{vib} (rad)			
	0.1-1 Hz	1-10 Hz	10-100 Hz	Total
None	1.00	2.81	1.22	3.22
Minus-K	1.77	0.96	0.22	2.02
Box + Minus-K	2.26	0.36	0.03	2.23

we observe that we mainly reduce higher frequency noise around 10 - 100 Hz. When the acoustic box was installed it further decreased the noise in the overall frequency range of 0.1 -100 Hz.

In Table 4.4a we show the difference in the standard deviation of the vibration phase noise when there is no isolation and when there is isolation (using the acoustic box and the Minus-K platform). This noise is estimated by convolving the four-pulse transfer function with the acceleration noise spectrum given in Fig. 4.13. We understand that adding the acoustic isolation box did not help us to remove low frequency vibration noise. For the $2T = 800$ ms four-pulse AI, this is even more evident [Table 4.4b] where the gain factor in the vibration rejection is lower than that for $2T = 480$ ms. This means the rejection of the vibration noise via correlation of the AI signal with the external sensor signal is necessary.

4.6 Temperature Stabilization

The acoustic box around the experiment not only cuts off the acoustic noise but also works as a thermal insulation system for the experimental structure. This thermal insulation is important specially for the temperature sensitive Titan accelerometers that we have installed on the experimental structure. We have presently two accelerometers placed on the top and the bottom of the experiment. For the structure shown in Fig. 4.14, we monitored how the temperature stabilized after we closed the acoustic box.

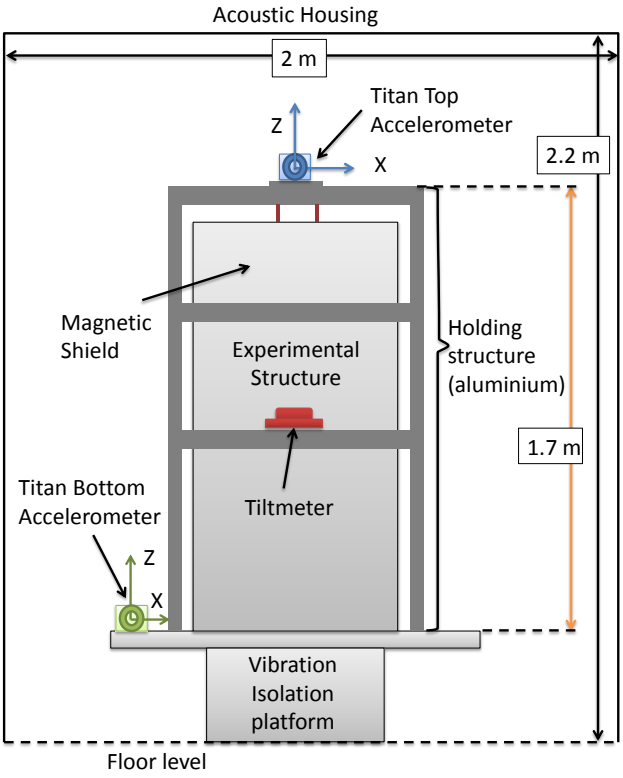

Figure 4.14: Schematic of the placement of the two Titan accelerometers. The entire system is enclosed by the acoustic box which is the black outside in the figure.

We attached a temperature sensor (LM35) [63] to the external housing of the Titan accelerometers to monitor the variation in temperature before and after closing the acoustic box. Fig. 4.15(a) shows from the starting point of closing the box, the temperature stabilizes from 22°C to 23°C at the top accelerometer position; and from 21.8°C to 22.8°C at the bottom accelerometer position. During this time, the external temperature close to the acoustic box fluctuates periodically around 21.5°C. this periodicity comes from the cycle of cooling of the air conditioning system. In Fig. 4.15(c) we study the fluctuations in the external temperature through its Fourier transform. We observe a peak at 6×10^{-4} Hz. This is possibly the cycle frequency of cooling for the air conditioning system. In Fig. 4.15(b) we observe the temperature after the relaxation inside the acoustic box and we see even with 1°C of change in temperature outside produces less that 0.1°C of temperature inside the acoustic box. This means the acoustic box works as a low pass filter for temperature fluctuations for frequencies as low as 6×10^{-4} Hz.

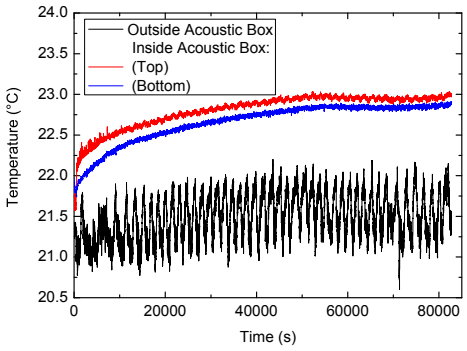

(a) During temperature relaxation

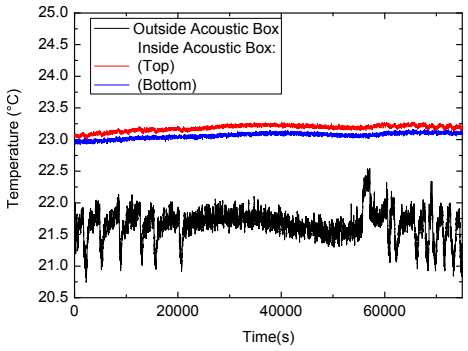

(b) After temperature relaxation

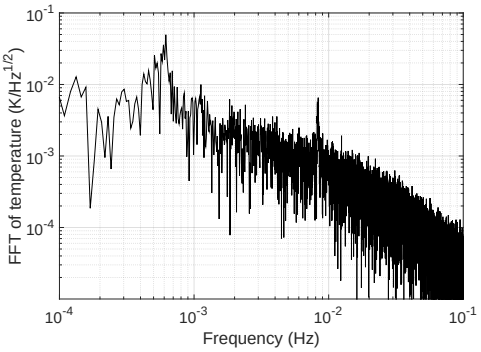

(c) FFT of temperature

Figure 4.15: Fig. 4.15(a) and 4.15(b) shows the temperature fluctuation outside and inside the acoustic box during and after relaxation of the temperatue. Inside the box, we monitor at the bottom and at the top of the experimental structure. Fig. 4.15(c) shows the Fourier transform of the recorded external temperature after the removal of the drift. It gives a fluctuation frequency at 6×10^{-4} Hz.

4.6.1 Thermal Isolation for the Accelerometers

Since the Titan accelerometers are susceptible to drift in temperature, we insulate the Titan accelerometers from the temperature variations inside the acoustic box. We prepared a thermal cover for the Titan accelerometers using the same foam layers used in the acoustic box.

Fig. 4.16(a) represents the change in the temperature variation, before and after putting the thermal cover, for the top accelerometer. Fig. 4.16(b) represents the same for the bottom accelerometer. We note that the temperature fluctuation is higher for the bottom accelerometer than that of the top one (the range of temperature depicted in figs.4.16(a) and 4.16(b) are the same). This can happen due to the convection of the

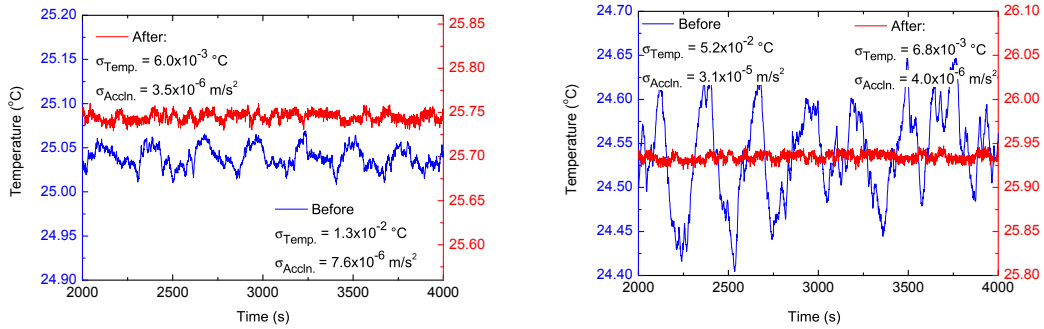

(a) Top Accelerometer temperature (b) Bottom Accelerometer temperature

Figure 4.16: Temperature stability difference before and after putting the thermal cover for the bottom and top accelerometers.

air inside the acoustic box where the temperature changes from bottom to top of the experiment. However, after putting the thermal cover, their temperature variations become almost identical.

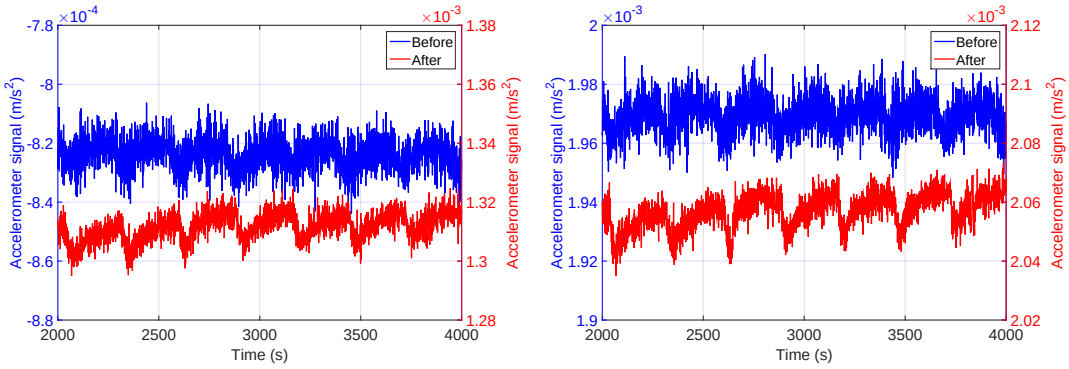

(a) Top Accelerometer (b) Bottom Accelerometer

Figure 4.17: Effect on the acceleration signal of the top and bottom accelerometer before (blue) and after (red) placing the thermal cover.

We studied the effects of this thermal cover on the signal of the accelerometer itself. Fig. 4.17 shows that the thermal cover produces a change in the accelerometer signal fluctuations.

Table 4.5 shows that we gain 2 times from the temperature isolation of the top accelerometer and a factor of $\simeq 8$ for the bottom accelerometer (as wee see in Fig. 4.16). But, from the true acceleration signals, we see the thermal cover reduces the noise by a factor of 1.3 for both accelerometers (as wee see in Fig. 4.17).

Table 4.5: Effect of thermal cover on Titan accelerometers

Thermal Cover	Standard deviation of :			
	Acceleration from temperature variation (m/s^2)		Acceleration from accelerometer signal (m/s^2)	
	Top	Bottom	Top	Bottom
Off	7.6×10^{-6}	3.1×10^{-5}	4.7×10^{-5}	5.7×10^{-5}
On	3.5×10^{-6}	4.0×10^{-6}	3.6×10^{-5}	4.5×10^{-5}

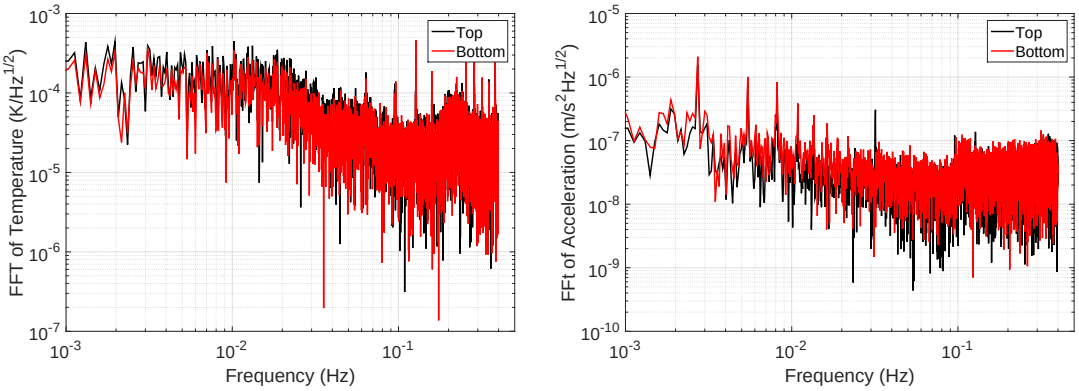

(a) FFT of temperature signals

(b) FFT of the acceleration signals

Figure 4.18: FFT of the temperature and acceleration signals from the two accelerometers after placing the thermal covers. The temperature FFT shows no noticeable frequency peaks after placing the thermal covers. The acceleration FFT still shows the frequency peaks, which means the low frequency fluctuations are real inertial signal uncorrelated to the temperature fluctuation of the accelerometers.

Furthermore, performing Fourier transform on the resulting data, we observe in Fig. 4.18 that the temperature has no noticeable low-frequency periodic fluctuations, but the acceleration has low frequency periodic fluctuations at 2.7×10^{-3} Hz (time scale of 370 s) with harmonics. This means there is true vibration noise at this very low frequency, which is not correlated to the temperature fluctuations of the accelerometers.

4.7 Active Low Frequency Stabilization

In the previous section, we found that there is very low frequency (periodic and harmonic) vibration noise on vibration sensors. We first verify this phenomenon by study-

ing the signal of the tiltmeter (mentioned in Section 4.1.1) and drawing a correlation between the accelerometer and the tiltmeter signal.

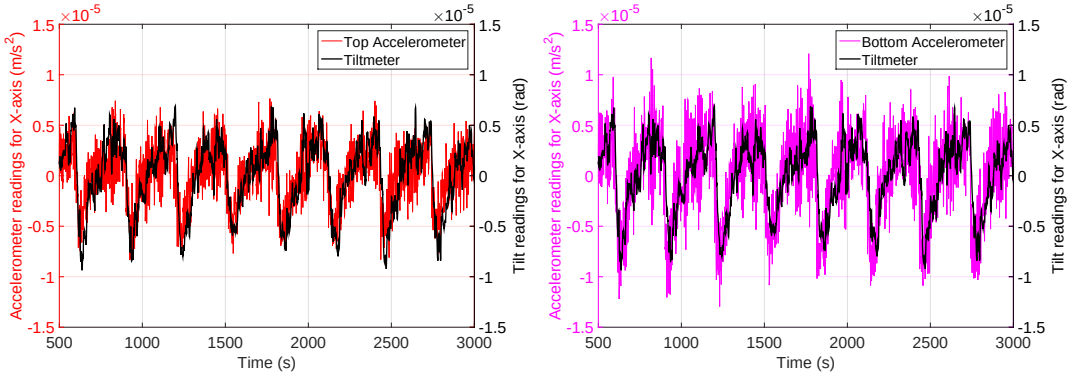

(a) Top Accelerometer and Tiltmeter (b) Bottom Accelerometer and Tiltmeter

Figure 4.19: Comparison of the accelerometer and the tiltmeter signals.

We acquire the two signals of the top and bottom accelerometers and the signal of tiltmeter simultaneously during each experimental cycle. In Fig. 4.19, we observe that the periodic fluctuations is present in both the accelerometer and the tiltmeter signals. Hence, we understand that this very low frequency vibrations is not diminished by the isolation platform. To compensate for this very low frequency noise at 2.7×10^{-3} Hz and its harmonics, we use an active low-frequency locking system using the signal of the tiltmeter.

4.7.1 Actuation System for Tilt Lock

The major component in this locking system is the magnetic actuator shown in Fig. 4.20. In this actuator, we use a solenoid clamped to the ground by a heavy ballast. There are 270 turns of a Cu coil and the hollow solenoid core is of the length, $L_S = 35$ mm. The inner radius is $r_S = 30$ mm and the outer radius is 41.5 mm. We use a neodymium magnet [64] which inserts inside the solenoid and has a radius of $r_M = 7.5$ mm and of length 100 mm. It has a relative permeability of 1.05. The edge of the magnet is placed near the centre of the solenoid, where the magnetic field produced is the maximum. Hence the magnet will experience the maximum force at the solenoid core centre, when a current is passed through the solenoid. The magnetic actuator pushes along the z-axis and produces tilt along the x-axis (the axis of the Raman beams) and near the edge of the base plate, as shown in Fig. 4.20.

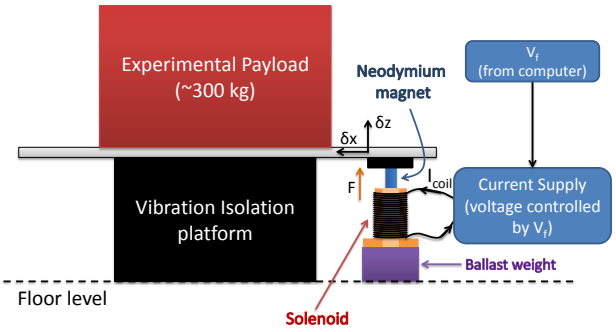

Figure 4.20: Illustration of the magnetic actuator and its placement w.r.t. the base of the experiment.

4.7.2 The Tilt Locking System

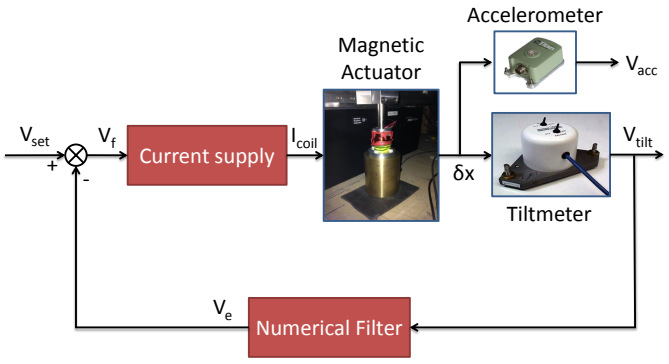

Figure 4.21: Low frequency "Tilt-lock" scheme.

When the magnetic actuator displaces the base of the experiment, the tiltmeter signal along the x-axis, V_{tilt} is used as the reference for the locking system. The locking system takes the input from the tiltmeter and passes it through a numerical filter designed inside the experimental code. The error signal is fed back as a compensation via a voltage controlled current supply. This current is a low noise (6 mA (rms)) power supply from Delta Elektronika (0-30 V, 0-1 A)[65]. It actuates the solenoid-magnet system and forms the feedback loop of the locking system (Fig. 4.21).

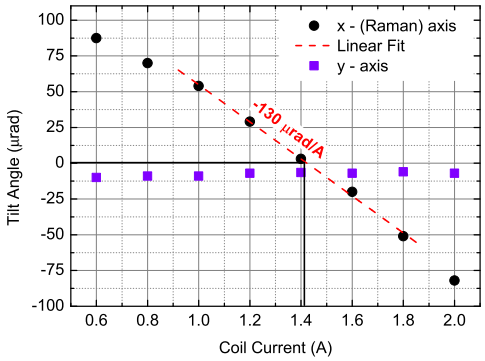

Figure 4.22: Calibration of Tilt angle vs. the solenoid current. The linear fit around ± 50 μrad of zero tilt gives a calibration of -130 μrad/A.

Fig. 4.22 shows the calibration of the output of the tiltmeter in μrad along the x-axis (along the Raman beams) and the y-axis. We linearly changed the solenoid current (send from the current supply) and acquired the tiltmeter value and converted it to radians. This gives us a calibration factor of -130 μrad/A. As we stated the current supply has a noise of 6 mA (rms), this means the tilt-lock has a limiting error of 0.8 μrad (rms) due to this supply current noise. We also understand from the plot that changing the current has almost no effect on the y-axis and hence there is no crosstalk between the two axes. If V_{set} is the voltage send to the programmable current supply to set a lock point, then corresponding to this V_{set} the x-axis tiltmeter value gives V^0_{tilt}. Between V_{set} and V^0_{tilt} there is global scaling factor, G. Fig. 4.21 shows the scheme of the tilt-locking system. The numerical filter is designed in the programming code of experimental control. We tested two kinds of filters:

Low pass filter (LPF) A low-pass filter is a filter that passes signals with a frequency lower than a certain cut-off frequency and attenuates signals with frequencies higher than that cut-off frequency. We set up a low-pass numerical filter which takes as input V_{tilt} and outputs V_e as the error signal at each experimental cycle. The tilt signal V^i_{tilt}, of the i-th experimental cycle is treated by the filter equation:

$$\begin{aligned} \widetilde{V}^i_{tilt} &= \frac{V^{i-1}_{tilt} + \alpha V^i_{tilt}}{1+\alpha}, \\ V^i_e &= \widetilde{V}^i_{tilt} - V^0_{tilt}, \\ V^i_f &= V_{set} - G_L \cdot V^i_e. \end{aligned} \tag{4.14}$$

In the above equation $\widetilde{V}^i_{tilt}$ is the filtered V^i_{tilt} by a frequency set by the parameter α. V^i_f is the final voltage value send to the coil current supple for voltage control. We used $\alpha = 0.1$. This means we take 10% weight of the tilt value of the present experimental cycle in the numerical low pass filter. G_L is the global scaling factor used in the loop to scale the correcting tilt voltage V^i_e in terms of the current control setting voltage V_{set}. The final value of V^i_f is send to the supply for current control. The optimum value of G_L was 0.1 to be below the oscillation regime of the lock loop.

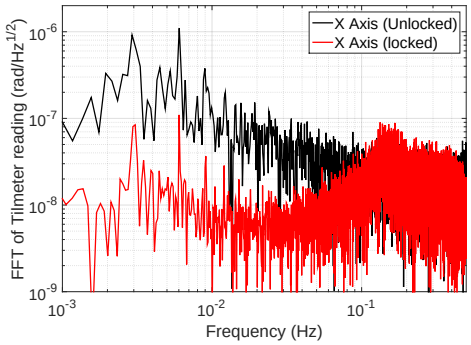

(a) Tiltmeter

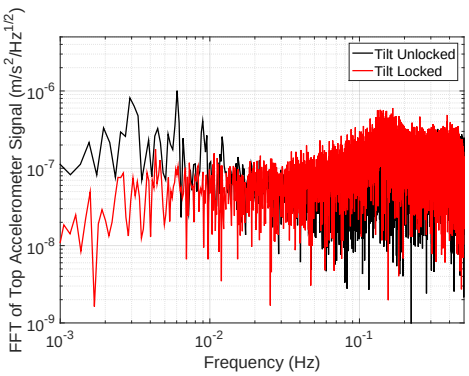

(b) Top accelerometer

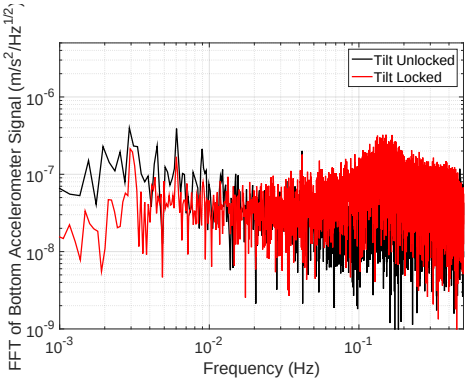

(c) Bottom accelerometer

Figure 4.23: Fig. 4.23(a) shows the Fourier transform of the accelerometer signals in $m/s^2/\sqrt{Hz}$, with (red) and without (black) the tilt-lock with LPF filter. Fig. 4.23(b) and 4.23(c) shows the Fourier transform of the accelerometer signals for the same case as Fig. 4.23(a). We observe here the bandwidth of the lock is upto 0.15 Hz where we have the peak at the higher frequency in the tilt-locked case.

In Fig. 4.23(a), we see how the Fourier transform of the tilt signal changes when we use the tilt-lock with the LPF. The peak we see in the FFT of the locked tilt signal portrays the bandwidth of the lock. Here, the locking system is able to minimize the low frequency periodic fluctuations in the x -axis tilt by a factor of 50. This LPF locking

system reduces the RMS of the tilt angle from 5.4 μrad to 2.1 μrad. We also studied the accelerometer signals of the top and bottom accelerometers, simultaneously. The Fourier spectrum of the accelerometer signals (Fig. 4.23(b) and 4.23(c)) shows that there is some mitigation of the periodic fluctuation in the acceleration signal. The suppression factor is 10 at the top of the experiment and 1.5 at the bottom of the experiment. The difference is because the tilt-lock is not actuated by a continuous signal but by the experimental control which changes every cycle. Hence, the efficiency of the lock is more evident for a position far from the discontinuous actuation of the magnet. In any case, we observe that the locking system is fruitful to minimize the low frequency acceleration noise. We note that the LPF filter does add some acceleration noise around the bandwidth of the locking system (at 0.15 Hz).

Proportional integrator The other numerical filter that has been tested is the proportional integrator. This is nothing else but a summation of the tilt signal error values from the previous experimental cycles, multiplied by a global scale factor G_I.

$$\begin{aligned} V_e^i &= V_e^{i-1} - V_{tilt}^i - V_{tilt}^0, \\ V_f^i &= V_{set} - G_I \cdot V_e^i. \end{aligned} \tag{4.15}$$

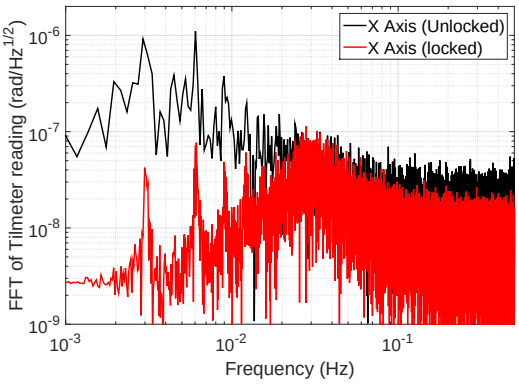

Figure 4.24: Fourier transform of the x-axis tilt signal in $rad/\sqrt{Hz}$, with tilt-lock with proportional integrator (red) and without (black) tilt-lock.

Fig. 4.24 shows the comparison of the FFT of the tiltmeter signal for the locked vs. the unlocked cases where we established the optimum gain, G_I. It reduces the RMS of the tilt angle from 5.4 μrad to 2.2 μrad. If G_I is too low, the locking system was not able to minimize the periodic fluctuations. If G_I is too high, it adds excess vibration

noise. We now compare the two filters that we have used for the tilt-lock and establish which one is optimum. Table.4.6 shows the optimum filter for the tilt-lock system is

Table 4.6: Vibration phase noise w.r.t. top and bottom accelerometers for different tilt-lock filters

Type of filter:	$\delta\Phi_{vib}$ (mrad)			
	$2T$ = 480 ms		$2T$ = 800 ms	
	Top	Bottom	Top	Bottom
No filter (open-loop)	7.1	2.6	31.6	11.6
Low pass filter (f_c=0.15 Hz)	10.0	4.0	44.9	18.1
Proportional Integrator ($G_I = 0.2$)	3.3	1.4	14.6	6.1
Proportional Integrator ($G_I = 0.1$)	2.9	1	12.9	4.3

the Proportional Integrator, with $G_I = 0.1$. Any $G_I < 0.1$ led to higher vibration phase noise. The table shows the vibration noise rejection at frequencies < 0.1 Hz. For the rejection above 0.1 Hz, we will be using the correlation method mentioned earlier. In the future a tilt-locking system along the y-axis can also be installed, for low frequency stability of the experimental platform. This will not affect the x-axis tilt as we saw in Fig. 4.22 there is no crosstalk between the two axes.

4.8 Conclusion

In this chapter the method for rejecting parasitic effect on the four-pulse interferometer were presented. We first classified the principal components affecting the interferometric phase and explained the methods applied to optimize the Raman transition for acquiring maximum signal-to-noise ratio from the the interferometer. Next, we presented the characterization and the optimization methods for the rejection of non-inertial effects, e.g., one photon light shift. For the minimization of parasitic inertial noise, various active and passive methods were presented. The residual vibration phase noise at low frequency is still substantial and the final vibration noise rejection will be performed via the correlation of the AI signal and the external sensor signals. This will be presented in the next chapter.

Chapter 5

Rotation Signal Extraction and Characterizations

We established in the previous chapter that the major source of the parasitic noise in the interferometric signal is vibration. The vibration adds a phase noise equivalent to $\delta\Phi_{vib}$ in the total interferometric phase, Φ. In this chapter we will present how we correlate, and therefore reject vibration signal from the interferometric signal. This vibration noise is recorded from external sensors mounted on the experiment. Such a correlation system was well incorporated for a cold atom gravimeter by Gouet *et al* in [66]. After the vibration rejection, we extract the rotation sensitivity after this rejection and characterize the limitations of the rejection procedure.

5.1 Methods to Estimate the Gyroscope Rotation Sensitivity

The signal of the interferometer that we detect is the transition probability of state $|F = 4\rangle$ of the Cs atoms. If we represent the transition probability, P which the general way can be written as

$$\begin{aligned} P &= P_0 + A\cos\Phi, \\ \Phi &= \delta\Phi_{vib} + \delta\Phi_{\Omega} + \delta\Phi_0. \end{aligned} \tag{5.1}$$

where, P_0 is the offset of the interferometric fringe and A is half of the contrast. Φ is the total interferometric phase accumulated during the measurement including $\delta\Phi_{vib}$ the vibration phase noise component, $\delta\Phi_{\Omega}$ the rotation phase component and $\delta\Phi_0$ the non-inertial phase component. We use the external vibration sensor (accelerometer or seismometer) to record the vibration noise during the duration of the atom gyroscope. We treat this recorded signal with the corresponding vibration noise transfer function (in acceleration or velocity depending on the external sensor) and acquire the vibration phase, $\delta\Phi_{vib}$. We then plot the transition probability, which is the interferometric signal vs. the acquired $\delta\Phi_{vib}$ and visualize the correlation. The better the estimation of the vibration noise that affects the interferometer, the better will be the correlation. Following Eqn. 5.1, the correlation should be linear in the regime where $\delta\Phi_{vib}$ (peak-to-peak) $< \pi$; and sinusoidal in the regime where $\delta\Phi_{vib}$ (peak-to-peak) $> \pi$. By rejecting this correlation, we can extract the rotation sensitivity. Now I will present two methods that we have tested, with simulations, in order to estimate the rotation signal in the presence of large vibration noise. The solution is not trivial because we have to perform a non-linear fit and we are subject to amplitude noise and the phase error in the estimation of the vibration noise.

Method 1: Residue of correlation In this method we place the interferometer at the centre of the fringe alternately place them on the two sides of the fringe. We find the residue of the correlation of the interferometric signal with the recorded vibration phase and perform half-difference of the residue to remove the probability offset noise of P_0. This results in the extraction of the rotation sensitivity. To simulate the vibration and residual rotation sensitivity in the interferometric phase, we consider Eqn. (5.1) as:

$$P = P_0 + A\cos(\delta\Phi_{vib} + \widetilde{\delta\Phi}), \tag{5.2}$$

where we simulate $\delta\Phi_{vib}$ as a Gaussian white noise with an RMS of $\sigma_{vib} = 0.3$ rad and the residual component, $\widetilde{\delta\Phi}$ with an RMS noise of $\sigma_{\widetilde{\delta\Phi}} = 0.2$ rad. For the simulated fringe, we put $P_0 = 0.5$ and $A = 0.1$ (20% contrast). To simulate a more realistic system, we added probability noise and contrast noise in P_0 (σ_P=3.3×10^{-3}) and A (σ_A=10^{-2}), respectively. The simulated σ_{P_0} corresponds to the technical noise limit we measured in the previous chapter.

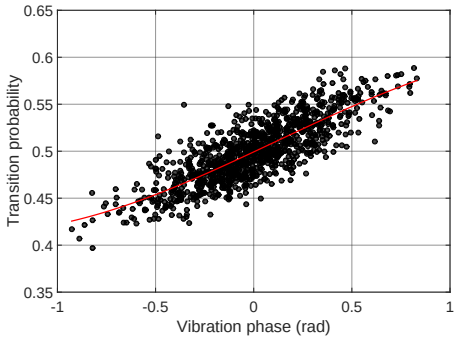

Figure 5.1: **Simulation** of the interferometric phase including vibration noise, $\delta\Phi_{vib}$ and an uncorrelated component $\widetilde{\delta\Phi}$. The red line is a sinusoidal fit. The residue of the sinusoidal fit (in red) gives the sensitivity of $\widetilde{\delta\Phi}$.

We plotted the simulated P with the simulated $\delta\Phi_{vib}$ and obtained the correlation observed in Fig. 5.1.

$$\delta\Phi = \cos^{-1}(\delta P/A). \tag{5.3}$$

After correlation, we look at the convert the residual probability, δP into phase noise $\delta\Phi$ following the above equation. The RMS of this residual phase was $\sigma_{\widetilde{\Phi}} \approx 0.2$ rad. This equals to the rotation noise that was added in the simulation. Hence, we verify this method works properly for correct extraction of rotation sensitivity, but when $\widetilde{\delta\Phi}$ reaches values near 0 or π, Eqn. 5.3 will diverge. This illustrates the case when the interferometric data points reaches the extremities of the fringe. So, the above residue method is useful when the peak-to-peak $\delta\Phi_{vib}$ is $< \pi$. For larger vibration noise, we use a different correlation method for vibration noise rejection.

Method 2: Packet-fitting of the offest phase To find the rotation sensitivity for high vibration regime, we perform *packet-fit* of the data points. This method has been used in [67]. Here we simulate for high vibration noise. We divide N_{data} data points into small packets of size N_{pack} and correlate the interferometric signal P of each packet with their corresponding $\delta\Phi_{vib}$. The correlation of each packet corresponds now

to a sinusoid and we acquire the phase offset, Φ_{pack} for the least square sinusoidal fit of these points.

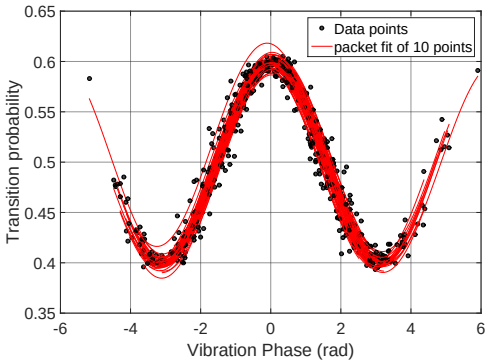

Figure 5.2: **Simulation** of the packet fitting of the data points, where N_{pack}=10. the red lines represent the correlation for best fit of a sinusoid for each packet. We simulated here for 100 packets. We extract the phase offset, Φ_{pack} for each packet-fit. The RMS of Φ_{pack} will provide us with the rotation phase sensitivity. The RMS of the simulated amplitude noise here is 10^{-2} of A=0.1. The probability noise was simulated to represent the technical noise limit.

In Fig. 5.2 we chose, $N_{pack} = 10$ and illustrate the correlation for 100 such packets. We use Eqn. (5.2) to simulate the interferometric system we put the same Gaussian noise in $\widetilde{\delta\Phi}$, P_0 and A as in the simulation of the previous section, but this time σ_{vib} = 1.5 rad (5 times higher than the previous section). Each sinusoidal fit corresponds to one packet and the RMS of the fitted phase offset, Φ_{pack} (the red lines in Fig. 5.2) provides us with the rotation phase sensitivity. When we fit for the sinusoid we allow some bounds on P_0 and A as to compensate for their corresponding noise we added in the simulation. The extracted rotation sensitivity gives $\sigma_{\widetilde{\Phi}} = 0.23$ rad. This value closely resembles the simulated noise in $\widetilde{\delta\Phi}$ and hence useful to reject high vibration noise when its correlation with the interferometric signal is non-linear. The sensitivity is slightly overestimated due to the presence of the probability and contrast noise. We will now explain how we can use the above correlation methods in practice.

5.2 Use of a Single Vibration Sensor

The interferometric phase is governed by the three basic contributions: (a) Raman Lasers, (b) Acceleration Noise, and (c) Rotation Noise.

We can scan the interferometric fringes by changing the difference of the phase of the Raman lasers, cycle-per-cycle. Fig. 5.3 shows one such scan of the four-pulse

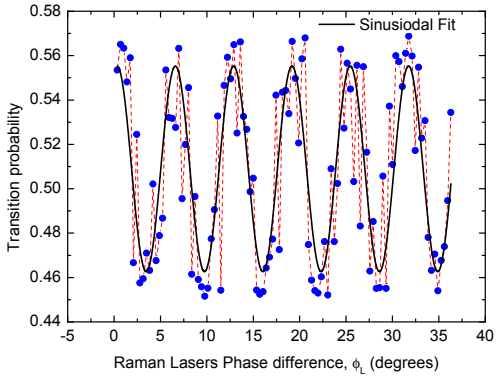

Figure 5.3: Scan of the four-pulse interferometric fringes for $2T = 480$ ms by scanning the Raman laser phase difference in consecutive cycles of the experiment. The black curve is a sinusoidal fit.

interferometric fringes for $2T = 480$ ms. The figure gives an example how the vibration noise deteriorates the signal-to-noise (SNR) of the interferometric signal which is visible in the fringe scan. We will now do a quantitative analysis of the vibration noise for our four-pulse gyroscope with $2T = 480$ ms and of its rejection using external vibration sensors.

For the characterization of the vibration noise, we first used the four-pulse interferometer of total interrogation time, $2T = 480$ ms. For this we required the Raman windows H1 and H2.

5.2.1 Correlation with Seismometer

We first used the Guralp seismometer (as presented in the previous chapter) as the external sensor of vibration. We placed the seismometer at the middle position shown in Fig. 5.4. This position is closest to the Raman mirrors H1 and H2 and the optimum position of placement (a priori). We recorded the signal of the seismometer and treated it with the velocity transfer function of the interferometer to find the vibration phase noise.

$$\delta\Phi_{Vib} = \frac{k_{eff}}{A_{vel}} \cdot \frac{1}{2Tf_S} \cdot \Big(\sum_{n=f_S\cdot\tau_R}^{f_S\cdot(\tau_R+T/2)} V_{vel}(n) - \sum_{n=f_S\cdot(\tau_R+T/2)}^{f_S\cdot(\tau_R+3T/2)} V_{vel}(n) + \sum_{n=f_S\cdot(\tau_R+3T/2)}^{f_S\cdot(\tau_R+2T)} V_{vel}(n) \Big). \tag{5.4}$$

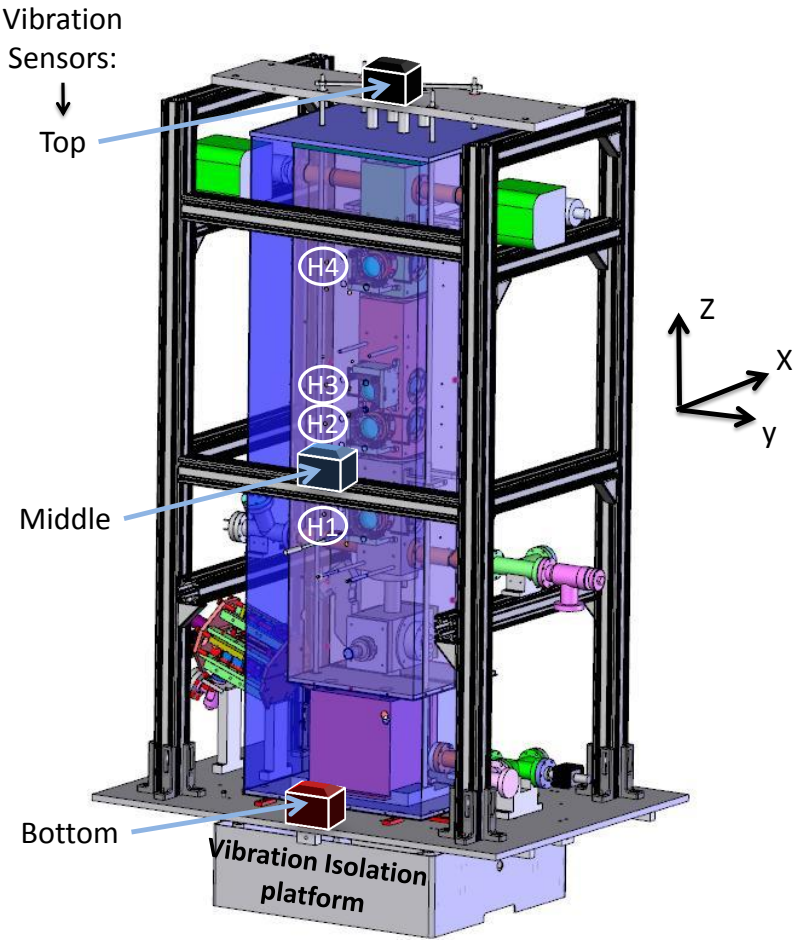

Figure 5.4: Schematic of the vibration sensor positioning on the experimental structure.

In the above equation A_{vel} is the voltage to velocity scaling of the seismometer = 400 V/ms^{-1}. As the seismometer signal is acquired in samples (V_{vel}), the vibration noise is given as a discrete sum in Eqn. (5.4). For the optimum correlation of P to $\delta\Phi_{vib}$, we have to add a time delay, τ_R for the sensor signal acquisition. This is because the seismometer has a response of a low pass filter at 40 Hz. This produces a time delay of the vibration noise experienced by the interferometer and the seismometer. The seismometer acquisition is started at $\tau_R = 5.5$ ms (optimized for best rejection). This method was also mentioned in [68].

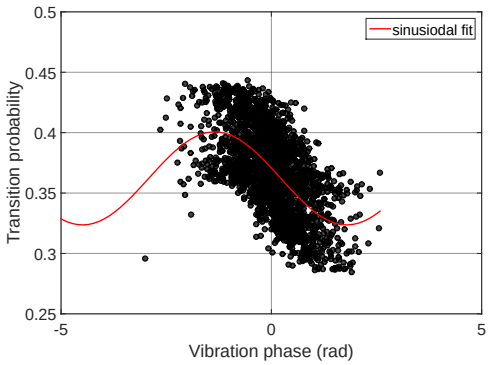

Figure 5.5: Correlation of the transition probability for four-pulse AI of $2T = 480$ ms and the vibration phase calculated from the seismometer signal. The correlation rejection factor is $\mathbf{R_{corr}} = 1.6$.

Fig. 5.5 shows the optimized correlation we obtained using the seismometer. In this case, we had to consider an additional scaling factor, S_{vib} with $\delta\Phi_{vib}$ such that the fitting function is:

$$P = P_0 + A\cos(S_{vib} \cdot \delta\Phi_{vib}^{seis} + \Phi_{fit}). \tag{5.5}$$

The best fit is the red curve in Fig. 5.5. As the seismometer and the Raman retro-reflection mirrors are separated in space, there is a scaling factor between the vibration experienced by the mirrors and the seismometer, even though they are a part of the same experimental structure. This scaling factor is S_{vib}.

From Fig. 5.5, we removed the correlation from the interferometric data and we performed the residue method to obtain the residual phase noise. We obtained a rejection factor from vibration noise to the phase noise signal:

$$R_{corr} = \frac{\sigma_{vib}}{\sigma_\Omega} = \frac{0.8}{0.5} = 1.6.$$

We treat this residual phase noise as the rotation phase sensitivity, σ_Ω. The above rejection factor is not very promising, therefore we went for another solution. We will now replace the Guralp seismometer with the Titan accelerometer as the vibration sensor.

5.2.2 Acquisition and Accelerometer Noise Characterisation

Before we try to correlate the interferometric signal (for $2T$= 480 ms) with the accelerometer signal, we first characterize the intrinsic noise of the sensor and the acquisition system. The acquisition of the accelerometer signal is performed by a NI 4474

24 bit PCI bus card [69], which has four entry ports. It has a range of +/- 10 V and and acquisition noise of 1.2 $\mu V/\sqrt{Hz}$. In between the accelerometers and the NI 4474 acquisition card we placed two low noise amplifiers (LNAs) from Stanford Research Systems (SR560) [70]. The complete sketch of the signal acquisition and the correla-

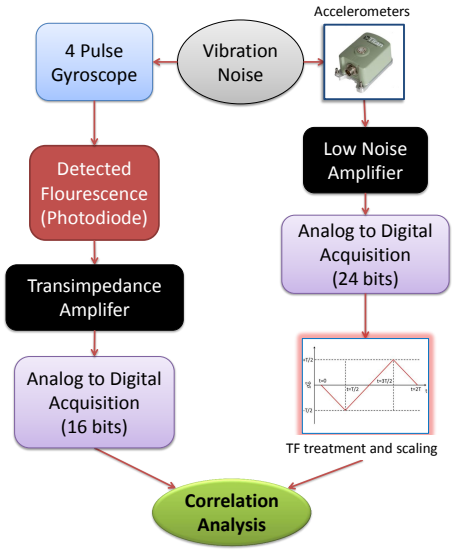

Figure 5.6: Scheme of the acquisition of the detected fluorescence of the atoms interfered, and in parallel the vibration noise acquisition system.

tion process is shown in Fig. 5.6. The LNAs has filtering capabilities and has a voltage noise level of 30 $nV/\sqrt{Hz}$. Using the LNA, we use a low pass filter on the accelerometer signals with pre-amplification to minimize the noise at frequencies higher than 500 Hz (where the gain response of the accelerometer is no longer 1). Fig. 5.7(a) shows the noise characteristics of the different components of the accelerometer acquisition. In blue is the noise level of the NI 4474 card. In black is the noise level of the LNA. The red curve depicts the intrinsic acceleration noise level of the accelerometer provided from the manufacturers. We use a gain of G=10 from the LNA pre-amplifier to scale down its noise w.r.t. the acquisition. We observe the strongest contributor to the noise is the accelerometer itself. Fig.5.7(b) shows that the the total phase noise contribution to the four-pulse interferometer is dominated by the intrinsic accelerometer noise and is 45 mrad for $2T = 480$ ms and 110 mrad for $2T = 800$ ms. So we understand that in post-correlation, this intrinsic sensor noise will be mixed inside the extracted rotation noise sensitivity.

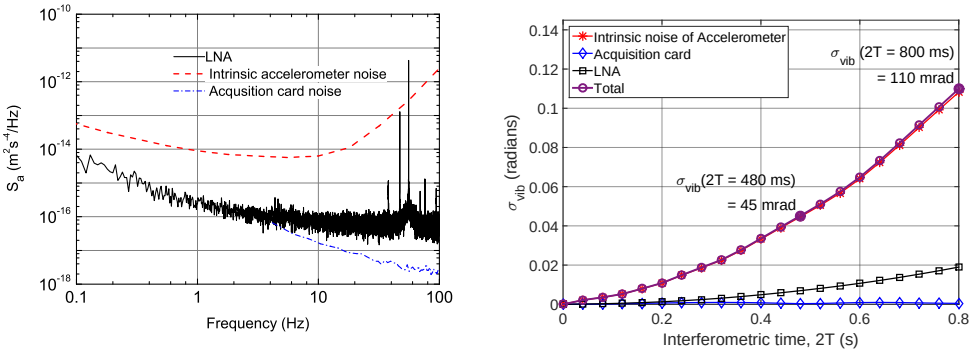

(a) Accleration noise spectrum (b) Vibration noise estimation

Figure 5.7: Fig. 5.7(a) shows the acceleration noise spectrum comparison for the vibration noise with the LNA and amplifier gain, G=10 .Fig. 5.7(b) shows the four-pulse interferometer phase noise estimation for the accelerometer; the LNA with G=10; and the acquisition card. The total contribution is limited by the intrinsic noise of the Titan accelerometer.

5.2.3 Correlation with Accelerometer

To correlate the signal acquired by the accelerometer, we will now use the acceleration transfer function in the discrete form:

$$\begin{aligned}\delta\Phi_{Vib} =& \frac{k_{eff}}{A_{acc}} \cdot \frac{1}{2Tf_S^2} \cdot \\ & \left[\left(\sum_{n=f_S\cdot\tau_R}^{f_S\cdot(\tau_R+T/2)} V_{acc}(n)\cdot n \right) - \left(\sum_{n=f_S\cdot(\tau_R+T/2)}^{f_S\cdot(\tau_R+3T/2)} V_{acc}(n)\cdot(n - Tf_S) \right) \right. \\ & \left. + \left(\sum_{n=f_S\cdot(\tau_R+3T/2)}^{f_S\cdot(\tau_R+2T)} V_{acc}(n)\cdot(n - 2Tf_S) \right) \right].\end{aligned} \tag{5.6}$$

Here, V_{acc} and A_{acc} is the signal and the voltage to acceleration scaling factor, respectively, for the accelerometer. τ_R here is much smaller than for the seismometer as the response of this accelerometer is flat up to 400 Hz. We found τ_R is negligible when using the accelerometer and smaller than the sampling frequency of the signal acquisition itself. Hence, use of τ_R was not necessary.

Using solely the vibration signal acquired from the Middle accelerometer, we see the correlation with the four-pulse; $2T$ = 480 ms interferometer in Fig. 5.8. The correlation is similar to the the seismometer correlation observed in Fig. 5.5. Here, we get R_{corr}= 1.4. Since R_{corr} did not improve, we will study if using more than one sensor at separate positions help us to improve our correlation.

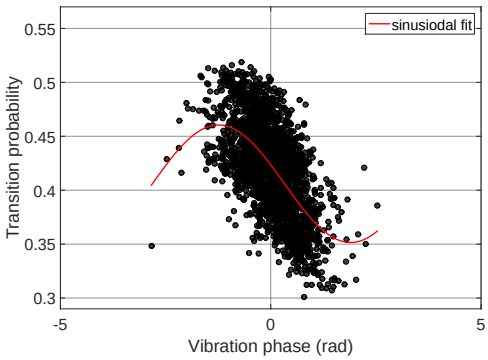

Figure 5.8: Correlation of the interferometric signal with the Middle accelerometer vibration signal. The correlation rejection factor, $\mathbf{R_{corr}} = 1.4$.

5.3 Use of Multiple Vibration Sensors

We mount the two accelerometers in the top and bottom positions shown in Fig. 5.4.

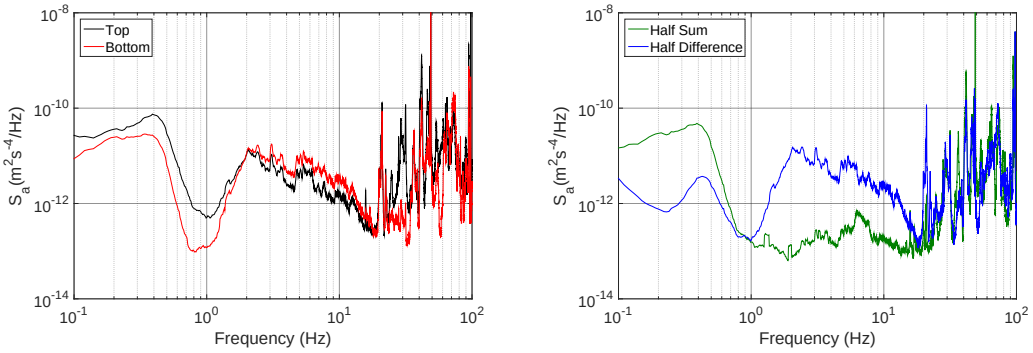

(a) Top and Bottom

(b) Half-sum and Half-difference

Figure 5.9: Fig. 5.9(a) shows the acceleration noise spectrum , $S_a(f)$ for the top (in black) and bottom (in red) accelerometers. Fig. 5.9(b) shows the acceleration noise spectra of the these two accelerometer acquisitions in half-sum (in green) and half-difference (in blue). We observe in the half-sum the spectrum has higher PSD in the range 0.1 - 1 Hz, representing acceleration noise. In the half-difference case, the spectrum has higher PSD in the range 1 - 10 Hz, representing rotation noise.

In Fig. 5.9(a) we show the acceleration noise spectrum of the top and bottom accelerometers. We perform the half-sum and half-difference of the top and bottom accelerometer signals and show the corresponding spectrum in Fig. 5.9(b). We see a clear difference in the two spectra. The half-sum has a greater contribution from the 0.1 - 1 Hz frequency range and the noise in the range 1 - 10 Hz almost disappears.

This is the opposite case for the half-difference case. This means acceleration noise dominates in the 0.1 - 1 Hz range and rotation noise dominates in the 1 - 10 Hz range.

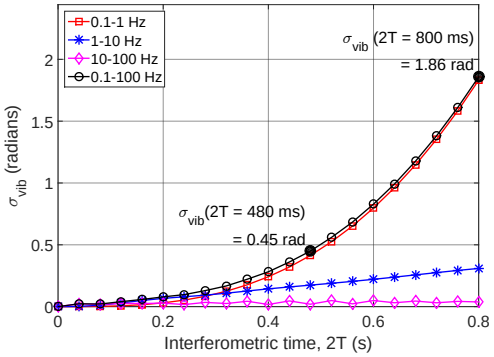

Figure 5.10: Estimation of the vibration noise from the half-sum spectrum treated by the acceleration transfer function. It shows that the frequency range of 0.1 - 1 Hz in dominating as acceleration noise. We estimate 0.45 rad of acceleration noise for $2T = 480$ ms and 1.86 rad for $2T = 800$ ms.

To estimate the noise in acceleration that is affecting the four-pulse interferometer, we first treated the half-sum spectrum by the acceleration transfer function $|H_a(\omega)|^2$ established in Chapter 2. This provides an idea of the phase noise for different interferometric interrogation times shown in Fig. 5.10. We clearly understand that the major contribution of the vibration phase noise comes from the low frequency range of 0.1 - 1 Hz. The estimation gives 500 mrad of acceleration phase noise at $2T = 480$ ms and increases quadratically upto 1.86 rad at $2T = 800$ ms. This vibration component is mainly produced by the isolation platform which is adjusted for a natural frequency of 0.4 Hz, along the horizontal axis.

5.3.1 Correlation Results using Two Accelerometers

After the internal noise characterization of the acceleration signal acquisition system, we used a weighted average of the temporal signals of the top and bottom accelerometers treated by the four-pulse transfer function with $2T = 480$ ms.

For the correlation in Fig. 5.11, we combine the transfer functioned treated accelerometer signal not directly in half-sum, but in weighted average to find the optimum correlation. We used a correlation function:

$$P = P_0 + A\cos\left(S_{vib}\frac{\delta\Phi^B_{vib} + r_{TB}\delta\Phi^T_{vib}}{1 + r_{TB}} + \Phi_0\right), \tag{5.7}$$

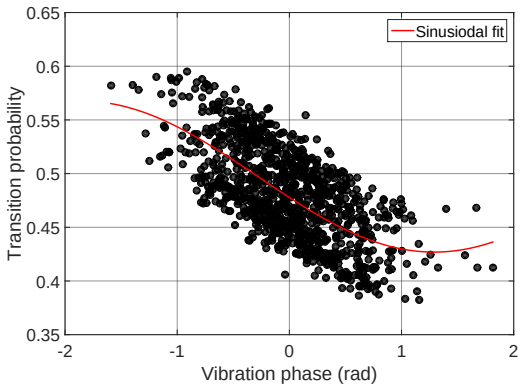

Figure 5.11: Optimized correlation of the interferometric signal with the **weighted average** of the Top and Bottom accelerometers' vibration signal. Here we obtained a rejection factor, $\mathbf{R_{corr}} = 1.5$.

where, r_{TB} is the weight of top vs. bottom accelerometer signal and S_{vib} is the scaling of the combination $\Phi_{vib}^{T,B}$. Using this equation we get the correlation as in Fig. 5.11 and we still observe a similar rejection correlation factor of $R_{corr} = 1.5$, after performing the residue method to extract the residual rotation sensitivity.

Table 5.1: Comparison of vibration rejection using different sensors for four-pulse; $2T$ = 480 ms gyroscope, where all methods yield similar vibration noise rejection.

Sensor Used	Phase noise σ_Φ (rad/$\sqrt{\text{Hz}}$)		Rejection Factor R_{corr}
	Vibration	Residue	
Single Seismometer (Middle)	0.79	0.49	1.6
Single Accelerometer (Middle)	0.69	0.49	1.4
Two Accelerometers (Top and Bottom)	0.43	0.28	1.5

Table 5.1 shows the phase noise comparison of the three above correlation schemes we has used for the four-pulse $2T$= 480 ms gyroscope. Since all the correlation rejection factors are in the same order and we did not find any improvement, we deduced that the vibration noise comprises not only of acceleration noise, but also rotation noise which we are not able to correlate. We get an indication of this fact from the half-difference frequency spectrum of the top and bottom accelerometer signals. But, since rotation

is proportional to rate of change of position, and the accelerometers are sensitive to rate of change of velocity, we would have to integrate the accelerometer signals to correlate for rotation noise. The following section explains this integration process and the correlation algorithm used on the integrated signal.

5.4 Transformation of Accelerometer to a Velocity Sensor

We converted the signal of the accelerometers into velocity by analog integration of their signals. After the integration, the velocity signal was correlated with the interferometric signal via a specific method. This method does not require extraction of acceleration and rotation noise separately for performing correlation. The above integration system and the correlation method is explained in the following sections.

5.4.1 Characterisation of the Integration Method

The integration of the accelerometer signals is performed analogically by the LNAs mentioned previously. The integration is performed by a low pass filter (LPF). This is because the transfer function of a LPF is given by

$$H_{LPF}(\omega) = \frac{Y(\omega)}{X(\omega)} = \frac{1}{1 + i\frac{\omega}{\omega_c}}, \tag{5.8}$$

where $X(\omega)$ is the Fourier transform of $x(t)$, the input of the filter; $Y(\omega)$ is the Fourier transform of $y(t)$, the output; and ω_c is the cut-off frequency. For all frequencies $\omega \gg \omega_c$, $H_{LPF}(\omega) \approx \omega_c/(i\omega)$. This means

$$\begin{aligned} Y(\omega) &\propto \frac{X(\omega)}{\omega}, \\ y(t) &\propto \int x(t)dt. \end{aligned} \tag{5.9}$$

The above equations shows that in the temporal regime, the LPF integrates $x(t)$ and gives $y(t)$ for frequencies $\gg \omega_c$. Following the same principal we will integrate the accelerometer signal using the LPF of the LNA. The minimum provided by the LNA is 0.03 Hz with a gain roll-off = -20 dB/decade. Since, the signal below this frequency cannot be integrated by the LPF, we simultaneously put a high pass-filter with the same cut-off frequency in the integration system of the accelerometer signal. Due to the DC dependence for the Titan accelerometer on the temperature, this HPF plays a role of not only removing un-integrated signals, but also the temperature sensitive DC

bias. The dual combination gives a triangular gain profile of the filter peaked at 0.03 Hz. Hence, we call this a *Triangular* filter. To test the fidelity of the filter, we send a swept sine wave signal to the input of the LNA with 0.1 Vpp magnitude. We used an Agilent 35670A FFT Analyser to produces this swept sine wave and compare this signal with the amplified triangular filter output. The FFT Analyser has two channels and has the ability to provide the transfer function between the two channels.

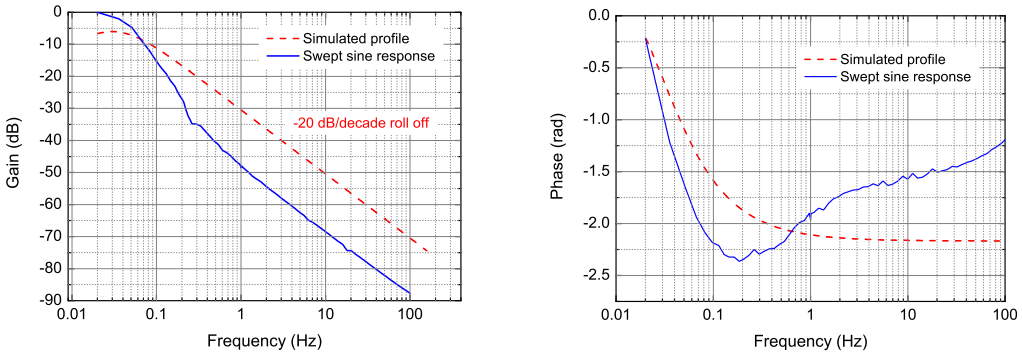

(a) Gain response

(b) Phase response

Figure 5.12: Comparison of the swept sine triangular filter response (blue) in gain and phase with the simulated profile (red). The transfer function for the swept sine was measured for the Triangular filter centred at 0.03 Hz of LNA. We see a deviation of the gain and phase response w.r.t. the simulated profile at a value of 0.2 Hz.

The minimum value of the start frequency for the swept sine was 0.02 Hz, hence we are not able to observe the triangular shape in the gain curve of the transfer function in Fig. 5.12(a). In the gain and the phase response in Fig. 5.12, we see a deviation of both gain and phase response w.r.t. the simulated profiles after 0.2 Hz. We deduce that this does produces signal distortion in the frequency range above 0.2 Hz. We will understand the effect of this phase deviation of the signal when we will perform true correlation of the four-pulse AI signal with the velocity signal we acquire. We next verified that after the integration of accelerometer signal, the velocity signal is not perturbed especially in the low frequency range where our four-pulse interferometer with $2T = 480$ ms is most sensitive. For this characterisation, we first acquired the direct acceleration signal from the bottom accelerometer and later the triangular filtered signal from the same accelerometer. We then differentiated numerically the velocity signal and compared the PSD of the two signals, obtained from two different methods , but from the same sensor.

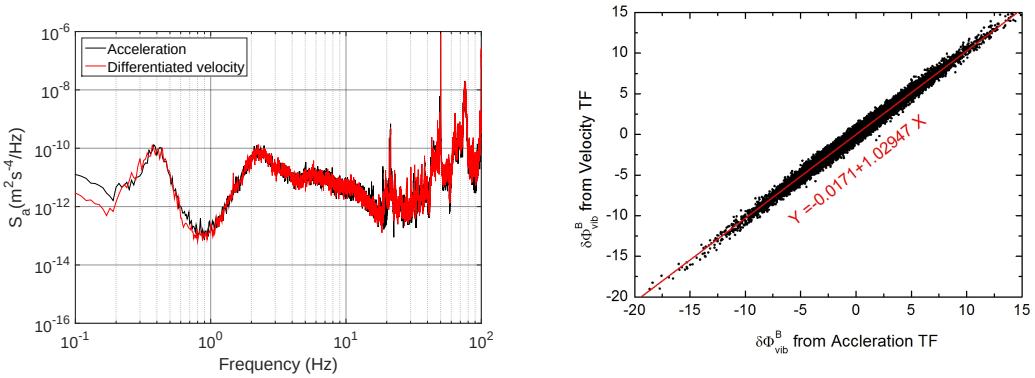

(a) Acceleration and differentiated velocity (b) Vibration phase: velocity vs. acceleration

Figure 5.13: 5.13(a) shows the comparison of the acceleration and differentiated velocity corresponding to the bottom accelerometer in terms of acceleration noise spectrum. 5.13(b) shows the relative vibration phase obtained from acceleration and velocity (triangular filtered acceleration) from the bottom accelerometer. The linearity gives a slope of 1.029 and a residual RMS phase of 0.4 rad vs. peak-peak phase of 4.5 rad. (9% noise).

In Fig. 5.13(a), we observe the spectra almost perfectly super-impose at a frequency range $>$ 1 Hz. We next treated the acceleration signal by the acceleration transfer function and the velocity signal by the velocity transfer function for $2T$ = 480ms; and compared the phases obtained for four-pulse AI. Fig. 5.13(b) shows the linear dependence of the vibration phase, $\delta\Phi_{vib}$ obtained for the bottom accelerometer from the acceleration and the the corresponding signals. The relationship is linear with a slope of 1.029 and the residue in phase has an RMS value of 0.4 rad w.r.t. peak-peak value of 4.5 rad. This means acceleration and the velocity signals agree within 9% in the full scale of the vibration noise. This represents the noise added by the integration system.

5.4.2 Projection of Integrated Signal on the Raman Retro-reflection Mirrors

After characterizing the integration system to obtain velocity signal from acceleration, we now set up the algorithm for correlation. Since, the signal is now converted to velocity we no longer need to distinguish between acceleration and rotation noise to correlate the two types of noise separately. We project the velocity signal as the velocity experienced by the Raman windows. Considering we use the four-pulse interferometer using H1 and H2, we then have to re-define the four-pulse phase equation in Chapter

2 as individual phase component added by the Raman beams: one used for the $\pi/2$ pulses and the other for the π pulses.

$$\begin{aligned}\Phi_{14} &= \Phi_1 - \Phi_4 \\ \Phi_{23} &= \Phi_2 - \Phi_3 \\ \Phi_{4p} &= \Phi_{14} - 2\Phi_{23}.\end{aligned} \tag{5.10}$$

In the above equation, Φ_{14} is the phase contribution of the 1st and the 4th Raman pulses at H1 and Φ_{23} is the phase contribution of the 2nd and the 3rd Raman pulses at H2. To find these phase contributions at H1 and H2 in terms of the velocity signals obtained from the Top and Bottom accelerometers, scale the velocity signals obtained from the accelerometers according to the distance between each of the accelerometers and the mirrors. In the equations shown in Fig. 5.14, $\delta\Phi_{14}^B$, $\delta\Phi_{14}^T$ represent the projec-

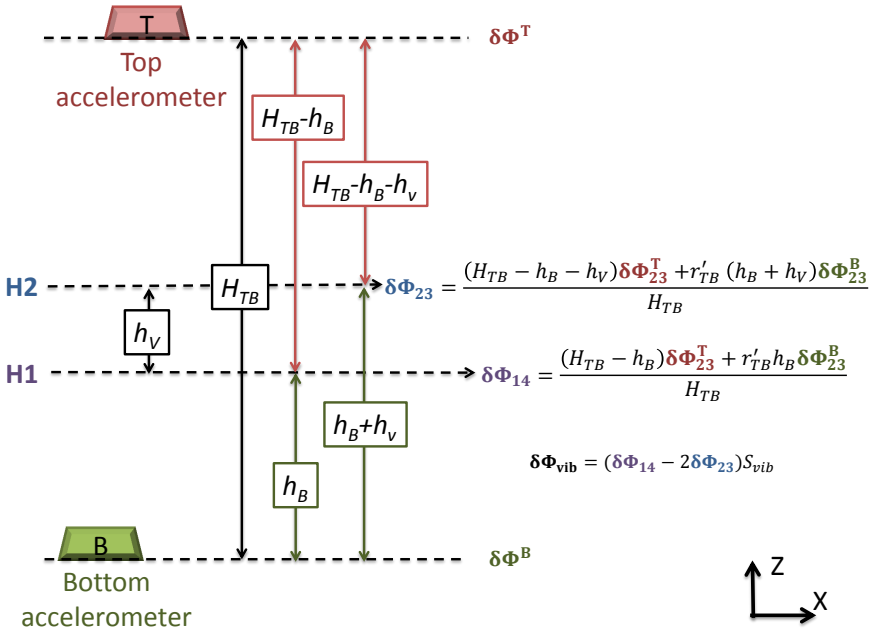

Figure 5.14: Schematic showing the distance of the top and bottom accelerometer from the Raman retro-reflection mirrors positions of H1 and H2. The equations on the left of the figure incorporates the projection of the top and bottom accelerometers on the the Raman mirrors at H1 and H2. The vibration phase signal as $\delta\Phi_{vib}$ is formulated from this projection.

tion of the top and bottom velocity signals on the first Raman mirror acquired from a time of $t = 0$ (1st pulse) to $2T$ (4th pulse); and $\delta\Phi_{23}^B$, $\delta\Phi_{23}^T$ represent the projection of the top and bottom velocity signals on the second Raman mirror acquired for a the

time $t = T/2$ (2nd pulse) to $3T/2$ (3rd pulse). H_{TB} is the distance between the accelerometers = 1.84 m. h_V is the distance between the Raman mirrors in the vertical. For $2T$ = 480 ms (using H1 and H2), h_V = 21 cm. h_B is the distance between the Bottom accel and the bottom Raman beam at H1 = 61 cm. r'_{TB} is the un-normalized weight of $\delta\Phi^B$ w.r.t. $\delta\Phi^T$. Substituting these values the equations of Fig. 5.14, we can finally have $\delta\Phi_{vib}$ and use it for correlation with the interferometric signal.

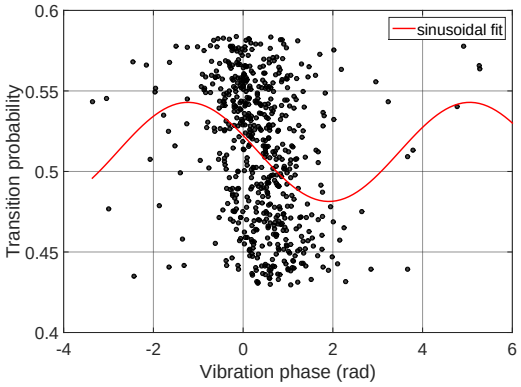

Figure 5.15: Plot of transition probability, P vs. vibration phase $\delta\Phi_{vib}$ projecting velocity signals of top and bottom accelerometers on the Raman mirrors. We observe no correlation.

Fig. 5.15 shows the correlation that we obtained using the above projection algorithm for correlation. It is evident that the correlation has become worse via this method where the correlation rejection factor we obtain is less than 1. Since this method deteriorated the correlation, we are now going to perform an in depth analysis of the uncorrelated non-inertial component of the interferometric signal and clarify if we are limited by the vibration sensors or other non-inertial noise sources.

5.5 Improvement of Probability Noise: Asymmetric Interferometer

As the above correlation methods in Section 5.2 and 5.3 did not give a good rejection factor, we are now going study the source the remaining noise and check if it is limited by the non-inertial probability noise that we characterized in the previous chapter. To estimate the probability noise, σ_P from the interferometric signal we do not need to perform correlation and this method of extraction is called the *Batman-fit* method. The method has been used to determine the SNR of interferometric signals in [71]. To

incorporate the Batman-fit method, we first acquire the histogram of interferometric dataset. This histogram is normalized to acquire the probability density distribution, $F_{\Delta P}$. This density function looks like the cowl of Batman, i.e., there are sharp density peaks on the extremities of the transition probability, when the contrast is high and the probability noise is low. The fitting function for this Batman's cowl structure is a convolution of the density functions corresponding to the probability noise and the phase noise affecting the transition probability.

$$F_P = \eta \int_{P_0-A}^{P_0+A} F_{\Delta r}(r') * \left[\frac{1}{\sigma_P\sqrt{2\pi}} e^{-r^2/2\sigma_P^2}\right](r-r')dr'. \tag{5.11}$$

In the above equation, $F_{\Delta r}$ is the density function of the arccos of $(P - P_0)/A$ in Eqn. (5.1). The second function represents a Gaussian distribution with a noise spread of σ_P. To have a dataset to fit with F_P we scan the phase of the interferometer by scanning the laser phase difference, Φ_L of the Raman lasers. This helps us to have enough density of the data points in the extremities of the interferometric fringe and hence the histogram should give us a Batman's cowl structure.

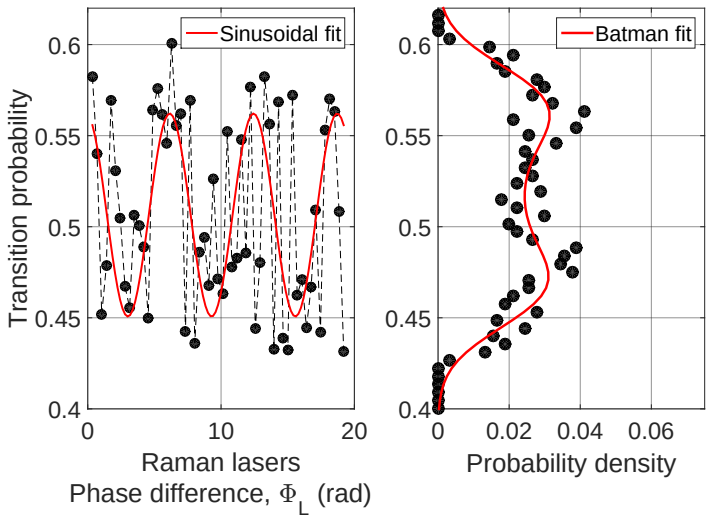

Figure 5.16: Plot of transition probability, P vs. the Raman laser phase difference, Φ_L. On the right we see the Batman fit of the probability density of the acquired data with the observed transition probability range.

In Fig. 5.16, we perform the Batman-fit of the observed transition probability for the scan of Φ_L. We use the σ_P obtained from the least square fit of the Batman function, F_P and compare it with the experimental probability noise that we characterised

in the previous chapter:

$$\sigma_P\,(experimental) \;=\; 3.3\times10^{-3};\quad \sigma_P\,(Batman fit) \;=\; 2\times10^{-2}.$$

The Batman fit shows that there is an uncharacterised noise in σ_P other than the technical sources. The answer to this uncharacterised noise is the presence of parasitic interferometers with the four-pulse fountain gyroscope where use symmetric interferometry [72].

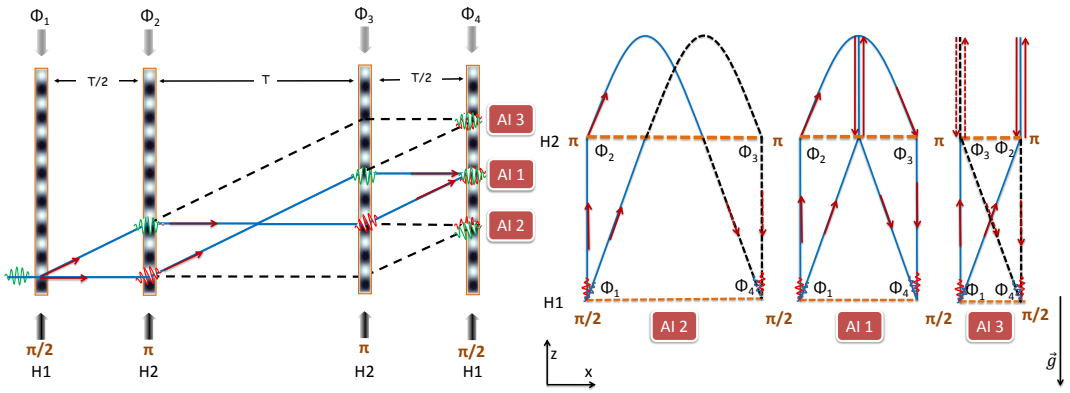

(a) Symmetric in time (b) Symmetric in space

Figure 5.17: Symmetric four-pulse fountain geometry, in time (Fig. 5.17(a)) and space (Fig. 5.17(b)) and its 3 alternative geometries. The blue paths are the paths for the four-pulse fountain gyroscope, AI 1. AI 2 and 3 are parasitic interferometers with zero rotation sensitivity.

In Fig. 5.17, we show the schematic of three separate interferometric geometries in AI 1, AI 2 and AI 3. We have shown before that the efficiency of the Raman beams were less than 100%. This means that the $\pi/2$ and π pulses are not able to interact with all the atoms in the atomic cloud and hence a certain proportion of the atoms travel without any change in their horizontal trajectories. Due to this phenomenon, there are formations of parasitic interferometers. For the four-pulse case, we have two extra interferometers: AI 2 and AI 3 in addition to our four-pulse fountain gyroscope. These two interferometers are also DC-insensitive, but then do not possess any rotation sensitivity because for the other two AIs, the area enclosed is zero in space. But, all three interferometers have AC sensitivity to inertial noise along the horizontal axis. When the atoms are detected after interference, the signal observed is actually the mix of the three different phases accumulated by AI 1, AI 2 and AI 3. So it is evident that the detected transition probability, which is a mixture of the three separate AIs. To

separate out the interferometer corresponding to the gyroscope (AI 1) and avoid the interference of the parasitic AIs, we make the four-pulse system **asymmetric**. This asymmetric technique in a four-pulse interferometer was also used in [72].

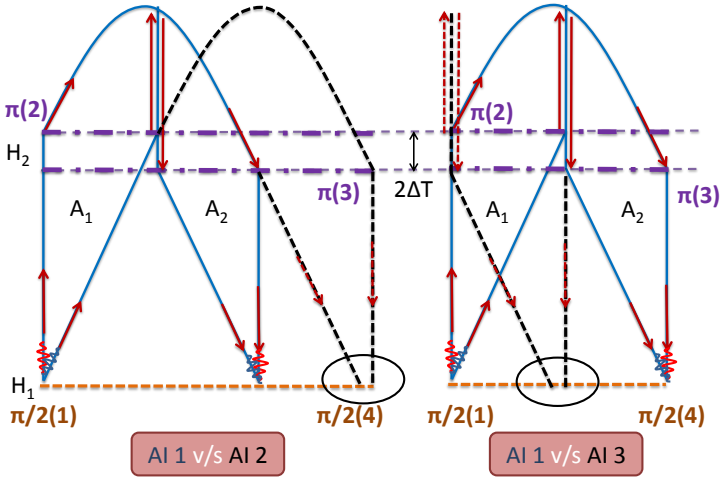

Figure 5.18: Schematic of the asymmetric four-pulse fountain geometry. Here we compare the interferometric paths of Rotation sensitive AI (AI 1) vs. the parasitic AIs (AI 2 and 3). Asymmetry by 2ΔT suppresses interference of AI 2 and 3.

By asymmetry we mean to change the separation of the $\pi/2-\pi-\pi-\pi/2$ pulses of T/2-T-T/2 by adding an equivalent shift in time, ΔT in the 2nd and 3rd π pulses, in the same direction. This will produce the asymmetry in the pulse separations: (T/2$\pm\Delta T$)-T-(T/2$\mp\Delta T$). In Fig. 5.18, we show the scheme for the asymmetric interferometer where we advanced the two π pulses w.r.t. the 1st and 4th $\pi/2$ pulses. By this technique, we can interfere the four-pulse rotation sensitive interferometer but not the other two parasitic interferometers. The asymmetry in time, ΔT gives a distance between the parasitic interferometric paths at the fourth pulse:

$$\delta X_{\Delta T} = 2\frac{\hbar k_{eff}}{m}\Delta T. \tag{5.12}$$

$\delta X_{\Delta T}$ should be greater than $2\sqrt{2\ln 2}\cdot L_{coh}$, where L_{coh} is the coherence length of the atoms, after the velocity selection by the Raman pulses. The factor $2\sqrt{2\ln 2}$ converts L_{coh} into the full width of the atomic wavepacket. Then we have

$$\Delta T_{min} = \sqrt{2\ln 2}\cdot\frac{mL_{coh}}{\hbar k_{eff}} = \frac{\sqrt{2\ln 2}}{2k_{eff}\sigma_v}. \tag{5.13}$$

The L_{coh} here is determined by the velocity selection of the atomic cloud performed by Raman pulses of the interferometer. Since the Rabi frequency is constant for all the pulses our interferometer, the π-pulse is the most velocity selective pulse. As the duration of theπ-pulse, $\tau_{\pi/2} = 20\ \mu$s, this means the velocity selection corresponds to:

$$\sigma_v^{\pi} = \frac{1}{2\sqrt{2\ln 2}\cdot\tau_{\pi}} \cdot \frac{v_{rec}}{\omega_{2ph}} = 2.55\, v_{rec}. \tag{5.14}$$

Using the standard values of ω_{2ph} and v_{rec}, we get $\sigma_v^{\pi} = 2.55\ v_{rec}$. This value is approximately equal to the velocity spread of the atomic cloud we measured before ($\sigma_v = 2.5\ v_{rec}$). So we can use the value of $L_{coh} = 27.5\ \mu$m (for the corresponding σ_v of the atom cloud) in Eqn. (5.13). Hence $\Delta T_{min} = 4.7\ \mu$s for our cold atoms. This represents the displacement $\delta X_{\Delta T}^{min} = 2\sqrt{2\ln 2}\cdot L_{coh} = 65$ nm.

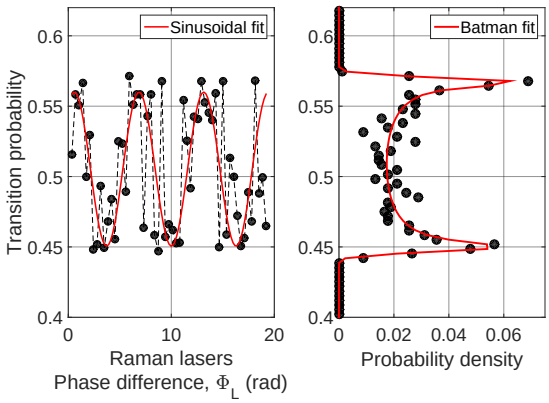

Figure 5.19: Plot of P vs. Φ_L for the asymmetric interferometer, with ΔT = -50 μs. On the right we see the Batman fit of the probability density of the acquired data with the observed transition probability range and the σ_P is much improved than in Fig. 5.16.

We performing the same scan of laser phase as in Fig. 5.16 and we see when we introduce asymmetry, e.g., with $\Delta T = 50\ \mu$s, the density peaks at the extremities of the histogram is much sharper. With the asymmetric interferometer we get

$$\sigma_P\,(Batman fit) \;=\; 2.7 \times 10^{-3}.$$

This clearly shows the benefit of introducing asymmetry. The disadvantage of the asymmetric interferometry is that it induces a sensitivity to DC acceleration of the

four-pulse interferometer:

$$\Phi_{acc}^{\Delta T} = 4k_{eff}g\sin\theta_{H1}T\Delta T. \tag{5.15}$$

For the four-pulse interferometer with $2T = 480$ ms; $\Delta T = 10$ μs, we have $\Phi_{acc}^{\Delta T} = 92$ rad. Since, asymmetric interferometry is sensitive to DC acceleration, the tilt-locking system, explained in the previous chapter, was crucial to stabilize the base of the experimental set-up. This stabilizes the DC projection of g on the horizontal axis due to tilting of the experiment, and hence stabilizes the phase bias, $\Phi_{acc}^{\Delta T}$. The RMS of the tilt angle , post-tilt-locking is 2.2 μrad. Using this value as the stability noise in θ_{H1}, we get a noise in $\Phi_{acc}^{\Delta T} = 3$ mrad for $2T = 480$ ms; $\Delta T = 10$ μs. This is a negligible value w.r.t. the residual phase noise we have extracted so far. Since we have resolved the problem of having excess probability noise, we will not re-perform our previous correlation methods to verify for improvements.

5.6 Optimum Rejection of Acceleration Noise

5.6.1 Results with Accelerometer as a Velocity Sensor

We now acquire the transition probability of the four-pulse; $2T = 480$ ms gyroscope in the asymmetric mode with $\Delta T = 60$ μs and a total cycle time, $T_c = 960$ ms. We put $\Delta T = 60$ μs to have a safe margin to avoid interference of the parasitic interferometers. The average contrast obtained was 12%. We then study the correlation of this transition probability with the $\delta\Phi_{vib}$ obtained from the velocity signals (from integration of the accelerometer signals). We first try the correlation algorithm of the projection of the velocity-meters on to the Raman beams positions.

In Fig. 5.20(a) we observe the correlation of the transition probability, P vs. $\delta\Phi_{vib}$ from velocity, with optimized weight, $r'_{TB} = 1.1$ and scaling of phase, $S_{vib} = 0.43$. We observe a big improvement in the correlation obtained w.r.t. the symmetric interferometer case using the same correlation method (Fig. 5.15). Here, the correlation rejection factor , $R_{corr} = 1.9$ which shows clear improvement w.r.t. the symmetric interferometer case. We note that the vibration noise, $\delta\Phi_{vib}$ is higher than the previous interferometric datasets. This happens due to the seasonal change in oceanic waves which produce surface waves at a frequency ≈0.16 Hz [73]. Noise at this frequency is not rejected by the isolation platform as its natural frequency (0.5 Hz) is close to this surface wave frequency. This un-isolated noise from the ground increased $\delta\Phi_{vib}$

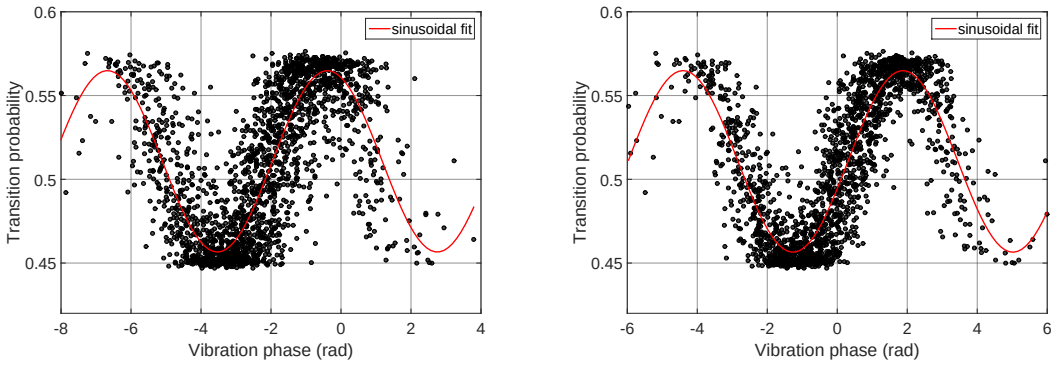

(a) Projection of sensors

(b) Weighted average

Figure 5.20: Fig 5.20(a) shows the correlation of using velocity signals using the **projection method**. The correlation rejection factor $\mathbf{R_{corr}} = 1.9$. Fig 5.20(b) shows the correlation of using velocity signals using **weighted average method**. The correlation rejection factor $\mathbf{R_{corr}} = 4.7$.

in the present datasets. Next we verify if the weighted average method gives a better correlation w.r.t. the projection method when we use the velocity signals. We performed the weighted average correlation on the same set of data as in Fig. 5.20(a). Fig. 5.20(b) clearly shows how the weighted average of the velocity signals improves the correlation. The correlation rejection factor here, $R_{corr} = 4.7$ and hence we observe a further improvement in the rejection.

Table 5.2: Improvement of the Rotation phase sensitivity for $2T = 480$ ms gyroscope with integrated accelerometer signals.

Velocity Combination	Phase noise σ_Φ (rad/$\sqrt{\text{Hz}}$)		Rejection Factor R_{corr}
	Vibration	packet-fit	
Projection of sensors	2.7	1.4	1.9
Weighted average	2.8	0.6	4.7

Table 5.2 summarizes the improvement we achieved in the rotation phase sensitivity, σ_Ω using the velocity signals. The extraction of σ_Ω in Table 5.2 was performed by the packet-fit method mentioned in Section 5.1. We obtain the optimum $\sigma_\Omega = 0.6$ rad/$\sqrt{\text{Hz}}$ for the weighted average correlation. Using this method we have further 2.6 times better phase sensitivity than using the projection method.

If we compare the recently improved σ_Ω value to the rotation phase sensitivity obtained using the weighted average correlation of the true accelerometer signals (σ_Ω

= 0.28 rad/$\sqrt{\text{Hz}}$ in Table 5.1), we see it is actually 2 times worse. Hence, we can deduce the integration method by the triangular filter is not optimum. This can be explained by the deviation in the transfer function in phase when we perform acceleration to velocity integration by the triangular filter (Fig. 5.12). The deviation at 0.2 Hz produces distortion in the velocity signal w.r.t. the true acceleration signal. So it is better to use a true velocity sensor in place of integrating the accelerometer signals via this specific analog filter. Unfortunately, mounting two Guralp seismometers would have pushed the weight of the experimental payload beyond the nominal value that the isolation platform can handle. Hence, we revert back to using the true acceleration signals from the top and bottom accelerometers for correlation and correlated only for acceleration noise, but this time using asymmetric interferometry.

5.6.2 Results using True Accelerometer Signal

In this section we will study the improvement in the correlation using asymmetry in the interferometer and correlating with the weighted average of the accelerometers. To avoid the effect of the drift in the DC bias due to temperature dependence, we still preserve the HPF with a cut-off frequency at 0.03 Hz for the acceleration signals. The pre-amplification is now provided by a Linear Technology low noise integrated circuit amplifier (LT1028) [74] with an added LPF with cut-off frequency at 500 Hz. The LT1028 is recommended for analog amplification of accelerometer signals and has a voltage noise of 35 nVp-p in the range of 0.1-10 Hz which is in the same range of the LNA noise (35 nV/$\sqrt{\text{Hz}}$). Using the band pass filtered acceleration signals of the top and bottom accelerometers, we treated them first with the acceleration transfer function for the four-pulse interferometer with $2T = 480$ ms.

We then performed their weighted average and studied the correlation of the four-pulse; $2T = 480$ ms interferometer with asymmetry $\Delta T = 60$ μs. We directly see the improvement of the correlation in Fig. 5.21. We get an optimized correlation of P vs. $\delta\Phi_{vib}$ with phase scaling, $S_{vib} = 0.97$ and normalized weight, $r_{TB} = 0.95$. We then perform packet-fitting method to extract the rotation phase sensitivity.

The comparisons of the Allan deviations of the phase noise in Fig. 5.22 gives a rejection factor:

$$R_{corr} = \frac{\sigma_{vib}}{\sigma_{\Omega}} = \frac{1.27}{0.16} = 7.9.$$

The correlation factor we see above is the best we have achieved for the $2T = 480$ ms; four-pulse gyroscope. It also corresponds to the best short-term rotation sensitivity, $\boldsymbol{\sigma_{\Omega} = 1.6\times10^{-7}\ \text{rad/s}/\sqrt{\text{Hz}}}$.

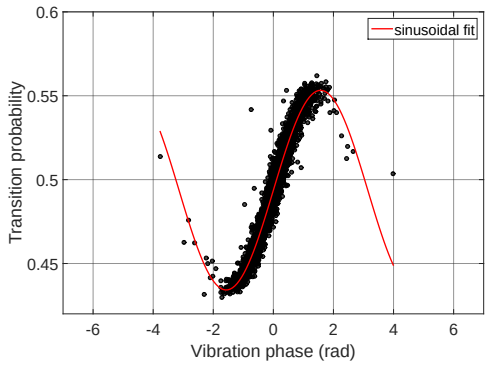

Figure 5.21: Correlation of Transition probability vs. vibration phase $\delta\Phi_{vib}$ using acceleration signals with a band pass filter at frequencies 0.03 Hz and 500 Hz. The signals are in weighted average and we use packet-fit of the phase offset to find the residual noise.

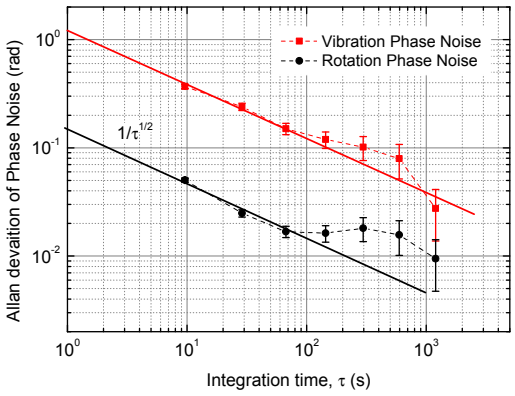

Figure 5.22: Allan deviation of the rotation phase sensitivity obtained from the optimum rejection of the vibration noise using band pass filtered acceleration signals. The signals obtained from the Top and Bottom accelerometers were optimized for best weighted average. The solid red and black line are guide to the eyes for $1/\sqrt{\tau}$ dependence of the sensitivity to integration time.

5.6.3 Results after Removal of Light Shift

Next, we perform the same interferometry and correlation method for $+k_{eff}$ and $-k_{eff}$ interferometers, to remove the long-term fluctuation due to light shift (Fig. 5.22 corresponds to $+k_{eff}$ interferometer). In Fig. 5.23 we observe the correlations of the $+k_{eff}$ and $-k_{eff}$ four-pulse interferometers. Here, we see for each set the $+\pi/2$ and $-\pi/2$ data sets. We can extract the residual rotation sensitivity by a hybrid method where

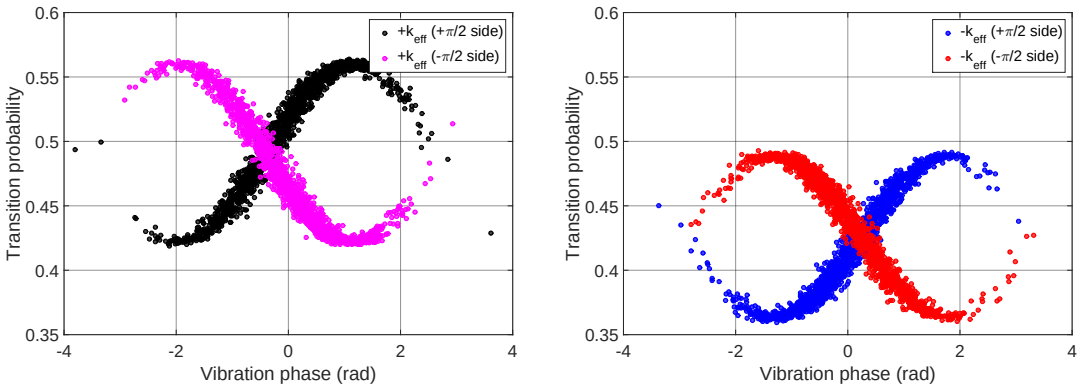

(a) Correlation of $+k_{eff}$ AI

(b) Correlation of $-k_{eff}$ AI

Figure 5.23: Correlation of Transition probability vs. vibration phase $\delta\Phi_{vib}$ with acceleration noise corresponding to $+k_{eff}$ and $-k_{eff}$ four-pulse interferometers for $2T$ = 480 ms. On each plot the two side of the fringe represent the P_+ and the $\Phi_L = pi$ shifted, P_- data points.

we mix $\pm\pi/2$ and the packet-fitting methods. For each k_{eff} datasets, we can add a phase of π to $\delta\Phi_{vib}$ corresponding to the $+\pi/2$ fringe side w.r.t. the $-\pi/2$ fringe side. E.g., in Fig. 5.23(a) this will produce one single fringe comprising of the black and pink points correlated to the re-adjusted $\delta\Phi_{vib}$ axis. Performing packet fitting of this re-adjusted correlation, we can then perform half-Δ and half-Σ of the $\pm k_{eff}$ fitted phase offset values. If there is light shift noise, half-Δ will provide us with the pure rotation sensitivity without the drift due to light shift.

The final Allan deviation plots for the half-Δ of $\pm k_{eff}$ (Fig. 5.24) provides the optimum short-term and long term rate of rotation sensitivity.

Table 5.3: Short and long term rotation sensitivity for **2T = 480 ms** after **correlation with Accelerometer** (from half-Δ of $\pm k_{eff}$ interferometers).

Sensitivity	Short-term ($/\sqrt{\text{Hz}}$)	Long-term @ 2000 s
Phase (rad)	0.15	3×10^{-3}
Rate of rotation (rad/s)	1.5×10^{-7}	3×10^{-9}

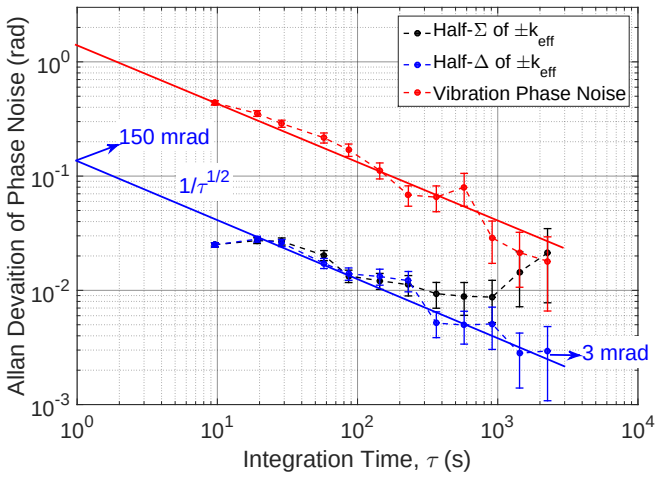

Figure 5.24: Allan deviation of the rotation phase sensitivity, σ_Ω for the half-Σ and half-Δ of $\pm k_{eff}$ for $2T = 480$ ms. The results are obtained after removal of vibration phase correlation. The solid red and blue line are guide to the eyes for $1/\sqrt{\tau}$ dependence of the sensitivity to integration time.

5.7 Results for Large Area (11 cm^2) Cold Atom Gyroscope

After establishing the best achieved rotation sensitivity for the the four-pulse gyroscope with total interrogation time, $2T = 480$ ms and an area of 2.4 cm^2, we moved on next to four-pulse interferometer with the highest Sagnac area possible for our experimental set-up: 11 cm^2, with $2T = 800$ ms. In this case, the Raman collimator at the position H2 had to be shifted up to H4.

5.7.1 Re-alignment of Raman Beams

All the protocols of alignment of the Raman beams were followed sequentially. To meet the interference condition, we first re-measured the Raman beam angle at H1 w.r.t. the vertical direction, $\theta_{H1} = 3.81^o$. Following the vertical beam alignment protocol set in Chapter 3, we reached a parallelism in the vertical direction of the Raman beams, $\delta\theta_z = 9.2$ μrad. In this case, we are still beyond the interference limit for $2T = 800$ ms four-pulse interferometry ($\delta\theta_z^{max} = 4.9$ μrad, $\delta\theta_y^{max} = 3$ mrad). We next moved on to Ramsey-Bordé interferometry. Since, to reach H4, the launching velocity of the cloud has to be high ($v_0 = 5$ m/s), the maximum time separation achieved between the first two $\pi/2$ pulse for the Ramsey-Bordé interferometer is dT = 5 ms.

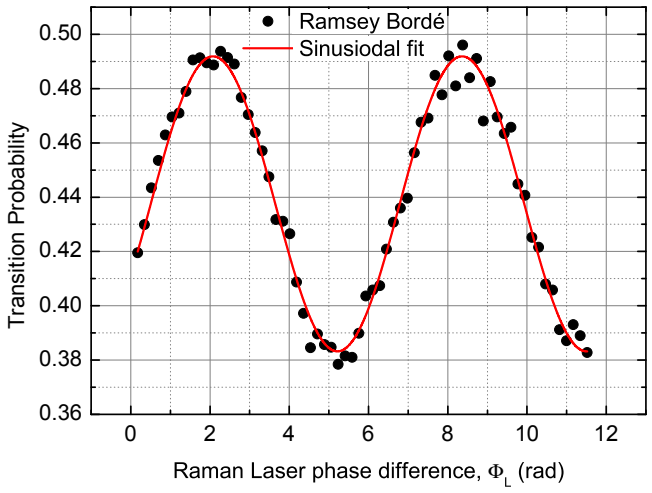

Figure 5.25: Interference fringe for the Ramsey-Bordé interferometer between H1 and H4 positions of the Raman beam with dT = 5 ms. We reached the parallelism limit of H1 and H4 Raman windows to $\delta\theta_y^{RB} = 28$ mrad.

Without any further alignment, we were able to achieve Ramsey-Bordé interferometry between H1 and H4 directly after the previous alignment protocol with a contrast of 11% as shown in Fig. 5.25. This means the alignment of the retro-reflection mirror is very close to optimum for the vertical and also the horizontal direction. For the horizontal alignment, with dT = 5 ms, we reached the parallelism accuracy of $\delta\theta_y^{RB}$ = 28 mrad. We finally went on to perform four-pulse interferometry in the fountain geometry with $2T$ = 800 ms. With a further alignment in the horizontal and vertical alignment via iteration, we were able to acquire a signal for the large area four-pulse interferometer.

5.7.2 Optimization of Asymmetry in Four-pulse Interferometer

We performed asymmetric interferometry for the four-pulse interferometer with various ΔT values. This is to re-optimize ΔT for $2T$ = 800 ms. We scanned the Raman laser phase difference and we found σ_P using the Batman-fit method for a different ΔT. We acquired the dependence of the probability noise, σ_P vs. ΔT. Fig. 5.26 shows that we need $\Delta T = 300$ μs to reach the non-inertial noise limit, σ_P^{det+L}. $\Delta T = 300$ μs corresponds to $\delta X_{\Delta T} = 4.3$ μm. This value is 150 times larger than the coherence length of the atomic cloud, $\delta X_{\Delta T}^{min} = 2\sqrt{2\ln 2}L_{coh} = 65$ nm. We were not able to

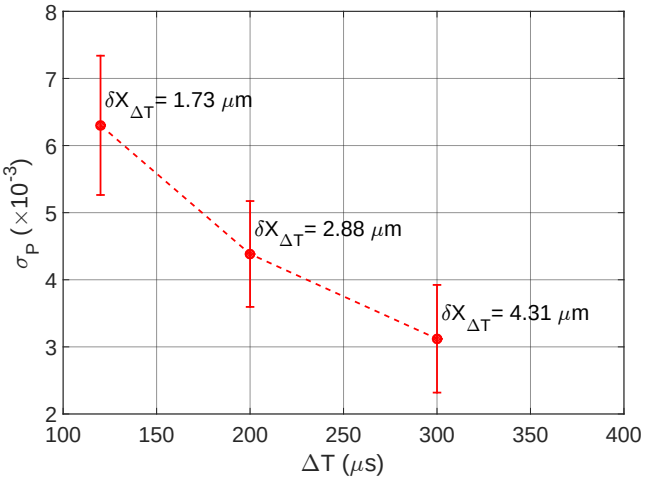

Figure 5.26: The dependence of the probability noise vs. asymmetry, ΔT in the 4 - pulse interferometer. $\delta X_{\Delta T}$ represents the separation of the parasitic paths to avoid their interferometry corresponding to ΔT for $2T = 800$ ms.

characterize the requirement for such a big ΔT to avoid interference of the parasitic interferometers for the $2T = 800$ ms four-pulse interferometer. The disadvantage of using this big ΔT, as mentioned before, is that it produces a DC phase bias due to acceleration component $g \sin\theta_{H1}$ (Eqn. (5.15)) $= 4.6\times10^3$ rad $\approx 734\times(2\pi)$ rad. Since the bias value is large, we study the effect of variation of g on this phase bias corresponding to $\Delta T = 300$ μs. According to the tide model, g changes by $\sim 2\times10^{-6}$ m/s^2 in around 10 hours during a high/low tide. Using these values in the phase bias $\delta\Phi_{acc}^{DC}$ in Eqn. (5.15) (with $\Delta T = 300$ μs; $2T = 800$ ms), we get a phase shift of $\delta\Phi_{acc}^{DC} = 2$ mrad for this daily variation of g. This is a negligible effect due to the DC acceleration sensitivity in our asymmetric interferometer for $2T = 800$ ms. Hence, we verify our final gyroscope sensitivity for $2T = 800$ ms will not be greatly affected by the variation of g even in the presence of large asymmetry. On the other hand due to the noise in the stabilization of the platform by the tilt-lock (2.2 μrad), we will have a DC acceleration noise of 152 mrad for $\Delta T = 300$ μs; $2T = 800$ ms. This enters as inertial noise in our experimental set-up which is not negligible anymore. A solution to remove this noise would be to perform interferometry with alternating $+\Delta T$ and $-\Delta T$ asymmetry. When we perform half-difference of the $\pm\Delta T$ datasets, the DC acceleration noise would be cancelled out, taking into account that the noise frequency is $< 1/T_c$ (T_c = experimental cycle time).

5.7.3 Extraction of Rotation Sensitivity

We now set $\Delta T = 300$ μs and perform interferometry with $+k_{eff}$ and $-k_{eff}$ momentum transfers. During the interferometry, we record the accelerometer signal with the same band pass filter and gain as for the $2T$ = 480 ms case (Section 5.6). We find the optimum weighted average of the top and bottom accelerometer signals which was now treated with the four-pulse temporal transfer function corresponding to $2T$ = 800 ms. This optimum weighted average is correlated with the interferometric signal, P.

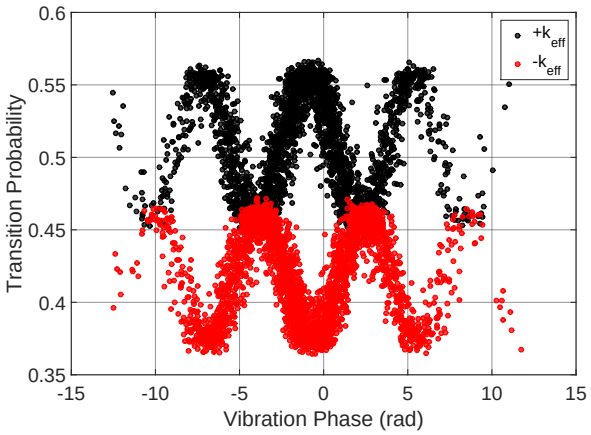

Figure 5.27: Correlation of Transition probability vs. vibration phase $\delta\Phi_{vib}$ with acceleration noise corresponding to $+k_{eff}$ and $-k_{eff}$ four-pulse interferometers for $2T$ = 800 ms. The rejection factor, $\mathbf{R_{corr}}$ = 10.1.

In the correlation observed for $2T$ = 800 ms in Fig. 5.27, we have a contrast, C = 10% for $+k_{eff}$ interferometer and C = 8.8% for $-k_{eff}$ interferometer. The $\delta\Phi_{vib}$ peak-to-peak is much higher than the $2T$ = 480 ms case, as the scaling of rotation to phase S_Ω for $2T$ = 800 ms is 4.6 times higher. We perform the packet fitting method to extract the rotation phase sensitivity. With the above correlation we observe in Fig. 5.27, we obtain a factor of rejection:

$$R_{corr} = \frac{\sigma_{vib}}{\sigma_\Omega} = \frac{7.5}{0.74} = 10.1.$$

We observe that R_{corr} is 1.3 times higher than $2T$ = 480 ms case, but on the contrary, the rotation phase sensitivity is 4.6 times worse. We establish that the remaining noise is coming from the uncorrelated rotation noise present on the experimental structure, which cannot be presently correlated by the accelerometers.

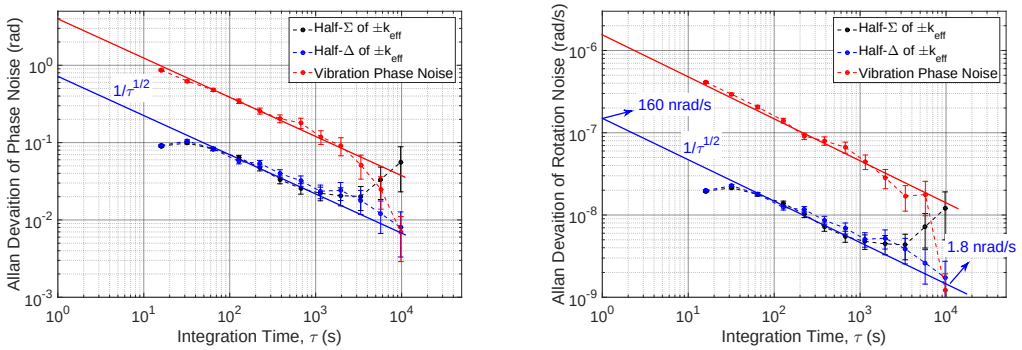

(a) Phase sensitivity (b) Rotation sensitivity

Figure 5.28: Allan deviation of the rotation sensitivity, σ_Ω in terms of pahse and rate of rotation for the half-Σ and half-Δ of $\pm k_{eff}$ for $2T = 800$ ms. Both results are obtained after removal of vibration phase correlation. The solid red and blue line are guide to the eyes for $1/\sqrt{\tau}$ dependence of the sensitivity to integration time.

The Allan deviations in Fig. 5.28 shows the rotation sensitivity we obtain for the four-pulse gyroscope with the large area of 11 cm^2. Here also we see the drift due to light shift in the Allan deviation in the half-Σ of $\pm k_{eff}$, which is eliminated in the half-Δ.

Table 5.4: Short and long term rotation sensitivity for **2T = 800 ms** after **correlation with Accelerometer** (from half-Δ of $\pm k_{eff}$ interferometers).

Sensitivity	Short-term ($/\sqrt{\text{Hz}}$)	Long-term @ 10000 s
Phase (rad)	0.74	8×10^{-3}
Rate of rotation (rad/s)	1.6×10^{-7}	1.8×10^{-9}

Table 5.4 shows the final sensitivity in short term and long term for rotation. The long term sensitivity of **1.8×10^{-9} rad/s in 10000 s** is the best achieved stability so far for such a large area atom gyroscope.

5.8 Comparison to State-of-the-art Performances of Atom Gyroscopes

Table 5.5 shows the evolution of atom gyroscopes in the recent years and compares their performances w.r.t. rotation sensitivity in short and long term time scales. We have presently achieved the state-of-the-art rotation sensitivity for atom gyroscopes where we reach down to < 2 nrad/s of stability for upto 3 hours of integration.

Table 5.5: Performance of atom gyroscopes through the years in terms of short-term and long-term sensivity to rotation.

Research Group	Interferometric Area	Short-term sensitivity (rad/s/$\sqrt{\text{Hz}}$)	Long-term stability (rad/s)	Integration Time
Yale, USA (Atomic beam) (2000) [9]	22 mm^2	6×10^{-10}		
Stanford, USA (Atomic beam)(2006) [75]	22 mm^2	4×10^{-8}	4×10^{-9}	30 mins
SYRTE, France (Cold atoms)(2009) [15]	4 mm^2	2.4×10^{-7}	1×10^{-8}	30 mins
Hannover, Germany (Cold atoms)(2015) [11]	41 mm^2	1.2×10^{-7}	2.6×10^{-8}	100 s
SYRTE, France (Cold atoms)(2015)	11 cm^2	1.6×10^{-7}	1.8×10^{-9}	~3 hours

5.9 Conclusion

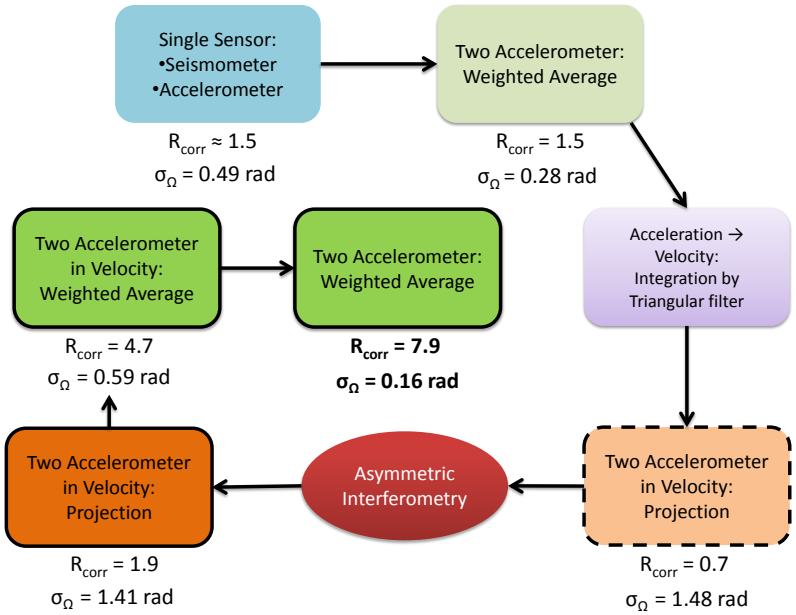

Figure 5.29: Chronological summary of the correlation methods used for $2T = 480$ ms four-pulse gyroscope. The boxes in green represent the weighted average method. The boxes in orange represent the projection method. The dark green and orange boxes represents use of asymmetry in the four-pulse interferometer. The boxes with dashed borders represent degradation of the correlation and the boxes with bold borders represent improvement of the correlation.

In this chapter we have shown the different correlation methods which are gradually implemented to obtain the pathway for acquiring the optimum rejection of the vibration noise from the interferometric phase. This pathway was established via two-years of rigorous characterization and analysis. Fig. 5.29 shows the chronological summary of the different correlation methods that we have used to finally achieve an optimized correlation rejection factor of $R_{corr} = 7.9$ for the $2T = 480$ ms four-pulse gyroscope. The rejection factor increased to 10 for $2T = 800$ ms, but the extracted rotation sensitivity was similar to the $2T = 480$ ms case. This is possibly because we were not rejecting the rotation noise for both cases. Increasing $2T$ from 480 ms to 800 ms increased the scale factor to rotation sensitivity ($\propto T^3$), but it also increased the scale of the rotation noise. Hence, the final sensitivity did not improve. This is the present short-term limit of the rotation sensitivity. Further rejection of this rotation noise will require replacement of the accelerometers with low noise velocity sensors which are more stable in the low frequency than the present accelerometers. Nonetheless, we have demonstrated state-of-the-art performance of the large area 11 cm^2 gyroscope with a short term rotation sensitivity of $\mathbf{1.6\times10^{-7}rad/s/\sqrt{Hz}}$ and a long term stability of $\mathbf{1.8\times10^{-9}}$ **rad/s in 10000 s**. We can even acquire data for longer periods of times and expect to integrate the stability down to $\sim10^{-10}$ rad/s. The presented results correspond to 8 hours of data acquisition and further acquisition was limited by the stability of the lock of the cooling laser with the rempumper.

Chapter 6

Continuous System for Inertial Interferometry

This chapter shows the demonstration of a new method of operation of an atom interferometer without dead time using a single cold atomic source. The method helps to overcome the dead time limitation in atom interferometers of high sensitivity. This method is inspired from atom juggling methods originally introduced in the context of cold atom collisions in atomic fountain clocks [76] and only realized so far for concurrent measurements [10, 77, 78]. The characterization and the results for this demonstration has been published in [14]. In the end, a proof of principle concept has been presented for continuous inertial AI using the four-pulse gyroscope of 11 cm^2 area.

6.1 Concept of Dead Time and Continuous Operation

Most cold atom interferometers such as clocks, accelerometers or gyroscopes are sequentially operated with a cycle time of T_c typically consisting of 3 main steps: atom trapping, cooling, and preparation of duration t_{prep}; AI sequence of duration , T; and

atomic state detection of duration t_{det}. The time required for the preparation and detection of the cold atoms, t_{prep} and t_{det}, leads to loss of data and the reduction of the acquisition rate. This is the dead time for the experimental system.

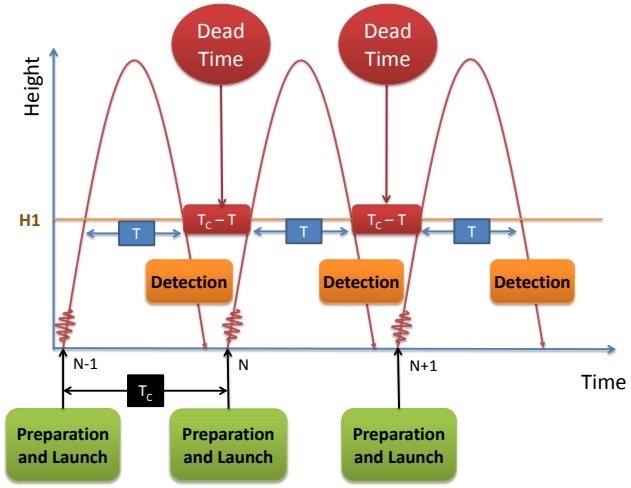

(a) Sequential operation with dead time

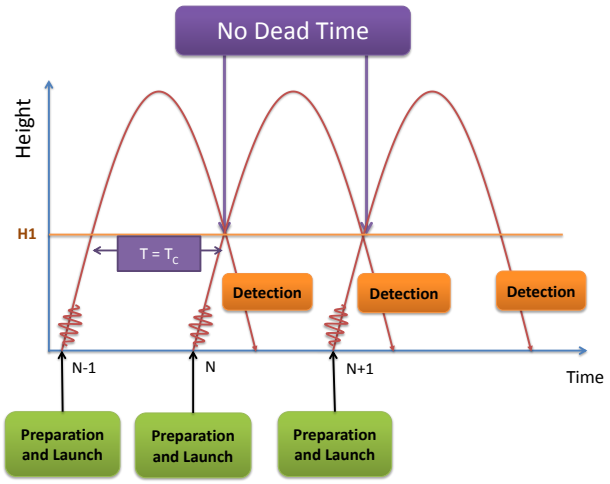

(b) Continuous mode of operation

Figure 6.1: Experimental operation (a) with dead time and (b) in continuous mode.

Due to presence of dead time there is loss of information in sampling the inertial signal by the interferometer and hence is a drawback for inertial sensors. This situation is improved by operating the experiment in a *continuous* mode: the interferometer is functioning and the cold atoms (for the next cycle) are being prepared at the same time. This kind of continuous functioning for inertial sensors using atom interferometry has been presented in [13, 79]. In Fig. 6.1 the normal-mode interferometer [Fig. 6.1(a)]

is operated sequentially following the 3 steps mentioned above with an interrogation time T and a cycle time T_c ($\geq T$). Fig. 6.1(b) presents the principle of the continuous mode of operation where the Raman interrogation pulse is shared by clouds $N-1$ (falling) and N (rising). As a proof principle, we perform a Ramsey interrogation using two $\pi/2$ co-propagating Raman pulses symmetric with respect to the apogee of the atom trajectory. This is a form of juggling with the clouds without re-capture as seen in [76].

6.2 Preparation of the Atoms for Continuous Operation

For an AI, we prepare the atoms in the non magnetic $m_F = 0$ state to be used in the interferometer. For the Ramsey interferometer we do not use the π^0 microwave transition for the state preparation. This is because in the continuous operation, there would be an overlap between the time of interferometry and the moment of application of the microwave pulse. This adds a perturbation from the selection pulse in the superposition of the states between $|F = 3\rangle$ and $|F = 4\rangle$ during interferometry.

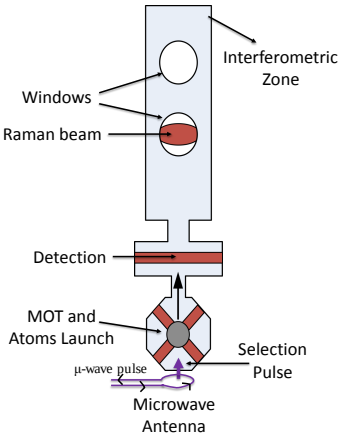

Figure 6.2: The experimental scheme showing the position of the microwave antenna at the bottom of the experiment. The selection pulse from the antenna propagates through the MOT chamber and into the interferometric zone.

The position of the microwave antenna is shown in Fig. 6.2. Since it is placed along the same central axis of the interferometric zone, the selection pulse from the antenna perturbs the atomic states of the interfering atoms. The perturbation in the continuous

mode, with $T_c = T = 480$ ms, appears as an amplitude modulation (AM) on the two-pulse Ramsey fringe pattern. This was shown in [16]. To avoid this perturbation, we use a σ transition instead of π^0 for the selection of the atoms. As we mentioned in Chapter 3, when the selection field $B_z = 16$ mG, the σ transition frequency is $f_\sigma = f_{HFS}$ - 5.6 kHz.

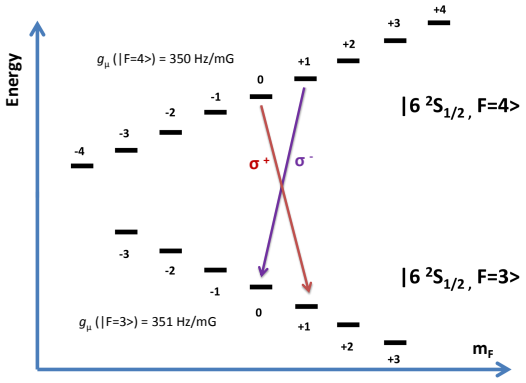

Figure 6.3: The splitting of the m_F states for $|F = 4\rangle$ and $|F = 3\rangle$ hyperfine states of a Cs atom. We are interested in a selection pulse which will produce σ^- transition from $|F = 4, m_F = -1\rangle \rightarrow |F = 3, m_F = 0\rangle$ state and avoid any transfer of $|F = 4, m_F = 0\rangle \rightarrow |F = 3, m_F = -1\rangle$ at the same transition frequency.

When we perform the σ transition, there is transfer of $|F = 4, m_F = -1\rangle$ to $|F = 3, m_F = 0\rangle$ state, but also from $|F = 4, m_F = 0\rangle$ to $|F = 3, m_F = -1\rangle$ state. We observed that by varying the duration of the microwave selection pulse, $\tau_{\mu w}$, we are able to reach an optimum where we can transfer the maximum number of atoms into $|F = 3, m_F = 0\rangle$ state and simultaneously the minimum number of atoms into $|F = 3, m_F = -1\rangle$ state. This happens due to partial reflections of the microwave pulse taking place inside the MOT chamber and for a certain orientation of the antenna the reflections gives an average microwave polarization that produces a maximally efficient σ^- transition from $|F = 4, m_F = -1\rangle \rightarrow |F = 3, m_F = 0\rangle$ state and simultaneously negligible amount of σ^+ transition from $|F = 4, m_F = 0\rangle \rightarrow |F = 3, m_F = -1\rangle$ state. We call this specific selection as a σ^{-1} transition.

To do the characterization of the σ^{-1} transition for $T = 480$ ms case ($v_0 = 3.91$ m/s), we vary $\tau_{\mu w}$ and observe the Raman frequency spectrum for a Raman pulse for π transition ($\Delta m_F = 0$) in co-propagating mode; i.e., the Raman beams are not retro-reflected and the Raman pulse only performs hyperfine state transfer in the atoms without momentum selection. We see two resonant peaks in the Raman spectrum in

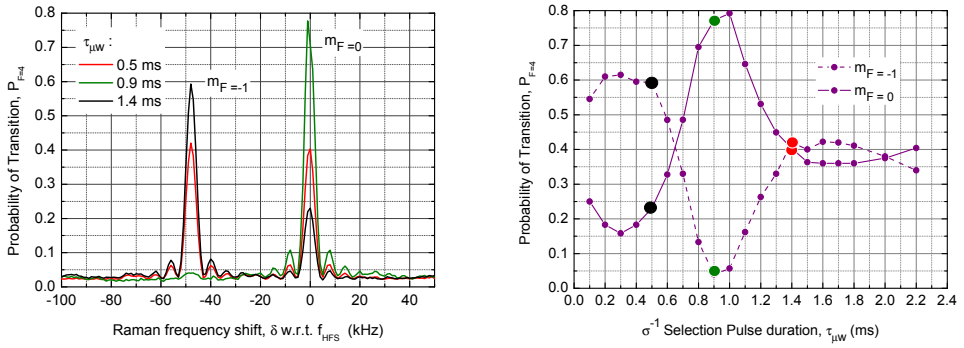

(a) Raman spectrum for σ selection (b) μw pulse duration scan for σ selection

Figure 6.4: Fig. 6.4(a) shows the Raman laser frequency spectrum for different duration of the σ^{-1} pulse. Fig. 6.4(b) shows the variation in peak heights of the transition probabilities corresponding to $m_F = 0$ and $m_F = -1$ vs. the σ^{-1} pulse duration, $\tau_{\mu w}$. At $\tau_{\mu w} = 0.9$ ms we have the optimum transfer to $m_F = 0$ and minimum transfer to m_F = -1.

Fig. 6.4(a) corresponding to $|F = 3, m_F = -1\rangle$ and $|F = 3, m_F = 0\rangle$. The distance between them is 47.5 kHz, which means the quantization field is set at 68 mG. Now, when we vary $\tau_{\mu w}$, we observe that transition probability of $m_F = 0$ and of $m_F = -1$ change comparatively. Fig. 6.4(b) shows the change in the corresponding transition probabilities vs. $\tau_{\mu w}$ and we see that for $\tau_{\mu w} = 0.9$ ms, we have the minimum number of $|F = 3\rangle$ atoms in $m_F = -1$ state but also simultaneously nearly maximum number of atoms in the $m_F = 0$ state.

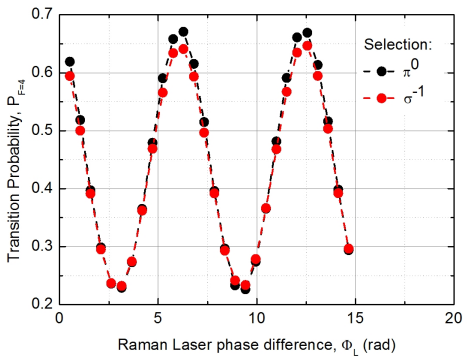

Figure 6.5: The comparison of the fringes obtained for the two-pulse Ramsey interferometer in normal operation (i.e. with dead time), using π^0 and σ^{-1} selections. The contrast loss due to the new selection scheme is negligible.

Performing the two pulse Ramsey interferometer for $T = 480$ ms with $T_c = 900$ ms, Fig. 6.5 shows the acquired interferometric fringe for the π^0 transition (in black) and for the σ^{-1} transition in red. This shows the contrast loss in the fringe due to σ^{-1} selection is negligible.

6.3 Continuous Mode for Ramsey Interferometry

6.3.1 Principle of Noise Rejection in a Zero Dead Time Interferometer

In the two-pulse Ramsey Interferometer that we perform with the Raman $\pi/2$ pulses, for the i-th interferometer, the phase accumulated is:

$$\Delta\Phi_i = \Phi(T + t_i) - \Phi(t_i), \tag{6.1}$$

where t_i is the time of the first Raman pulse. We can then express the variance of this phase as a variance of the laser phase:

$$\sigma^2(\Delta\Phi_i) = 2\sigma_\Phi^2. \tag{6.2}$$

in the above equation we consider the length of the Raman pulse is negligible w.r.t. the duration of the cycle. At the end of N interferometers, considering N is large, we derive the total accumulated phase as:

$$\Delta\Phi = \frac{1}{N}\sum_{i=1}^{N}\Delta\Phi_i. \tag{6.3}$$

Considering the laser phase noise is Gaussian, random and uncorrelated between the pulses, the variance of $\Delta\Phi$ gives

$$\sigma_{\Delta\Phi}^2 = \frac{1}{N^2}\sum_{i=1}^{N}\sigma_i^2 = \frac{2\sigma_\Phi^2}{N}. \tag{6.4}$$

This is the variance for the normal operation condition, and when we replace N by the ratio of the integration time τ vs. the cycle time, T_c we find the well known results of the deviation of $\sigma_{\Delta\Phi}$ to be proportional as $1/\sqrt{\tau}$.

In case of the continuous two-pulse Ramsey interferometer, Eqn. (6.1) evolves to:

$$\Phi(t_{i+1}) = \Phi(T + t_i). \tag{6.5}$$

This is because the first pulse for the $(i+1)$-th interferometer is common to the last pulse of the i-th interferometer as shown in Fig. 6.1(b). Hence, for the continuous operation, there is a cancellation of the laser phase in the total accumulation of the interferometric phase after N cycles. By substituting Eqn. (6.5) into Eqn. (6.1), we get

$$\Delta\Phi = \frac{1}{N}\left[\Phi(NT) - \Phi(0)\right] \tag{6.6}$$

for the total accumulated phase, and

$$\sigma^2_{\Delta\Phi} = \frac{2\sigma^2_{\Phi}}{N^2} \tag{6.7}$$

for its variance. Hence, in the continuous operation of the interferometer, the deviation of the interferometric phase, σ_Φ is proportional to the $1/\tau$, instead of $1/\sqrt{\tau}$. In this configuration not only there is no dead time, but due to the sharing of the laser pulse, we average the phase noise and reach the detection noise limit faster, thanks to the $1/\tau$ scaling. This is called the *joint* operation of the Ramsey interferometer in clock mode. The joint operation helps to reject the local oscillator noise usually encountered when performing independent measurements of the phase with dead times. The rejection applies as long as the local oscillator noise spectrum has a bandwidth lower than the Rabi frequency of the clock pulses, which means we cannot consider the pulse duration to be infinitely short. A detailed theoretical study of this rejection has included in the thesis work of [16].

6.4 Proof of Principle of Joint Mode in Clock Configuration

We set up a two-pulse Ramsey interferometer with $T = 480$ ms in the normal mode with $T_c = 900$ ms. For this we use $\pi/2$ pulses of duration $\tau_p = 22$ μs (Rabi frequency $\Omega_R/2\pi = 11.4$ kHz). Fig. 6.6(a) shows the fringe scan for the Ramsey interferometer for the normal (black) and the joint (red) operations. The phase stability extrapolated at 1 s of the two-pulse Raman interferometer for the normal and joint operations are 13 mrad and 16 mrad, respectively (from Fig. 6.6(b)). This phase stability scales to relative frequency stability w.r.t. f_{HFS} as

$$\left[\frac{\sigma_{\Delta f}}{f_{HFS}}\right] = \frac{\sigma_{\Delta\Phi}}{2\pi f_{HFS} T}. \tag{6.8}$$

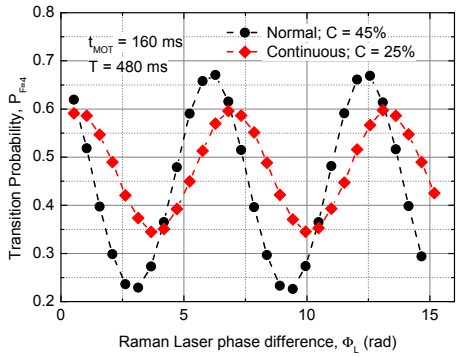

(a) Phase scan for Ramsey Interferometer

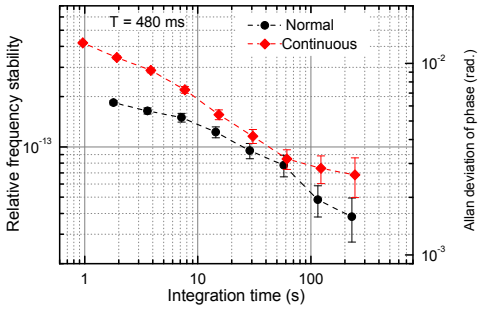

(b) Allan deviation with no added noise.

Figure 6.6: 6.6(a) shows scan of the Raman lasers phase difference, Φ_L for the Ramsey interferometer in case of the normal and the joint mode. Here we decrease the number of atoms used in the interferometer by reducing the MOT loading time. 6.6(b) shows the corresponding Allan deviation of the frequency stability obtained from Ramsey Interferometry via normal and joint operations. The contrast loss and the corresponding phase shift is due to the fluorescence from the MOT during interferometry in the joint mode.

The sensitivity is limited by the Raman laser noise and the detection noise. The small difference in detection noise can be explained by the fringe contrast loss from 45% to 25% when implementing the joint operation. This contrast loss originates from the stray light scattered from the MOT atoms which interacts with the atoms in the interferometric region.

In Fig. 6.7(a) we observe the decrease of the fringe contrast C and the shift in the phase offset, Φ_0 for the joint case with increasing MOT loading times, t_{MOT}. Both C and Φ_0 are linearly dependant on the number of atoms that we trap in the MOT which is seen in Fig. 6.7(b). These effects of the MOT scattered light could be suppressed with the use of a vacuum compatible controllable shutter [80] between the MOT and interrogation region. Next, to demonstrate the local oscillator (LO) phase noise rejection, we introduce a white noise of controlled amplitude and bandwidth in the Raman laser phase lock loop. Fig. 6.8 shows the Raman laser set-up scheme in which we add the externally controlled noise to artificially degrade the reference of the Raman lasers. The noise is added directly to the error signal in the phase lock of the Raman lasers L3 and L4. It is generated using a Direct Digital Synthesizer DS345 from Stanford Research Systems [81] and filtered by an analog -115 dB/octave low-pass filter SR650 [82]. We will now study the improvement in the long-term stability when

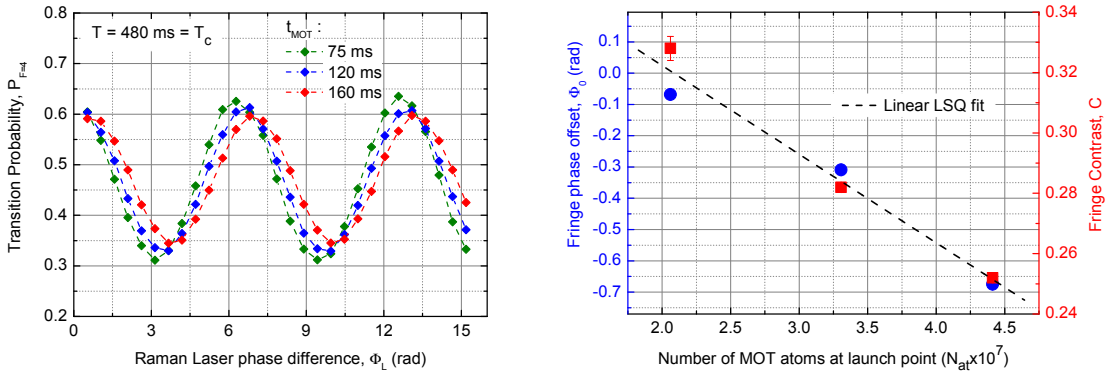

(a) Ramsey joint Interferometer phase scan (b) Contrast and phase offset vs. N_{at}

Figure 6.7: 6.7(a) shows scan of Φ_L the fringes for the Ramsey joint interferometer. Fig. 6.7(b) shows the dependence of the Contrast, C and the phase offset, Φ_0 of the Ramsey fringes corresponding to 6.7(a). The black line is the linear LSQ fit for both C and Φ_0.

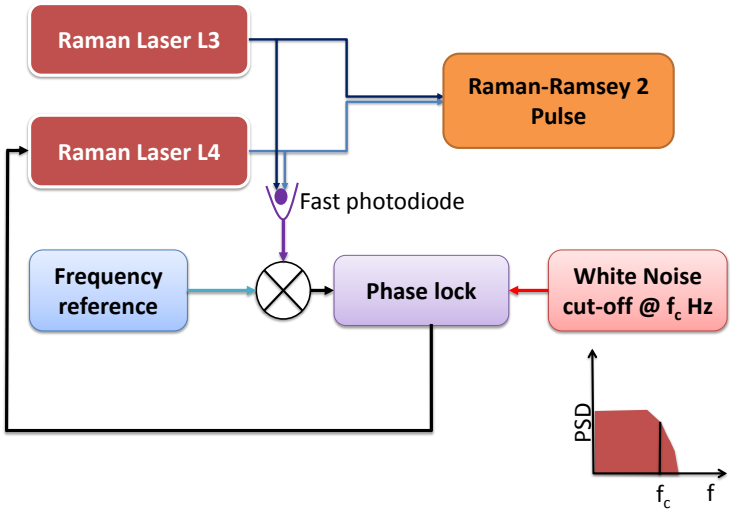

Figure 6.8: Scheme of the addition of the white noise with a frequency cut-off at f_c. The noise is generated from an external source and is added to the error signal of the phase lock of Raman laser pair L3+L4.

we use this degraded frequency reference in the joint mode compared to the normal mode of operation.

Using the degraded reference by adding a white noise that is cut-off at $f_c = 400$ Hz, we measured the Allan deviation of the interferometric phase at first via normal op-

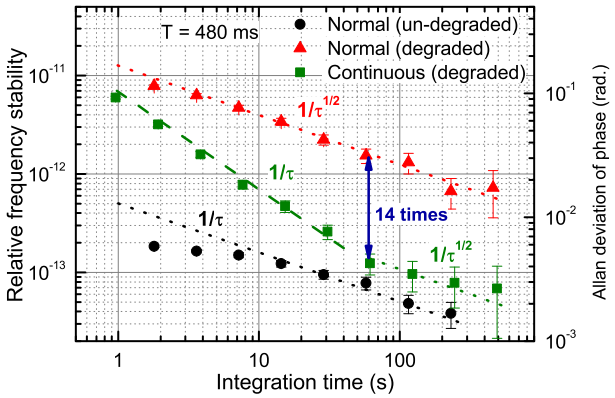

Figure 6.9: Allan deviations of the relative frequency and phase stability in normal and joint operation of the Ramsey interferometer after adding a white noise over a bandwidth of 400 Hz to the LO. The black curve shows the fundamental limit without the added noise in the normal mode. We compare the Allan deviation for the normal mode (red triangle) and the joint operation (green square) and obtain a 14-fold gain in stability at 60 s of integration. The dashed line ($\propto 1/\tau$) and the dotted lines ($\propto 1/\sqrt{\tau}$) are guides for the eyes.

eration. The f_c is well below the Rabi frequency of 11.4 kHz. The Allan deviation is plotted in Fig. 6.9 as the red triangles. This plot is degraded by more than an order of magnitude w.r.t. the unperturbed system in Fig. 6.9 (black circles). The measurement of the phase stability in the joint mode is shown as the green squares. We clearly observe the expected $1/\tau$ scaling of the joint operation. In comparison to normal operation, the Allan deviation for joint operation (green square) gives a 14 times gain in frequency stability of 1×10^{-13} at 60 s of integration. Integrating to this frequency stability level in normal operation would require 1200 s. A change of slope in the Allan deviation is observed at 60 s when we reach the uncorrelated noise floor limited by the detection noise. Fig. 6.9 thus shows that joint operation allows fast averaging of the low frequency phase noise.

6.4.1 Analysis of Local Oscillator Degradation

As mentioned earlier, in the joint method where we use the same interrogation pulse for two consecutive atomic clouds, the stability enhancement takes place as long as the LO noise spectrum has a bandwidth lower than the Rabi frequency, f_R. In this section we will characterize this phenomenon by putting a white noise in the Raman laser phase lock with different cut-off frequencies. To calibrate the noise level, we applied

a sinusoidal modulation of known amplitude (in Volts) and frequency (f_{mod}) to the Raman laser phase lock loop and performed joint interferometry in clock mode. The difference of phase of the Raman lasers is then:

$$\Phi_L(t) = \Phi_0 \cos(2\pi f_{mod} t), \tag{6.9}$$

where, f_{mod} is the modulation frequency and Φ_0 is the phase amplitude of the added noise. Substituting this phase in Eqn. (6.3) for $N = 1$, we find the total contribution of this modulation in the two-pulse clock after one experimental cycle is

$$\begin{aligned} \Delta\Phi &= \Phi_L(T+t) - \Phi_L(t), \\ &= 2\Phi_0 \sin\left(2\pi f_{mod}\left(t + \frac{T}{2}\right)\right) \sin\left(\frac{2\pi f_{mod} T}{2}\right). \end{aligned} \tag{6.10}$$

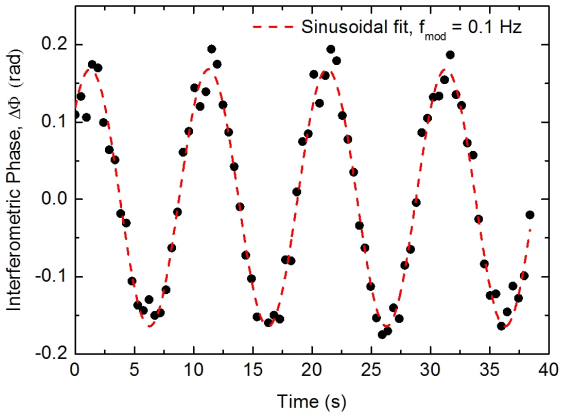

Figure 6.10: The phase modulation of the Ramsey interferometer (T= 480 ms) by the added sinusoidal noise of 5 V (peak-to-peak) in the Raman laser phase lock. Here the peak-to-peak phase modulation is $\Delta\Phi_{pp} = 0.4$ rad.

Fig. 6.10 shows the phase modulation of the $T = 480$ ms; Ramsey interferometer in the joint mode due to the added noise in the Raman laser phase lock. The modulation frequency is 0.1 Hz and the peak-to-peak phase due to the modulation is $\Delta\Phi_{pp} =$ 0.4 rad. This was obtained by the added sinusoidal modulation of 5 V (peak-to-peak). When substituting $\Delta\Phi_{pp}$ in Eqn. 6.10 as the spread of $\Delta\Phi$, one finds

$$\Delta\Phi_{pp} = 2\Phi_0 \sin\left(\frac{2\pi f_{mod} T}{2}\right). \tag{6.11}$$

Table 6.1: Added white noise level, S_0 corresponding to the different cut-off frequencies, f_c.

Cut-off frequency f_c (kHz)	S_0 (rad^2/Hz)
0.40	$1.5\pm0.3\times10^{-4}$
3.85	$6.8\pm1.4\times10^{-6}$
61.00	$6.7\pm1.3\times10^{-7}$

Fig. 6.11(a) shows the calibration of the added phase noise in the laser lock, Φ_0 as a

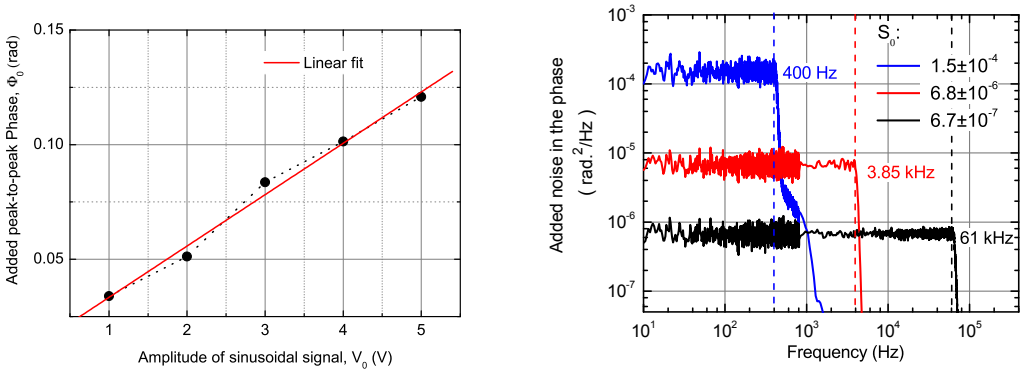

(a) Added noise calibration

(b) Added noise spectrum

Figure 6.11: (a) shows the calibration of the added peak-to-peak phase, Φ_0 w.r.t. the added peak-to-peak voltage into the Raman laser phase lock. (b) shows the spectra of the added noise, S_0 in rad^2/Hz with three different cut-off frequencies. S_0 is higher at lower f_c to to preserve the total noise power added for the three different values of f_c.

function of the added voltage noise, V_0. Fig. 6.11(b) shows the added noise spectrum in terms of phase for three different bandwidths: 400 Hz, 3.85 kHz, and 61 kHz. The spectrum here corresponds to RMS noise, S_0 and hence an extra factor $2\sqrt{2}$ was divided from Φ_0 to convert it from peak-to-peak to RMS value.

The spectral densities of added noise, S_0 in rad^2/Hz are given in the Fig. 6.11(b). S_0 is decreased for increasing f_c to keep the total added noise power constant for the three different f_c. To quantitatively analyse our data, we use the AI sensitivity function formalism, which provides the response of the atom interferometer to a perturbation at a given frequency [83, 84]. The Allan variance of the phase reads as:

$$\sigma^2(\tau) = \frac{1}{2m^2}\int_0^{+\infty}\frac{d\omega}{2\pi}|H(\omega)|^2 S_\phi(\omega)\frac{\sin^4(m\omega T_c)}{\sin^2(\omega T_c/2)}, \tag{6.12}$$

where $|H(\omega)|^2$ is the interferometer sensitivity function, $S_\phi(\omega)$ is the noise power spectral density of the Raman laser relative phase, and $\tau = mT_c$; m is therefore the number of averaged samples in the calculation of the Allan variance. The two-pulse interferometer sensitivity function is given by [83, 84]

$$|H(\omega)|^2 = \frac{4\omega^2\Omega_R^2}{(\omega^2-\Omega_R^2)^2}\Big[\cos\omega(\frac{T}{2}+\tau_p)+\frac{\Omega_R}{\omega}\sin\frac{\omega T}{2}\Big]^2, \tag{6.13}$$

with τ_p the duration of the Raman $\pi/2$ pulse. This way, we are able to simulate the Allan variance for any given spectrum of added noise.

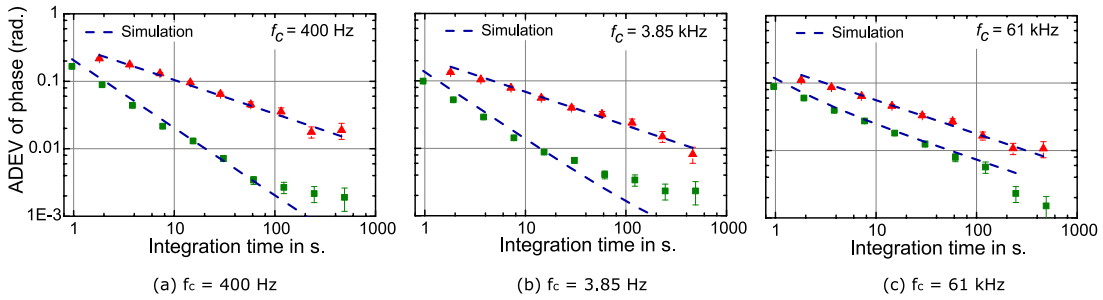

Figure 6.12: Comparison of normal mode (red triangles) and joint (green squares) for several cut off frequencies f_c of added white noise to the Raman laser phase lock loop: 400 Hz (a), 3.85 kHz (b) and 61 kHz (c). The Raman pulse Rabi frequency is f_R = 11.4 kHz. Dashed blue lines: theoretical calculation based on Eqn. (6.12) without any free parameter.

Fig. 6.12 presents the Allan deviations in phase for measurements corresponding to LO noise bandwidths of 400 Hz (a), 3.85 kHz (b) and 61 kHz (c). The $1/\tau$ region expands over longer interrogation times for f_c = 400 Hz than for f_c = 3.85 kHz. In the latter case, the Allan deviation changes its slope after ∼10 s of integration time. In the 61 kHz case, the $1/\tau$ scaling is no longer visible. This means joint operation no longer samples the LO noise. Hence, there exists no correlation between successive measurements. Using the measured white Raman phase noise levels $S_\phi(\omega) = S_0$ (Fig. 6.11(b)) and evaluating Eqn. (6.12) numerically, we obtained the dashed lines in Fig. 6.12 (a)-(c) for the normal mode (T_c = 900 ms, T = 480 ms) and for the joint ($T_c = T + \tau_p$). Our calculation (without any free parameters) is in good agreement with the experimental results as seen in Fig. 6.12. The change of slope from $1/\tau$ to $1/\sqrt{\tau}$ is also visible in the simulated case. It occurs at the point in time when the contribution of the high frequency noise ($f_c > f_R$) starts overcoming the low frequency noise ($f_c < f_R$). Hence, we verify that joint method is useful to integrate faster to the detection limit as the phase noise occurs at a frequency lower than f_R. In the previous

chapter, since we observed the vibration noise has a significant contribution only at frequencies less than 100 Hz., the fast averaging of the vibration noise should also be observed for our inertial interferometer.

6.5 Interleaved Joint System: Proof of Principle

The joint operation for the Ramsey interferometer was extended to an interleaved operation where we carry out more than two atom interferometric measurements simultaneously. This ability is essential to reject the Dick effect associated with vibration noise in cold atom inertial sensors which use more than two light pulses to build the interferometer and thus require more than two clouds being jointly interrogated.

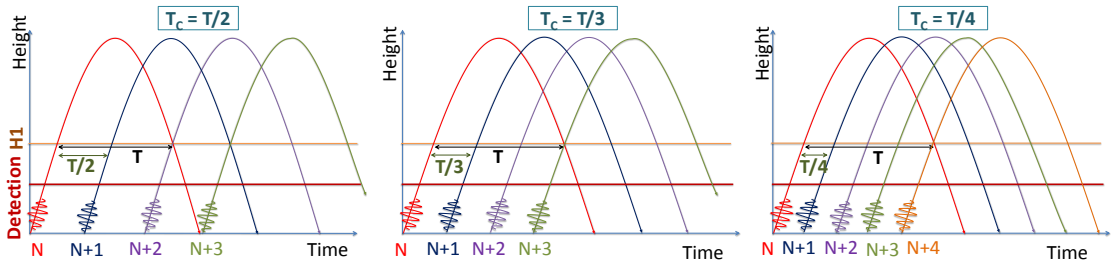

(a) $f_{cycle} = 2$ (b) $f_{cycle} = 3$ (c) $f_{cycle} = 4$

Figure 6.13: The three schemes of interleaved interferometry with the cycling frequency, $f_{cycle} = T/T_c$ spanning from 2 top 4 for the three schemes.

The agility of our experimental setup allows us to further enhance the interferometric sensitivity by juggling with more than two atom clouds, resulting in a cycle time T_c being a sub-multiple of the Ramsey time T. The interleaving scheme is portrayed in Fig. 6.13. Increasing T to 801 ms, we present four configurations of the interleaved operation with $T/T_c = f_{cycle} = 2$ to 4. To characterize the gain in the sensitivity of the interleaved operation, we proceed as before by introducing a white noise of 400 Hz bandwidth to the Raman laser phase lock loop.

Fig. 6.14 shows the Ramsey interferometric fringes we obtained with $T = 801$ ms for 5 different configurations: from normal operation upto $f_{cycle} = 4$. The further loss of contrast and the shift of phase due to the perturbation by the stray light from the MOT is clearly visible here.

For the four different configurations of T_c=[801, 400.5, 267, 200.25] ms, we observed similar $1/\tau$ scaling of the phase sensitivity in the different joint interleaving modes. As the contrast decreases the detection noise limit increases for increasing interleaving

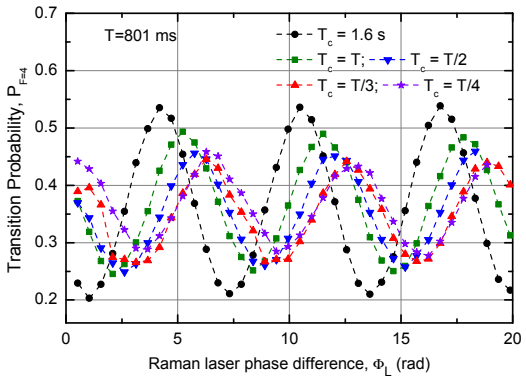

Figure 6.14: Interference fringes with Ramsey interrogation time T =801 ms for the normal (black dots), joint (green squares) and multiple joint operations (from blue to violet). As the multiplicity increases, there is further shift in the fringe phase and decrease in the contrast because of the scattered light from the MOT.

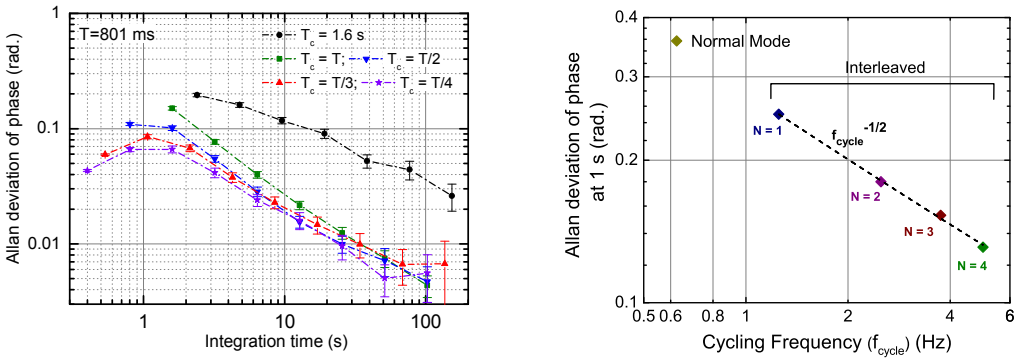

(a) Allan deviation for different f_{cycle} (b) Allan deviation @ 1s vs. f_{cycle}

Figure 6.15: (a) shows the different phase sensitivity curves for increasing cycling frequencies, f_{cycle}. After an integration time of 10 s, the sensitivities merges due to increasing of the detection noise from the loss of contrast for higher f_{cycle}. (b) shows that the short term phase sensitivity of the different interferometric operations decrease as $1/\sqrt{f_{cycle}}$.

frequencies. Hence, the $1/\sqrt{\tau}$ region is lost sooner for higher f_{cycle}. This leads to the overlap of the Allan deviation curves for higher f_{cycle} in Fig 6.15(a). Fig. 6.15(b) shows the short term sensitivity at 1 s vs. f_{cycle}. For the joint un-interleaved interferometer with T=801 ms, the short-term phase sensitivity is 250 mrad, while it is 131 mrad for $f_{cycle} = 4$. This demonstrates a sensitivity enhancement of 1.9 close to the expected

value of $\sqrt{f^1_{cycle}/f^4_{cycle}} = 2$. The minimum value of the cycle time in the interleaved operation is limited by the duration of preparation of the cold atoms. In our setup, we use a 150 ms long MOT loading stage where the detection noise is at the limit between quantum projection noise and technical noise. Going beyond could be achieved with faster loading of the MOT.

6.6 Continuous Four-pulse Gyroscope

After the proof of principle of the joint operation for cold atom interferometry, we will now use a continuous operation (zero dead time) for the first time in inertial cold atom interferometry. This will correspond to our four-pulse gyroscope with counter-propagating Raman pulses.

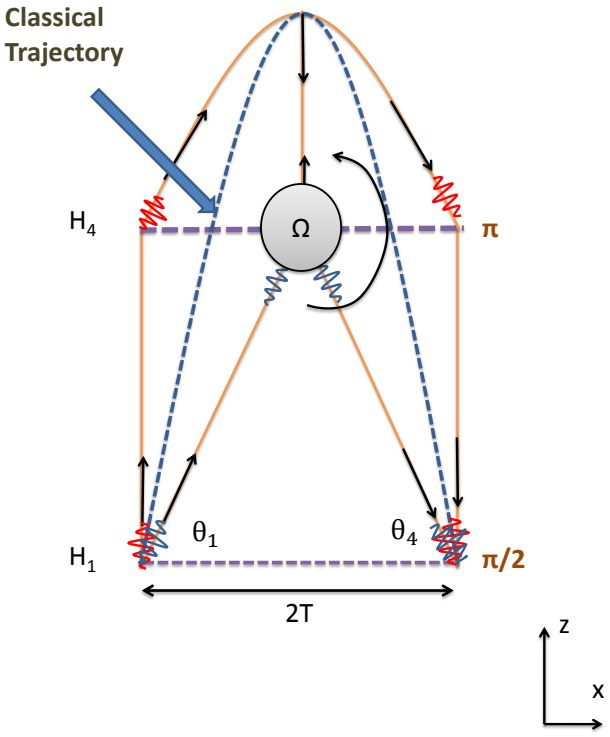

Figure 6.16: The Four-pulse Butterfly gyroscope scheme where we take rotation axis at the position of the the π-pulse. This gives a rotation sensitivity dependant on the 1st 4th pulse of the gyroscope configuration.

Considering the rotation axis of the gyroscope is at the π-pulse position (H4 in

Fig. 6.16), the rotation rate Ω will be given by:

$$\Omega = \frac{\theta_4 - \theta_1}{2T}, \tag{6.14}$$

where θ_1 and θ_4 are the relative angles produced at position H1 due to Ω [Fig. 6.16] corresponding to the 1st and the last $\pi/2$-pulses, respectively. We assume Ω is in the low frequency range and the accumulated interferometric phase in one cycle for Ω is then:

$$\Delta\Phi_\Omega = -2h_{14}\tan\left(\frac{\theta_4 - \theta_1}{2}\right) = -2h_{14}\tan\left(\Omega T\right), \tag{6.15}$$

where h_{14} is the vertical distance between positions H1 and H4. The above equation is inspired from the detailed derivation of the rotation phase in Page 96 of the thesis work of [16]. When we perform continuous operation of this four-pulse gyroscope, then we use the same $\pi/2$ Raman pulse to simultaneously interact with the two atom clouds of the consecutive cycles (as in the joint Ramsey interferometer case). We can then draw an analogy to Eqn. (6.5) and have:

$$\theta_1(t_i) = \theta_4\left(2T + t_{i-1}\right), \tag{6.16}$$

According to this equation, the rotation phase in Eqn. (6.15) should average down as $1/\tau$ due to the sharing of the same pulse and hence imprinting the same rotation phase information simultaneously for consecutive cycles. There will still be acceleration noise contribution coming from the Raman retro-reflection mirror vibrations at H4. This acceleration noise can be reduced using the correlation method as illustrated in the previous chapter. With the implementation of the low frequency vibration noise rejection in our continuous gyroscope scheme we should be able to demonstrate the rotation sensitivity enhancement.

For state preparation of the cold-atoms, we use the σ^{-1} pulse (as described in Section 6.2). We did not achieve the same efficiency of the σ^{-1} pulse (as in Section 6.2) to have ~100% atoms in m_F=0 state for our continuous gyroscope operation. This is because the microwave antenna had moved since the joint operation in clock configuration and we were never able to re-adjust it to its optimum position.

6.6.1 Results with Continuous Operation of Four-pulse Gyroscope

We performed measurements for the four-pulse gyroscope in normal and continuous operation with interrogation time $2T = 800$ ms. We use a MOT loading time, $t_{MOT} =$

200 ms. The vibration phase was obtained using the weighted average of the two accelerometers, and their correlation with the interferometric signal is shown in Fig. 6.17. The correlation in blue corresponds to the normal operation with π^0 selection pulse.

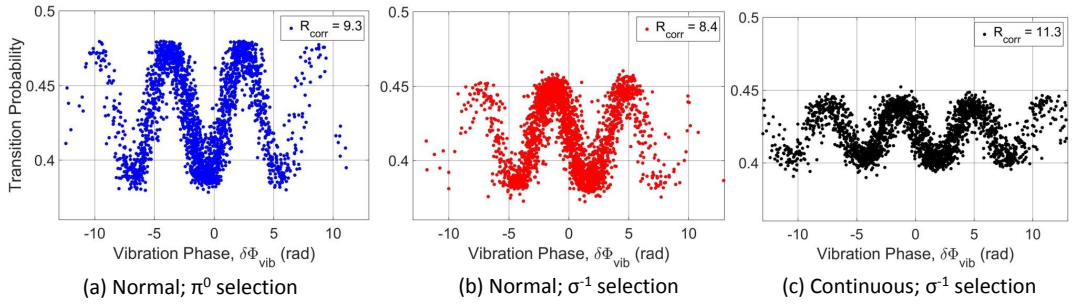

Figure 6.17: The correlation of the interferometric signal vs. the vibration noise recorded for the different configurations with $2T = 800$ ms: Fig.(a) with π^0 selection; Fig.(b) with σ^{-1} selection; and Fig.(c) with σ^{-1} selection in the continuous mode. The continuous operation gives the best vibration rejection factor $R_{corr} = 11.3$.

The contrast here is slightly better than the σ^{-1} selection as the later is not as efficient for m_F=0 selection. The correlation using σ^{-1} selection (in red) is also worse than π^0 selection due to presence of magnetic noise on atoms in the m_F=-1 state which also take part in interferometry. In the continuous operation (in black), the contrast is even slightly lower due to the perturbation of the atomic states by the MOT stray light. We observe the continuous operation provides the optimum correlation rejection factor of $R_{corr} = 11.3$ and the corresponding extracted rotation noise $\sigma_\Omega = 0.7$ rad.

To extract the rotation phase we used the packet-fit method (as explained in the previous chapter) and obtained the Allan deviation of the rotation noise, σ_Ω for the normal (red) and continuous (black) operations shown in Fig. 6.18. The continuous mode shows improvement of the sensitivity but we do not observe any fast averaging of the phase noise. This is because many of the interferometric data are situated at the extremities of the fringe (top and bottom of the sinusoidal correlation) in Fig. 6.18(c). This is where the phase sensitivity of the interferometer is zero and hence for these data points Eqn. (6.16) is no more valid. Hence, the $1/\tau$ scaling of continuous integration is lost. We anyways win by a factor $\sqrt{2}$ as the continuous cycle time ($T_c = 2T = 0.8$ s) is half the normal cycle of operation ($T_c = 1.6$ s). So the vibration noise is sampled with twice the frequency with no loss of information. Hence, the short term sensitivity improves by $\sqrt{2}$ as rotation phase sensitivity $\sigma_\Omega \propto 1/\sqrt{\tau}$.

Table 6.2 summarizes the enhancement of the four pulse gyroscope in the continuous operation vs. the normal operation, under same experimental condition. We

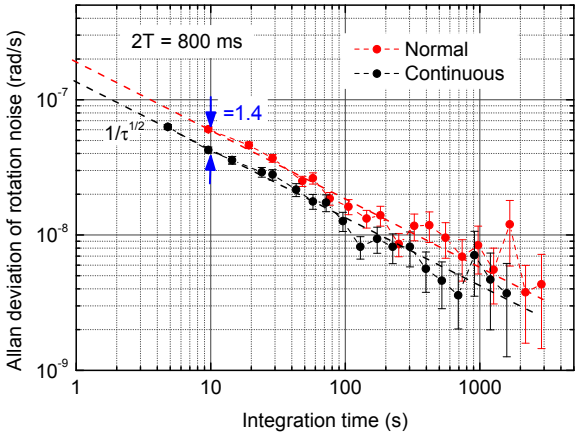

Figure 6.18: Allan deviation curves for the normal (red) and continuous operation (black) for the four-pulse gyroscope. When used σ^{-1} state selection pulse for the atomic state preparation. This led to worsening of the short-term rotation sensitivity w.r.t. π_0 selection, but we have a gain factor of $\sqrt{2}$ from normal to continuous in the sensitivity. The dashed lines are guides to the eye for $1/\sqrt{\tau}$ dependence of the sensitivity to integration time.

Table 6.2: Comparison of the short-term rotation sensitivity for different configurations of the four pulse guroscope.

Condition of four-pulse Interferometry	Short-term rotation sensitivity, σ_Ω (rad/s/$\sqrt{\text{Hz}}$)
Normal; π^0 selection	1.6×10^{-7}
Normal; σ^{-1} selection	1.9×10^{-7}
Continuous; σ^{-1} selection	1.4×10^{-7}

establish the best ever short-term rotation sensitivity of $\mathbf{1.4\times10^{-7}rad/s/\sqrt{Hz}}$ thanks to continuous operation.

6.7 Conclusion

We have demonstrated a new method for operating an atom interferometer in a joint configuration where the atom clouds are interrogated by a common Raman pulse with no dead time between the experimental cycles. In the clock mode, our method highly rejects the LO noise at a frequency bandwidth lower than the Rabi frequency of the Raman pulses. It enables faster averaging of the phase noise to achieve the detection

noise limit. We also demonstrated an extension of this method to an interleaved scheme: more than two interferometers are overlapped in time resulting in further improvement of the stability. After the proof of principle, we performed no-dead-time operation for inertial interferometry for the first time with the four-pulse gyroscope. We observe that we enhanced the sensitivity due to the no-dead-time cycling of the gyroscope. We were not able to achieved the fast averaging of the rotation noise due to spread of the interferometric data to the extremities of the fringe. This is where phase sensitivity is zero and these interferometric cycles are analogous to presence of dead time. This can be avoided by real-time compensation of the vibration phase in the Raman laser phase difference via feedback before the end of the interferometric cycle. This method was demonstrated in [13]. After implementing the real-time phase compensation, we would be able to demonstrate $1/\tau$ integration of the rotation phase and could average down to even lower phase noise by lowering the detection limit. This can be achieved via optimizations such as: higher laser intensity in the detection system and a better optical system for fluorescence collection. Among other improvements, we can avoid the contrast reduction by: (i) replacing the microwave state selection scheme by magnetic Stern-Gerlach selection; (ii) installing an obstruction system of the MOT stray light inside the vacuum chamber; (iii) Beam shaping of the Raman pulses for better homogeneity of the beam intensity to have a homogeneous Rabi frequency for all pulses.

Chapter 7

Conclusion

7.1 Summary of the Thesis Work

In this thesis work I have presented the performance of a large area cold-atom gyroscope with a maximum Sagnac area of 11 cm^2. This area is 27 times bigger than the second largest cold-atom gyroscope [11]. Our gyroscope represents a four-pulse AI in the "Butterfly" configuration implemented in a fountain geometry. We have later shown the proof of principle for the continuous operation of this gyroscope which was the first ever demonstration of the functioning of an inertial AI without dead time.

We first characterized the different systems of the experimental system: the laser system used for atom cooling and for the Raman beams; the frequency reference chain for the lasers; the magnetic selection procedure of the atoms and the detection system. We also measured the noise contribution from the different non-inertial sources and established that we are mainly limited by the detection noise.

To perform large area interferometry, we set-up a protocol for the alignment of the Raman beams which are separated in space. Using this protocol we reached to μrad level of parallelism in the vertical and mrad level of parallelism in the horizontal direction for the two Raman beams which was necessary for the interference condition. After we established the above protocol, we addressed the main source of inertial noise which is parasitic vibrations. We mounted external vibration sensors to estimate the vibration noise that affects our AI. We then implemented active and passive vibration mitigation systems for the experimental structure. This includes using a vibration isolation platform; constructing an acoustic isolation box around the whole structure (which also helps in temperature stabilization) and an active tilt locking system which stabilizes the base of the experimental platform. For the remaining vi-

bration noise, we use external sensors to reject the vibration from the interferometric signal via correlation. To characterize the rejection we used the four-pulse gyroscope with 2.4 cm^2 area and interrogation time $2T = 480$ ms. We tested different methods of correlation and established the best one giving us an optimum rejection factor to obtain the rotation sensitivity if this gyroscope. This gave us a state-of-the-art performance of 1.5×10^{-7} rad/s/$\sqrt{\text{Hz}}$ and a long-term stability of 3×10^{-9} rad/s in 2000 s. The optimized rejection method includes using two accelerometers and introducing an asymmetry in the four-pulse interferometric configuration. We applied the same rejection method for the 11 cm^2 area gyroscope with $2T = 800$ ms. This gave us a state-of-the-art performance 1.6 $\times10^{-7}$ rad/s/$\sqrt{\text{Hz}}$ of rotation sensitivity and a long-term stability of 1.8 $\times10^{-9}$ rad/s for an integration time as long as 10000 s.

We then performed a proof of principle of a joint operation of an AI with no dead time and sharing the same interrogating light pulse between consecutive experimental cycles. We used the two-pulse Ramsey clock configuration for this proof and also extended it for interleaved functioning of the Ramsey interferometer. We observed that the joint scheme helps us to integrate the phase noise faster to the detection noise limit of the interferometer w.r.t. the normal $1/\sqrt{\tau}$ integration when dead time is present. For inertial interferometry, we also performed a proof of principle for the four-pulse interferometer in a continuous mode of operation where we have no dead time between the interferometric cycles establishing the best ever short-term rotation sensitivity of 1.4×10^{-7} rad/s/$\sqrt{\text{Hz}}$.

7.2 Improvements leading to Operation of Continuous Gyroscope with Extreme Sensitivity

The signal-to-noise ratio of our AI joint operation can be improved by optimizing the cold-atom preparation system. This means obtaining a faster loading of the MOT by optimizing the intensity of the cooling lasers and also an improved method of state selection of the atoms. For this we have presently replaced the microwave selection procedure with a selection via a Stern-Gerlach magnetic deflection system. Here we produce a very high gradient of magnetic field in a region after the termination of the atom launching stage. This allows atoms in $m_F = 0$ state to travel into the interferometric zone and deflects all other atoms in the $m_F \neq 0$ state. Another improvement could be to obstruct the stray light from the MOT, and avoid the loss of interferometric contrast. This could be done by introducing a graphite cylinder with a hollow core in

the vacuum at the exit of the MOT chamber allowing the sole passage of the atomic cloud and not the stray light.

We observed how using only two external sensors we were able to reject acceleration noise efficiently. Unfortunately, we do not correlate for parasitic rotation noise. The rejection can be improved further by installing a better external vibration sensor than the Titan accelerometers. We already established that the Titan accelerometers has an intrinsic noise equivalent to 110 mrad for the four-pulse gyroscope with $2T = 800$ ms. These accelerometers are going to be replaced by seismometers which has lower instrumental noise especially in the low frequency range and since they are velocity sensors, they should be efficient to reject rotation and acceleration noise from the atomic signal.

We observed in Chapter 6 that the continuous operation helps us in the enhancement of the rotation sensitivity due to continuous sampling of the vibration noise. On the other hand, we were not able to achieve faster scaling of the rotation noise to the detection noise limit. One principal reason is that many data points are lying on the extremities of the interferometric fringe. This happens due to the spreading of the data by the vibration noise and these data points lead to zero sensitivity to phase. This is equivalent to operating with dead time (loss of inertial information) corresponding to those data sets. This can be avoided by implementing real-time vibration phase compensation as demonstrated in [13]. We will estimate the vibration phase from the sensors for each interferometric cycle and compensate this noise via feedback in the Raman laser phase difference, just before applying the last pulse of the interferometer. This will put each atomic signal near the centre of the fringe where the phase sensitivity is maximum. The better the correlation of the externally acquired vibration phase with the atomic signal, better will be the compensation.

On implementing the above mentioned improvements, we aim to obtain a slope in the rotation sensitivity $<10^{-9}$ rad/s/$\sqrt{\tau}$. We can then integrate down to $\sim 10^{-11}$ rad/s stability in 10000 s integration.

7.3 Application Perspectives

We showed that using two sensors, we are able to efficiently reject the acceleration noise from the atomic sensor. This dual sensor system could then be an inspiration for multi-axis inertial noise rejection for AI experiments aiming for test of fundamental physics e.g., the Airborne AI (ICE) [71] and the space based AI for test of Weak Equivalence

Principle: STE-QUEST [85]. In both these experiments, the atomic sensor is or will be operated in microgravity where it can rotate w.r.t. the Earth's reference. Spurious inertial noise for such a dynamic system can be rejected for more than one axis by mounting vibration sensors on the moving experimental set-up. Such rejection has been demonstrated in [71] but only using a single sensor.

The continuous operation of the cold-atom gyroscope also has application for inertial navigation. With this continuous cold atomic system there is a possibility of achieving long integration to 10^{-11} rad/s stability in less than an hour and hence will be very useful for extremely stable continuous inertial sensing for navigation. This kind of performance exists for commercial fiber-optic gyroscopes requiring several days of integration [17]. Another important application of the continuous cold-atom gyroscope is in geophysics where real-time acquisition of the inertial signal is necessary to study seismic events such as earthquakes and also study variation in gravity gradient due to change in the surface or underground mass distribution. Our continuous AI system is an inspiration for the MIGA project [86] which will also be used for geophysical studies.

The Cesium atom

Physical properties

Property	Parameter	Value	Unit
Atomic number	Z	55	
Number of nucleons	A	133	
Nuclear spin	I	7/2	
Atomic mass	m	$2.21 \cdot 10^{-25}$	kg
Density at 25^0C	ρ	1.93	g/cm^3
Fusion temperature	T_F	28.5	^0C
Boiling point	T_E	671	^0C
Saturated vapour pressure	P_v	$2.0 \cdot 10^{-4}$	Pa

Transition properties of D_2 : $\mathbf{6^2S_{1/2} \rightarrow 6^2P_{3/2}}$

Property	Parameter	Value	Unit
Wavelength (Vacuum)	λ	852.347	nm
Wavelength (Air)	λ_{air}	852.121	nm
Line-width	Γ	$2\pi \cdot 5.222$	MHz
Recoil velocity	v_{rec}	3.52	mm/s
Recoil Temperature	T_r	198.34	nK
Doppler shift ($v_{atom} = v_{rec}$)	$\Delta\omega_D$	$2\pi \cdot 4.133$	kHz
Saturation Intensity ($\sigma_\pm$ light)	I_{sat}	1.1023	mW/cm^2

Reference: Daniel A. Steck, "Cesium D Line data"

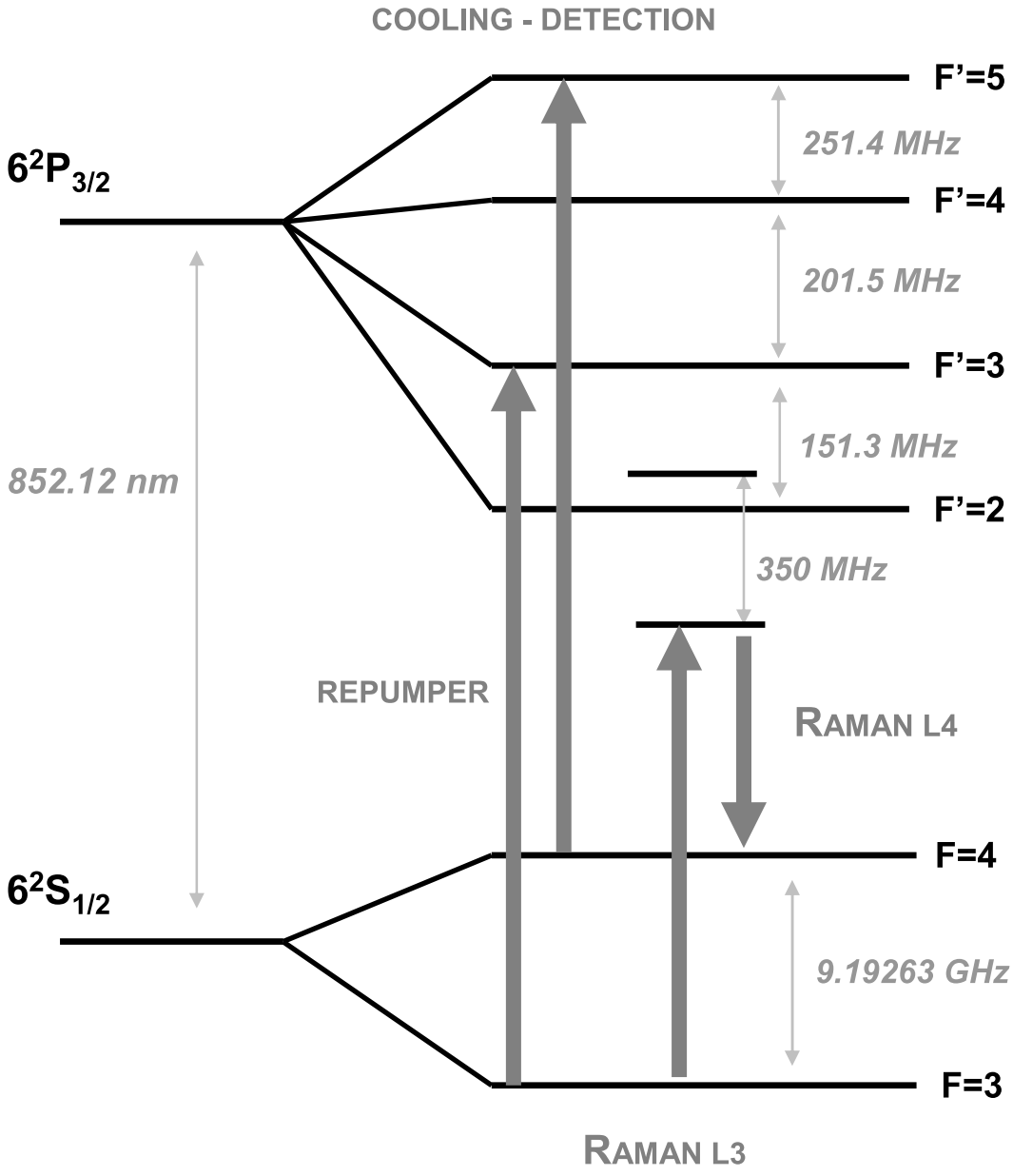

Figure .1: Optical transition diagram of the D_2 line of Cesium

Publications

- M. Meunier, I. Dutta, R. Geiger, C. Guerlin, C. L. Garrido Alzar, and A. Landragin, "Stability enhancement by joint phase measurements in a single cold atomic fountain," Phys. Rev. A, vol. 90, no. 6, p. 063633, Dec. 2014.
- B. Barrett, R. Geiger, I. Dutta, M. Meunier, B. Canuel, A. Gauguet, P. Bouyer, and A. Landragin, "The Sagnac effect: 20 years of development in matter-wave interferometry," Comptes Rendus Physique, vol. 15, no. 10, pp. 875-883, Dec. 2014.
- R. Geiger, L. Amand, A. Bertoldi, B. Canuel, W. Chaibi, C. Danquigny, I. Dutta, B. Fang, S. Gaffet, J. Gillot, D. Holleville, A. Landragin, M. Merzougui, I. Riou, D. Savoie, and P. Bouyer, "Matter-wave laser Interferometric Gravitation Antenna (MIGA): New perspectives for fundamental physics and geosciences," arXiv:1505.07137 [gr-qc, physics:physics], May 2015.

Stability enhancement by joint phase measurements in a single cold atomic fountain

M. Meunier,[*] I. Dutta,[*] R. Geiger,[†] C. Guerlin,[‡] C. L. Garrido Alzar, and A. Landragin[§]

LNE-SYRTE, Systèmes de Références Temps-Espace, Observatoire de Paris, CNRS, UPMC, 61 Avenue de l'Observatoire, 75014 Paris, France

(Received 25 August 2014; published 22 December 2014)

We propose a method of joint interrogation in a single atom interferometer which overcomes the dead time between consecutive measurements in standard cold atomic fountains. The joint operation enables for a faster averaging of the Dick effect associated with the local oscillator noise in clocks and with vibration noise in cold atom inertial sensors. Such an operation allows one to achieve the lowest stability limit due to atom shot noise. We demonstrate a multiple joint operation in which up to five clouds of atoms are interrogated simultaneously in a single setup. The essential feature of multiple joint operation, demonstrated here for a microwave Ramsey interrogation, can be generalized to go beyond the current stability limit associated with dead times in present-day cold atom interferometer inertial sensors.

DOI: 10.1103/PhysRevA.90.063633 PACS number(s): 37.25.+k, 03.75.Dg, 06.30.Ft, 95.55.Sh

I. INTRODUCTION

Over the past two decades, important progress in cold atom physics has established atom interferometry (AI) as a unique tool for precision measurements of time and frequency, and of gravitoinertial effects. Atom interferometry now addresses various applications ranging from precision measurements of fundamental constants [1–3], to inertial navigation [4–6], to geophysics [7,8], and has been proposed for gravitational wave detection (see, e.g., Ref. [9]). In order to address these promising applications beyond the strict scope of atomic physics, new methods must be formulated and demonstrated experimentally to use the full potentialities of AI. The main limitation of current cold atom interferometers is dead times between successive measurements, corresponding to the preparation of the atom source and the detection of the atoms at the output of the interferometer.

In cold atom or ion clocks, dead times lead to the well-known Dick effect, where aliasing of the local oscillator noise results in a degradation of the clock short-term sensitivity [10]. Several experiments have previously demonstrated a way to bypass this effect in relative comparisons between two clocks [11–13], and in realizing a clock in the specific case of a continuous cold beam atomic source [14]. Zero-dead-time operation of two interleaved atomic clocks was recently demonstrated, resulting in a reduction of the contribution of the local oscillator noise [15]. However, besides the relevance of this proof-of-principle experiment, this method used two different atomic clocks (interrogated by the same local oscillator) and therefore requires more experimental maintenance as well as control over more systematic effects. Moreover, considering applications to inertial sensors, it is required to interrogate successive atom clouds at the same location in order to reject all parasitic inertial terms, such as centrifugal accelerations of gradients of accelerations.

Here, we propose and demonstrate a method of joint interrogation of cold atom clouds in a single atomic fountain which overcomes the dead-time limitation in atom interferometers of high sensitivity. Our joint interrogation method is inspired from atom juggling methods that were originally introduced in the context of cold atom collisions in atomic fountain clocks [16] and only realized so far for concurrent measurements [3,4,17]. With an innovative and simple control sequence, we demonstrate the simultaneous joint interrogation of up to five cold atom clouds, resulting in a long Ramsey interrogation time (800 ms), high sampling rate (up to 5 Hz), and leading to a faster reduction of the Dick effect. As cold atom inertial sensors use more than two light pulses, rejection of the Dick effect associated with vibration noise in these sensors requires more than two clouds being interrogated simultaneously in the same setup. Our multiple joint operation proposes this possibility and demonstrates it experimentally in a multiclock configuration.

II. PRINCIPLE OF THE JOINT OPERATION AND EXPERIMENTS

Most cold atom interferometers such as clocks, accelerometers, or gyroscopes are sequentially operated in a sequence of total duration T_c, and typically consist of three main steps: (i) atom trapping, cooling, and preparation; (ii) N-microwave or light-pulse AI sequence (Ramsey-like interrogation with a total duration T); and (iii) atomic state detection. Here we present experiments operating in joint mode ($T_c = T$) or multiple joint modes ($T/T_c = 2,3,4$), resulting in a null dead time and enhanced stability of the interferometer.

The normal-mode interferometer is operated sequentially following steps (i)–(iii), with an interrogation time $T =$ 480 ms and a cycle time $T_c = 900$ ms. Figure 1(b) presents the principle of the joint mode operation where the Raman interrogation pulse is shared by clouds $N - 1$ (falling) and N. Figure 1(a) shows a schematic view of the experiment. Cesium atoms loaded from a two-dimensional (2D) magneto-optical trap (MOT) are trapped and cooled in a three-dimensional (3D) MOT; 4×10^7 atoms are launched vertically towards the interferometer region using moving molasses with a temperature of 1.3 μK. The launching is followed by a microwave

[*]These authors contributed equally to this work.

[†]remi.geiger@obspm.fr

[‡]Present address: Laboratoire Kastler Brossel, ENS-PSL Research University, CNRS, UPMC-Sorbonne Universités, Collège de France.

[§]arnaud.landragin@obspm.fr

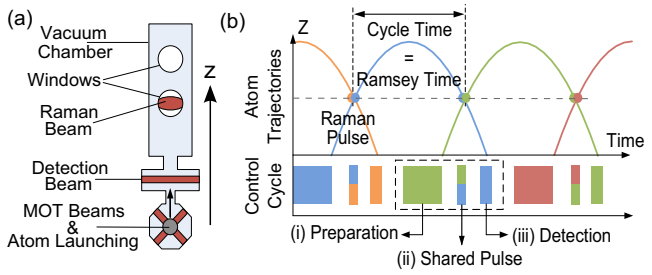

FIG. 1. (Color online) (a) Schematic of the instrument. (b) Principle of the joint mode operation: (i) Preparation of cloud N, (ii) Raman light pulse shared by clouds $N-1$ (falling) and N (rising), and (iii) detection of cloud $N-1$.

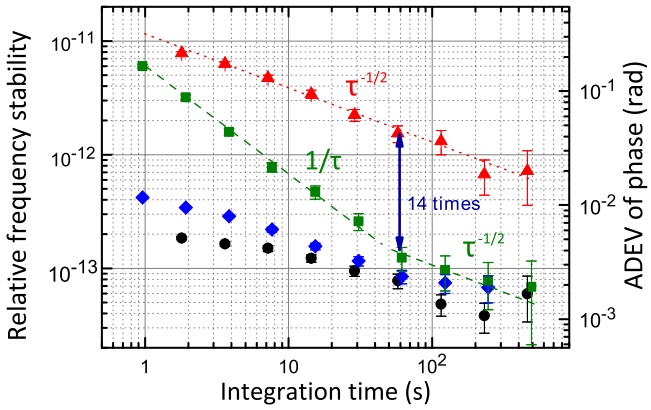

FIG. 2. (Color online) Allan deviations (ADEV) of the fountain relative frequency stability in normal and joint modes, for an interrogation time $T = 480$ ms. Stability without adding noise for the normal (black circle) and joint (blue rhombus) operations. Allan deviation for the normal mode (red triangle) and the joint mode (green square) when adding white noise over a bandwidth of 400 Hz. The $1/\tau$ (dashed) and $\tau^{-1/2}$ (dotted) lines are guide to the eyes. We observe a 14-fold gain in frequency stability from the normal to joint mode at 60 s. Integrating to this frequency stability level in a normal operation would require 12 000 s.

pulse selecting 6×10^6 atoms in the $|F = 3, m_F = 0\rangle$ state, which are used for interferometry. Light pulse interferometry is realized using copropagating Raman lasers which couple the $|F = 3, m_F = 0\rangle$ and $|F = 4, m_F = 0\rangle$ clock levels characterized by a hyperfine splitting of 9.192 GHz. Several windows enable versatile configurations for the interferometer where interrogation times up to 800 ms can be reached. In this work, we perform a Ramsey interrogation using two $\pi/2$ Raman pulses symmetric with respect to the apogee of the atom trajectory [see Fig. 1(b)]. Experimentally, the joint operation implies trapping a cloud of atoms in the bottom part of the chamber, while another atom cloud is in the interferometer or detection regions. This is a form of juggling with the clouds without recapture [16].

A microwave pulse prepares atoms in the nonmagnetic ($m_F = 0$) state before the interferometer in order to maximize the interferometer contrast. The selection is performed on the $|F = 4, m_F = +1\rangle \rightarrow |F = 3, m_F = 0\rangle$ transition, which is separated from the clock transition using a bias field of 18 mG. This scheme allows avoiding perturbation of the atoms being interrogated in the Ramsey zone by the microwave selection radiation.

With $\pi/2$ pulses of duration $\tau_p = 22$ μs (Rabi frequency $\Omega_R/2\pi = 11.4$ kHz), the phase sensitivities extrapolated at 1 s of the two-pulse Raman interferometer for the normal ($T = 480$ ms, $T_c = 900$ ms) and joint mode ($T_c = T = 480$ ms) operations are 13 and 16 mrad, respectively (see Fig. 2, black circles and blue rhombus). The sensitivity is limited by both the performance of the Raman laser phase-lock system and by the detection noise. The small difference in detection noise can be explained by a fringe contrast loss from 50% to 30% when implementing the joint operation. This contrast loss originates from stray light scattered from the MOT atoms which interacts with the atoms in the interferometer region, starting 0.5 m above, transferring them in unwanted states. Moreover, this stray light induces a light shift on the interference fringes (see Appendix, Fig. 5). The effects of the MOT scattered light could be suppressed with the use of a vacuum-compatible controllable shutter [18] between the MOT and interrogation regions.

III. REJECTION OF THE LOCAL OSCILLATOR NOISE IN JOINT OPERATION

The phase of the two-pulse atom interferometer is determined by the Raman laser phase difference imprinted on the atomic wave function at the light pulses; at time t_i it reads $\Delta\Phi_i = \phi(T + t_i) - \phi(t_i)$, where $\phi(t)$ is the Raman laser relative phase. In the case of a white relative phase noise and after N cycles, the variance $\langle \Delta\Phi_N^2 \rangle$ of the accumulated atomic phase is inversely proportional to N. In the time domain, this means that the phase Allan deviation scales as $1/\sqrt{\tau}$ (τ is the integration time), which is the well-known result for successive uncorrelated measurements. With the cycle time T_c equal to the Ramsey time T, the second laser pulse $\phi(T + t_i)$ of cloud i is the same as the first pulse $\phi(t_{i+1})$ of cloud $i + 1$: $\phi(T + t_i) = \phi(t_{i+1})$. As a result, the consecutive phase terms in the accumulated atomic phase cancel each other, so that the variance of the accumulated phase $\langle \Delta\Phi_N^2 \rangle$ scales as $1/N^2$ (Allan deviation of phase $\sim 1/\tau$). In other words, the joint operation rejects the aliasing of the local oscillator noise (here the Raman laser relative phase noise) usually encountered when performing independent measurements of the phase with dead times. The rejection applies as long as the local oscillator noise spectrum has a bandwidth that is lower than the pulse Rabi frequency Ω_R. We quantitatively analyze the rejection efficiency below.

To demonstrate the local oscillator (LO) phase noise rejection, we introduce a white noise of controlled amplitude and bandwidth in the Raman laser phase-lock loop. The noise is generated using a direct digital synthesizer (SRS DS345) and filtered by an analog 115 dB/octave low-pass filter (SR 650). The spectrum of added noise and the details of its calibration

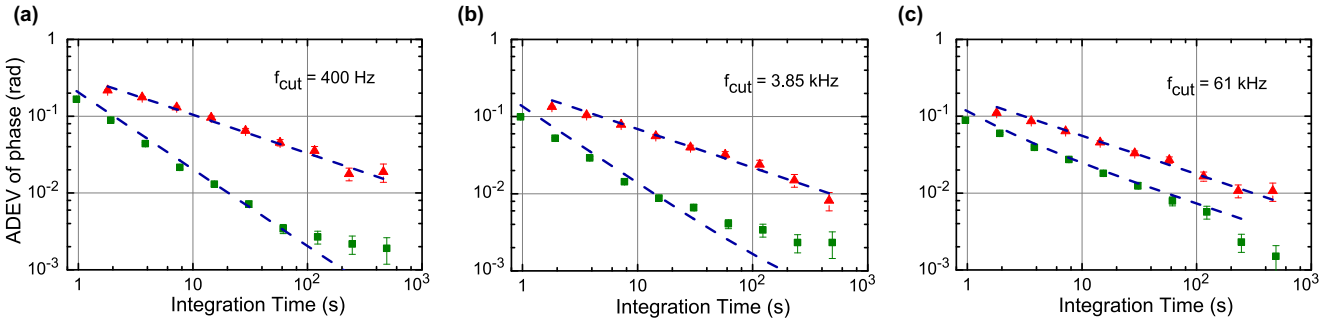

FIG. 3. (Color online) Comparison of the normal mode (red triangles) and joint mode (green squares) for several cutoff frequencies $f_{\rm cut}$ of added white noise to the Raman laser phase-lock loop: (a) 400 Hz, (b) 3.85 kHz, and (c) 61 kHz. The Raman pulse Rabi frequency is $f_R = 11.4$ kHz. Dashed blue lines: Theoretical calculation based on Eq. (1) without a free parameter.

are given in Appendix, Fig. 6. Figure 2 shows the measured phase Allan deviation (ADEV) for a white noise of 400 Hz bandwidth (green squares), well below the Rabi frequency of 11.4 kHz. We clearly observe the expected $1/\tau$ scaling of the joint operation. A change of slope in the ADEV is observed at 60 s when reaching the uncorrelated noise floor at a level of 1×10^{-13} in relative frequency stability, corresponding to detection noise. Figure 2 thus shows that the joint operation allows for fast averaging to the fundamental noise linked to the detection noise, even with a low stability local oscillator.

The joint operation efficiently rejects the Dick effect associated with low frequencies in the LO noise, but the rejection is less efficient for LO noise bandwidths $f_{\rm cut}$ that are higher than the Raman pulse Rabi frequency $f_R = \Omega_R/2\pi$. In the following we explore the limits of the rejection. Figure 3 presents phase ADEV for measurements corresponding to LO noise bandwidths of 400 Hz [Fig. 3(a)], 3.85 kHz [Fig. 3(b)], and 61 kHz [Fig. 3(c)]. The $1/\tau$ region expands over longer interrogation times for $f_{\rm cut} = 400$ Hz than for $f_c = 3.85$ kHz. In the latter case, the Allan deviation changes its slope after $\sim$10 s of integration time. In the 61 kHz case, the $1/\tau$ scaling is no longer visible: The joint mode no longer samples the LO noise so that correlation does not exist between successive measurements.

To quantitatively analyze our data, we use the AI sensitivity function formalism, which provides the response of the atom interferometer to a perturbation at a given frequency [19,20]. The Allan variance of the phase reads

$$\sigma^2(\tau) = \frac{1}{2m^2}\int_0^{+\infty}\frac{d\omega}{2\pi}|H(\omega)|^2 S_\phi(\omega)\frac{4\sin^4(m\omega T_c/2)}{\sin^2(\omega T_c/2)}, \quad (1)$$

where $|H(\omega)|^2$ is the interferometer sensitivity function, $S_\phi(\omega)$ is the noise power spectral density of the Raman laser relative phase, and $\tau = mT_c$; m is therefore the number of averaged samples in the calculation of the Allan variance. The two-pulse inteferometer sensitivity function is given by [19,20]

$$|H(\omega)|^2 = \frac{4\omega^2\Omega_R^2}{\left(\omega^2-\Omega_R^2\right)^2}\left[\cos\omega\left(\frac{T}{2}+\tau_p\right)+\frac{\Omega_R}{\omega}\sin\frac{\omega T}{2}\right]^2, \quad (2)$$

with τ_p the duration of the Raman $\pi/2$ pulse. Using the measured white Raman phase noise levels $S_\phi(\omega) = S_0$ (Fig. 6) and evaluating Eq. (1) numerically, we obtained the dashed lines in Figs. 3(a)–3(c) for the normal mode ($T_c = 900$ ms, $T = 480$ ms) and for the joint mode ($T_c = T + \tau_p$). Our calculation reproduces well the experimental results, without a free parameter. In particular, the change of slope from τ^{-1} to $\tau^{-1/2}$ is well captured. It occurs at the point in time

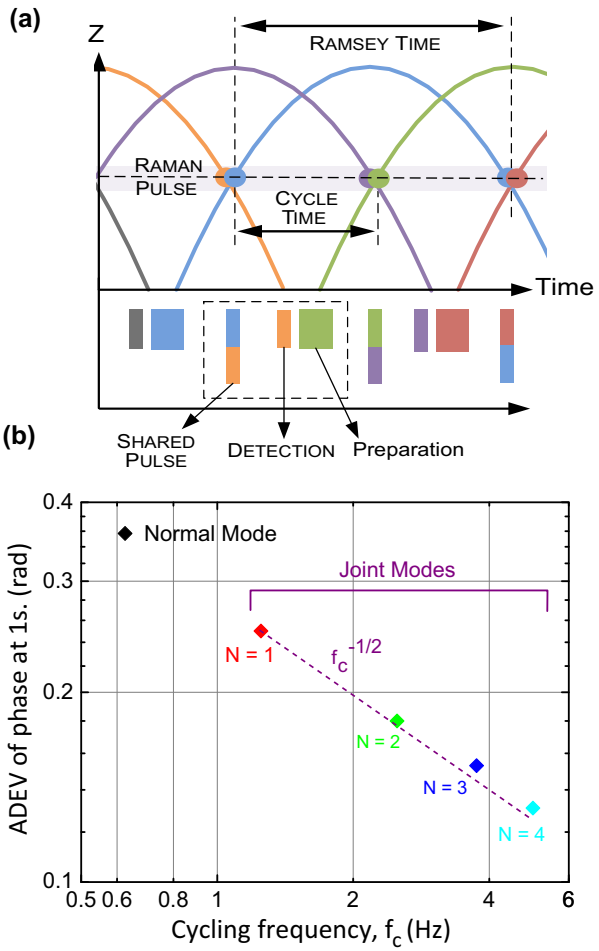

FIG. 4. (Color online) (a) Schematic of the double joint operation where $T/T_c = 2$, where three atom clouds simultaneously interact with the Raman laser pulses. (b) Short-term sensitivity at 1 s for each of the operation modes and $T = 801$ ms, from the normal operation ($T_c = 1.6$ s) to the quadrupole joint mode ($T/T_c = 4$). The dashed line is a guide to the eye showing the $1/\sqrt{f_c}$ scaling.

when the contribution of the high-frequency noise ($f_{\rm cut} > f_R$) starts overcoming the low-frequency noise contributions ($f_{\rm cut} < f_R$), which are well correlated in successive joint measurements.

IV. MULTIPLE JOINT OPERATION

We now present the extension of our method to a multiple joint operation where we interleave more than two atom interferometry measurements. This ability is essential to reject the Dick effect associated with vibration noise in cold atom inertial sensors which use more than two light pulses to build the interferometer and thus require more than two clouds being jointly interrogated. The agility of our experimental setup allows us to further enhance the interferometric sensitivity by juggling with more than two atom clouds, resulting in a cycle time T_c being a submultiple of the Ramsey time T. Increasing T to 801 ms, we present four configurations of the joint operation with $T/T_c = 1$–4. Figure 4(a) presents the principle of the double joint configuration where $T/T_c = 2$. To characterize the sensitivity gain of the multiple joint operation, we proceed as before by introducing a 400 Hz bandwidth white noise to the Raman laser phase-lock loop. For the four different configurations of $T_c = [801, 400.5, 267, 200.25]$ ms, we observed a similar $1/\tau$ scaling of the phase ADEV in the different joint modes. Figure 4(b) shows the short-term sensitivity at 1 s versus the cycling frequency $f_c = 1/T_c$. For the single joint mode interferometer with $T = 801$ ms, the short-term phase sensitivity is 250 mrad, while it is 131 mrad in a quadrupole joint mode. This demonstrates a sensitivity enhancement of 1.9 close to the expected value $(f_c^{\rm quad}/f_c^{\rm single})^{1/2} = 2$.

The minimum value of the cycle time in the multiple joint mode is limited by the duration of preparation of the cold atoms. In our setup, we used a 150-ms-long MOT loading stage where the detection noise is at the limit between quantum projection noise and technical noise. Going beyond could be achieved with optimum loading of the MOT.

V. CONCLUSION

We have demonstrated a method for operating an atom interferometer in a joint configuration where five atom clouds are interrogated simultaneously by common interrogation lasers. Our method highly rejects the Dick effect present in standard atomic fountains operated with dead times. It enables faster averaging of the phase noise to achieve the fundamental noise floor linked to the detection noise. This method remains efficient as soon as the noise frequency components are below the pulse Rabi frequency. We also demonstrated an extension of this method to a multiple joint scheme, where several interleaved interrogations result in further improvement of the stability.

The joint method enables one to run microwave frequency standards at the best performances (i.e., at the quantum projection noise limit) without sophisticated and expensive ultrastable oscillators [21–23] by canceling the Dick effect (and increasing the locking bandwidth of the local oscillator). Our method can be directly used for the rejection of parasitic vibrations in cold atom inertial sensors operated with dead times. In such systems, in which the signal is fluctuating, dead times not only reduce drastically the stability but lead to loss of information [24]. Moreover, the multiple joint operation gives access to high-frequency components while maintaining high sensitivity linked to long interaction times achievable with cold atom sensors.

ACKNOWLEDGMENTS

We thank Bertrand Venon, Thomas Lévèque, David Horville, and Michel Lours for their contributions to the design of the experiment and the first stages of the realization, and Denis Savoie for his contribution to the simulations. We thank DGA (Délégation Générale pour l'Armement), IFRAF (Institut Francilien de Recherche sur les Atomes Froids) for funding. M.M was supported by Délégation Générale pour l'Armement (DGA), and I.D. by Centre National d'Etudes Spatiales (CNES) and LABEX Cluster of Excellence FIRST-TF (ANR-10-LABX-48-01) within the Program "Investissements d'Avenir" operated by the French National Research Agency (ANR).

APPENDIX

A. Influence of the light scattered by the atoms in the MOT

See Fig. 5.

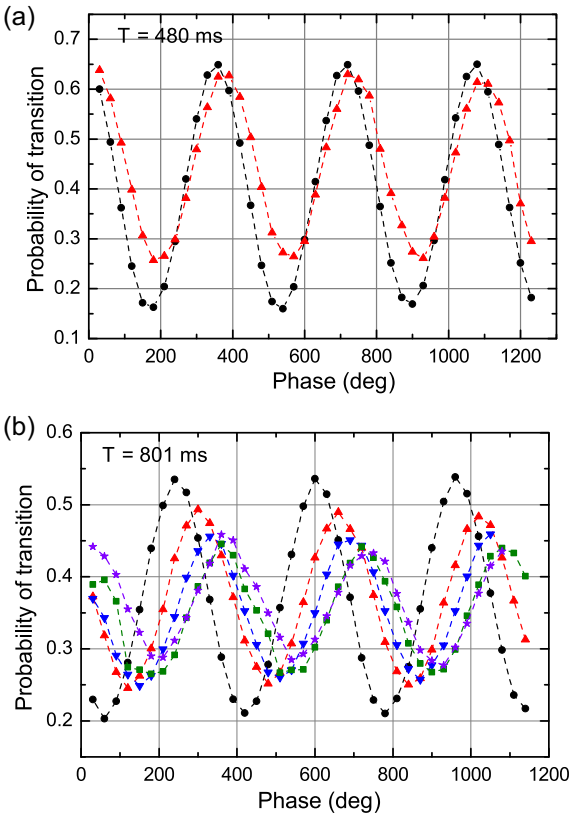

FIG. 5. (Color online) Interference fringes for two different Ramsey interrogation times: (a) $T = 480$ ms for the normal (black dots) and joint (red triangles) modes; (b) $T = 801$ ms for the normal (black dots), joint (red triangles), and multiple joint operations (double joint: blue triangles; triple joint: green squares; quadrupole joint: violet stars).

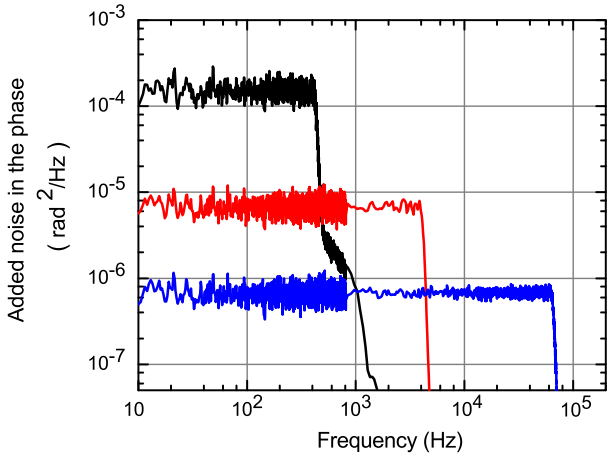

FIG. 6. (Color online) Power spectral density of the white added noise for the three different values of $f_{\rm cut}$. Black (top) $f_{\rm cut} = 400$ Hz; red (middle) $f_{\rm cut} = 3.85$ kHz; blue (bottom) $f_{\rm cut} = 61$ kHz.

B. Added Raman laser phase noise

The white noise was generated using a direct digital synthesizer (SRS DS345) and filtered by an analog 115 dB/octave low-pass filter (SR 650), and directly added to the Raman laser phase-lock loop. The spectrum of the added noise is given in Fig. 6. Its exact calibration was important for the quantitative analyses presented in Fig. 3 of the main text. To calibrate the noise level, we applied a sinusoidal modulation of known amplitude (in volts) and frequency (0.1 Hz) to the Raman laser phase-lock loop and measured the corresponding modulation of the interferometer phase (in radians). This yielded the conversion factor from volts to radians and the following white-noise levels: $S_0 = 1.5 \pm 0.3 \times 10^{-4}$ rad^2/Hz for 400 Hz; $S_0 = 6.8 \pm 1.4 \times 10^{-6}$ rad^2/Hz for 3.85 kHz; and $S_0 = 6.7 \pm 1.3 \times 10^{-7}$ rad^2/Hz for 61 kHz. These measured noise levels were used in Eq. (1).

[1] J. Guéna, M. Abgrall, D. Rovera, P. Rosenbusch, M. E. Tobar, P. Laurent, A. Clairon, and S. Bize, Phys. Rev. Lett. **109**, 080801 (2012), and references therein.

[2] R. Bouchendira, P. Cladé, S. Guellati-Khelifa, F. Nez, and F. Biraben, Ann. Phys. **525**, 484 (2013).

[3] G. Rosi, F. Sorrentino, L. Cacciapuoti, M. Prevedelli, and G. M. Tino, Nature (London) **510**, 518 (2014).

[4] B. Canuel, F. Leduc, D. Holleville, A. Gauguet, J. Fils, A. Virdis, A. Clairon, N. Dimarcq, C. J. Bordé, A. Landragin *et al.*, Phys. Rev. Lett. **97**, 010402 (2006).

[5] R. Geiger, V. Ménoret, G. Stern, N. Zahzam, P. Cheinet, B. Battelier, A. Villing, F. Moron, M. Lours, Y. Bidel, A. Bresson, A. Landragin, and P. Bouyer, Nat. Commun. **2**, 474 (2011).

[6] B. Barrett, P.-A. Gominet, E. Cantin, L. Antoni-Micollier, A. Bertoldi, B. Battelier, P. Bouyer, J. Lautier, and A. Landragin, in *Atom Interferometry, Proceedings of the International School of Physics "Enrico Fermi," Course CLXXXVIII, Varenna, 2013*, edited by G. M. Tino and M. A. Kasevich (IOS, Amsterdam, 2014), p. 493.

[7] Z. Jiang, V. Palinkas, F. E. Arias, J. Liard, S. Merlet, H. Wilmes, L. Vitushkin, L. Robertsson, L. Tisserand, F. Pereira Dos Santos *et al.*, Metrologia **49**, 666 (2012).

[8] P. Gillot, O. Francis, A. Landragin, F. Pereira Dos Santos, and S. Merlet, Metrologia **51**, L15 (2014).

[9] S. Dimopoulos, P. W. Graham, J. M. Hogan, M. A. Kasevich, and S. Rajendran, Phys. Rev. D **78**, 122002 (2008).

[10] G. J. Dick, J. D. Prestage, C. A. Greenhall, and L. Maleki, in *Proceedings of the 22nd Annual Precise Time and Time Interval (PTTI) Applications and Planning Meeting*, edited by R. L. Sydnor (NASA, Hampton, VA, 1990), pp. 487–508, http://oai.dtic.mil/oai/oai?verb=getRecord&metadataPrefix=html&identifier=ADA515721.

[11] S. Bize., Y. Sortais, P. Lemonde, S. Zhang, P. Laurent, G. Santarelli, C. Salomon, and A. Clairon, IEEE Trans. Ultrason. Ferroelectr. Freq. Control **47**, 1253 (2000).

[12] M. Takamoto, T. Takano, and H. Katori, Nat. Photonics **5**, 288 (2011).

[13] C. W. Chou, D. B. Hume, M. J. Thorpe, D. J. Wineland, and T. Rosenband, Phys. Rev. Lett. **106**, 160801 (2011).

[14] L. Devenoges, A. Stefanov, A. Joyet, P. Thomann, and G. Di Domenico, IEEE Trans. Ultrason. Ferroelectr. Freq. Control **59**, 211 (2012).

[15] G. W. Biedermann, K. Takase, X. Wu, L. Deslauriers, S. Roy, and M. A. Kasevich, Phys. Rev. Lett. **111**, 170802 (2013).

[16] R. Legere and K. Gibble, Phys. Rev. Lett. **81**, 5780 (1998).

[17] Z.-K. Hu, X.-C. Duan, M.-K. Zhou, B.-L. Sun, J.-B. Zhao, M.-M. Huang, and J. Luo, Phys. Rev. A **84**, 013620 (2011).

[18] F. Füzesi, A. Jornod, P. Thomann, M. D. Plimmer, G. Dudle, R. Moser, L. Sache, and H. Bleuler, Rev. Sci. Instrum. **78**, 103109 (2007).

[19] P. Lemonde, G. Santarelli, P. Laurent, F. Pereira dos Santos, A. Clairon, and C. Salomon, in *Proceedings of the 1998 IEEE International Frequency Control Symposium* (IEEE, Piscataway, NJ, 1998), pp. 110–115.

[20] P. Cheinet, B. Canuel, F. Pereira Dos Santos, A. Gauguet, F. Leduc, and A. Landragin, IEEE Trans. Instrum. Meas. **57**, 1141 (2008).

[21] S. Grop, P.-Y. Bourgeois, R. Boudot, Y. Kersalé, E. Rubiola, and V. Giordano, Electron. Lett. **46**, 420 (2010).

[22] J. G. Hartnett, N. R. Nand, and C. Lu, Appl. Phys. Lett. **100**, 183501 (2012).

[23] Ultra Low Instability Signal Source, http://www.uliss-st.com/.

[24] C. Jekeli, Navigation **52**, 1 (2005).

C. R. Physique 15 (2014) 875–883

Contents lists available at ScienceDirect

Comptes Rendus Physique

www.sciencedirect.com

The Sagnac effect: 100 years later / L'effet Sagnac : 100 ans après

The Sagnac effect: 20 years of development in matter-wave interferometry

L'effet Sagnac : 20 ans de développements des interféromètres à ondes de matière

Brynle Barrett [a], Rémy Geiger [b], Indranil Dutta [b], Matthieu Meunier [b], Benjamin Canuel [a], Alexandre Gauguet [c], Philippe Bouyer [a], Arnaud Landragin [b,*]

[a] *LP2N, IOGS, CNRS and Université de Bordeaux, rue François-Mitterrand, 33400 Talence, France*
[b] *LNE-SYRTE, Observatoire de Paris, CNRS and UPMC, 61, avenue de l'Observatoire, 75014 Paris, France*
[c] *Laboratoire Collisions Agrégats Réactivité (LCAR), CNRS, Université Paul-Sabatier, 118, route de Narbonne, 31062 Toulouse cedex 09, France*

ARTICLE INFO

Article history:
Available online 12 November 2014

Keywords:
Matter-wave Sagnac interferometer
Light-matter interactions
Stimulated Raman transitions
Cold atoms
Precision measurements
Inertial navigation
Geophysics

Mots-clés :
Interféromètre Sagnac à ondes de matière
Interaction lumière-matière
Transitions Raman stimulées
Atomes froids
Mesures de précision
Navigation inertielle
Géophysique

ABSTRACT

Since the first atom interferometry experiments in 1991, measurements of rotation through the Sagnac effect in open-area atom interferometers have been investigated. These studies have demonstrated very high sensitivity that can compete with state-of-the-art optical Sagnac interferometers. Since the early 2000s, these developments have been motivated by possible applications in inertial guidance and geophysics. Most matter-wave interferometers that have been investigated since then are based on two-photon Raman transitions for the manipulation of atomic wave packets. Results from the two most studied configurations, a space-domain interferometer with atomic beams and a time-domain interferometer with cold atoms, are presented and compared. Finally, the latest generation of cold atom interferometers and their preliminary results are presented.

RÉSUMÉ

Depuis les premières expériences d'interférométrie atomique en 1991, les mesures de rotation basées sur l'effet Sagnac dans des interféromètres possédant une aire physique ont été envisagées. Les études expérimentales ont montré de très bons niveaux de sensibilité rivalisant avec l'état de l'art des interféromètres Sagnac dans le domaine optique. Depuis le début des années 2000, de tels développements ont été motivés par de possibles applications dans les domaines de la navigation inertielle et de la géophysique. La plupart des interféromètres à ondes de matière qui ont été étudiés depuis sont basés sur des transitions Raman à deux photons pour la manipulation des paquets d'ondes atomiques. Nous présentons et comparons ici les résultats portant sur les deux configurations les plus étudiées : un interféromètre dans le domaine spatial utilisant un jet atomique et un interféromètre dans le domaine temporel utilisant des atomes froids. Finalement, la

* Corresponding author.
E-mail address: arnaud.landragin@obspm.fr (A. Landragin).

http://dx.doi.org/10.1016/j.crhy.2014.10.009
1631-0705/

dernière génération d'interféromètres à atomes froids et leurs résultats préliminaires sont présentés, ainsi que les perspectives d'évolution du domaine.

1. Introduction

Rotation sensors are useful tools in both industry and fundamental scientific research. Highly accurate and precise rotation measurements are finding applications in inertial navigation [1], studies of geodesy and geophysics [2], and tests of general relativity [3]. Since the early 1900s, there have been many manifestations of Georges Sagnac's classic experiments [4] that utilize the "Sagnac" interference effect to measure rotational motion, both with light and with atoms [5]. Gyroscopes based on this effect measure a rotation rate, Ω, via a phase shift between the two paths of an interferometer. The Sagnac phase shift, for both photons and massive particles, can be written as:

$$\Phi_{\text{Sagnac}} = \frac{4\pi E}{hc^2}\mathbf{A}\cdot\boldsymbol{\Omega} \tag{1}$$

where $\mathbf{A}$ is the area vector of the Sagnac loop (normal to the plane of the interferometer and equal to the area enclosed by the interferometer arms) and E is the energy of the particle ($E = \hbar\omega$ for a photon of angular frequency ω and $E = Mc^2$ for a particle of rest mass M). Eq. (1) shows that the Sagnac phase for a matter-wave interferometer is larger by a factor of $Mc^2/\hbar\omega$ compared to an optical one with equivalent area. This scale factor is $\sim 10^{11}$ when comparing the rest energy of an atom to that of an optical photon in the visible range—emphasizing the high sensitivity of atom-based sensors to rotations. In this article, we will review some of the key developments that have taken place over the last 20 years regarding matter-wave Sagnac interferometers.

There has been dramatic progress in the field of atom interferometry in recent history. During the late 1980s, various types of atom interferometers were proposed as sensitive probes of different physical effects [6–9], and by the early 1990s the first experimental demonstrations had been realized [10–13]. As a result of their intrinsically high sensitivity to inertial effects, atom interferometers are now routinely used as tools for studies of fundamental physics and precision measurements [14]. The first experiments that exploited the rotational sensitivity of atom interferometers were carried out by Riehle et al. [13] using optical Ramsey spectroscopy with a calcium atomic beam. Fig. 1 shows their interferometer configuration and experimental results. By rotating their entire apparatus at various rates Ω, and recording the fringe shift of a Ramsey pattern, they were the first to demonstrate the validity of Eq. (1) for atomic waves.

In 1997, two other research groups [15,16] simultaneously published results pertaining to rotation sensing with atom interferometers.[1] Although both experiments relied on atomic beams, they each employed a different method to generate matter-wave interference.

In Ref. [15], a beam of sodium atoms (longitudinal velocity ~ 1030 m/s) was sent through three nano-fabricated transmission gratings (200 nm period, 0.66 m separation) which acted to split, reflect and recombine atomic wave packets taking part in the interferometer. By precisely controlling the applied rotation of their apparatus, they measured rotation rates of the same magnitude as that of the Earth ($\Omega_e = 73$ μrad/s), with a short-term sensitivity of about 3×10^{-6} rad/s/$\sqrt{\text{Hz}}$. Furthermore, they showed agreement with theory at the 1% level over a relatively large range of $\pm 2\Omega_e$—corresponding to an improvement by a factor of 10 over the first measurements of Ref. [13]. Some of their experimental results are shown in Fig. 2a.

In contrast to Ref. [15], counter-propagating light pulses were used in Ref. [16] to manipulate a beam of cesium atoms (longitudinal velocity ~ 290 m/s). In this work, the atoms entered a ~ 2-m-long interrogation region where they traversed three pairs of counter-propagating laser beams that drove a $\pi/2 - \pi - \pi/2$ sequence of velocity-selective two-photon Raman transitions between long-lived hyperfine ground states. We explain in detail this interferometer scheme in Section 2.1. Each pair of Raman beams was separated by 0.96 m and aligned perpendicular to the atomic trajectory. By rotating the Raman beams at different rates, an interference pattern was constructed in the number of $|F = 4, m_F = 0\rangle$ atoms at the output of the interferometer, as shown in Fig. 2b. The resulting short-term sensitivity of their rotation measurements was 2×10^{-8} rad/s/$\sqrt{\text{Hz}}$.

Comparing the short-term sensitivity achieved by these two experiments, there seems to be a clear advantage to using light pulses over nano-fabricated transmission gratings to split and recombine the atomic wave packets (although some gain in sensitivity can be attributed the difference in the enclosed area between the two interferometers). The main advantage of using light pulses to interact with the atoms is their versatility and precision. One can easily modify the strength, bandwidth and phase of the light–matter interaction through precise control of the laser parameters. In comparison, nano-fabricated gratings are passive objects that must be carefully handled and placed within the vacuum system—making their modification or replacement much more challenging. For example, to change the phase of the gratings in Ref. [15] by $\pi/2$ requires a

[1] In 1996, Oberthaler et al. [17] also carried out sensitive rotation measurements with atoms using a Moiré deflectometer—a device consisting of an atomic beam and three mechanical gratings that can be considered the classical analog of a matter-wave interferometer. No quantum interference was involved in these measurements.

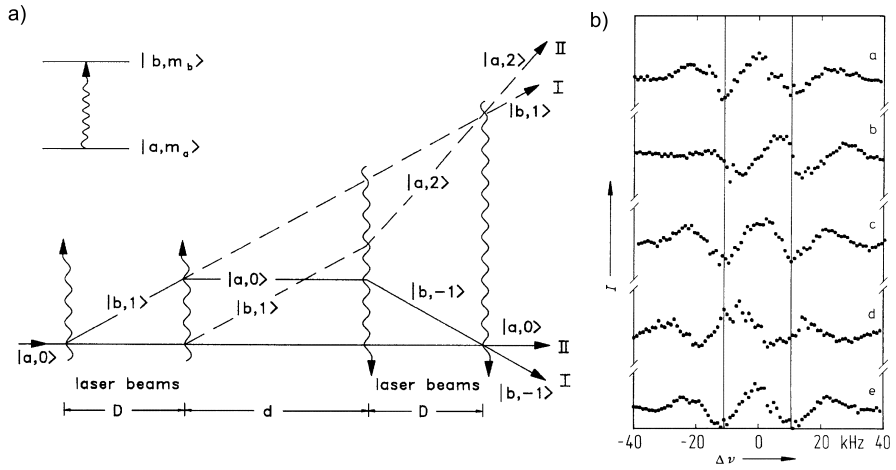

Fig. 1. a) Ramsey–Bordé configuration of a state-labeled atom interferometer based on single-photon transitions. Here, a beam of atoms traverses two pairs of traveling wave fields. The laser fields within each pair are separated by a distance D, while the two pairs are separated by d and are counter-propagating with respect to each other. b) Optical Ramsey fringes measured for the apparatus standing still (curves labeled a, c, and e), for the apparatus rotating at a rate of $\Omega = -90$ mrad/s (curve b), and for a rate $\Omega = +90$ mrad/s (curve d). The center of the Ramsey patterns for $\Omega = \pm 90$ mrad/s are clearly shifted to the right and left, respectively, relative to those for which $\Omega = 0$. Both figures were taken from Ref. [13].[2]
Reprinted with permission from F. Riehle, T. Kisters, A. Witte, J. Helmcke, C.J. Borde, Phys. Rev. Lett. 67 (1991) 177.

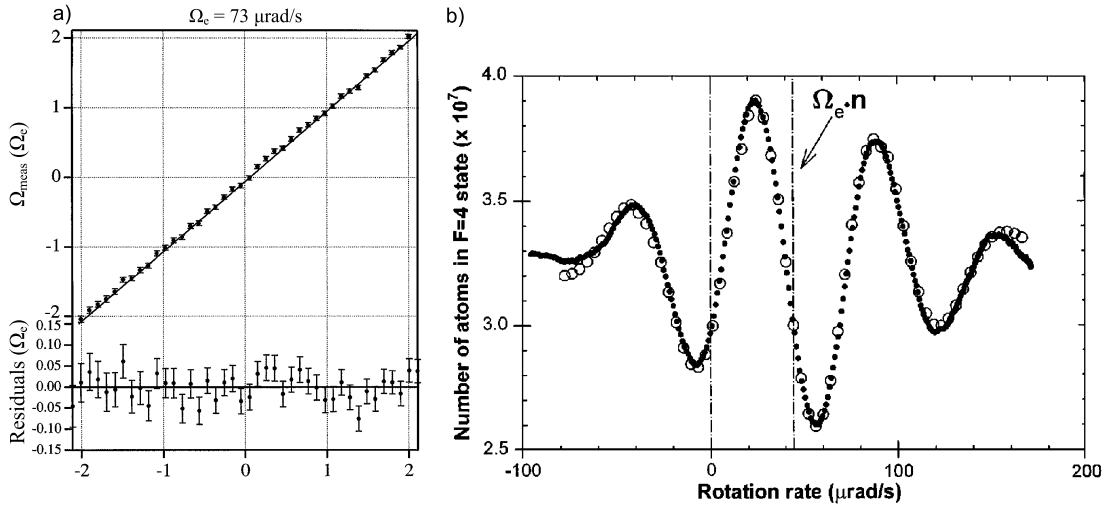

Fig. 2. a) Experimental results from Ref. [15]. Here, the rotation rate inferred from the interferometer, Ω_{meas}, is plotted with respect to the applied rate, Ω, inferred from accelerometers attached to the apparatus. The slope of the linear fit was measured to be 1.008(7). The residuals of the fit are shown below. b) Atomic interference pattern as a function of applied rotation rate from Ref. [16]. The horizontal offset from zero rotation provides a direct measurement of the Earth's rotation rate, Ω_e. (See footnote 2.)
Reprinted with permission from A. Lenef, T. Hammond, E. Smith, M. Chapman, R. Rubenstein, D.E. Pritchard, Phys. Rev. Lett. 78 (1997) 760 and from T.L. Gustavson, P. Bouyer, M.A. Kasevich, Phys. Rev. Lett. 78 (1997) 2046.

physical displacement of only 50 nm perpendicular to the atomic trajectory. Modifying the phase of the light–matter interaction requires no moving parts, and can be done electro-optically with high precision. Furthermore, the use of two Raman lasers allows the use of state-labeling techniques to address the diffracted and undiffracted pathways of the interferometer [9]. Usually, one detects the number of atoms remaining in either state by scattering many photons per atom, and inferring the phase shift from the ratio of state populations. This technique, which is not possible with transmission gratings, is less sensitive to fluctuations in total atom number and exhibits a high signal-to-noise ratio.

[2] Readers may view, browse, and/or download material for temporary copying purposes only, provided these uses are for noncommercial personal purposes. Except as provided by law, this material may not be further reproduced, distributed, transmitted, modified, adapted, performed, displayed, published, or sold in whole or part, without prior written permission from the American Physical Society.

With the conclusion of these proof-of-principle experiments, the study of atomic gyroscopes entered a new phase which focused primarily on developing them as rotation sensors. This meant understanding and reducing sources of noise and systematic error, as well as improving the short-term sensitivity, linearity, long-term stability and accuracy of the devices. Furthermore, there remained a question regarding the type of coherent matter-wave source to design the sensor around: atomic beams or cold atoms. Modern (since the year 2000) atomic rotation sensors and the improvement of their performances will be described below.

The remainder of this article is organized as follows. In Section 2.1, we review the basic operation principles of Sagnac interferometers based on two-photon Raman transitions, which represents the key experimental technique used in modern atomic gyroscopes. Section 2.2 presents two examples of experiments using respectively atomic beam and cold atoms, and the comparison of their performances. Section 2.3 describes the most recent experiments of cold atom Sagnac interferometers. Finally, we give some perspectives for future improvements to these sensors and conclude in Section 3.

2. Atomic rotation sensors

2.1. Principles of atomic Sagnac interferometers

In this section, we describe the basic operation principles of an atom-based gyroscope based on optical two-photon Raman transitions. All light-pulse interferometers work on the principle of momentum conservation between atoms and light. When an atom absorbs (emits) a photon of momentum $\hbar\mathbf{k}$, it undergoes a momentum impulse of $\hbar\mathbf{k}$ ($-\hbar\mathbf{k}$). In the case of Raman transitions, the momentum state of the atom is manipulated between two long-lived electronic ground states. Two laser beams with frequencies ω_1 and ω_2, respectively, are tuned such that their frequency difference, $\omega_1 - \omega_2$, is resonant with a microwave transition between two hyperfine ground states, which we label $|1\rangle$ and $|2\rangle$. When the Raman beams are counter-propagating (*i.e.* when the wave vector $\mathbf{k}_2 \approx -\mathbf{k}_1$), a momentum exchange of approximately twice the single photon momentum accompanies these transitions: $\hbar(\mathbf{k}_1 - \mathbf{k}_2) \approx 2\hbar\mathbf{k}_1$. This results in a strong sensitivity to the Doppler frequency, $\mathbf{k}_{\text{eff}} \cdot \mathbf{v}$, associated with the motion of the atoms, where $\mathbf{k}_{\text{eff}} = \mathbf{k}_1 - \mathbf{k}_2$ is the effective k-vector of the light field. Under appropriate conditions, a Raman laser pulse can split the atom into a superposition of states $|1, \mathbf{p}\rangle$ and $|2, \mathbf{p} + \hbar\mathbf{k}_{\text{eff}}\rangle$ (with a pulse area of $\pi/2$), or it can exchange these two states (with a pulse area of π). With these tools, it is possible to coherently split, reflect and recombine atomic wave packets such that they enclose a physical area—forming an interferometer that is sensitive to rotations.

Fig. 3 shows the most common matter-wave interferometer configuration, which consists of a $\pi/2 - \pi - \pi/2$ sequence of Raman pulses, each separated by a time T (analog to an optical Mach–Zehnder interferometer). If there is a phase shift between the wave packets associated with each internal state at the output of the interferometer, it manifests as a simple sinusoidal variation between the state populations:

$$\frac{N_2}{N_1 + N_2} = \frac{1 - \cos \Phi_{\text{tot}}}{2} \tag{2}$$

Here, N_1 and N_2 are the number of atoms in states $|1, \mathbf{p}\rangle$ and $|2, \mathbf{p} + \hbar\mathbf{k}_{\text{eff}}\rangle$, respectively, and Φ_{tot} is the total phase shift of the interferometer given by:

$$\Phi_{\text{tot}} = \left(\phi_1 - \phi_2^{\text{A}}\right) - \left(\phi_2^{\text{B}} - \phi_3\right) \tag{3}$$

The individual phases, ϕ_i, in this expression are imprinted on the atom by each Raman pulse. They take the form $\phi_i = \mathbf{k}_{\text{eff}}^{(i)} \cdot \mathbf{r}(t_i) + \phi_L^{(i)}$, based on the orientation of the effective k-vector, $\mathbf{k}_{\text{eff}}^{(i)}$, the position of the center of mass of the wave packet, $\mathbf{r}(t_i)$, and the relative phase between the two Raman lasers, $\phi_L^{(i)}$, at the time of the ith pulse, $t = t_i$. The superscripts "A" and "B" on ϕ_2 indicate the upper and lower pathways of the interferometer, respectively, as shown in Fig. 3.

In general, there are two types of interferometer signals that can be detected within the realm of inertial effects: changes in absolute velocity (*i.e.* accelerations) and changes in the velocity vector (*i.e.* rotations). For accelerations, the sensitivity axis of the interferometer is along the propagation axis of the Raman lasers, while for rotations the interferometer is sensitive along an axis perpendicular to the plane defining the enclosed area. The evaluation of interferometer phase shifts in a non-inertial reference frame (accelerating or rotating) has been described in detail in previous publications [8,18–21]. Here, we give an intuitive calculation of the phase shift for an atom interferometer in a frame rotating at a constant rate. Fig. 3 illustrates the situation from the atom's perspective, where the Raman lasers are rotating at a rate Ω. At $t = 0$, the orientation of the Raman beams is rotated by an angle $\theta_1 = -\Omega T$ relative to the propagation axis of the atomic trajectory. Provided that $|\theta_1| \ll 1$, this imprints a phase shift on the atoms of $\phi_1 = k_{\text{eff}}\theta_1 L$. At $t = T$, the Raman beam is perpendicular to the atomic trajectory, thus the rotation-induced phase shift is zero and, in the center-of-mass coordinate frame, it can be shown that $\phi_2^{\text{A}} = -\phi_2^{\text{B}}$. Similarly, at $t = 2T$, the phase is $\phi_3 = -k_{\text{eff}}\theta_3 L$, where $\theta_3 = \Omega T$. Using Eq. (3), the total interferometer phase shift due to the rotation is $\Phi_{\text{rot}} = k_{\text{eff}}(\theta_1 + \theta_3)L = -2k_{\text{eff}}\mathbf{v}\Omega T^2$. Here, we have used the fact that the separation between Raman pulses is $L = \mathbf{v}T$ with $\mathbf{v}$ the initial atomic velocity at the entrance of the interferometer. A more general form of this expression, where the rotation vector $\boldsymbol{\Omega}$ is not necessarily perpendicular to the plane of the interferometer, is given by [18]:

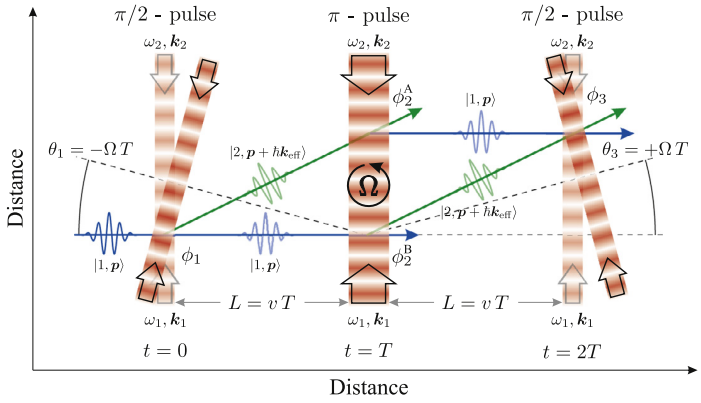

Fig. 3. (Color online.) Schematic of a matter-wave Sagnac interferometer based on two-photon Raman transitions. An atom in state $|1\rangle$, with center-of-mass velocity $\mathbf{v} = \mathbf{p}/M$, is subjected to a sequence of counter-propagating laser pulses that are rotating relative to the atomic trajectory at a constant rate Ω.

$$\Phi_{\text{rot}} = -2(\mathbf{k}_{\text{eff}} \times \mathbf{v}) \cdot \mathbf{\Omega}\, T^2 \tag{4}$$

Clearly, the rotation phase shift scales linearly with $\mathbf{v}$ and Ω, and it scales quadratically with T (or L). This implies that the rotation sensitivity of the matter-wave interferometer scales with the enclosed area—in the same manner as an optical Sagnac interferometer. In fact, Eq. (4) can be recast to highlight this area dependence by defining the area vector as $\mathbf{A} = -(\hbar\mathbf{k}_{\text{eff}}/M)T \times \mathbf{v}T$. Then $\Phi_{\text{rot}} = 2M\mathbf{A} \cdot \mathbf{\Omega}/\hbar$, which is equivalent to the Sagnac phase for matter waves given by Eq. (1).

2.2. Space-domain or time-domain atom interferometers: atomic beams versus cold atoms

Following Eq. (4), two strategies exist for maximizing the sensitivity of the rotation sensor: increasing the atomic velocity, *i.e.* increasing the distance $L = \mathbf{v}T$ between the beam splitters, or increasing the interrogation time T. The former requires an atomic beam source and will be referred to as a space-domain interferometer. In this configuration, the Raman lasers are running continuously and the Sagnac area is defined, in practice, by physical quantities L and $\mathbf{v}$ (area proportional to $L^2/\mathbf{v}$). The latter will instead work in the time domain and requires the use of cold atoms that can be interrogated for sufficiently long times (typically 100 ms). In this second configuration, the Raman lasers are pulsed in order to define the interaction time with the atoms, and the Sagnac area is defined by physical quantities T and $\mathbf{v}$ (area proportional to $\mathbf{v}T^2$). We will give two examples of such experiments.

Space-domain interferometers with an atomic beam: Refs. [22,23] By the early 2000s, Sagnac interferometers based on atomic beams had been significantly improved compared to the first experiments in the 1990s [13,15,16]. Specifically, the work of Gustavson et al. [22] at Yale helped realize short-term sensitivities of $\sim 6 \times 10^{-10}$ rad/s/$\sqrt{\text{Hz}}$. This gain in sensitivity arose mainly due to the implementation of a high-flux atom source. Moreover, it solved for the first time the problem of discriminating between phase shifts from rotation and from acceleration by the implementation of a counter-propagating atomic beam geometry. Since the sign of the rotation-induced phase shift given by Eq. (4) depends on the velocity vector, reversing the direction of the atomic beam results in a phase shift with opposite sign. Thus, by measuring the interference fringes from two separate counter-propagating sources, one can suppress via common-mode rejection parasitic phase shifts arising, for example, from the acceleration due to gravity or vibrations of the Raman laser optics.

In an effort to further reduce systematic effects and improve the long-term accuracy of the gyroscope, an additional technique was later introduced by Durfee et al. [23] at Stanford to eliminate spurious non-inertial phase shifts, such as those produced by magnetic fields or ac Stark effects. This involved periodically reversing the direction of $\mathbf{k}_{\text{eff}}$ between measurements of the two interference signals from each atomic beam, which facilitated a sign reversal of the inertial phase while maintaining the sign of the non-inertial phase. Combining these four signals drastically reduced systematic shifts and long-term drift of rotation phase measurements (stability of $\sim 2.5 \times 10^{-9}$ rad/s in 15 min), at the cost of the short-term sensitivity. Further correlation analysis with measured environmental variables, such as temperature, indicate that the long-term sensitivity could considerably be reduced to $\sim 3 \times 10^{-10}$ rad/s in 5 h [23] by a correction proportional to those measurements, as shown in Fig. 4b.

Time-domain interferometers with laser cooled atoms: Refs. [24,25] In contrast to atomic gyroscopes using the propagation of atomic beams over meter-long distances, cold atom interferometers make use of the T^2 scaling of the gyroscope sensitivity by interrogating laser-cooled atoms during ~ 100 ms. They allow for more compact setups and for a better control of atomic trajectories and thus of systematic effects. A pioneering experiment that started at SYRTE (France) in the early 2000s used two counter-propagating clouds of cesium atoms launched in strongly curved parabolic trajectories. Three single Raman beam pairs, pulsed in time, were successively applied in three orthogonal directions leading to the measurement of the three

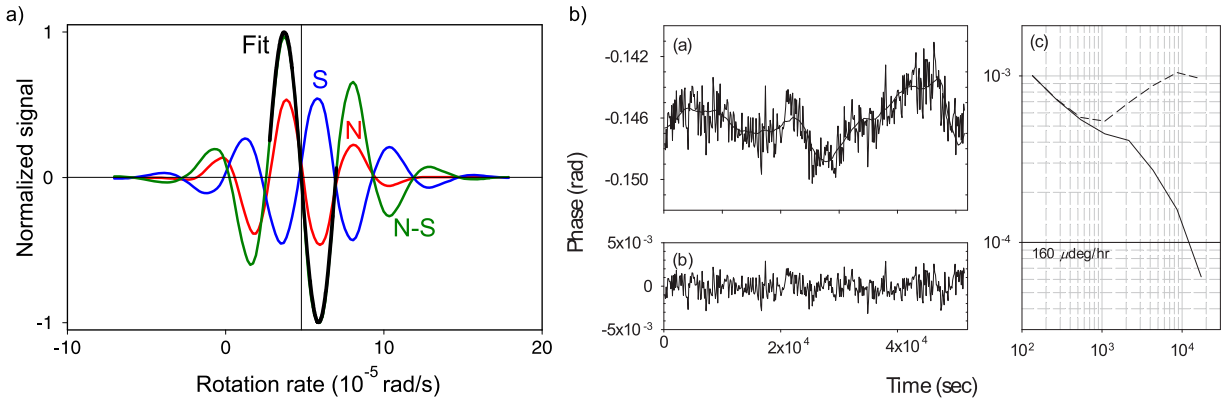

Fig. 4. (Color online.) Space-domain interferometer with an atomic beam. a) Interference fringes from the counter-propagating atomic beam experiments in Ref. [22] (figure adapted from [22]). Here, the fringes labeled "N" and "S" are from north- and south-facing beams, respectively, while the difference is labeled "N–S". A fit to this signal, shown as the solid black line, gives an estimate of the Earth's rotation rate where the line crosses zero. b) Rotation phase measurements recorded over 14 h from Ref. [23]. The middle plot labeled "(a)" shows the raw measurements compensated with k-reversal, along with a fit to sum of five independent temperature measurements (solid line). Plot "(b)" shows the temperature-compensated phase, and "(c)" is the Allan deviation of the rotation signal (dashed line: Allan deviation of the uncorrected data, solid line: Allan deviation of the corrected data). (See footnote 2.)
Fig. 4b is reprinted with permission from D.S. Durfee, Y.K. Shaham, M.A. Kasevich, Phys. Rev. Lett. 97 (2006) 240801.

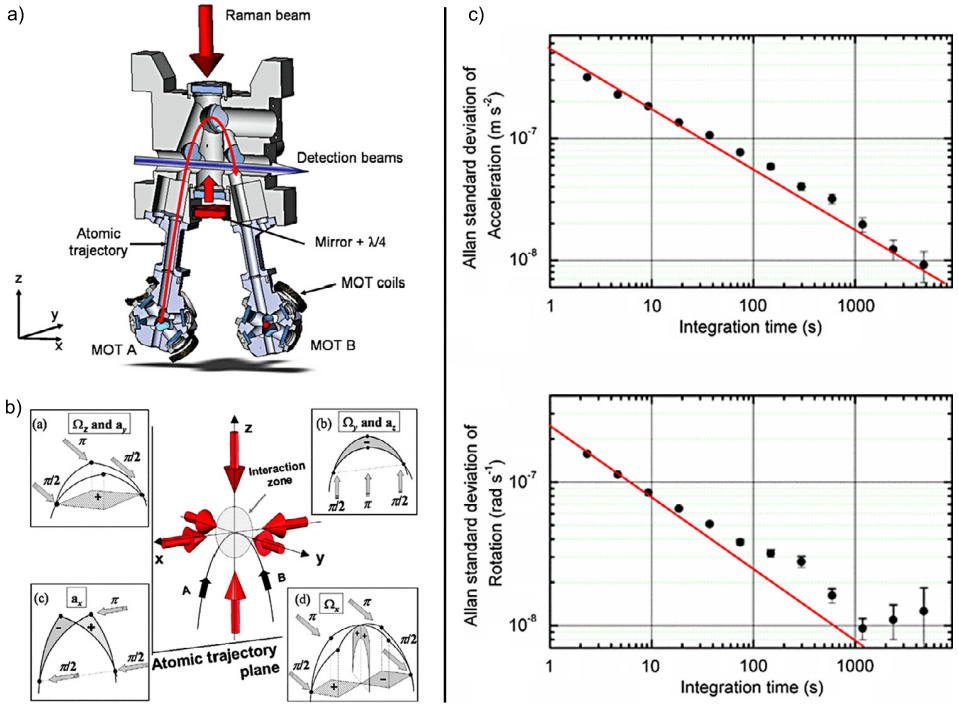

Fig. 5. (Color online.) a) Schematic of the SYRTE atomic gyroscope–accelerometer experiment using two cold atom clouds, from Ref. [25]. b) Interferometer configurations leading to information on the three axes of inertia, from Ref. [24]. Performances of the accelerometer-gyroscope obtained in 2009 by Gauguet et al. [25]. c) The acceleration sensitivity is limited by residual vibrations of the platform (top panel), while the rotation measurement is limited by quantum projection noise (bottom panel).

axes of rotation and acceleration, thereby providing a full inertial base [24]. The SYRTE atomic gyroscope–accelerometer experiment is shown in Fig. 5a. Fig. 5b presents the various interrogation configurations that enable extraction of the three components of acceleration and rotation. The short-term acceleration and rotation sensitivity of the instrument (with 1 s of integration) was first 4.7×10^{-6} m/s^2 and 2.2×10^{-6} rad/s in the work of Canuel et al. [24], respectively. The setup (in particular the detection system and atom source preparation) was then improved to reach the quantum projection noise limit on the rotation measurement at the level of 2.4×10^{-7} rad/s/$\sqrt{\text{Hz}}$, and a long-term sensitivity of 1×10^{-8} rad/s at 1000 s integration time [see Fig. 5c, bottom panel], which was ultimately limited by the fluctuation of the atomic trajectories due

Table 1
Comparison of gyroscope properties for systems based on cold atoms and atomic beams. The Yale (2000) experiment demonstrated exceptional short term sensitivity but did not demonstrate long-term stability [22]. The short term sensitivity of the Stanford (2006) experiment is extrapolated back to one second using the long-term stability of 2.5×10^{-9} rad/s and assuming a rotation rate stability scaling as $1/\sqrt{\tau}$ from Ref. [23].

Domain	Time (SYRTE, 2009)	Space (Yale, 2000/Stanford, 2006)
Atomic source	MOT	Atomic beam
Flux	Low	High
Sagnac area	4 mm^2	24 mm^2
Velocity	33 cm/s	290 m/s
Interferometer length	2.7 cm	2 m
Sensor size	0.5 m	2.5 m
Velocity control	Good (molasses)	Poor (Oven)
T control	Very good	Poor ($T = L/\mathbf{v}$)
Acceleration sensitivity	Very high (large T)	Moderate
Acceleration rejection	Very good (T symmetric)	Moderate (asymmetry in $\mathbf{v}$)
Wavefront distortion limited	Yes	Probably
Short-term sensitivity (1 s)	2.3×10^{-7} rad/s/Hz$^{1/2}$	Yale (2000): 6×10^{-10} rad/s/Hz$^{1/2}$ Stanford (2006): 8×10^{-8} rad/s/Hz$^{1/2}$
Long-term sensitivity (15 min)	1.0×10^{-8} rad/s	Yale (2000): not specified Stanford (2006): 2.5×10^{-9} rad/s

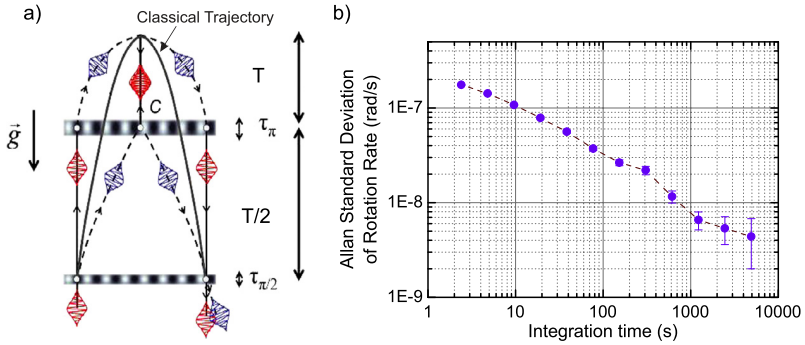

Fig. 6. (Color online.) a) Atomic trajectories of the SYRTE four-pulse interferometer from Ref. [26]. b) The Allan deviation of rotation rate measurements for an interrogation time $2T = 480$ ms. The preliminary results indicate a sensitivity of 4×10^{-9} rad/s with 5000 s of integration time.

to wavefront distortions of the Raman lasers [25]. Two other important features of this device had been tested: the linearity with the rotation rate and the independence of the rotation measurement from the acceleration. First, the evaluation of the non-linearities from a quadratic estimation of the scaling factor evolution has been demonstrated to be below 10^{-5}. Second, the effect of the acceleration on the rotation phase shift is canceled at a level better than 76 dB when adding a well-controlled DC acceleration on the apparatus.

To conclude this section, we present in Table 1 a comparison of the gyroscopes using atomic beams and cold atoms. Although the geometries are very different, the final sensitivity levels are similar (atomic beams show increased sensitivity by a factor of ~ 3). Furthermore, cold atoms offer better control of systematic effects and more compact setups with margins of improvements by an optimization of the geometry. In particular, an improvement of both short-term and long-term stabilities should arise from a larger average velocity, which was chosen to be very small in this first experiment (33 cm/s). In the next section, we present the new generation of cold atom experiments since 2009 aiming at improving the performances by more than one order of magnitude.

2.3. Latest generation of cold atom gyroscopes [26–30]

Following the experiments discussed previously, the strategy to enhance the sensitivity of the gyroscope essentially consists in increasing the interferometer area. Two geometries have been developed so far. First, keeping the same three Raman pulses configuration, but with a straighter horizontal trajectory ($\mathbf{v} = 2.8$ m/s), the gyroscope of the University of Hannover [28] has an area five times larger (19 mm^2) with preliminary results [30] similar to those of SYRTE.

The second solution is based on four Raman light pulses and an atom cloud following a vertical trajectory [see Fig. 6a]. In that case, the atom interrogation is symmetric with respect to the apogee of the atom trajectory and is not sensitive to the DC acceleration. This new geometry was first demonstrated in Ref. [24] and has shown improved performances in Ref. [27]. Since the interferometer phase shift scales as $\Phi_{\text{rot}} \sim k_{\text{eff}} g\, \Omega\, T^3$, and the maximum possible area is 300 times larger (11 cm^2 with a total interrogation time of $2T = 800$ ms), substantial improvements in sensitivity are anticipated. Preliminary results presented in Fig. 6b have already shown a short-term sensitivity similar to the one obtained in the

three-pulse configuration (improved by one order of magnitude compared to the previous four-pulse experiment), as well as an improvement in long-term stability to 4×10^{-9} rad/s in 5000 s of integration time.

The present limit to the sensitivity arises from vibration noise of the Raman beam retro-reflecting mirrors at frequencies higher than those of the rotation signal of interest (which has a characteristic time scale of variation of several hours). The impact of the Raman mirror vibrations is a commonly encountered problem in cold atom inertial sensors and has been addressed in various works, e.g. in atomic gravimeters [31]. The corresponding limit to the sensitivity arises from the dead time between consecutive measurements (due to the cold atom cloud preparation and detection), which results in an aliasing effect when the high-frequency noise is projected onto the measurements. In other words, the dead time corresponds to a loss of information on the vibration noise spectrum, making it difficult to remove from the measurements.

3. Conclusion and perspectives

After the first proof-of-principle experiments in the early 1990s, Sagnac interferometry with matter-waves has benefited from the important progress of atomic physics in the last 20 years. These advances have allowed the continuous improvement in performances of atomic gyroscopes in terms of sensitivity, long-term stability, linearity and accuracy, making atomic setups competitive or better than state-of-the-art commercial laser gyroscopes. These improvements are motivated by possible applications in inertial guidance and in geophysics. Both space- and time-domain interferometers have their own advantages. For space-domain interferometers with atomic beams this includes zero dead time between measurements, high dynamic range and a relative simplicity, versus better control of the scaling factor and smaller size for time-domain interferometers with cold atoms.

For applications in inertial navigation, the use of straight horizontal trajectories [28] is more favorable than highly curved parabolic trajectories [25]. On the one hand, using horizontal trajectories with fast atoms reduces the interrogation time T, thereby reducing the acceleration sensitivity (scaling as T^2), while keeping a high Sagnac scale factor (proportional to the atomic velocity), thus optimizing the ratio of rotation sensitivity over residual acceleration sensitivity. On the other hand, as demonstrated in the optical domain by laser-based gyroscopes [32], very-large-area atom interferometers based on highly curved parabolic trajectories [26,29] are of important potential interest in the field of geophysics. In the latter case, the possibility to measure rotation rates and accelerations simultaneously is advantageous in order to distinguish between fluctuations of the Earth's rotation rate and fluctuations of the projection of this rate on the measurement axis of the gyroscope. Another possibility for enhancing the Sagnac interferometer area could consist in transferring a large momentum to the atoms during the matter-wave diffraction process. Such large momentum transfer beam splitters, studied since 2008 by several groups, could result in more compact Sagnac cold atom gyroscopes of reduced interrogation times.

Nevertheless, the main limitation on increasing the sensitivity of time-domain interferometers in both applications (inertial navigation and geophysics) comes from aliasing of high-frequency noise due to measurement dead times. One solution consists in increasing the measurement repetition rate [33], but at the cost of a reduction of the interrogation time and, consequently, the sensitivity. A second method could consist in hybridizing a conventional optical gyroscope with the atom interferometer in order to benefit from the large bandwidth of the former, and the long-term stability and accuracy of the latter. This method has been demonstrated in the case of the measurement of a component of acceleration by hybridizing a classical accelerometer and an atomic gravimeter [31,34]. Another possibility could consist in operating a cold-atom interferometer without dead time between successive measurements in a so-called joint interrogation scheme [35,29].

Besides the improvement of these Sagnac interferometers using atoms in free fall, the development of confined ultra-cold atomic sources opens the way for new types of matter-wave Sagnac interferometers in which the atoms are sustained or guided [36,37]. Under these conditions, the interrogation time should no longer be limited by the free-fall time of the atoms in the vacuum system, and larger interferometer areas can be achieved. The present limitation on long-term stability due to wavefront distortions of the Raman laser could be lifted, since the position of the atoms will be well controlled. In contrast, the interaction with the guide or between ultra-cold atoms should bring new systematic effects that will require further study.

Acknowledgements

This work is supported by Délégation générale pour l'armement grant REI n° 2010.34.0005 and the French space agency CNES (Centre national d'etudes spatiales). B. Barrett and I. Dutta also thank CNES and FIRST-TF for financial support. The laboratory SYRTE is part of the Institut francilien pour la recherche sur les atomes froids (IFRAF) supported by the Région Île-de-France.

References

[1] A. Lawrence, Modern Inertial Technology, Springer, New York, 1998.
[2] H. Igel, A. Cauchard, J. Wassermann, A. Flaws, U. Schreiber, A. Velikoseltsev, N.P. Dinh, Broad-band observations of earthquake-induced rotational ground motions, Geophys. J. Int. 168 (2007) 182, http://dx.doi.org/10.1111/j.1365-246X.2006.03146.x, http://gji.oxfordjournals.org/content/168/1/182.short.
[3] C.M. Will, The confrontation between general relativity and experiment, Living Rev. Relativ. 9 (2006) 3, http://dx.doi.org/10.12942/lrr-2006-3, http://www.livingreviews.org/lrr-2006-3.
[4] G. Sagnac, L'éther lumineux démontré par l'effet du vent relatif d'éther dans un interféromètre en rotation uniforme, C.R. Acad. Sci. 157 (1913) 708.

[5] R. Anderson, H.R. Bilger, G.E. Stedman, “Sagnac” effect: a century of Earth-rotated interferometers, Am. J. Phys. 62 (1994) 975, http://dx.doi.org/10.1119/1.17656, http://scitation.aip.org/content/aapt/journal/ajp/62/11/10.1119/1.17656.
[6] C.J. Bordé, J. Sharma, P. Tourrenc, T. Damour, Theoretical approaches to laser spectroscopy in the presence of gravitational fields, J. Phys. Lett. 44 (1983) 983, http://dx.doi.org/10.1051/jphyslet:019830044024098300, http://jphyslet.journaldephysique.org/articles/jphyslet/abs/1983/24/jphyslet_1983__44_24_983_0/jphyslet_1983__44_24_983_0.html.
[7] V. Chebotayev, B. Dubetsky, A. Kasantsev, V. Yakovlev, Interference of atoms in separated optical fields, J. Opt. Soc. Am. B 2 (1985) 1791, http://dx.doi.org/10.1364/JOSAB.2.001791, http://www.opticsinfobase.org/josab/abstract.cfm?uri=josab-2-11-1791.
[8] J.F. Clauser, Ultra high sensitivity accelerometers and gyroscopes using neutral atom matter wave interferometry, Phys. B C 151 (1988) 262, http://dx.doi.org/10.1016/0378-4363(88)90176-3, http://www.sciencedirect.com/science/article/pii/0378436388901763.
[9] C.J. Bordé, Atom interferometry with internal state labelling, Phys. Lett. A 140 (1989) 10, http://dx.doi.org/10.1016/0375-9601(89)90537-9, http://www.sciencedirect.com/science/article/pii/0375960189905379.
[10] O. Carnal, J. Mlynek, Young's double-slit experiment with atoms: a simple atom interferometer, Phys. Rev. Lett. 66 (1991) 2689, http://dx.doi.org/10.1103/PhysRevLett.66.2689, http://link.aps.org/doi/10.1103/PhysRevLett.66.2689.
[11] D.W. Keith, C.R. Ekstrom, Q.A. Turchette, D.E. Pritchard, An interferometer for atoms, Phys. Rev. Lett. 66 (1991) 2693, http://dx.doi.org/10.1103/PhysRevLett.66.2693, http://link.aps.org/doi/10.1103/PhysRevLett.66.2693.
[12] M.A. Kasevich, S. Chu, Atomic interferometry using stimulated Raman transitions, Phys. Rev. Lett. 67 (1991) 181, http://dx.doi.org/10.1103/PhysRevLett.67.181, http://link.aps.org/doi/10.1103/PhysRevLett.67.181.
[13] F. Riehle, T. Kisters, A. Witte, J. Helmcke, C.J. Borde, Optical Ramsey spectroscopy in a rotating frame: Sagnac effect in a matter-wave interferometer, Phys. Rev. Lett. 67 (1991) 177, http://dx.doi.org/10.1103/PhysRevLett.67.177, http://link.aps.org/doi/10.1103/PhysRevLett.67.177.
[14] A. Cronin, J. Schmiedmayer, D.E. Pritchard, Optics and interferometry with atoms and molecules, Rev. Mod. Phys. 81 (2009) 1051, http://dx.doi.org/10.1103/RevModPhys.81.1051, http://link.aps.org/doi/10.1103/RevModPhys.81.1051.
[15] A. Lenef, T. Hammond, E. Smith, M. Chapman, R. Rubenstein, D.E. Pritchard, Rotation sensing with an atom interferometer, Phys. Rev. Lett. 78 (1997) 760, http://dx.doi.org/10.1103/PhysRevLett.78.760, http://link.aps.org/doi/10.1103/PhysRevLett.78.760.
[16] T.L. Gustavson, P. Bouyer, M.A. Kasevich, Precision rotation measurements with an atom interferometer gyroscope, Phys. Rev. Lett. 78 (1997) 2046, http://dx.doi.org/10.1103/PhysRevLett.78.2046, http://link.aps.org/doi/10.1103/PhysRevLett.78.2046.
[17] M.K. Oberthaler, S. Bernet, E.M. Rasel, J. Schmiedmayer, A. Zeilinger, Inertial sensing with classical atomic beams, Phys. Rev. A 54 (1996) 3165, http://dx.doi.org/10.1103/PhysRevA.54.3165, http://link.aps.org/doi/10.1103/PhysRevA.54.3165.
[18] P. Storey, C. Cohen-Tannoudji, The Feynman path integral approach to atomic interferometry. A tutorial, J. Phys. II 4 (1994) 1999, http://dx.doi.org/10.1051/jp2:1994103, http://jp2.journaldephysique.org/articles/jp2/abs/1994/11/jp2v4p1999/jp2v4p1999.html.
[19] C.J. Bordé, Theoretical tools for atom optics and interferometry, C.R. Acad. Sci., Ser. IV 2 (2001) 509.
[20] C.J. Bordé, Atomic clocks and inertial sensors, Metrologia 39 (2002) 435, http://dx.doi.org/10.1088/0026-1394/39/5/5, http://iopscience.iop.org/0026-1394/39/5/5/pdf/0026-1394_39_5_5.pdf.
[21] C. Antoine, C.J. Bordé, Exact phase shifts for atom interferometry, Phys. Lett. A 306 (2003) 277, http://dx.doi.org/10.1016/S0375-9601(02)01625-0, http://www.sciencedirect.com/science/article/pii/S0375960102016250.
[22] T.L. Gustavson, A. Landragin, M.A. Kasevich, Rotation sensing with a dual atom-interferometer Sagnac gyroscope, Class. Quantum Gravity 17 (2000) 2385, http://dx.doi.org/10.1088/0264-9381/17/12/311, http://iopscience.iop.org/0264-9381/17/12/311/.
[23] D.S. Durfee, Y.K. Shaham, M.A. Kasevich, Long-term stability of an area-reversible atom-interferometer Sagnac gyroscope, Phys. Rev. Lett. 97 (2006) 240801, http://dx.doi.org/10.1103/PhysRevLett.97.240801, http://link.aps.org/doi/10.1103/PhysRevLett.97.240801.
[24] B. Canuel, F. Leduc, D. Holleville, A. Gauguet, J. Fils, A. Virdis, A. Clairon, N. Dimarcq, C.J. Bordé, A. Landragin, P. Bouyer, Six-axis inertial sensor using cold-atom interferometry, Phys. Rev. Lett. 97 (2006) 010402, http://dx.doi.org/10.1103/PhysRevLett.97.010402, http://link.aps.org/doi/10.1103/PhysRevLett.97.010402.
[25] A. Gauguet, B. Canuel, T. Lévèque, W. Chaibi, A. Landragin, Characterization and limits of a cold-atom Sagnac interferometer, Phys. Rev. A 80 (2009) 063604, http://dx.doi.org/10.1103/PhysRevA.80.063604, http://link.aps.org/doi/10.1103/PhysRevA.80.063604.
[26] T. Lévèque, Développement d'un gyromètre à atomes froids de haute sensibilité fondé sur une géométrie repliée, Ph.D. thesis, Université Pierre-et-Marie-Curie, Paris-6, 2010.
[27] J. Stockton, K. Takase, M.A. Kasevich, Absolute geodetic rotation measurement using atom interferometry, Phys. Rev. Lett. 107 (2011) 133001, http://dx.doi.org/10.1103/PhysRevLett.107.133001, http://link.aps.org/doi/10.1103/PhysRevLett.107.133001.
[28] G. Tackmann, P. Berg, C. Schubert, S. Abend, M. Gilowski, W. Ertmer, E.M. Rasel, Self-alignment of a compact large-area atomic Sagnac interferometer, New J. Phys. 14 (2012) 015002, http://dx.doi.org/10.1088/1367-2630/14/1/015002, http://iopscience.iop.org/1367-2630/14/1/015002.
[29] M. Meunier, Étude d'un gyromèetre à ondes de matière de très grande aire, Ph.D. thesis, Université Pierre-et-Marie-Curie, Paris-6, 2013.
[30] G. Tackmann, P. Berg, S. Abend, C. Schubert, W. Ertmer, E.M. Rasel, Large area Sagnac atom interferometer with robust phase read out, C. R. Physique 15 (2014) 884–897, in this issue.
[31] J. Lautier, L. Volodimer, T. Hardin, S. Merlet, M. Lours, F. Pereira Dos Santos, A. Landragin, Hybridizing matter-wave and classical accelerometers, Appl. Phys. Lett. 105 (2014) 144102, http://dx.doi.org/10.1063/1.4897358, http://scitation.aip.org/content/aip/journal/apl/105/14/10.1063/1.4897358.
[32] K.U. Schreiber, T. Klügel, J.-P.R. Wells, R.B. Hurst, A. Gebauer, How to detect the chandler and the annual wobble of the earth with a large ring laser gyroscope, Phys. Rev. Lett. 107 (2011) 173904, http://dx.doi.org/10.1103/PhysRevLett.107.173904, http://link.aps.org/doi/10.1103/PhysRevLett.107.173904.
[33] A.V. Rakholia, H.J. McGuinness, G.W. Biedermann, Dual-axis, high data-rate atom interferometer via cold ensemble exchange, arXiv:1407.3847, 2014.
[34] J. Lautier, Développement d'un accéléromètre atomique compact pour la gravimétrie de terrain et la navigation inertielle, Ph.D. thesis, Université Pierre-et-Marie-Curie, Paris-6, 2014.
[35] M. Meunier, I. Dutta, R. Geiger, C. Guerlin, C. Garrido-Alzar, A. Landragin, Stability enhancement by joint phase measurements in a single cold atomic fountain, Aug. 2014, submitted for publication.
[36] S. Wu, E. Su, M. Prentiss, Demonstration of an area-enclosing guided-atom interferometer for rotation sensing, Phys. Rev. Lett. 99 (2007) 173201, http://dx.doi.org/10.1103/PhysRevLett.99.173201, http://link.aps.org/doi/10.1103/PhysRevLett.99.173201.
[37] C.L. Garrido-Alzar, W. Yan, A. Landragin, Towards high sensitivity rotation sensing using an atom chip, in: Research in Optical Sciences, OSA Technical Digest (Optical Society of America 2012), JT2A.10, 2012, http://dx.doi.org/10.1364/HILAS.2012.JT2A.10, http://www.opticsinfobase.org/abstract.cfm?URI=HILAS-2012-JT2A.10.

Matter-wave laser Interferometric Gravitation Antenna (MIGA): New perspectives for fundamental physics and geosciences

R. Geiger[1], L. Amand[1], A. Bertoldi[2], B. Canuel[2], W. Chaibi[4], C. Danquigny[5,6], I. Dutta[1], B. Fang[1], S. Gaffet[3], J. Gillot[2], D. Holleville[1], A. Landragin[1], M. Merzougui[4], I. Riou[2], D. Savoie[1] and P. Bouyer[2]

[1]*SYRTE, Observatoire de Paris, PSL Research University, CNRS, Sorbonne Universités, UPMC Univ. Paris 06, LNE, 61 avenue de lObservatoire, 75014 Paris, France*

[2]*LP2N, Laboratoire de Photonique Numérique et Nanosciences, Institut d'Optique Graduate School IOA, Rue Francois Mitterrand, 33400 Talence, France*

[3]*LSBB, UMS UNS, UAPV, CNRS, 84400 Rustrel, France*

[4]*ARTEMIS Observatoire de la Côte dAzur, Boulevard de l'Observatoire CS 34229, 06304 Nice Cedex 04, France*

[5]*UAPV, UMR1114 EMMAH, F-84000 Avignon, France*

[6]*INRA, UMR1114 EMMAH, F-84914 Avignon, France*

The MIGA project aims at demonstrating precision measurements of gravity with cold atom sensors in a large scale instrument and at studying the associated powerful applications in geosciences and fundamental physics. The firt stage of the project (2013-2018) will consist in building a 300-meter long optical cavity to interrogate atom interferometers and will be based at the low noise underground laboratory LSBB based in Rustrel, France. The second stage of the project (2018-2023) will be dedicated to science runs and data analyses in order to probe the spatio-temporal structure of the local gravity field of the LSBB region, which represents a generic site of hydrological interest. MIGA will also assess future potential applications of atom interferometry to gravitational wave detection in the frequency band $\sim 0.1 - 10$ Hz hardly covered by future long baseline optical interferometers. This paper presents the main objectives of the project, the status of the construction of the instrument and the motivation for the applications of MIGA in geosciences. Important results on new atom interferometry techniques developed at SYRTE in the context of MIGA and paving the way to precision gravity measurements are also reported.

1 Introduction

After more than 20 years of fundamental research, atom interferometers have reached sensitivity and accuracy levels competing with or beating inertial sensors based on different technologies. Atom interferometers offer interesting applications in geophysics (gravimetry, gradiometry, Earth rotation rate measurements), inertial sensing (submarine or aircraft autonomous positioning), metrology (new definition of the kilogram) and fundamental physics (tests of the standard model, tests of general relativity). Atom interferometers already contributed significantly to fundamental physics by, for example, providing stringent constraints on quantum-electrodynamics through measurements of the hyperfine structure constant [1], testing the Equivalence Principle with cold atoms [2], or providing new measurements for the Newtonian gravitational constant [3].

Cold atom sensors have moreover been established as key instruments in metrology for the new definition of the kilogram [4] or through international comparisons of gravimeters [5]. The field of atom interferometry (AI) is now entering a new phase where very high sensitivity levels must be demonstrated, in order to enlarge the potential applications outside atomic physics laboratories. These applications range from gravitational wave (GW) detection in the $[0.1 - 10$ Hz$]$ frequency band to next generation ground and space-based Earth gravity field studies to precision gyroscopes and accelerometers.

The Matter-wave laser Interferometric Gravitation Antenna (MIGA) project will explore the use of AI techniques to build a large-scale matter-wave sensor which will open new applications in geoscience and fundamental physics. The MIGA consortium gathers 15 expert French laboratories and companies in atomic physics, metrology, optics, geosciences and gravitational physics, with the aim to build a large-scale underground atom-interferometer instrument by 2018 and operate it till at least 2023. In this paper, we present the main objectives of the project, the status of the construction of the instrument and the motivation for the applications of MIGA in geosciences. Important results on new atom interferometry techniques developed at SYRTE in the context of MIGA and paving the way to precision gravity measurements are also reported.

2 MIGA principle and sensitivity

The AI geometry of MIGA is similar to the one of a Mach-Zenhder Interferometer for optical waves. The geometry is described in Fig. 1a) where matter waves are manipulated by a set of counter- propagating laser pulses. At the input of the interferometer, a $\pi/2$ pulse creates an equiprobable coherent superposition of two different momentum states of the atom. The matter-waves are then deflected by the use of π pulse before being recombined with a second $\pi/2$ pulse. To realize these beam-splitters and mirror pulses, MIGA will make use of Bragg diffraction of matter-waves on light standing waves [6]. Conservation of energy-momentum during this process imposes to couple only atomic states of momentum $|+\hbar k\rangle$ to state $|-\hbar k\rangle$ where $k = 2\pi\nu_0/c$ is the wave vector of the interrogation field. At the output of the interferometer, the transition probability between these states is obtained by a two waves interference formula $P = \frac{1}{2}(1 + \cos\phi)$. The atom phase shift ϕ depends on the phase difference between the two couterpropagating lasers which is imprinted on the diffracted matter-wave during the light pulse. MIGA will make use of a set of such AIs interrogated by the resonant field of an optical cavity as described in Fig. 1b). In this configuration, each AI will measure the inertial effects $s_X(X_i)$ along the cavity axis at position X_i together with GW effects associated to the cavity propagation of the interrogation laser. Spurious effects such as fluctuations of the cavity mirror position $x_1(t)$ and $x_2(t)$ or laser frequency noise $\delta\nu(t)$ also affect the AI signal. Taking into account these different effects, the atom phase shift $\phi(X_i)$ measured by the AI at position X_i reads:

$$\phi(X_i) = 2ks_{x2} + 2k\left(\frac{s_{\delta\nu}}{\nu_0} + \frac{s_h}{2}\right)(X_i - L) + 2ks_X(X_i) \tag{1}$$

where h is the GW strain amplitude, L is the mean cavity length and s_u accounts for the convolution of the time-fluctuations of effect $u(t)$ by the AI sensitivity function $s(t)$ [7]. The last term in Eq. (1) accounts for the acceleration of the center of mass of the free falling atom cloud which depends on the local position of the AI because of the non-homogeneous gravitational field. Common mode rejection between the AI signals at different positions will enable to cancel out most of the contribution of cavity mirror position fluctuations s_{x2}. The influence of laser frequency noise will be kept negligible in the first version of the MIGA instrument (till 2023) by using state-of-the-art ultra stable laser techniques, yielding relative stabilities better than $\delta\nu/\nu_0 \sim 10^{-15}$. Eq. (1) thus shows that the instrument can be used for local monitoring of mass motion encoded in the last term s_X and, in the future, for GW detection without being affected by position noise of the optics.

The last term of Eq. (1) can be written as $\phi(X) = 2ka(X)T^2$ where $a(X)$ is the local acceleration of gravity of the atoms at position X and T is the time between the light pulses in a 3 light pulse geometry (see Fig. 1a)). For two AI separated by the baseline $L = X_2 - X_1$ and assuming a constant gravity gradient γ, the gradiometer sensitivity of the instrument is given by $\sigma_\gamma = \sigma_\phi/(2kLT^2\sqrt{\tau})$ where σ_ϕ is the AI phase sensitivity and τ the integration time. For $L = 100$ m, a shot-noise limited AI with 10^6 atoms (1 mrad phase sensitivity) and $T = 0.5$ s yields a gradiometer sensitivity of 2.4×10^{-13} s^{-2} after $\tau = 100$ s of measurement time, which corresponds to a mass anomaly of few tons (of water) in a 100 meter region around the instrument. Combining the different measurements provided by the different AIs of the array allows better positioning the mass anomaly and potentially following its motion.

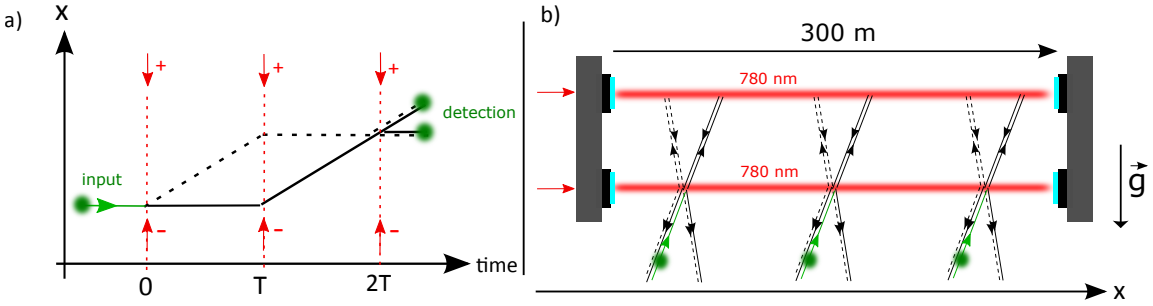

Figure 1 – **MIGA geometry.** a) Schematic of the 3 pulse atom interferometer. Two laser beams propagating in opposite directions are used to split and recombine the matter waves. The atoms are detected at the output using fluorescence detection. b) Sketch of the MIGA baseline: 3 atom interferometers are interrogated by the 780 nm laser beams resonating inside two optical cavities and operating in parallel.

3 MIGA subsytems

3.1 Cold atom source

The atom source unit delivers cold atom clouds which will be interrogated by the MIGA cavity Bragg beams to form the atom interferometer (AI). The general design of the unit is presented in Fig. 2. Its main functions are *(i)* the loading and laser cooling of ^{87}Rb atoms, *(ii)* the launching of the atomic cloud along a quasi-vertical trajectory and the control of the angle of the trajectory with respect to the cavity beams, *(iii)* the preparation of the cold atom source before it enters the interferometer, and *(iv)* the detection of the atoms at the interferometer output.

In order to optimize the contrast of the atom interferometer, the quantum state of the atoms is prepared on their way up, before the interrogation region. A first counter-propagating velocity-selective Raman pulse (bottom red beam in Fig. 2) is used to select the atoms in the $m_F = 0$ Zeeman sub-level of the $F = 2$ hyperfine state, with a relatively narrow velocity class (width of 1 photon recoil, corresponding to a temperature of ≈ 400 nK in the direction of the Raman lasers). The unselected atoms are then pushed by a laser tuned on resonance with the cycling transition. This Raman/push procedure is repeated a second time to clean the remaining unwanted atoms produced by spontaneous emission on the first Raman selection pulse. For this purpose, we use the Raman 2 beam (top big red beam) with the approximately same duration and Rabi frequency as the Raman 1 beam to transfer the atoms back to the $F = 2$ state. The remaining atoms in the $F = 1$ state are pushed with an orthogonal push beam tuned on the $F = 1 \rightarrow F' = 0$ transition (gray beam at the top). The angle of the Raman beams can be tuned by few degrees around zero in order to introduce a Doppler effect which allows lifting the degeneracy between the $|p\rangle \rightarrow |p + 2\hbar k\rangle$ and $|p\rangle \rightarrow |p - 2\hbar k\rangle$ transitions. In this way, the atoms will enter the interferometer in a well-defined momentum state. Moreover, the Raman beam angle enables to control the angle of the trajectory with respect to the vertical direction, i.e. the Bragg angle. After this all-optical preparation steps, the atoms enter the interferometer in the

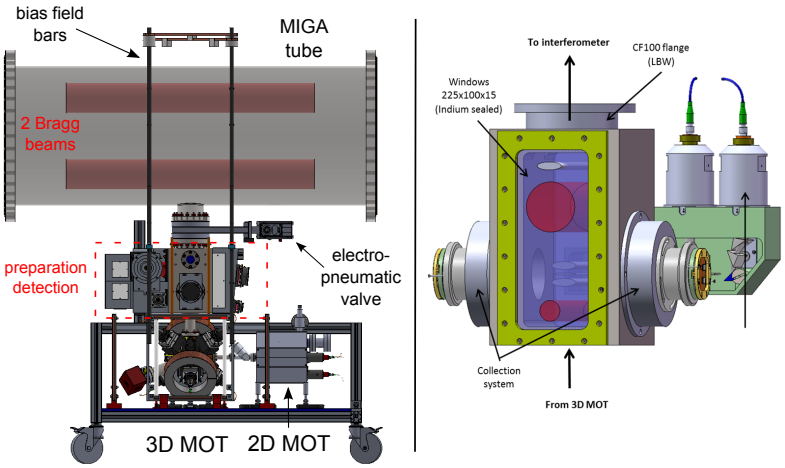

Figure 2 – Left: Global view of the cold atom source unit. Right: technical drawing of the cold atom preparation and detection region.

$|F = 2, m_F = 0\rangle$ internal state, with a relatively narrow velocity distribution in the longitudinal direction of the Bragg interrogation beams and with a well-controlled trajectory.

After their interrogation by the Bragg beams in the atom interferometer, the two different momentum states $|\pm \hbar k\rangle$ of the atoms are labelled to two different internal states with the Raman 2 laser. More precisely, the velocity selective feature of the Raman transition is used to transfer the $|F = 2, \hbar k\rangle$ atoms to the $F = 1$ internal state, while the $|F = 2, -\hbar k\rangle$ atoms remain in the $F = 2$ internal state. The atoms can then be resolved with common fluorescence techniques. Detection of the atoms labelled in $F = 2$ is first realized with a light sheet beam (see Fig. 2) tuned on resonance on the $F = 2 \rightarrow F' = 3$ transition. The beam is partially blocked at the retroreflection mirror so that the atoms acquire a net momentum in the beam direction and will therefore not be resonant with the following light beams. The $F = 1$ atoms are re-pumped to the $F = 2$ state using a thinner intermediate light sheet, before these $F = 2$ atoms enter the third light sheet. The fluorescence light of the two light sheets is collected by a 2% collection efficiency lens and imaged on a two-quadrant photodiode, one quadrant recording the fluorescence associated with one detection zone. The fluorescence signal is used to reconstruct the normalized atomic populations and then the transition probability, yielding the atom interferometer phase.

3.2 Laser System.

The different lasers used to cool and manipulate the atoms are delivered from an all-fibered laser module developed by the company muQuans[8]. The laser architecture is based on frequency doubled telecom lasers, as already described in various publications, see e.g. Refs.[9]. A Master laser is locked using a Rubidium 85 saturated absorption spectroscopy signal and references 3 slave diodes which are respectively used for the 2D MOT cooling laser, the 3D MOT cooling/Raman 2 laser, and the 3D MOT repumper/Raman 1 laser. The 3 slave diodes are all phase locked to the Master laser. The repumping light for the 2D MOT is generated from a fiber electro-optic phase modulator at 1560 nm fed with the appropriate microwave frequency.

After amplification in Erbium doped fiber amplifiers and second harmonic generation in PPLN waveguide cristals, the 780 nm light is send to optical splitters and guided to the experiment chamber in several optical fibers. The laser module nominally delivers 170 mW total power for the 2D MOT (fiber outputs), 150 mW total power for the 3D MOT, and 100 + 75 mW in each of the two Raman beams used for the preparation stage and the detection. The power and polarization fluctuations at the fiber outputs are close to the one percent level. The phase

lock signals are controlled by various radio-and-microwave frequency sources all referenced to a stable 100 MHz oscillator. The full laser system is hosted in a $1.7 \times 0.5 \times 0.5$ m^3 transportable rack.

3.3 Optical cavity setup

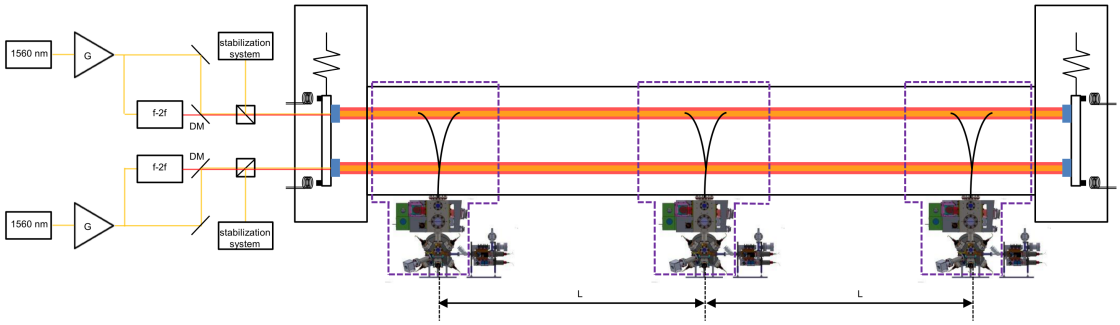

Figure 3 – **Overview of the MIGA cavity with the main sub-systems.** The three atomic heads separated by a distance L launch atomic clouds in an almost vertical parabolic flight. The atoms are manipulated in the upper part of the parabola with a Bragg interferometric sequence by way of radiation pulses at 780 nm (red lines) resonant with two horizontal cavities. The resonance condition for the interrogation light relies on generating the 780 nm via frequency doubling of a 1560 nm laser (yellow lines) locked to one of the two cavities, and using stabilized, common payloads for the mirrors on each side of the cavities to avoid relative length fluctuations of the two resonators. The Ultra High Vacuum system encompassing the optical cavities, the mirror payloads and their stabilization system is represented with gray solid lines; to it are connected the atomic source units. Each interferometric region and most of the related atomic head are enclosed in a mu-metal shield, represented in dashed violet lines. The control system of the experimental setup and the laser systems dedicated to each atomic head are not represented in the plot.

The intensity of the Bragg pulses is enhanced thanks to two cavities, one for the splitting and projection $\pi/2$ pulses, and one at the trajectories' apogee for the π pulse. The solution adopted to have the 780 nm interrogation pulses at resonance with the cavities relies on obtaining the probe radiation via frequency doubling of a telecom laser at 1560 nm continuously locked to one of the two resonators to track its length variations. The servo system is used also to control the payload tilts and rotations so as to maintain the phase coherence between the two cavities. The Bragg pulses are shaped with acousto-optic modulators (AOMs) on the two beams at 780 nm before their injection in the cavities. The telecom laser is phase modulated and locked to the cavity on one frequency sideband, and the modulation frequency Ω is chosen so as to have the doubled component of the carrier resonant with the resonator. Ω has to account for the different cavity length at 780 nm and 1560 nm, because of the refraction index of the two coatings on the mirrors, as well as for the frequency shift imposed by the AOM used to pulse the interrogation beams. The LP2N laboratory is currently developing a prototype system using low power laser sources (100 mW at 1560 nm, and 1 W at 780 nm). The CELIA laboratory at Bordeaux 1 University is developing a high power solution, which targets 100 W of radiation at 780 nm before the injection in the cavity.

The two cavities share a common payload on each side to hold the mirrors, placed at a vertical distance of ≈ 30.6 cm to have an interrogation time $T = 250$ ms. The impact of ground seismic noise on the position of the cavity mirrors will be reduced by way of an antivibration system, which must limit the related phase noise contribution on each atom interferometer. Two different approaches are being considered: a passive system of mechanical filters to suspend each payload, and an active stabilization of each mirror position using piezoelectric actuators. The main constraints on the system are set by the level of the seismic noise at the installation site

(LSBB), and the response function of the atom interferometers to mirror acceleration noise, as in Eq. (1).

4 High sensitivity atom interferometry techniques

The performance of the MIGA antenna will rely on the possibility to achieve high sensitivity gravito-inertial measurements. Moreover, future applications to gravitational wave detection will require higher bandwidth (~ 10 Hz) cold atom interferometers than what is currently obtained in laboratories (about 1 Hz for long T AIs). In this section, we briefly present two results obtained at the SYRTE laboratory on an atom interferometer which geometry is similar to the fountain-like architecture of the MIGA sensors.

First, we demonstrated a new method to interrogate several clouds of cold atoms simultaneously in the interferometer in a so-called joint interrogation scheme [10] (the principle of the joint interrogation is represented in Fig. 4, left panel). Conventional cold atom interferometers run in sequential mode: after laser cooling, the cold atoms are injected in the interferometer where the inertial effects are measured. Thus, the sensor does not operate continuously. Information on signals varying during the cold atom source preparation is lost, which is a major drawback for various applications. Moreover, the aliasing effect of the vibration noise associated with the dead time results in a degradation of the short term sensitivity. To circumvent this problem, the joint interrogation solution compatible with the MIGA fountain geometry allows interrogating the atoms in the interferometer region, while another cold atom cloud is being prepared simultaneously. This leads to a zero-dead time gyroscope. Moreover, if the different atom clouds share common (Bragg) interrogation pulses, the vibration noise is correlated between the successive measurements, which leads to a faster averaging of the vibration noise. We demonstrated a multiple joint operation in which up to five clouds of atoms were interrogated simultaneously in a single fountain with $2T = 800$ ms interrogation time [10]. The essential feature of the multiple joint operation, which we demonstrated for a micro-wave Ramsey interrogation is currently being generalized to the inertial sensor operation. The multiple joint operation gives access to high-frequency components while maintaining high sensitivity linked to long interaction times achievable with cold atom sensors.

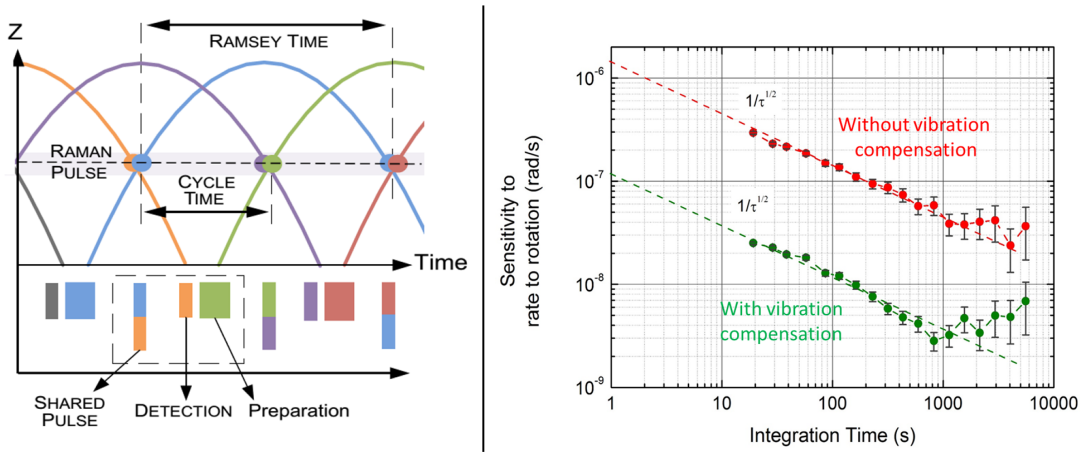

Figure 4 – **New atom interferometry techniques for high precision inertial measurements.** Left: schematic of the joint interrogation technique allowing the interrogation of several clouds of atoms simultaneously in the interferometer and rejection of vibration noise aliasing due to dead times. From Ref. [10]. Right: SYRTE cold atom gyroscope with a 3 nrad/s after 1000 s of integration time using a Sagnac matter-wave interferometer of 2.4cm^2 area [11,12].

A second key feature of MIGA will be to operate an atom interferometer with a long inter-

rogation time, $2T = 500$ ms, yielding a high accelerometer scale factor $2kT^2$. In this regime, the effect of vibrations from the payload results in several radians of AI phase noise and must be managed to keep it below the targeted phase sensitivity level (ideally below the atom shot noise of ~ 1 mrad). While vibration noise is common to the different AIs in the gradiometer configuration of MIGA, the extraction of the AI phase still requires the Atom interferometer to be operated in its linear range, i.e. $[0 - \pi]$. Moreover, being able to extract the individual AI phase yields the absolute local gravity field (in the direction of the Bragg beams) and therefore provides additional information to the gravity gradient and its curvature. To this end, we demonstrated in the SYRTE experiment the possibility to reject the vibration noise with a factor up to 20 using classical accelerometers in an interferometer with $2T = 800$ ms interrogation time. This noise rejection was performed in a gyroscope configuration where the AI mainly senses rotation rates, allowing us to demonstrate a gyroscope with 3 nrad/s long term stability (see Fig. 4, right panel). These results strongly support the possibility to obtain high sensitivity gravity measurements with the MIGA interferometers.

5 MIGA: new perspectives in geosciences

5.1 Hydrological interest of the Fontaine de Vaucluse/LSBB site

Almost a quarter of the world population obtains its drinking water from karst hydrosystems [13] (see Fig. 5 for a schematic). Efficient protection and sustainable management of such resources require appropriate tools and strategies to be developped [14]. The numerical modelling of karst aquifers is probably the major stumbling block in developing such tools. Karst remains aside from other hydrosystems, because the paroxismal [15] and self-organized [16] heterogeneity of that medium limits the relevance of classical hydrogeological tools, such as physically-based and gridded flow models, and because of the difficulty of characterisation of this heterogeneity. Hopefully, recent improvements of computing power and computational techniques in the one hand and geophysical measurement techniques in the other hand [17] enable considering now the applicability of physically-based and gridded flow models to karst hydrodynamics. However the Holy Grail to achieve developing and fitting such tools remains acquiring 4D hydro-geo-physical data (water content, flux and velocities, ...) at different scales.

In south-eastern France, the Fontaine-de-Vaucluse karst hydrosystem is one of the biggest karst watershed in the world: its catchment area is around 1115 km^2 and composed of a nearly 1500 m thick massive and continuous limestone [18,19] from Necomanian marls to upper Aptian marls. The Fontaine-de-Vaucluse spring is quite the only outlet of this hydrosystem and the biggest karst spring in Europe with an average outlet discharge of 19 m^3/s between 1877 and 2004 [20]. Within this peculiar karst hydrosystem, LSBB (Low Noise Underground Research Laboratory) is an almost horizontal tunnel coming across the karst medium and intersecting arbitrarily faults, karst networks and flowpaths at depths between 0 and 519 m. All these elements make the Fontaine-de-Vaucluse and LSBB sites a relevant multi-scales observatory to develop physically-based and gridded flow models to karst hydrodynamics based on innovative 4D hydro-geo-physical data acquisition.

5.2 Methods

Whereas recent developments of geophysical methods enable to expect better characterization of complex hydrosystems [17], their application to karst remains not obvious [21]. Nevertheless, various conventional techniques and instruments are currently applied to karst hydrogeology such as Electrical Resisitivty Tomography (ERT) and 2D Ground Penetration Radar (GPR). One of the important questions is to have enough resolution and depth of investigation all at once to detail all the features controlling the groundwater circulation and storage from matrix porosity or micro-fracturing to major faults and karst conduits . On the other hand, estimating

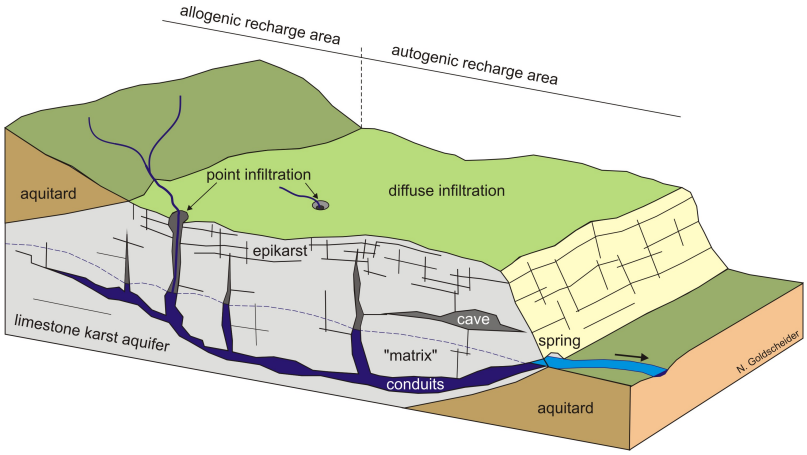

Figure 5 – Block diagram illustrating the hydrogeological functioning of a karst aquifer, from N Goldscheider, D Drew (2007), *Methods in Karst Hydrogeology*, Taylor et Francis, http://www.agw.kit.edu/english/3851.php.

the variation of water mass requires the use of integrating methods directly or indirectly related to water content such as seismic, ERT, Magnetic Resonance Sounding (MRS) or Gravimetry. For instance, as shown in Ref. [22], GPR results supply a near surface high resolution ($\sim$ 10 cm) imaging and thus can provide relevant geological information such as stratifications and fractures. However, GPR's investigation depth remains limited to around 12 meters. ERT surveys shows strong lateral and vertical variations which can inform on general geological structuring and feature orientation. ERT is able to prospect down to 40 meters but is a low resolution integrative technique. Finally, active seismic reflection imaging or transmission tomography (at frequencies $\sim 10 - 500$ Hz) allows measuring the ground seismic velocities and probing the rock elasticity and porosity, yielding information on the rock structure and fractures [23]. The corresponding resolution is $\sim$ 10 m with accessible depth $\sim$ 100 m.

In contrast to these techniques requiring an inversion model, Atom Interferometry can provide direct measurements of the surrounding mass distribution and thus represents an interesting complementary method. Moreover, long-term (years) measurements of the gravity field can be obtained thanks to the long term stability of cold atom sensors. In this context, MIGA will provide non-invasive long-term (years) measurements of the gravity field on a $\sim$ 1 km-long baseline. As discussed in section 2, the typical gradiometer sensitivity of MIGA will be $\sim 10^{-13}$ s^{-2} after 100 s of measurement time, with a maximum sensitivity in the direction of the baseline. Such gravity gradients typically correspond to water masses of 1 ton at 100 meter from the instrument. If the source mass producing such gravity gradients moves in time, the AI antenna signal will vary accordingly. The spatial resolution of the antenna will depend on the number of atom interferometers and their relative distance (3 units separated by 100 m in the first version of MIGA) and the targeted confidence level for the positioning of the source mass. Tuning the AI geometry (inter-pulse duration T, more light pulses, etc.) allows changing the response of the sensor to the source mass thus yielding more information.

6 Conclusion and perspectives

The MIGA instrument will use long baseline (300 m) optical and matter-wave interferometry for high precision gravity field measurements, in order to monitor subsurface mass transfers in the LSBB region, which represents a unique site of hydrological interest. Combining conventional instruments and methods from hydrogeology with cold atom gravitation sensor measurements will allow better modelling of karst acquifers, for which only very few (3+1)-dimensional data are currently available to constrain the models. MIGA will also investigate the applications of

atom interferometry to extend the sensitivity of future GW detectors at frequencies below 10 Hz.

The first cold atom source unit has been characterized and will be installed at LP2N (Talence) in June 2015, where the first experiments on AI in the 1 meter optical cavity will be performed. A 6 meter AI gradiometer prototype based at LP2N is currently under design and will allow testing at a reduced scale the measurement strategy for mass monitoring at LSBB. Digging of the galleries at LSBB is planed for the beginning of 2016, with an installation of the 300 meter long vacuum cavity and the three AI units in 2017. Following the final optimizations of the instrument, the operation phase should start in 2018.

The MIGA Equipex aims at being the first step to a larger, more ambitious program that may lead to a future European infrastructure. The development, the scientific operation and the technical implementation of this first version of the gravitational antenna will pave the way to a more sensitive version that will take advantage of the current fundamental research in advanced atom interferometry. The MIGA instrument and its envisioned evolution will ensure France and Europe's position at the forefront of subterranean instrumentation and a leadership in key quantum technologies. Beyond the development of this equipment, the results of the MIGA project can be anticipated for use in future gravitational wave detectors in order to enhance their low frequency sensitivity.

Acknowledgments

The MIGA Equipex is funded by ANR under the programme *Investissement d'Avenir* (ANR-11-EQPX-0028). We also thank funding from the city of Paris (Emergence project HSENS-MWGRAV), Délégation Générale pour l'Armement (DGA) and CNES.

References

1. Rym Bouchendira and et al. New determination of the fine structure constant and test of the quantum electrodynamics. Phys. Rev. Lett., 106:080801, Feb 2011.
2. D. Schlippert and et al. Quantum test of the universality of free fall. Phys. Rev. Lett., 112:203002, May 2014.
3. G. Rosi and et al. Precision measurement of the newtonian gravitational constant using cold atoms. Nature, 510(7506):518–521, June 2014.
4. M Thomas and et al. First determination of the planck constant using the lne watt balance. Metrologia, 52(2):433, 2015.
5. P Gillot and et al. Stability comparison of two absolute gravimeters: optical versus atomic interferometers. Metrologia, 51(5):L15, 2014.
6. Peter J. Martin, Bruce G. Oldaker, Andrew H. Miklich, and David E. Pritchard. Bragg scattering of atoms from a standing light wave. Phys. Rev. Lett., 60:515–518, Feb 1988.
7. P. Cheinet and et al. Measurement of the sensitivity function in time-domain atomic interferometer. IEEE Trans. on Instrum. Meas, 57:1141, 2008.
8. http://www.muquans.com/.
9. V. Ménoret and et al. Dual-wavelength laser source for onboard atom interferometry. Opt. Lett., 36(21):4128–4130, Nov 2011.
10. M. Meunier, I. Dutta, and et al. Stability enhancement by joint phase measurements in a single cold atomic fountain. Phys. Rev. A, 90:063633, Dec 2014.
11. I. Dutta, D. Savoie, B. Fang, R. Geiger, A. Landragin, in preparation.
12. Brynle Barrett and et al. The sagnac effect: 20 years of development in matter-wave interferometry. Comptes Rendus Physique, 15(10):875–883, December 2014.
13. D. C. Ford and P. W. Williams. Karst hydrogeology and geomorphology,. John Wiley & Sons, Chichester., 2007.
14. M. Mudarra, B. Andreo, and J. Mudry. Hydrochemical heterogeneity in the discharge

zone of a karstic aquifer. In Environmental Earth Sciences, pages 163–168. Springer Berlin Heidelberg, 2010.
15. de Marsily, Mthodes et domaines d'application de la mcanique des fluides en milieux poreux et fissurs. Annales des Mines, 1984, 5-6, 5-10 (1984).
16. S.R.H. Worthington and D.C. Ford. Self-organized permeability in carbonate aquifers. Ground Water, 47(3):326–336, 2009.
17. Brian Berkowitz. Characterizing flow and transport in fractured geological media: A review. Advances in Water Resources, 25(8??12):861–884, August 2002.
18. Masse, J.P. 1969. Contribution a l'tude de l'Urgonien (Barrmien - Bdoulien) des Monts de vaucluse et du Luberon. Bureau de Recherches Gologiques et Mini?res, Orlan, 59 p.
19. Masse, J.P. 1976. Les calcaires urgoniens de Provence ; Valanginien - Aptien infrieur ; Tome 1 : Stratigraphie - Palontologie ; Tome 2 : Les paloenvironnements et leur volution. Thesis: Univ. d'Aix-Marseille, 445 p.
20. Cognard-Plancq, A. L., C. Gevaudan, and C. Emblanch. 2006. Historical monthly rainfall-runoff database on Fontaine de Vaucluse karst system : review and lessons. Proceedings of 3rd international symposium on karst "Groundwater in the Mediterranean Countries", Malaga, Spain, IGME Publications, vol 18, pp 465-475.
21. Konstantinos Chalikakis and et al. Contribution of geophysical methods to karst-system exploration: an overview. Hydrogeology Journal, 19:1169–1180, 2011.
22. Simon D. Carrière and et al. Combining electrical resistivity tomography and ground penetrating radar to study geological structuring of karst unsaturated zone. Journal of Applied Geophysics, 94(0):31–41, July 2013.
23. Emeline Maufroy et al, Travel time inversion from ground level to gallery: protocol for the characterization of P-wave seismic signature in a fractured-porous Urgonian platform at hectometric scale, Near Surface Geophysics Vol 12, No 6, December 2014 pp. 697 - 708.

Bibliography

[1] Anthony Lawrence. *Modern Inertial Technology*. Mechanical Engineering Series. Springer New York, New York, NY, 1998. ISBN 978-1-4612-7258-8 978-1-4612-1734-3. URL http://link.springer.com/10.1007/978-1-4612-1734-3. ↑ 1

[2] Heiner Igel, Alain Cochard, Joachim Wassermann, Asher Flaws, Ulrich Schreiber, Alex Velikoseltsev, and Nguyen Pham Dinh. Broad-band observations of earthquake-induced rotational ground motions. *Geophysical Journal International*, 168(1):182–196, January 2007. ISSN 1365-246X. doi: 10.1111/j.1365-246X.2006.03146.x. URL http://onlinelibrary.wiley.com/doi/10.1111/j.1365-246X.2006.03146.x/abstract. ↑ 1

[3] Clifford M. Will. The Confrontation between General Relativity and Experiment. *Living Reviews in Relativity*, 9, 2006. ISSN 1433-8351. doi: 10.12942/lrr-2006-3. URL http://www.livingreviews.org/lrr-2006-3. ↑ 1

[4] G. Sagnac. Effet tourbillonnaire optique. La circulation de l'éther lumineux dans un interférographe tournant. *Journal de Physique Théorique et Appliquée*, 4(1): 177–195, 1914. ISSN 0368-3893. doi: 10.1051/jphystap:019140040017700. URL http://www.edpsciences.org/10.1051/jphystap:019140040017700. ↑ 1, ↑ 13

[5] T. L. Gustavson, P. Bouyer, and M. A. Kasevich. Precision Rotation Measurements with an Atom Interferometer Gyroscope. *Physical Review Letters*, 78 (11):2046–2049, March 1997. doi: 10.1103/PhysRevLett.78.2046. URL http://link.aps.org/doi/10.1103/PhysRevLett.78.2046. ↑ 1, ↑ 2

[6] Alan Lenef, Troy D. Hammond, Edward T. Smith, Michael S. Chapman, Richard A. Rubenstein, and David E. Pritchard. Rotation Sensing with an Atom Interferometer. *Physical Review Letters*, 78(5):760–763, February 1997. doi: 10.1103/PhysRevLett.78.760. URL http://link.aps.org/doi/10.1103/PhysRevLett.78.760. ↑ 1, ↑ 2, ↑ 7

[7] Brynle Barrett, Rémy Geiger, Indranil Dutta, Matthieu Meunier, Benjamin Canuel, Alexandre Gauguet, Philippe Bouyer, and Arnaud Landragin. The Sagnac effect: 20 years of development in matter-wave interferometry. *Comptes Rendus Physique*, 15(10):875–883, December 2014. ISSN 1631-0705. doi: 10.1016/j.crhy.2014.10.009. URL http://www.sciencedirect.com/science/article/pii/S1631070514001467. ↑ 1

[8] F. Riehle, Th. Kisters, A. Witte, J. Helmcke, and Ch. J. Bordé. Optical Ramsey spectroscopy in a rotating frame: Sagnac effect in a matter-wave interferometer. *Physical Review Letters*, 67(2):177–180, July 1991. doi: 10.1103/PhysRevLett.67.177. URL http://link.aps.org/doi/10.1103/PhysRevLett.67.177. ↑ 1, ↑ 2

[9] T. L. Gustavson, A. Landragin, and M. A. Kasevich. Rotation sensing with a dual atom-interferometer Sagnac gyroscope. *Classical and Quantum Gravity*, 17(12):2385, 2000. ISSN 0264-9381. doi: 10.1088/0264-9381/17/12/311. URL http://stacks.iop.org/0264-9381/17/i=12/a=311. ↑ 2, ↑ 112

[10] B. Canuel, F. Leduc, D. Holleville, A. Gauguet, J. Fils, A. Virdis, A. Clairon, N. Dimarcq, Ch. J. Bordé, A. Landragin, and P. Bouyer. Six-Axis Inertial Sensor Using Cold-Atom Interferometry. *Physical Review Letters*, 97(1):010402, July 2006. doi: 10.1103/PhysRevLett.97.010402. URL http://link.aps.org/doi/10.1103/PhysRevLett.97.010402. ↑ 2, ↑ 16, ↑ 115

[11] P. Berg, S. Abend, G. Tackmann, C. Schubert, E. Giese, W.?P. Schleich, F.?A. Narducci, W. Ertmer, and E.?M. Rasel. Composite-Light-Pulse Technique for High-Precision Atom Interferometry. *Physical Review Letters*, 114(6):063002, February 2015. doi: 10.1103/PhysRevLett.114.063002. URL http://link.aps.org/doi/10.1103/PhysRevLett.114.063002. ↑ 2, ↑ 112, ↑ 135

[12] K. U. Schreiber, T. Klügel, J.-P. R. Wells, R. B. Hurst, and A. Gebauer. How to Detect the Chandler and the Annual Wobble of the Earth with a Large Ring Laser Gyroscope. *Physical Review Letters*, 107(17):173904, October 2011. doi: 10.1103/PhysRevLett.107.173904. URL http://link.aps.org/doi/10.1103/PhysRevLett.107.173904. ↑ 2

[13] J. Lautier, L. Volodimer, T. Hardin, S. Merlet, M. Lours, F. Pereira Dos Santos, and A. Landragin. Hybridizing matter-wave and classical accelerometers. *Applied Physics Letters*, 105(14):144102, October 2014. ISSN 0003-6951, 1077-3118. doi:

10.1063/1.4897358. URL http://scitation.aip.org/content/aip/journal/apl/105/14/10.1063/1.4897358. ↑ 3, ↑ 116, ↑ 134, ↑ 137

[14] M. Meunier, I. Dutta, R. Geiger, C. Guerlin, C. L. Garrido Alzar, and A. Landragin. Stability enhancement by joint phase measurements in a single cold atomic fountain. *Physical Review A*, 90(6):063633, December 2014. doi: 10.1103/PhysRevA.90.063633. URL http://link.aps.org/doi/10.1103/PhysRevA.90.063633. ↑ 3, ↑ 115

[15] A. Gauguet, B. Canuel, T. Lévèque, W. Chaibi, and A. Landragin. Characterization and limits of a cold-atom Sagnac interferometer. *Physical Review A*, 80(6):063604, December 2009. doi: 10.1103/PhysRevA.80.063604. URL http://link.aps.org/doi/10.1103/PhysRevA.80.063604. ↑ 3, ↑ 36, ↑ 112

[16] Matthieu Meunier. *Etude d'un gyromètre à ondes de matière de très grande aire*. phdthesis, Université Pierre et Marie Curie - Paris VI, December 2013. URL https://tel.archives-ouvertes.fr/tel-01053196/document. ↑ 3, ↑ 4, ↑ 34, ↑ 52, ↑ 69, ↑ 118, ↑ 121, ↑ 131

[17] Hervé C. Lefèvre. The fiber-optic gyroscope, a century after Sagnac's experiment: The ultimate rotation-sensing technology? *Comptes Rendus Physique*, 15(10):851–858, December 2014. ISSN 1631-0705. doi: 10.1016/j.crhy.2014.10.007. URL http://www.sciencedirect.com/science/article/pii/S1631070514001443. ↑ 3, ↑ 138

[18] Karl Ulrich Schreiber, André Gebauer, Heiner Igel, Joachim Wassermann, Robert B. Hurst, and Jon-Paul R. Wells. The centennial of the Sagnac experiment in the optical regime: From a tabletop experiment to the variation of the Earth's rotation. *Comptes Rendus Physique*, 15(10):859–865, 2014. ISSN 1631-0705. doi: 10.1016/j.crhy.2014.10.003. URL http://www.sciencedirect.com/science/article/pii/S1631070514001406. ↑ 3

[19] Thomas Lévèque. *Développement d'un gyromètre à atomes froids de haute sensibilité fondé sur une géométrie repliée*. phdthesis, Université Pierre et Marie Curie - Paris VI, September 2010. URL https://tel.archives-ouvertes.fr/tel-00532789/document. ↑ 4, ↑ 27, ↑ 37

[20] Paul R. Berman. *Atom Interferometry*. Academic Press, January 1997. ISBN 978-0-08-052768-0. ↑ 7

[21] Michael S. Chapman, Christopher R. Ekstrom, Troy D. Hammond, Jörg Schmiedmayer, Bridget E. Tannian, Stefan Wehinger, and David E. Pritchard. Near-field imaging of atom diffraction gratings: The atomic Talbot effect. *Physical Review A*, 51(1):R14–R17, January 1995. doi: 10.1103/PhysRevA.51.R14. URL http://link.aps.org/doi/10.1103/PhysRevA.51.R14. ↑ 7

[22] G. Rosi, L. Cacciapuoti, F. Sorrentino, M. Menchetti, M. Prevedelli, and G.?M. Tino. Measurement of the Gravity-Field Curvature by Atom Interferometry. *Physical Review Letters*, 114(1):013001, January 2015. doi: 10.1103/PhysRevLett.114.013001. URL http://link.aps.org/doi/10.1103/PhysRevLett.114.013001. ↑ 7

[23] Nadine Dörre, Jonas Rodewald, Philipp Geyer, Bernd von Issendorff, Philipp Haslinger, and Markus Arndt. Photofragmentation Beam Splitters for Matter-Wave Interferometry. *Physical Review Letters*, 113(23):233001, December 2014. doi: 10.1103/PhysRevLett.113.233001. URL http://link.aps.org/doi/10.1103/PhysRevLett.113.233001. ↑ 7

[24] Mark Kasevich and Steven Chu. Atomic interferometry using stimulated Raman transitions. *Physical Review Letters*, 67(2):181–184, July 1991. doi: 10.1103/PhysRevLett.67.181. URL http://link.aps.org/doi/10.1103/PhysRevLett.67.181. ↑ 8, ↑ 12, ↑ 13

[25] Kathryn Moler, David S. Weiss, Mark Kasevich, and Steven Chu. Theoretical analysis of velocity-selective Raman transitions. *Physical Review A*, 45(1):342–348, January 1992. doi: 10.1103/PhysRevA.45.342. URL http://link.aps.org/doi/10.1103/PhysRevA.45.342. ↑ 9

[26] L. Allen and J. H. Eberly. *Optical Resonance and Two-Level Atoms*. Courier Corporation, May 2012. ISBN 978-0-486-13617-2. ↑ 10

[27] F. Hasselbach and M. Nicklaus. An electron optical sagnac experiment. *Physica B+C*, 151(12):230–234, July 1988. ISSN 0378-4363. doi: 10.1016/0378-4363(88)90171-4. URL http://www.sciencedirect.com/science/article/pii/0378436388901714. ↑ 13

[28] Franz Hasselbach and Marc Nicklaus. Sagnac experiment with electrons: Observation of the rotational phase shift of electron waves in vacuum. *Physical Review A*, 48(1):143–151, July 1993. doi: 10.1103/PhysRevA.48.143. URL http://link.aps.org/doi/10.1103/PhysRevA.48.143. ↑ 13

[29] W. W. Chow, J. Gea-Banacloche, L. M. Pedrotti, V. E. Sanders, W. Schleich, and M. O. Scully. The ring laser gyro. *Reviews of Modern Physics*, 57(1):61–104, January 1985. doi: 10.1103/RevModPhys.57.61. URL http://link.aps.org/doi/10.1103/RevModPhys.57.61. ↑ 13

[30] Benjamin Canuel. *Étude d'un gyromètre à atomes froids*. phdthesis, Université Paris Sud - Paris XI, March 2007. URL https://tel.archives-ouvertes.fr/tel-00193288/document. ↑ 14, ↑ 28, ↑ 63

[31] Athanasios Papoulis and S. Unnikrishna Pillai. *Probability, Random Variables, and Stochastic Processes, Fourth Edition*. 2002. ISBN 978-0-07-366011-0. URL http://adsabs.harvard.edu/abs/2002prvs.book.....P. ↑ 20

[32] P. Cheinet. *Conception et réalisation d'un gravimètre à atomes froids*. phdthesis, Université Pierre et Marie Curie - Paris VI, March 2006. URL https://tel.archives-ouvertes.fr/tel-00070861/document. ↑ 21, ↑ 27, ↑ 49

[33] BM-1 Bench Top Vibration Isolation Platform. URL http://www.minusk.com/products/bm1-bench-top-vibration-isolation-platforms.html. ↑ 21, ↑ 69

[34] Titanium Vacuum Technology - Vista Corporation, . URL http://www.vista-vac.com/titanium_english.html. ↑ 25

[35] ASM Material Data Sheet. URL http://asm.matweb.com/search/SpecificMaterial.asp?bassnum=MTP641. ↑ 25

[36] K. Dieckmann, R. J. C. Spreeuw, M. Weidemüller, and J. T. M. Walraven. Two-dimensional magneto-optical trap as a source of slow atoms. *Physical Review A*, 58(5):3891–3895, November 1998. doi: 10.1103/PhysRevA.58.3891. URL http://link.aps.org/doi/10.1103/PhysRevA.58.3891. ↑ 27

[37] J. Schoser, A. Batär, R. Löw, V. Schweikhard, A. Grabowski, Yu. B. Ovchinnikov, and T. Pfau. Intense source of cold Rb atoms from a pure two-dimensional magneto-optical trap. *Physical Review A*, 66(2):023410, 2002. doi: 10.1103/PhysRevA.66.023410. URL http://link.aps.org/doi/10.1103/PhysRevA.66.023410. ↑ 27

[38] E. L. Raab, M. Prentiss, Alex Cable, Steven Chu, and D. E. Pritchard. Trapping of Neutral Sodium Atoms with Radiation Pressure. *Physical Review Letters*, 59 (23):2631–2634, 1987. doi: 10.1103/PhysRevLett.59.2631. URL http://link.aps.org/doi/10.1103/PhysRevLett.59.2631. ↑ 28

[39] P. L. Gould, P. D. Lett, and W. D. Phillips. New Measurements with Optical Molasses. In Dr Willy Persson and Professor Sune Svanberg, editors, *Laser Spectroscopy VIII*, number 55 in Springer Series in Optical Sciences, pages 64–67. Springer Berlin Heidelberg, 1987. ISBN 978-3-662-15166-2 978-3-540-47973-4. URL http://link.springer.com/chapter/10.1007/978-3-540-47973-4_16. ↑ 28

[40] Ennio Arimondo, W. D. Phillips, and F. Strumia. *Laser Manipulation of Atoms and Ions*. Elsevier, April 1993. ISBN 0-444-59785-9. ↑ 28

[41] J. L. Hall, M. Zhu, and P. Buch. Prospects for using laser-prepared atomic fountains for optical frequency standards applications. *Journal of the Optical Society of America B*, 6(11):2194, November 1989. ISSN 0740-3224, 1520-8540. doi: 10.1364/JOSAB.6.002194. URL https://www.osapublishing.org/josab/abstract.cfm?uri=josab-6-11-2194. ↑ 29

[42] A Clairon, C Salomon, S Guellati, and W. D Phillips. Ramsey Resonance in a Zacharias Fountain. *Europhysics Letters (EPL)*, 16(2):165–170, September 1991. ISSN 0295-5075, 1286-4854. doi: 10.1209/0295-5075/16/2/008. URL http://stacks.iop.org/0295-5075/16/i=2/a=008?key=crossref.0b0242c2d77ff1e2c91f5f87dffffc56. ↑ 29

[43] AD9959 | datasheet and product info 4 Channel 500 MSPS DDS with 10-bit DACs | Analog Devices, . URL http://www.analog.com/en/products/rf-microwave/direct-digital-synthesis-modulators/ad9959.html. ↑ 30

[44] J. Dalibard and C. Cohen-Tannoudji. Laser cooling below the Doppler limit by polarization gradients: simple theoretical models. *Journal of the Optical Society of America B*, 6(11):2023, November 1989. ISSN 0740-3224, 1520-8540. doi: 10.1364/JOSAB.6.002023. URL https://www.osapublishing.org/josab/abstract.cfm?uri=josab-6-11-2023. ↑ 30

[45] C. S. Adams and E. Riis. Laser cooling and trapping of neutral atoms. *Progress in Quantum Electronics*, 21(1):1–79, 1997. ISSN 0079-6727. doi: 10.1016/S0079-6727(96)00006-7. URL http://www.sciencedirect.com/science/article/pii/S0079672796000067. ↑ 30

[46] J. L. Hall, L. Hollberg, T. Baer, and H. G. Robinson. Optical heterodyne saturation spectroscopy. *Applied Physics Letters*, 39(9):680–682, November 1981. ISSN

0003-6951, 1077-3118. doi: 10.1063/1.92867. URL http://scitation.aip.org/content/aip/journal/apl/39/9/10.1063/1.92867. ↑ 31

[47] Si PIN photodiode S5870 | Hamamatsu Photonics. URL http://www.hamamatsu.com/jp/en/product/alpha/S/4106/S5870/index.html. ↑ 37

[48] P. Cheinet, F. Pereira Dos Santos, T. Petelski, J. Le Gouët, J. Kim, K. T. Therkildsen, A. Clairon, and A. Landragin. Compact laser system for atom interferometry. *Applied Physics B*, 84(4):643–646, May 2006. ISSN 0946-2171, 1432-0649. doi: 10.1007/s00340-006-2266-2. URL http://link.springer.com/article/10.1007/s00340-006-2266-2. ↑ 41

[49] T. Lévèque, A. Gauguet, W. Chaibi, and A. Landragin. Low noise amplification of an optically carried microwave signal: application to atom interferometry. *Applied Physics B*, 101(4):723–729, June 2010. ISSN 0946-2171, 1432-0649. doi: 10.1007/s00340-010-4082-y. URL http://link.springer.com/article/10.1007/s00340-010-4082-y. ↑ 43

[50] J Guéna, M Abgrall, A Clairon, and S Bize. Contributing to TAI with a secondary representation of the SI second. *Metrologia*, 51(1):108–120, February 2014. ISSN 0026-1394, 1681-7575. doi: 10.1088/0026-1394/51/1/108. URL http://stacks.iop.org/0026-1394/51/i=1/a=108?key=crossref.4bce0097c4ecc9299f9e9eb4cb278d02. ↑ 45

[51] RF Signal Generator - SG380 Series. URL http://www.thinksrs.com/products/SG380.htm. ↑ 46

[52] James R. Kellogg, Nan Yu, James M. Kohel, Robert James Thompson, David C. Aveline, and Lute Maleki. Longitudinal coherence in cold atom interferometry. *Journal of Modern Optics*, 54(16-17):2533–2540, November 2007. ISSN 0950-0340. doi: 10.1080/09500340701553030. URL http://dx.doi.org/10.1080/09500340701553030. ↑ 47

[53] AD9852 | datasheet and product info CMOS 300 MSPS Complete DDS | Analog Devices, . URL http://www.analog.com/en/products/rf-microwave/direct-digital-synthesis-modulators/ad9852.html. ↑ 49

[54] Ch J. Bordé. Atomic interferometry with internal state labelling. *Physics Letters A*, pages 10–12, 1989. ISSN 0375-9601. ↑ 50

[55] G. Tackmann, P. Berg, C. Schubert, S. Abend, M. Gilowski, W. Ertmer, and E. M. Rasel. Self-alignment of a compact large-area atomic Sagnac interferometer. *New Journal of Physics*, 14(1):015002, January 2012. ISSN 1367-2630. doi: 10.1088/1367-2630/14/1/015002. URL http://iopscience.iop.org/1367-2630/14/1/015002. ↑ 50

[56] C. Cohen-Tannoudji. Observation d'un déplacement de raie de résonance magnétique causé par l'excitation optique. *Comptes rendus des séances de l'Académie des Sciences*, (252):394–396, January 1961. URL http://www.phys.ens.fr/~cct/articles/CR-Acad-Sc/CR-Acad-Sc-16-janvier-1961.pdf. ↑ 54

[57] 700 Series High-Precision Tiltmeters. URL http://www.jewellinstruments.com/sensors-and-controls-2/geophysicaltech-sensors/tilt-meters-and-clinometers/700-series-high-precision-tiltmeters/. ↑ 57

[58] NI PCI-4474 - National Instruments, . URL http://sine.ni.com/nips/cds/view/p/lang/en/nid/12205. ↑ 60

[59] W. M. Itano, J. C. Bergquist, J. J. Bollinger, J. M. Gilligan, D. J. Heinzen, F. L. Moore, M. G. Raizen, and D. J. Wineland. Quantum projection noise: Population fluctuations in two-level systems. *Physical Review A*, 47(5):3554–3570, May 1993. doi: 10.1103/PhysRevA.47.3554. URL http://link.aps.org/doi/10.1103/PhysRevA.47.3554. ↑ 62

[60] D. S. Weiss, B. C. Young, and S. Chu. Precision measurement of ?/m Cs based on photon recoil using laser-cooled atoms and atomic interferometry. *Applied Physics B*, 59(3):217–256, September 1994. ISSN 0946-2171, 1432-0649. doi: 10.1007/BF01081393. URL http://link.springer.com/article/10.1007/BF01081393. ↑ 63

[61] CMG-40. URL http://www.guralp.com/products/instruments/cmg-40. ↑ 67

[62] Titan Strong Motion Accelerometer, . URL http://www.nanometrics.ca/products/titan. ↑ 67

[63] LM35 | Analog Output | Local Temperature Sensors | Online datasheet. URL http://www.ti.com/product/LM35/datasheet. ↑ 71

[64] S-15-100-N: Rod magnet Ø 15 mm, height 100 mm (Neodymium Magnets). URL http://www.supermagnete.fr/eng/rod-magnets-neodymium/rod-magnet-diameter-15mm-height-100mm-neodymium-n35-nickel-plated_S-15-100-N. ↑ 75

[65] ES300-series | Products. | Delta-Elektronika.nl. URL http://www.delta-elektronika.nl/en/products/es300-series.html. ↑ 76

[66] J. Le Gouët, T. E. Mehlstäubler, J. Kim, S. Merlet, A. Clairon, A. Landragin, and F. Pereira Dos Santos. Limits to the sensitivity of a low noise compact atomic gravimeter. *Applied Physics B*, 92(2):133–144, June 2008. ISSN 0946-2171, 1432-0649. doi: 10.1007/s00340-008-3088-1. URL http://link.springer.com/article/10.1007/s00340-008-3088-1. ↑ 81

[67] S. Merlet, J. Le Gouët, Q. Bodart, A. Clairon, A. Landragin, F. Pereira Dos Santos, and P. Rouchon. Operating an atom interferometer beyond its linear range. *Metrologia*, 46(1):87, 2009. ISSN 0026-1394. doi: 10.1088/0026-1394/46/1/011. URL http://stacks.iop.org/0026-1394/46/i=1/a=011. ↑ 83

[68] Julien Le Gouët. *Étude des performances d'un gravimètre atomique absolu : sensibilité limite et exactitude préliminaire*. phdthesis, Université Paris Sud - Paris XI, February 2008. URL https://tel.archives-ouvertes.fr/tel-00311422/document. ↑ 86

[69] NI PCIe-6341 - National Instruments, . URL http://sine.ni.com/nips/cds/view/p/lang/en/nid/207407. ↑ 88

[70] Low Noise Voltage Preamplifier - SR560. URL http://www.thinksrs.com/products/SR560.htm. ↑ 88

[71] R. Geiger, V. Ménoret, G. Stern, N. Zahzam, P. Cheinet, B. Battelier, A. Villing, F. Moron, M. Lours, Y. Bidel, A. Bresson, A. Landragin, and P. Bouyer. Detecting inertial effects with airborne matter-wave interferometry. *Nature Communications*, 2:474, September 2011. doi: 10.1038/ncomms1479. URL http://www.nature.com/ncomms/journal/v2/n9/full/ncomms1479.html. ↑ 97, ↑ 137, ↑ 138

[72] J. K. Stockton, K. Takase, and M. A. Kasevich. Absolute Geodetic Rotation Measurement Using Atom Interferometry. *Physical Review Letters*, 107 (13):133001, September 2011. doi: 10.1103/PhysRevLett.107.133001. URL http://link.aps.org/doi/10.1103/PhysRevLett.107.133001. ↑ 99, ↑ 100

[73] M. S. Longuet-Higgins. A Theory of the Origin of Microseisms. *Philosophical Transactions of the Royal Society of London A: Mathematical, Physical and Engineering Sciences*, 243(857):1–35, September 1950. ISSN 1364-503X, 1471-2962. doi: 10.1098/rsta.1950.0012. URL http://rsta.royalsocietypublishing.org/content/243/857/1. ↑ 102

[74] LT1028 - Ultra Low Noise Precision High Speed Op Amps - Linear Technology. URL http://www.linear.com/product/LT1028. ↑ 104

[75] D. S. Durfee, Y. K. Shaham, and M. A. Kasevich. Long-Term Stability of an Area-Reversible Atom-Interferometer Sagnac Gyroscope. *Physical Review Letters*, 97 (24):240801, 2006. doi: 10.1103/PhysRevLett.97.240801. URL http://link.aps.org/doi/10.1103/PhysRevLett.97.240801. ↑ 112

[76] Ronald Legere and Kurt Gibble. Quantum Scattering in a Juggling Atomic Fountain. *Physical Review Letters*, 81(26):5780–5783, 1998. doi: 10.1103/PhysRevLett.81.5780. URL http://link.aps.org/doi/10.1103/PhysRevLett.81.5780. ↑ 115, ↑ 117

[77] Zhong-Kun Hu, Xiao-Chun Duan, Min-Kang Zhou, Bu-Liang Sun, Jin-Bo Zhao, Mao-Mao Huang, and Jun Luo. Simultaneous differential measurement of a magnetic-field gradient by atom interferometry using double fountains. *Physical Review A*, 84(1):013620, 2011. doi: 10.1103/PhysRevA.84.013620. URL http://link.aps.org/doi/10.1103/PhysRevA.84.013620. ↑ 115

[78] G. Rosi, F. Sorrentino, L. Cacciapuoti, M. Prevedelli, and G. M. Tino. Precision measurement of the Newtonian gravitational constant using cold atoms. *Nature*, 510(7506):518–521, 2014. ISSN 0028-0836. doi: 10.1038/nature13433. URL http://www.nature.com/nature/journal/v510/n7506/abs/nature13433.html. ↑ 115

[79] Jay Hyoun Kwon and Christopher Jekeli. Gravity Requirements for Compensation of Ultra-Precise Inertial Navigation. *The Journal of Navigation*, 58(03):479–492, September 2005. ISSN 1469-7785. doi: 10.1017/S0373463305003395. URL http://journals.cambridge.org/article_S0373463305003395. ↑ 116

[80] F. Füzesi, A. Jornod, P. Thomann, M. D. Plimmer, G. Dudle, R. Moser, L. Sache, and H. Bleuler. An electrostatic glass actuator for ultrahigh vacuum: A rotating light trap for continuous beams of laser-cooled atoms. *Review of Scientific*

Instruments, 78(10):103109, October 2007. ISSN 0034-6748, 1089-7623. doi: 10.1063/1.2800777. URL http://scitation.aip.org/content/aip/journal/rsi/78/10/10.1063/1.2800777. ↑ 122

[81] Function Generator - DS345. URL http://www.thinksrs.com/products/DS345.htm. ↑ 122

[82] Programmable Filter - SR640, SR645, SR650. URL http://www.thinksrs.com/products/SR600.htm. ↑ 122

[83] P. Lemonde, G. Santarelli, P. Laurent, F. Pereira dos Santos, A. Clairon, and C. Salomon. The sensitivity function: a new tool for the evaluation of frequency shifts in atomic spectroscopy. In *Frequency Control Symposium, 1998. Proceedings of the 1998 IEEE International*, pages 110–115, 1998. doi: 10.1109/FREQ.1998.717890. ↑ 126, ↑ 127

[84] P. Cheinet, B. Canuel, F. Pereira Dos Santos, A. Gauguet, F. Yver-Leduc, and A. Landragin. Measurement of the Sensitivity Function in a Time-Domain Atomic Interferometer. *IEEE Transactions on Instrumentation and Measurement*, 57(6): 1141–1148, June 2008. ISSN 0018-9456. doi: 10.1109/TIM.2007.915148. ↑ 126, ↑ 127

[85] Brett Altschul, Quentin G. Bailey, Luc Blanchet, Kai Bongs, Philippe Bouyer, Luigi Cacciapuoti, Salvatore Capozziello, Naceur Gaaloul, Domenico Giulini, Jonas Hartwig, Luciano Iess, Philippe Jetzer, Arnaud Landragin, Ernst Rasel, Serge Reynaud, Stephan Schiller, Christian Schubert, Fiodor Sorrentino, Uwe Sterr, Jay D. Tasson, Guglielmo M. Tino, Philip Tuckey, and Peter Wolf. Quantum tests of the Einstein Equivalence Principle with the STEQUEST space mission. *Advances in Space Research*, 55(1):501–524, January 2015. ISSN 0273-1177. doi: 10.1016/j.asr.2014.07.014. URL http://www.sciencedirect.com/science/article/pii/S0273117714004384. ↑ 138

[86] R. Geiger, L. Amand, A. Bertoldi, B. Canuel, W. Chaibi, C. Danquigny, I. Dutta, B. Fang, S. Gaffet, J. Gillot, D. Holleville, A. Landragin, M. Merzougui, I. Riou, D. Savoie, and P. Bouyer. Matter-wave laser Interferometric Gravitation Antenna (MIGA): New perspectives for fundamental physics and geosciences. *arXiv:1505.07137 [gr-qc, physics:physics]*, May 2015. URL http://arxiv.org/abs/1505.07137. arXiv: 1505.07137. ↑ 138

Indranil DUTTA **20/11/2015**

Sujet : Amélioration de la Stabilité d'un Interféromètre Sagnac à Atomes Froids: vers un Fonctionnement Continu

Résumé : Cette thèse a pour objet de repousser les performances d'un interféromètre à atomes froids principalement sensible aux rotations selon un axe particulier. Des atomes de Cesium sont refroidis par laser, piégés, et lancés verticalement selon une configuration en fontaine. La sensibilité du gyromètre repose sur l'effet Sagnac et est proportionnelle à l'aire physique qu'entourent les deux bras de l'interféromètre. Nous utilisons des transitions Raman stimulées pour séparer les ondes atomiques et former une géométrie d'interféromètre de type Mach-Zehnder replié. Avec un temps d'interrogation de 800 ms, nous parvenons à une aire physique de 11 cm^2. Le manuscrit décrit les améliorations apportées au dispositif expérimental pour faire fonctionner le gyromètre avec une telle aire Sagnac. Une procédure d'alignement relatif des faisceaux Raman au niveau du μrad est présentée et est particulièrement importante pour permettre aux ondes de matière d'interférer. La caractérisation des bruits de vibration impactant la sensibilité du gyromètre, ainsi que sa réjection sont également décrites. Nous démontrons une sensibilité de 160 nrad/s à 1 s, et une stabilité long terme de 1.8 nrad/s après 10000 s d'intégration. Ce niveau de stabilité représente une amélioration d'un facteur 5 par rapport à la précédente expérience de gyromètre du SYRTE de 2009, et d'un facteur 15 par rapport aux autres résultats publiés. Cette thèse présente également une nouvelle méthode d'interrogation des atomes pour opérer le gyromètre sans temps morts, un aspect important pour diverses applications des capteurs à atomes froids en navigation inertielle, en géophysique et en physique fondamentale.

Mots clés : Interférométrie atomique, atomes froids, gyromètre, effet Sagnac, transitions Raman stimulées, capteur inertiel

Subject : Stability Improvement of a Sagnac Cold Atom Interferometer: towards Continuous Operation

Abstract: This thesis aims at pushing the performances of a cold atom interferometer principally sensitive to rates of rotation in a particular axis. In our experiment, Cesium atoms are laser cooled, trapped and launched in a fountain configuration. According to the Sagnac effect, the sensitivity of the interferometer to rotation is proportional to the area enclosed by the interferometer arms. We use stimulated Raman transitions to split the atoms in two paths and to form a folded Mach-Zehnder-like interferometer architecture using four Raman pulses. With an interrogation time of the atoms of 800 ms, we achieve a Sagnac area as high as 11 cm^2. The thesis describes the improvements to the experimental setup to operate the gyroscope with such a high Sagnac area. A procedure for the relative alignment of the Raman beams at the μrad level is presented, which is critical to meet the interference condition of the cold atoms at the interferometer output. The characterization and mitigation of the vibration noise, affecting the gyroscope, is also demonstrated. We finally demonstrate a short term rotation stability of 160 nrad/s at 1 s and a long term stability of 1.8 nrad/s after 10000 s of integration time. This stability level represents a factor 5 improvement compared to the previous SYRTE gyroscope experiment of 2009 and a factor 15 compared to other published results. The thesis work also presents a new method of interrogation to operate the gyroscope without dead times, which is important for various applications of cold atom sensors in inertial navigation, geophysics and in fundamental physics.

Keywords : Atom interferometry, cold atoms, gyroscope, Sagnac effect, stimulated Raman transitions, inertial sensor